High resolution gamma-ray spectroscopy of neutron rich Br and Kr fission fragments

Daniela Reygadas Tello

Université Grenoble Alpes

THÈSE

Pour obtenir le grade de

DOCTEUR DE L'UNIVERSITE GRENOBLE ALPES

Spécialité : **Physique Subatomique et Astroparticules**

Arrêté ministériel : 25 mai 2016

Présentée par

Daniela Reygadas Tello

Thèse dirigée par **Grégoire Kessedjian, CEA**, et
coencadré par **Caterina Michelagnoli, Institut Laue-Langevin**
préparée au sein de l'**Institut Laue-Langevin (ILL) et du Laboratoire de Physique Subatomique et Cosmologie de Grenoble (LPSC)**
dans **l'École Doctorale de Physique**

High resolution gamma-ray spectroscopy of neutron rich Br and Kr fission fragments

Thèse soutenue publiquement le **30 Septembre 2021**
devant le jury composé de :

M Mourad Ramdhane
Professeur à l'Université Grenoble Alpes, President
M^{me} Amel Korichi
Directrice de Recherche au CNRS, IJCLab Orsay, Rapporteur
M Olivier Litaize
Chercheur au CEA Cadarache, Rapporteur
M Alain Astier
Chargé de Recherche au CNRS, IJCLab Orsay, Membre
M Patrick Regan
Professeur à l'Université de Surrey, Membre

Abstract

This thesis work presents new spectroscopic information for neutron rich krypton and bromine nuclei populated in fission experiments. New nuclear excited states were identified in $^{90-95}$Kr, in particular a significant extension of the known level scheme of ^{94}Kr was achieved. For the case of the Br isotopes, new γ-ray transitions were assigned to ^{87}Br, and excited states in ^{89,91,93}Br were observed for the first time. The results presented in this thesis were obtained from the analysis of two fission experiments. A first fission campaign took place at the GANIL facility, where fission of a ^{238}U beam on a Be target was used to produce the isotopes of interest. The fission fragments were identified according to mass and proton number by the VAMOS++ spectrometer, and their structure probed through γ-ray emission detected by the Advanced Gamma Tracking Array (AGATA). A second campaign took place at the research reactor of the Institut Laue-Langevin (ILL), where neutron induced fission of ^{235}U was combined with the FIssion Product Prompt γ-ray Spectrometer (FIPPS). The FIPPS fission campaign employed, for the first time at an intense neutron beam facility, an active fission target. The active target allowed a selection of the fission events, and consequently increased the selectivity and reduced the γ-ray background following β-decay of the fission fragments. The complementarity of the two experimental setups was exploited to perform investigations into prompt γ-ray transitions as well as isomeric states in the range of tens of nanoseconds. Double and triple γ-ray coincidence techniques were employed to construct level schemes of excited states in the Kr and Br isotopes. The capabilities of the FIPPS array for angular correlation measurements, which can be employed for the determination of spins of excited states, were examined. The investigated neutron rich Kr isotopes are located in the low Z boundary of the $A \sim 100$ region, known for a rapid shape change. The study of excited states in the Kr chain allowed a discussion of the evolution of collectivity as well as the appearance of isomeric states as a function of neutron number. An analysis of systematics in the Br chain and neighbouring nuclei enabled the interpretation of a series of newly observed excited states as proton excitations in the $\pi p_{3/2}$, $\pi f_{5/2}$, $\pi p_{1/2}$ and $\pi g_{9/2}$ orbitals. These results were compared to Large Scale Shell Model calculations, providing a benchmark for a new nucleon-nucleon interaction above the ^{78}Ni core.

Résumé

Ce travail de thèse présente de nouvelles informations spectroscopiques sur les noyaux de Kr et de Br, dans la région des nucleides riches en neutron. Ces isotopes ont été produits par des réactions de fission. De nouveaux états excités ont été identifiés dans les noyaux de $^{90-95}$Kr, en particulier une extension significative du schéma de niveaux connu du noyau de ^{94}Kr a été réalisée. Dans le cas des isotopes de Br, de nouvelles transitions ont été attribuées au noyau de ^{87}Br et des états excités dans les noyaux de ^{89,91,93}Br ont été observés pour la première fois. Les résultats présentés dans cette thèse ont été obtenus à partir de l'analyse des données acquises pendant deux expériences de fission. Une première campagne de fission a eu lieu au laboratoire de GANIL, où la fission d'un faisceau de ^{238}U sur une cible de Be a été utilisée pour produire les isotopes d'intérêt. Les fragments de fission ont été identifiés par le spectromètre VAMOS++ en fonction de leur masse et du nombre de protons. Leur structure a été étudiée grâce à l'émission des rayons γ détectés par l'Advanced Gamma Tracking Array (AGATA). Une deuxième campagne s'est déroulée auprès du réacteur de recherche de l'Institut Laue-Langevin (ILL), où la fission de l'^{235}U induite par neutrons a été utilisée comme source des nucleides à etudier, au sein du dispositif FIPPS (FIssion Product Prompt γ-ray Spectrometer). Dans la campagne avec FIPPS, une cible active a été utilisée pour la première fois avec un faisceau intense de neutrons. La cible active a permis de sélectionner les événements de fission et, par conséquent, d'augmenter la sélectivité et de réduire le bruit de fond des rayons γ après la désintégration β des fragments de fission. La complémentarité des deux dispositifs expérimentaux a été exploitée pour étudier les transitions γ promptes ainsi que les états isomériques avec un temps de vie de l'ordre de la dizaine de nanosecondes. Des techniques de coïncidences γ doubles et triples ont été utilisées pour construire/compléter les schémas de niveaux des isotopes du Kr et du Br. Les capacités de FIPPS pour les mesures de corrélation angulaire ont été utilisées pour déterminer les spins des états excités. Les isotopes du Kr riches en neutrons étudiés sont situés dans la limite basse Z de la région $A \sim 100$, connue pour un changement de forme nucléaire rapide. L'étude des états excités dans la chaîne du Kr a permis de discuter l'évolution de la collectivité ainsi que l'occurrence des états isomériques en fonction du nombre de neutrons. Une analyse de la systématique dans la chaîne du Br et des noyaux voisins a permis d'interpréter une série d'états excités nouvellement observés comme des excitations de protons dans les orbitales $\pi p_{3/2}$, $\pi f_{5/2}$, $\pi p_{1/2}$ et $\pi g_{9/2}$. Ces résultats ont été comparés avec des calculs de modèle en couche avec un large espace de valence, permettant de tester une nouvelle interaction nucléon-nucléon au dessus du ^{78}Ni.

Contents

List of Figures

List of Tables

Acknowledgements

Even after years of research specialised in nuclear structure, I am still amazed by the fact that we are capable of studying nuclear properties in such detail. We would not be able to access the nucleus without the combined effort of many scientists over the years. In a similar way, this thesis work would not have been possible without the help of many in the nuclear community. I am thankful to all of you, from the students I have had the pleasure of crossing paths with up to the jury members who have kindly taken the time to discuss my work.

I am extreme grateful to Caterina Michelagnoli, my supervisor for the past three years, for giving me the opportunity to carry out my thesis at the ILL. This work would not have been possible without all that you have taught me. I particularly admire your passion and dedication to the work that you do. Thank you for always being available to discuss, despite all your other commitments. And thank you for all your valuable comments during the writing of the manuscript. I would also like to thank my other supervisor Grégoire Kessedjian. Your feedback during the writing of this manuscript has been very valuable. I also appreciate the help navigating French bureaucracy and the advice on future career options.

Working with the FIPPS collaboration has allowed me to learn from amazing people, I am thankful to all of you. I feel lucky to have shared the office with Felix Kandzia for most of my PhD, thank you for all the help and showing me your way of tackling problems. A sincere thank you to Jérémie Dudouet for all his huge work on the AGATA-VAMOS++ data preparation, the FIPPS programs and always being available for questions. I am grateful to Lukasz Iskra for sharing his knowledge on the data analysis of prompt-delayed coincidences. I highly appreciate the time that Silvia Leoni, Bogdan Fornal, Silvia Lenzi and have taken out of their busy schedules to discuss the interpretation of results and nuclear models. I am very grateful to Frédéric Nowacki for the Large Scale Shell Model calculations he performed for the neutron rich Br isotopes. During my time at the ILL, I have enjoyed sharing FIPPS with many students: Mara, Julia, Chloe, Antonella, Michela and specially Giacomo whom I have spent the most time with and whose Monte Carlo simulations have turned out to be so useful for this work. I would also like to acknowledge the AGATA collaboration, whose combined efforts led to the high quality AGATA-VAMOS++ data presented in this thesis.

It has been a pleasure meeting so many interesting people in the nuclear structure community at workshops, conferences and experiments. A special mention to Alison Bruce and Eugenio Gamba who helped me take my first steps in nuclear structure research and who posses the characteristics that in my opinion make the best scientists: curious and intelligent, while remaining humble and always willing to help.

It has been a privilege carrying out my PhD at the ILL. From the NPP group I would like to acknowledge Michael Jentschel, Yung Hee Kim, Ulli Koester, Tobias Jenke, Thomas Neulinger, Jakob Micko and Mathieu Vialat. I am grateful for the opportunity to learn from such great scientists and value all our discussions. Thank you for also providing a friendly environment. I will take with me good memories of coffee breaks, shared lunches, barbecues and volley-ball matches. A huge thank you to the big ILL PhD family with too many students to list; but with special mention to Shelby and Maddy, for all the wonderful moments lived together, the interesting conversations and all the support throughout this PhD journey. From the LPSC side I am greatly indebted to the CSI formed of Jacob Lamblin and David Maurin.

In addition to a fantastic scientific environment, I have deeply enjoyed the beautiful mountains that Grenoble has to offer. My time here would not have been the same without all the amazing people with whom I have shared many climbing adventures: Rafal, Nico, Aina, Ivan, Milos, Lucas, Arianna, Lucile and Martin.

Mil gracias a mi familia. Gracias a mis padres por su apoyo todos estos años, por enseñarme el poder del conocimiento y por fomentar mi curiosidad por el mundo que nos rodea. Gracias a mi hermana Fer, que se ha convertido en una gran fuente de inspiración y sabiduría a pesar de su juventud.

Enfin, ma plus profonde gratitude à Gabriel, mon partenaire tout au long de ces dernières années. Qui a été là pour me soutenir dans mes moments difficiles de doctorante, ainsi que pour célébrer mes victoires. Merci de croire en moi et de m'inspirer à regarder la vie avec une attitude positive.

Introduction

The atomic nucleus is a complex many body quantum system formed of protons and neutrons interacting through the strong force. In R. Casten's words, the huge number of different nuclides that exist in nature, give rise to an "unbelievably rich and fascinating variety of phenomena" [1]. The goal of nuclear structure studies is to explain this rich phenomenology in the most comprehensive way, ideally starting from the nucleon-nucleon interaction. Since Rutherford's revolutionary discovery of the atomic nucleus in 1911 [2], huge steps forward in the understanding of nuclear structure have been taken, thanks to the development of both nuclear theory and experimental techniques. Theoretical approaches based on a microscopic description of the nucleus such as the Shell Model [3, 4], as well as collective models employing a macroscopic approach [5], are in agreement with basic nuclear properties observed mainly in nuclei close to stability. More than 100 years after the discovery of the nucleus, the nuclear structure community is still facing the challenge of a unified description of structure of nuclei across the nuclear chart.

Theories of nuclear stability predict the existence of up to 7000 nuclei. For decades, nuclear structure studies were dedicated to properties of stable nuclei (~ 250) and nuclei close to stability. In recent years, the development of stable and radioactive beam facilities has opened the door to nuclei increasingly far from stability. These exotic nuclei have led to the discovery of remarkable phenomena and deeper insights into nuclear structure. Nowadays, approximately 4000 nuclei have been experimentally studied. The remaining ~ 3000 define the region of the nuclear chart still to be explored, which is commonly referred to as the *terra incognita* (see Fig. 1). The lack of experimental knowledge is particularly pronounced for the neutron rich side, which is difficult to access experimentally. In addition to their interest from a purely nuclear structure perspective, basic properties of neutron rich nuclei are key ingredients in the understanding of the r-process, responsible for the formation of heavy elements in the universe [6].

The goal of this study is the experimental investigation of the evolution of structure from $N = 50$ to $N = 60$ along the krypton ($Z = 36$) and bromine ($Z = 35$) isotopic chains. The neutron rich Kr isotopes of interest are located at the low Z boundary of the $A \sim 100$ region, region characterised by a rapid onset of deformation. The microscopic origin of this behaviour remains under debate. The odd-mass bromine isotopes investigated in this work are used as a test study of the development

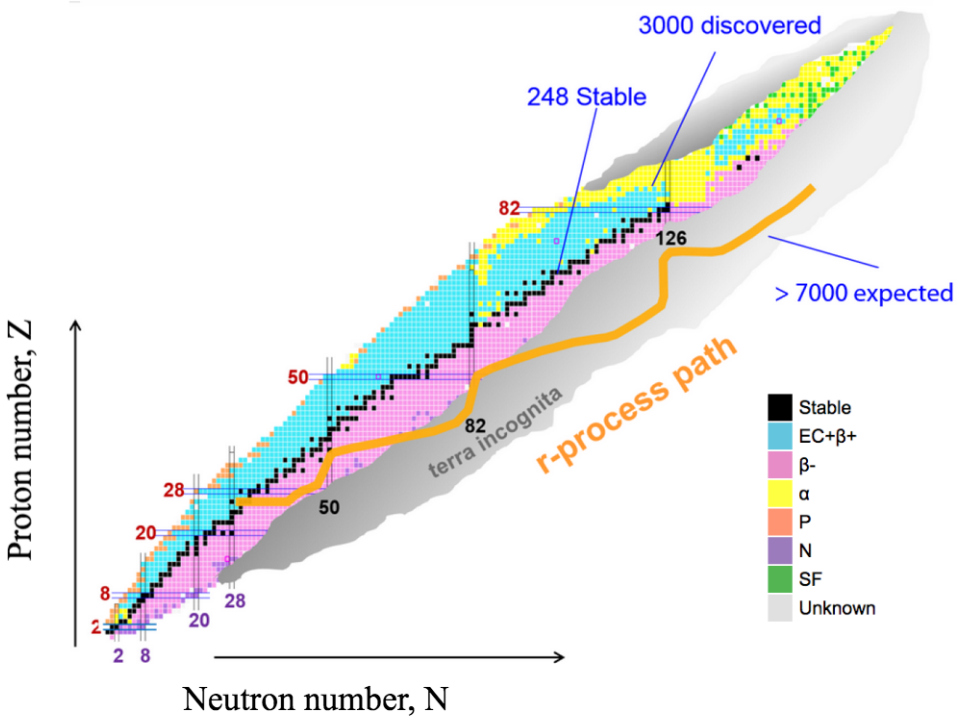

Figure 1: The nuclear chart showing both experimentally measured isotopes and theoretically predicted ones (region labelled as "terra incognita"). Stable isotopes are shown in black, while the colour of unstable isotopes reflects their mode of decay. The path of the r-process is schematically shown in yellow. Image adapted from [7].

of collectivity in neutron rich nuclei. In addition, being odd-mass nuclei, they provide experimental access to single particle energies, which are key ingredients for modern Shell Model calculations in this mass region.

In the past, neutron rich nuclei have been studied using spontaneous fission sources such as ^{252}Cf and ^{248}Cm [8, 9]. However, the fission yields of the Kr and Br isotopes of interest are relatively low in these fissioning systems. The fission of ^{235}U and ^{238}U employed in this work, provide higher fission yields in the mass region of the Kr and Br isotopes. The fission experiments were carried out at two facilities using different reaction mechanisms and complementary detector systems. A first experimental campaign took place at GANIL in 2015 using fission of ^{238}U beam on a Be target and combining the VAMOS++ mass spectrometer [10] with the Advanced Gamma Tracking Array (AGATA) [11]. A second experimental campaign was performed in 2018 employing the FIssion Product Prompt γ-ray Spectrometer (FIPPS) [12]. In this case, the thermal neutron beam provided by the reactor of the Institut Laue Langevin was employed to induce fission on a ^{235}U target. High resolution γ-ray spectroscopy techniques were employed for the analysis of both the AGATA-VAMOS++ and FIPPS data-sets in order to extract new information of excited states in neutron rich $^{90-95}$Kr and odd mass $^{87-93}$Br.

This thesis manuscript is organised as follows:

- Chapter 1 starts with an overview of the theoretical framework describing single particle and collective behaviour in nuclei. The motivation behind nuclear structure studies of neutron rich Kr and Br isotopes will thus be introduced. A summary of the nuclear structure information available prior to this work, from both a theoretical and experimental point of view will be given, highlighting the need for further investigations. In addition, the fission mechanism used as a tool to produce neutron rich nuclei and the combination of fission reactions with high resolution γ-ray arrays will be discussed.
- The characteristics of both the FIPPS and AGATA-VAMOS++ experimental setups used in this work will be detailed in Chapter 2. A particular focus will be given to the FIPPS fission campaign carried out at the ILL, which employed for the first time an active fission target to tag fission events. The challenges of analysing such complex data-sets will be discussed. The performance of the FIPPS HPGe array will be evaluated in terms of energy resolution and efficiency.
- Chapter 3 describes the γ-ray spectroscopy analysis techniques employed to extract the relevant nuclear structure information from both the FIPPS and AGATA-VAMOS++ data-sets. The strengths of the γ-ray coincidence technique as well as the additional selectivity provided by the active fission target will be shown.
- Chapters 4 and 5 show the γ-ray spectroscopy results obtained for the the neutron rich Kr and Br isotopes by combining the FIPPS and AGATA-VAMOS++ data-sets and exploiting the techniques introduced in the previous chapter. The nature of the newly observed excited states will be interpreted by analysing the systematics, as well as existing theoretical predictions.

CHAPTER 1

Theoretical framework and physics motivation

Contents

This chapter aims to introduce the theoretical framework of modern nuclear structure studies and highlight the need for further experimental investigations into excited states of neutron rich Kr and Br isotopes. To begin, a brief overview of the theoretical models relevant for the discussion of the nuclear structure of the isotopes of interest will be given in section 1.1. First of all, the Shell Model and the single particle approach will be presented. This will be followed by a discussion of nuclear deformation and collective excitations as well as the Nilsson model and Hartree-Fock-Bogoliubov calculations. A second part of this chapter is dedicated to the current status of the region of interest, both from experimental and theoretical points of view. The interest of studying neutron rich Kr isotopes, situated at the low Z boundary of the $A \sim 100$ region of deformation, will be discussed in section 1.2. The physics case associated to odd-mass neutron rich Br isotopes will be presented in section 1.3. Section 1.4 will examine the nuclear fission reaction as a way of populating neutron rich nuclei. Past experimental campaigns, which combined fission reactions with high resolution γ-ray arrays for nuclear structure studies, will be introduced. Finally, the advantages and improvements of the experimental setups used in this thesis work (with respect to previous campaigns) will be highlighted.

1.1 Theoretical framework

Since its discovery in 1911, the description of the atomic nucleus has proven to be a challenge for theoretical models. A major breakthrough was made towards the late 1940's by Haxel and Mayer with the explanation of magic numbers using the Shell Model [3, 4], taking a microscopic approach. This was soon followed by the development of the collective model, which considers only the macroscopic degrees of freedom of the nucleus, in the hands of Bohr [5]. Both models can successfully explain general properties of nuclei close to stability and have set the basis for modern nuclear theory. However, as one moves away from the valley of stability, theoretical predictions diverge. Nowadays the goal of nuclear structure research is to produce a unified description of the nucleus, which can be applied across the entire nuclear chart. Modern theoretical models follow a variety of different approaches to describe nuclear properties. The most fundamental approach consists of *ab initio* calculations based on realistic interactions [13]. Our limited knowledge of the strong force together with the need to consider three body forces leads to calculations that can only be applied to excited states of nuclei with less than 20 nucleons. In order to explain characteristics of heavier nuclei, theoretical models based on effective interactions derived from experimental measurements have been developed. This is the case of the Shell Model which will be presented in the following section.

1.1.1 From the magic numbers to the Monte Carlo Shell Model

The nuclear Shell Model considers that the neutrons and protons forming the nucleus occupy discrete energy levels that are grouped into shells, analogous to atomic electronic shells. As opposed to the atomic shells, the idea of nuclear shells was initially difficult to reconcile with the notion of a densely packed nucleus when it was first proposed by E. Gapon and D. Iwanenko in 1932 [14].

However, there was increasingly abundant experimental evidence supporting the existence of nuclear shells. Measured neutron and proton separation energies exhibited sharp drops after the so called "magic numbers" (2, 8, 20, 28, 50, 82, and 126), which were attributed to shell closures. In addition, nuclei with magic number of protons, neutrons or both were observed to be more abundant than other isotopes.

In its simplest form the Shell Model relies on the Pauli principle and considers the nucleons as independent particles moving in a "self generated" central potential V. This is in contrast with the atomic model, where the electrons move in a Coulomb potential created by the nucleus. In this approximation the Schrödinger equation for a given nucleon of mass m with wave function ψ will take the form of:

$$\Big[\frac{-\hbar^2}{2m}\nabla + V(\vec{r})\Big]\psi(\vec{r}) = E\psi(\vec{r}), \tag{1.1}$$

where $\vec{r}$ is the distance from the centre of the potential, and E are the allowed energy values. The resulting shell structure is strongly dependent on the functional form of the potential. The initial choices of potential such as a simple harmonic oscillator or Wood-Saxon potential [15] were only able to reproduce the first three magic numbers.

It was not till the late 1940's that the independent work of M. Goeppert-Mayer [3] and O. Haxel [4] led to the development of a nuclear Shell Model capable of reproducing the experimentally determined magic numbers. The key was the addition of a strong spin-orbit interaction, $\vec{l}.\vec{s}$, to account for the interaction of the intrinsic spin of an individual nucleon, s, with its own angular momentum, l. A schematic diagram of the resulting orbits and single particle energies (SPE) is shown in Fig. 1.1. Before the introduction of the spin-orbit term each energy level is characterised by the quantum number n and orbital angular momentum l, and has a degeneracy of $2(2l+1)$. The spin-orbit interaction produces a splitting of the levels with $l \neq 0$ into two, causing a reordering of the orbitals and successfully reproducing the magic numbers. Each orbital is now characterised by n, l and the total angular momentum: $\vec{j} = \vec{l} + \vec{s}$. In this case a degeneracy of $2j+1$ is obtained.

In the framework of the Shell Model, neutrons and protons in closed shells are considered as an inert core. The remaining nucleons are referred to as the valence nucleons, which determine the properties of the nucleus. Excitations are created by the movement of individual nucleons to higher energy levels, known as single-particle excitations. In the *Independent Particle Model* (IPM) [16], the interactions between nucleons in the valence shell are assumed to be non existing. Despite the simplicity of this approximation, this model is able to reproduce general properties of nuclei such as spin and parity of the ground states of odd-mass nuclei. Nevertheless, when moving away from shell closures, where valence nucleons can no longer be considered independent, the IPM loses predictive power.

The residual interaction between valence nucleons is taken into account by the *Interacting Shell Model*. The first step when performing calculations in the framework of the Interacting Shell Model is the definition of a valence space. The next difficult step is to derive an effective interaction for the chosen model space [16, 17]. The final step is to diagonalize the Hamiltonian matrix. Nowadays this is done with Large Scale Shell Model codes such as OXBASH [18], ANTOINE [16], NATHAN [16] and MSSHELL [19]. The main difficulty arising from this type of calculation is the combinatorial growth

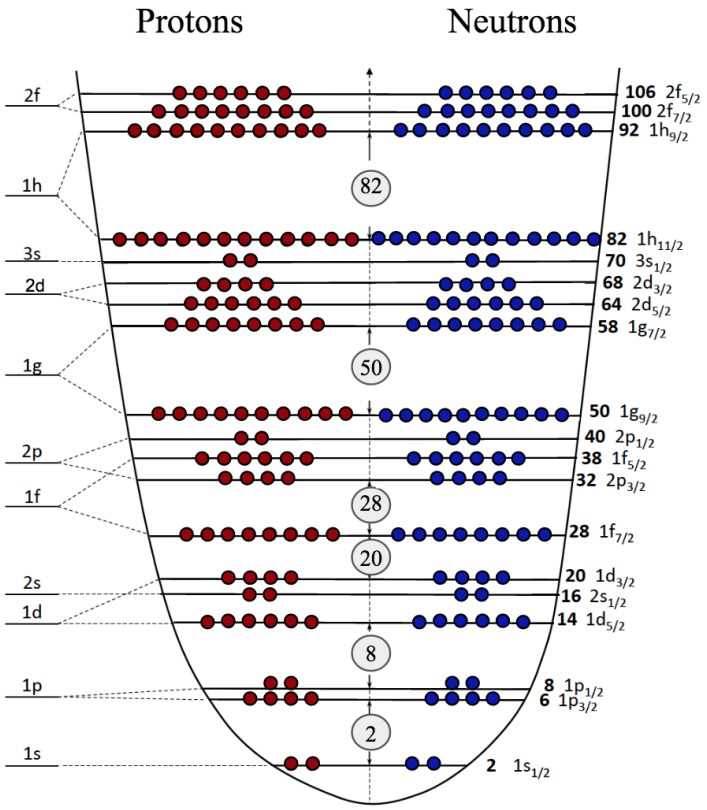

Figure 1.1: Single particle energies of protons and nucleons in the context of the Shell Model. Obtained using a Wood-Saxon potential without (left) and with (right) the contribution of the spin-orbit interaction. The resulting orbitals are grouped into shells defined by the magic numbers.

of the matrix dimension when moving away from the shell closures. For example for $^{44}_{22}\mathrm{Ti}_{22}$, with only two protons and two neutrons outside of the $^{40}_{20}\mathrm{Ca}_{20}$ inert core, 10^4 configurations have to be taken into account. For the case of $^{88}_{44}\mathrm{Ru}_{44}$, the number of configurations to consider increases to 10^{28}.

Even with the most advanced Shell Model codes, many regions of the nuclear chart are out of reach due to the large size of the model space necessary to take into account all the excitations. This is the case for heavy nuclei far from closed shells or cases for which mixing between major shells needs to be considered. To study the structure of nuclei in these regions, two different approaches can be followed. On the one hand a macroscopic point of view describing the collective behaviour of the nucleus can be adopted. On the other hand, the state-of-the-art the *Monte Carlo Shell Model* can be employed.

The Monte Carlo Shell Model (MCSM) was first introduced in 1995 [20], with the aim of accessing regions of the nuclear chart that are out of reach for current Shell Model calculations due to computational limitations. This model has then been developed by Otsuka *et al.* [21, 22]. The advantage of the MCSM is that a full diagonalization is not performed, but a few relevant eigenstates are selected using the Quantum Monte Carlo Diagonalization method (QMCD) [23]. One of the main advantages of the MCSM is its ability to deal with many single particle states, considering both spherical and

deformed states with the same Hamiltonian in the same valence space [21]. Recently MCSM calculations [24] have provided for the first time a microscopic explanation to nuclear deformation, which will be presented in the following section.

1.1.2 Nuclear deformation

The *shape* is a fundamental property of the nucleus which depends on the neutron-proton ratio, excitation energy and spin [25]. As one moves away from spherical magic nuclei towards mid-shell regions, the average spatial distribution of the nucleons is not necessarily spherically symmetric. The wave function of the s-orbital remains spherical, but all other orbitals exhibit a preferential direction with respect to a symmetry axis [26]. Nuclei deviating from a spherical shape are referred to as *deformed nuclei*. The first indications of a non-spherical nucleus resulted from high precision hyper-fine studies in atomic physics, which pointed towards a non spherical charge distribution [27]. Nowadays a large variety of shapes, as well as shape coexisting phenomena, have been observed across the nuclear landscape [28].

The shape of the nucleus can be described by the nuclear radius $R(\theta, \phi)$, defined as the distance of a point on the nuclear surface (θ, ϕ) from the origin. The radius can be expressed in terms of the spherical harmonics $Y_{\lambda,\mu}(\theta, \phi)$:

$$R(\theta, \phi) = R_{av}\Big[1 + \sum_{\lambda=0}^{\infty} \sum_{\mu=-\lambda}^{\lambda} \alpha_{\lambda,\mu} Y_{\lambda,\mu}(\theta, \phi)\Big], \tag{1.2}$$

where R_{av} is the average radius, which is commonly expressed as $R_{av} = 1.2A^{1/3}$ fm with A representing the nuclear mass number. The $\alpha_{\lambda,\mu}$ coefficients determine the amplitude of the spherical harmonics. The multipolarity of the shape is given by the value of λ. The monopole deformation, $\lambda = 0$, represents a compression of the nucleus, while the $\lambda = 1$ term describes a net displacement of the centre of charge. The first component which describes a nuclear deformation is the $\lambda = 2$ term which gives rise to a quadrupole deformation. The octupole deformation, which results in *pear-shaped* nuclei [29], is given by the term with $\lambda = 3$. For the nuclei of interest for this thesis work, as is the case in general across the nuclear chart, quadrupole deformation is prevalent. Therefore, considering only the quadrupole deformation, equation 1.2 can be written as:

$$R(\theta, \phi) = R_{av}\Big[1 + \alpha_{20} Y_{20}(\theta, \phi) + \alpha_{22} Y_{22}(\theta, \phi)\Big], \tag{1.3}$$

which can in turn be parametrized using the Hill-Wheeler coordinates β and γ [30]:

$$\begin{cases} \alpha_{20} = \beta \cos\gamma \\ \alpha_{22} = \frac{1}{\sqrt{2}} \beta \sin\gamma. \end{cases} \tag{1.4}$$

The β parameter represents the extent of the quadrupole deformation, with $\beta = 0$ corresponding to a spherical nucleus and $\beta \neq 0$ to an ellipsoid. The γ parameter accounts for *nuclear triaxiality*. Axially symmetric nuclei have values of $\gamma = n\pi/3$, with $n \in \mathbb{Z}$. For the case of $\gamma = 0$, the α_{20} parameter is

equal to β, and is often referred to as the β_2 parameter. Negative values of β_2 correspond to *oblate* shapes, while positive values are associated to *prolate* nuclei. The deformed nuclear shapes, classified using the Hill-Wheeler coordinates, are shown in Fig. 1.2.

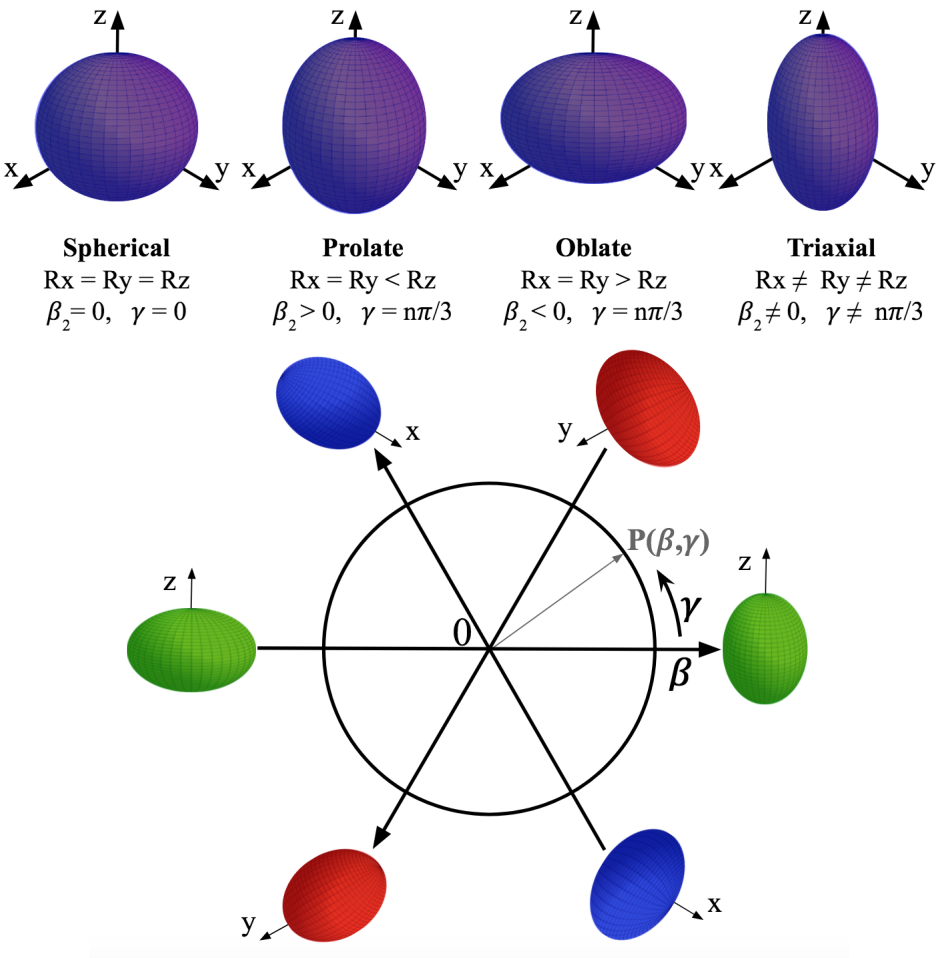

Figure 1.2: TOP: main nuclear shapes showing spherical, prolate, oblate and triaxial nuclei. BOTTOM: diagram of nuclear deformation in Hill-Wheeler coordinates. Spherical nuclei are located at the origin, 0. The point P represents a deformed nucleus with parameters (β, γ). Axially asymmetric nuclei have values of $\gamma \neq n\pi/3$ with $n \in \mathbb{Z}$.

A permanent nuclear deformation gives rise to a non zero electric quadrupole moment. The intrinsic quadrupole moment Q_0, can be expressed as a function of the deformation parameter β_2 using the equation [31]:

$$Q_0 = \frac{3}{\sqrt{5\pi}} R_{av}^2 Z \beta_2 \left(1 + \frac{2}{7}\sqrt{\frac{5}{\pi}}\beta_2 + \frac{1}{14\pi}\beta_2^2 + ...\right), \tag{1.5}$$

where Z is the atomic number. The intrinsic quadrupole moment is in turn related to the reduced transition probability, which depends on the properties of the initial and final wave-functions. Assuming an electric quadrupole transition, the reduced transition probability $B(E2)$ from an initial state

J_i to a final state J_f can be written as:

$$B(E2; J_i \rightarrow J_f) = \frac{5}{16\pi} e^2 Q_0^2 \langle J_i K 20 | J_f K \rangle^2, \tag{1.6}$$

where the factor in $\langle ... \rangle$ is the Clebsch-Gordon coefficient and K is the projection of the total angular momentum onto the symmetry axis. The reduced transition probability is related to the lifetime of the excited state, which can be measured experimentally, and can therefore be used as an "indicator" of deformation.

1.1.3 Collective behaviour of nuclei

Some features of excited states in atomic nuclei far from shell closures can be described using a macroscopic approach which considers collective degrees of freedom. The models that use this macroscopic point of view are known as *collective models*. The first collective model was the Liquid Drop Model (LDM) introduced in 1935 by Weizsacker [32]. The LDM treats the nucleus as an incompressible liquid, and was used to reproduce nuclear binding energies in different nuclei. Combined efforts in the following years led to the development of the collective model by Bohr and Mottelson [33, 34, 5, 26], which introduced a dynamical component and described certain excited states in nuclei as vibrational and rotational collective modes of motion. These collective excitations successfully explain the low energy bands of excited states observed in even-even nuclei in mid shell regions, which could not be reproduced using the standard Shell Model.

Nuclear vibrations

Nuclear vibrations are one of the main collective excitations observed in nuclei close to shell closures. In analogy to photons, which represent a quantum of electromagnetic energy, phonons are used as a quantum of vibrational energy. The vibrations can be decomposed into multipoles given by equation 1.2, with a dominant quadrupole term ($\lambda = 2$) in the region of the nuclear chart studied in this work. In this context the nucleus behaves as a liquid drop with quadrupole deformation that varies with time around a spherical equilibrium shape.

Assuming a harmonic vibration with oscillation frequency ω, the excitation energy E is given by:

$$E = \hbar\omega\Big(n + \frac{5}{2}\Big), \tag{1.7}$$

where n is the principal quantum number which can take values $n = 0, 1, 2, ..$, and the $5/2$ term comes from the fact that a quadrupole deformation is a five dimensional oscillator [1]. For even-even nuclei with a $0+$ ground state, the addition of a phonon with $\lambda = 2$ gives rise to a $2+$ excited state. If an additional phonon is considered, a triplet of states with spins $0+$, $2+$, $4+$ exists. In this model, the ratio of the excitation energies of the 2_1+ and 4_1+ states, known as the $R_{4/2}$, will take the value of 2 (with respect to the ground state energy $E_0 = 5/2\hbar\omega$). Nuclei close to shell closures indeed have often an experimental $R_{4/2} \approx 2.2$. This points to a good description of these nuclei, despite the simplicity of the model.

Nuclear rotations

Low energy excited states in permanently deformed nuclei can be explained using the collective behaviour of nuclear rotations. If the nucleus is considered as an axially symmetric quantum rigid rotor with moment of inertia $\Im$ the excitation energy E_{rot} is given by:

$$E_{rot} = \frac{\hbar^2}{2\Im} J(J+1), \tag{1.8}$$

where J is the angular momentum, which can only take even values [26]. This gives rise to a rotational ground state band with $J^\pi = 2^+, 4^+, 6^+...$ In this case the resulting value of $R_{4/2} = 3.3$ is obtained. There is a remarkable agreement with experimental values of $R_{4/2}$ in the $150 < A < 190$ and $A > 230$ regions of the nuclear chart [35], supporting the existence of permanent deformation far from shell closures.

1.1.4 The Nilsson Model

In order to describe single particle states for deformed nuclei, the Nilsson Model (or deformed Shell Model) was introduced in the early 1950s [36]. This model has been particularly successful at providing a theoretical description for single particle states in deformed odd-mass nuclei [26].

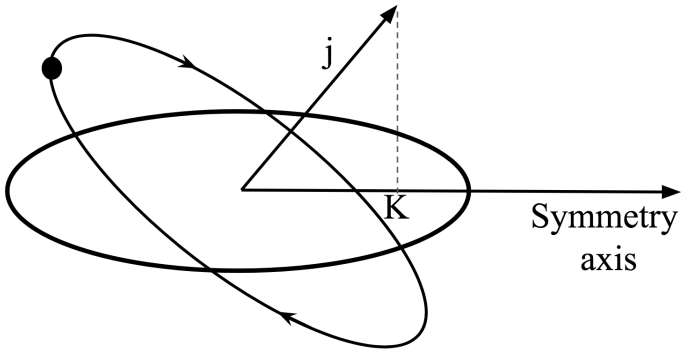

Figure 1.3: Schematic representation of a single particle orbit in a prolate deformed nucleus. The projection of the total angular momentum j on the symmetry axis is denoted by K.

In contrast to the Shell Model, which assumes a spherical potential, the Nilsson model uses a deformed potential. In a deformed potential the energy of the single particle orbits will depend on their orientation, breaking the $2j + 1$ degeneracy. As illustrated in Fig. 1.3, the interaction of the single particle orbit with the core depends on the value of K, defined as the projection of the total angular momentum j along the symmetry axis of the deformed nucleus. For the case of prolate nuclei the single particle energy increases with larger values of K, while for oblate deformed nuclei the energy increases with lower values of the projection. The splitting of the energy levels can be seen in Fig. 1.4, which shows single particle energies as a function of deformation, known as *Nilsson diagrams*. For example, the single particle orbit $1p_{3/2}$ in spherical nuclei ($\epsilon_2 = 0$) can take K values of 1/2 or 3/2,

causing a splitting into two states. The splitting of the states increases with increasing deformation. Each level is labelled using the Nilsson notation $K[Nn_z m_l]$, where N is the principal quantum number, n_z is the number of oscillation quanta along the symmetry axis, and m_l is the projection of the orbital angular momentum onto the symmetry axis [26]. The Nilsson diagram shown is applicable for nuclei with $N, Z \leq 50$, where only quadrupole deformation is considered, as is the case of the Kr ($Z = 36$) and Br ($Z = 35$) isotopes studied in this work.

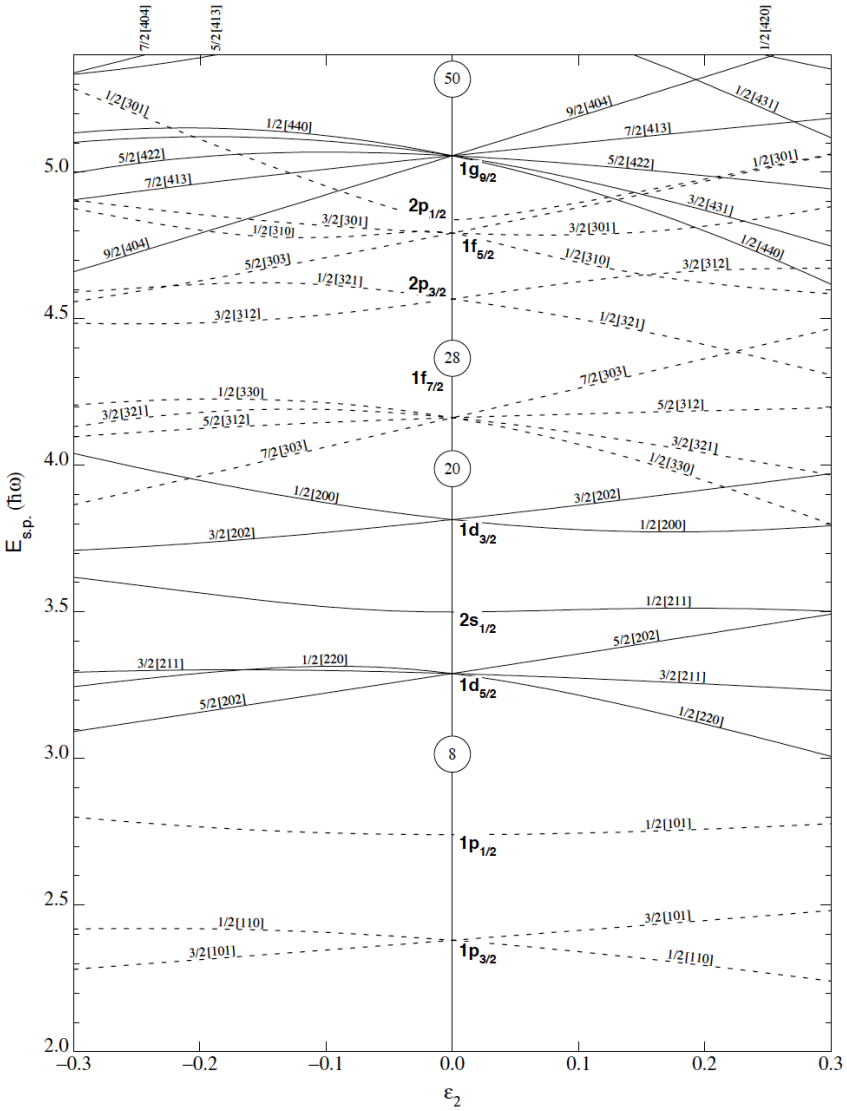

Figure 1.4: Nilsson diagrams for Z or $N \leq 50$. The single particle energies are shown as a function of the deformation parameter ϵ_2 related to the deformation parameter β ($\epsilon_2 \approx 3/2\sqrt{(5/4\pi)}\beta$). Only quadrupole deformation is considered.

1.1.5 Mean field Hartree-Fock-Bogoliubov calculations

To describe the nuclear many body system, the number of degrees of freedom can be reduced by assuming that all the nucleons move independently in an average potential or *mean field*. The mean field can be determined using phenomenological models or using self consistent calculations, which is the case of Hartree-Fock-Bogoliubov (HFB) calculations. These calculations generalize and unify [37] the Hartree-Fock theory [37] with the Bardeen-Cooper-Schrieffer (BCS) theory [38], in order to include the pairing correlations. The mean field is derived from nucleon-nucleon interactions applying the variational principle to the Slater determinants used as trial wave functions. The calculations can employ different effective interactions such as the Gogny interaction [39] and Skyrme interaction [40, 41, 42].

In the past decades HFB calculations have been used to describe basic nuclear properties such as binding energies and nuclear radii. The main advantage of the HFB technique is that it is applicable throughout the nuclear chart, to predict the deformation of the nuclear ground state and the first excited states. This is of particular interest in the $A \sim 100$ region presented in the following section, which was not accessible by other calculations until recent MCSM developments. In this thesis work, HFB calculations using the Gogny D1S interaction performed by the CEA DAM [43, 44] will be mentioned to discuss the evolution of deformation and ground state spin values in the Kr isotopes.

1.2 Onset of nuclear deformation in the A∼100 region

In general, nuclear properties such as shape, radii and lifetimes tend to change gradually as a function of nucleon number. However, there are some regions in the nuclear chart where the change occurs rapidly, as is the case of the $A \sim 100$ region. Why would a difference of a single nucleon cause such drastic changes in properties along only certain isotopic or isotonic chains, while causing gradual changes in others? To correctly answer this question one must take into account the subtle interplay between the single particle and collective behaviours of nuclei, challenging modern theoretical models.

Neutron rich nuclei with mass $A \sim 100$ are situated in a mid-shell region both for protons ($28 < Z < 50$) and neutrons ($50 < N < 82$), giving rise to collectivity and deformation. The $A \sim 100$ region presents a drastic change in nuclear shape along isotopic chains (see Fig. 1.5). Nuclei in this region undergo a shape transition, going from spherical to strongly deformed as a function of neutron number. Furthermore, a sudden change in behaviour is observed when comparing isotonic chains. Even though this phenomenon has been studied for the past five decades and much progress has been made, there is currently no complete interpretation.

The deformation in the $A \sim 100$ region was first theoretically predicted in 1969 on the basis of microscopic calculations of equilibrium deformations using the Mottelson-Nilsson procedure [45]. Only a few months later, the first experimental evidence was provided by Cheifetz *et al.* [46]. A rapid onset of deformation was observed in the ground states of Zr and Sr isotopes populated in spontaneous

fission of ^{252}Cf. In the following years, many experimental efforts were devoted to study isotopes of Ru ($Z = 44$), Mo ($Z = 42$), Zr ($Z = 40$), and Sr ($Z = 38$), as described in [8, 47]. More recently, due to the evolution of experimental facilities and the possibility to populate more exotic nuclei, investigations towards finding the low Z boundary of this island of deformation have been performed. In the low Z region of the island of deformation, we can find the Rb ($Z = 37$) isotopic chain (studied in [48, 49, 50]) and the Kr ($Z = 36$) isotopic chain, which will be discussed in detail in the following section.

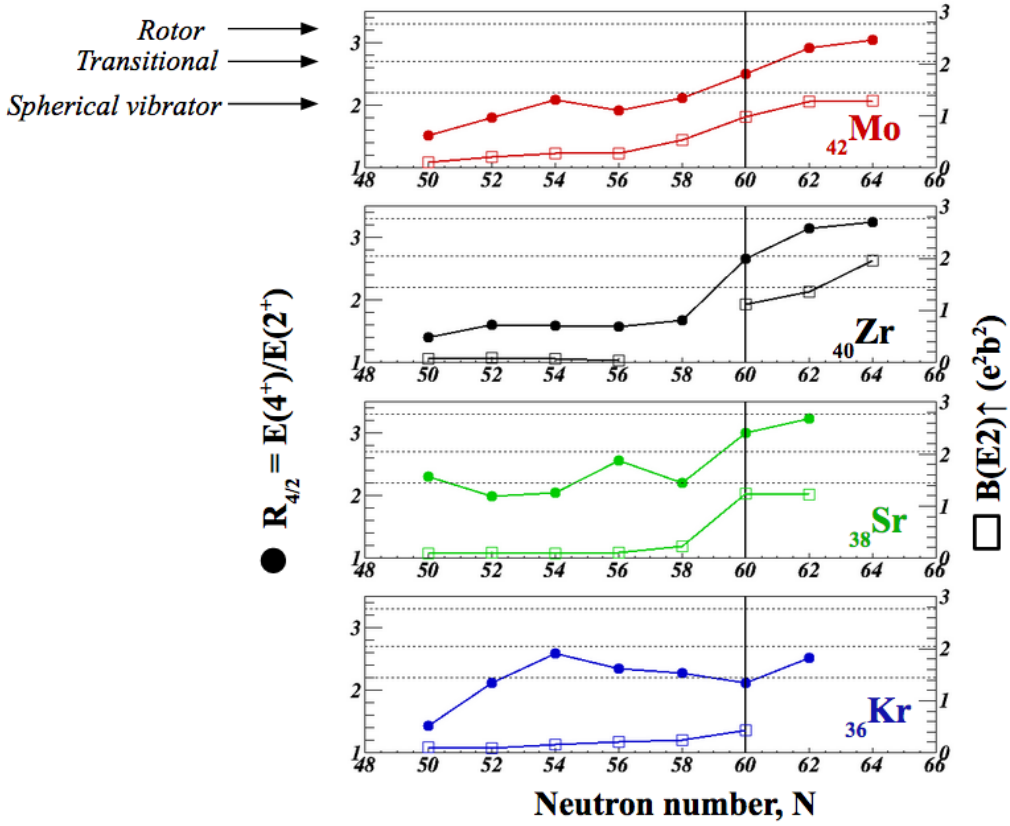

Figure 1.5: $R_{4/2}$ ratio (filled circle) and reduced transition probabilities $B(E2) \uparrow = B(E2; 0^+_{gs} \rightarrow 2^+_1)$ (open rectangle) for even-even nuclei in the $A \sim 100$ region as a function of neutron number N. The values were taken from [51] and more recent publications [52, 53].

As introduced in section 1.1.2, the ratio of the energy of the first 2^+ and 4^+ excited states ($R_{4/2}$), as well as the reduced transition probability ($B(E2)$), are good indicators of deformation. Fig. 1.5 shows the evolution of the available experimental data of these two indicators as a function of neutron number, for even-even isotopes in the $A \sim 100$ region. As a general trend, the $R_{4/2}$ ratio increases with increasing neutron number, indicating an evolution from spherical to deformed shapes. However, it can be seen that for the Sr and Zr isotopic chains the shape change is more pronounced and occurs rapidly when going from $N = 58$ to $N = 60$. These nuclei have a $R_{4/2} \approx 3.3$ for $N = 62$, displaying the feature of well deformed symmetric rotors. For the Mo isotopic chain there is an increase of deformation but the transition is smoother, pointing towards a high Z limit to this region of sudden

onset of deformation. On the low Z side, the Kr isotopic chain manifests a different behaviour. Looking solely at the $R_{4/2}$ ratio, a decrease is observed for $54 < N < 60$ while the ratio increases when going from $N = 60$ to $N = 62$. As suggested in [53], this could indicate that the shape transition observed in Zr and Sr is delayed in neutron number for the Kr isotopic chain. In the Mo, Zr, and Sr isotopic chains a correlation is observed between the change of $R_{4/2}$ ratio and the reduced transition probability $B(E2)$. However, for the Kr isotopic chain, for $54 < N < 60$ the $R_{4/2}$ ratio decreases while the $B(E2)$ increases. This inconsistency is not yet understood, motivating the need for more experimental information such as lifetimes, excitation energy and spin and parity of high lying nuclear states on the low Z boundary of the $A \sim 100$ region.

The description of the sudden onset of deformation presents a challenge to state-of-the-art theoretical models. At first, the cause of the drastic shape change was attributed to proton-neutron interactions between the $\pi g_{9/2}$ orbital and the $\nu g_{7/2}$ orbital [54]. Since then, different theoretical approaches have been used such as: the Interacting Boson Model (IBM) [55], Hartree–Fock–Bogoliubov (HFB) calculations [56] and the Finite Range Droplet Model (FRDM) [57]. Although some models successfully explain some features, until recently no theoretical approach was able to reproduce the experimental information on both sides of $N = 60$, as well as the rapid shape change at this neutron number.

Recent MCSM calculations [21, 58] were used to investigate the neutron rich Zr isotopes in the $A \sim 100$ region [24]. As can be seen from Fig. 1.6, the calculations reproduce the drastic shape change experimentally established at $N = 60$. The model suggests that the cause of the shape transition lies in the inversion of two 0+ states: a spherical 0+ state that is "pushed up" at $N = 60$, and a prolate deformed 0+ state comes which down to the ground state. The inversion is caused by a large increase in the occupation of the intruder $\pi g_{9/2}$ orbital across the $Z = 40$ sub-shell closure when going from $N = 58$ to $N = 60$. This in turn is a consequence of the change in monopole central and tensor components of the proton-neutron interaction. Future MCSM calculations, capable of providing a microscopic explanation to the sudden onset of deformation, will be key for further interpretation of properties in this region.

1.2.1 Neutron rich krypton isotopes

In recent years there has been increasing interest in studying the low Z boundary of the $A \sim 100$ island of deformation [28], and therefore the shape evolution of neutron rich Kr isotopes. One of the focuses of this work is the study of the structure of the $^{90-95}$Kr isotopes, situated well above the $N = 50$ shell closure, approaching $N = 60$ (see Fig. 1.7).

The first experimental investigations into excited states in neutron rich Kr isotopes were carried out in the 1970s for $^{87-88}$Kr, which are accessible using transfer and capture reactions [59, 60, 61]. For the more neutron rich isotopes a wealth of experimental spectroscopic information has been obtained combining fission reactions and large γ-ray detector arrays. Both spontaneous fission sources such as ^{248}Cm [62] and ^{252}Cf [63, 64, 65] have been used, as well as neutron induced fission [66, 67]. Infor-

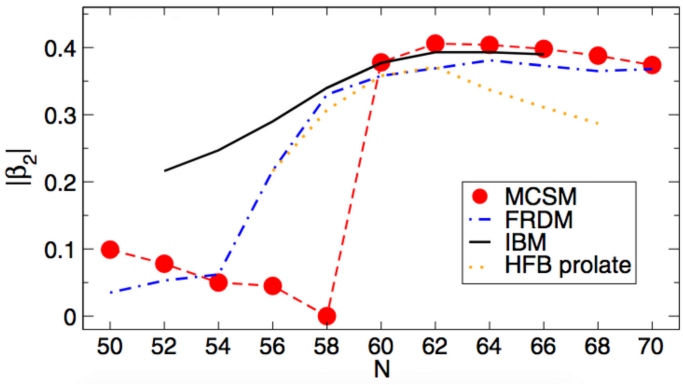

Figure 1.6: Calculated values of the deformation parameter, β_2, for Zr isotopes using different theoretical approaches. The MCSM is the only model capable of predicting a sharp shape change at $N = 60$. Image taken from [24].

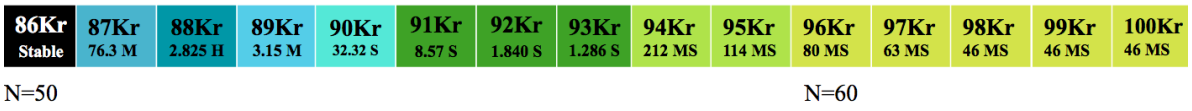

Figure 1.7: Schematic representation of neutron rich Kr isotopes, including the $^{90-95}$Kr isotopes studied in this work. The $N = 50$ value, corresponding to the stable ^{86}Kr, as well as the $N = 60$ expected region of shape transitions are indicated [7].

mation on nuclear binding energies of neutron rich Kr isotopes was obtained through high precision mass measurements performed at ISOLTRAP (ISOLDE-CERN) [68, 69]. As one approaches $N = 60$, and therefore more exotic isotopes, less experimental information is known. For ^{94}Kr the only known excited levels were obtained from an experimental campaign with EUROGAM 2 and a spontaneous fission source of ^{248}Cm [62]. The reduced transition probability of the decay from the first 2+ state to the ground state was measured using Coulomb excitation at the REX-ISOlDE facility at CERN [70, 71]. Experimental studies on the ^{95}Kr neighbour are even more limited. The only published spectroscopic information resulted from an experiment that took place at the ILL using the Lohengrin fission fragment separator [72]. ^{95}Kr was produced by thermal-neutron induced fission, and only two γ rays deexcting a microsecond isomer were observed at the focal plane of the spectrometer.

If the Kr isotopic chain behaved as the Zr and Sr isotopic chains, a large shape transition would be expected at $N = 60$. For this reason, ^{96}Kr has been the subject of many experimental and theoretical investigations. The first spectroscopic information comes from [73], where the energy of the first 2+ excited state was measured at 241 keV. The measured value indicated a deformed ground state for ^{96}Kr. However, shortly after, mass measurements performed at the ISOLTRAP at CERN-ISOLDE pointed to a non-deformed ground state [69]. The disagreement between measurements was later resolved by a Coulomb excitation experiment [70] that measured an energy of 554 keV for the first 2+ excited state. This was later confirmed by an experiment performed at the GANIL facility using the AGATA array and the VAMOS++ spectrometer [52], where the energy of the of the 4+ to 2+ transition was also measured. The obtained $R_{4/2} = 2.12$ indicated a near spherical ground state. As

can be seen from Fig. 1.5, no sudden onset of deformation is observed for the Kr isotopes when going from $N = 58$ to $N = 60$, establishing the low Z boundary for this $A \sim 100$ region of deformation.

The first spectroscopic information on Kr isotopes with $N > 60$ was obtained at RIKEN, where the $R_{4/2}$ value was measured in ^{98}Kr and the first excited state was observed in ^{100}Kr [53]. As can be seen from Fig. 1.5, an increase in deformation is observed in the Kr isotopic chain when going from $N = 60$ to $N = 62$. This suggests that the shape change observed in Sr and Zr could be delayed in neutron number, albeit smoother. To provide experimental evidence of the possibility of a delayed shape transition, measurements of more exotic isotopes are necessary. However, as suggested by [53], this might require next-generation facilities. Nevertheless, more spectroscopic information on the excited bands of less exotic neutron rich Kr isotopes will provide a vital contribution towards refining theoretical models and explaining shape changes and shape coexistence phenomena in this interesting region of the nuclear chart.

1.3 Neutron rich Br isotopes above the $N = 50$ shell closure

Odd-mass Br isotopes, located just above $N = 50$, were investigated in this work in order to address the evolution of structure around shell closures for very neutron rich nuclei. With one proton less than the Kr isotopes discussed in the previous section, the Br isotopes of interest are closer to the doubly magic $^{78}_{28}$Ni$_{50}$. This doubly magic nucleus has been the subject of numerous theoretical studies in recent years. In addition to its importance in the modelling of the r-process [74], the knowledge of the structure of ^{78}Ni can address the strength of shell closures for very neutron rich nuclei [75, 76, 77]. A direct observation of excited states in ^{78}Ni is challenging, with the energy of the 2+ state just recently being measured and published in *Nature* [78]. Further insight into the structure of excited states in ^{78}Ni can be gained studying neighbouring nuclei (such as the Br isotopic chain) which are accessible through fission reactions.

Excited states of neutron rich Br isotopes can provide insight into the evolution of collectivity above the $N = 50$. Moreover, these Br isotopes provide an ideal testing ground for the proton-neutron interaction between the πfp and νdg orbits, which is a key ingredient for modern Shell Model calculations in the region. Furthermore, excited states in odd-mass nuclei provide information on single particle energies. Of particular interest is the single particle energy of the $\pi g_{9/2}$ orbital, which gives rise to a 9/2+ state. Previous studies suggest an isomeric character of the 9/2+ state in the tens of ns range [79], that can be discussed using the data collected in this thesis work.

From an experimental point of view, knowledge of excited states in Br isotopes rapidly decreases when moving away from the shell closure. High spin excitations of ^{85}Br ($N = 50$) have been studied using fusion-fission reactions in [80, 81]. Both the ground state and first excited states were associated with protons in the $\pi f_{5/2}$, $\pi p_{3/2}$, $\pi p_{1/2}$, and $\pi g_{9/2}$ orbits. More recently, ^{87}Br ($N = 52$) has been extensively studied after beta decay in [79] and after ^{235}U fission in [82]. Excited states associated with single proton excitations were identified and compared with Large-Scale Shell Model calculations using the NATHAN code [16]. A good agreement between measured and predicted excitation energies

was found for negative parity states. In contrast, positive parity states (including those built on the $\pi g_{9/2}$ configuration) could not be reproduced. The odd-odd ^{86,88}Br isotopes were also studied using neutron induced fission of ^{235}U during the EXILL campaign and with Large-Scale Shell Model Calculations [83, 84]. Before this work, no spectroscopic information was known for the Br isotopic chain above ^{88}Br [1].

1.4 Prompt γ-ray spectroscopy of fission fragments

1.4.1 Fission as a tool to produce neutron rich nuclei

The process of nuclear fission was discovered in the midst of a complex political climate in 1939 by a team led by Lise Meitner and Otto Hahn [86, 87]. Even though much progress has been made in the understanding of the fission process many questions, such as how angular momentum is generated at the scission point or how the fission yields vary with fissioning system, remain unanswered [88]. A detailed review of recent developments in fission studies can be found in [89]. In the context of this work, nuclear fission is of interest as a tool to populate exotic neutron rich nuclei in excited states. The excited states of certain very neutron rich isotopes, such as the neutron rich Kr and Br isotopes investigated, are only accessible through fission reactions.

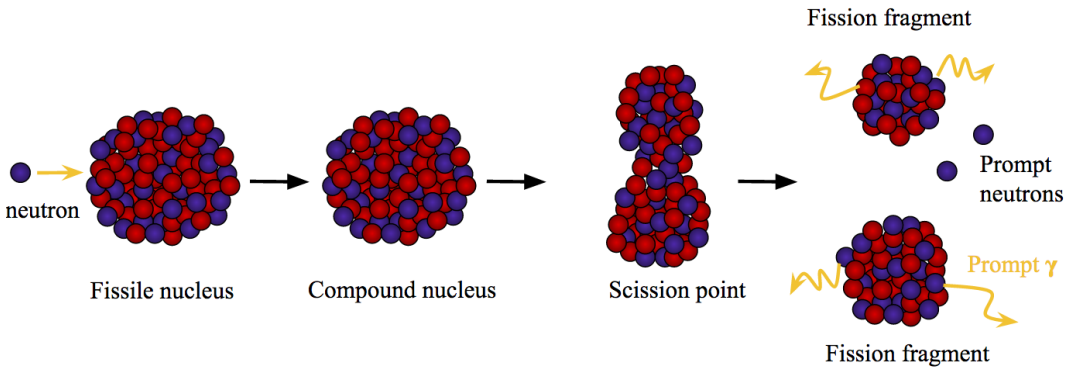

Figure 1.8: Schematic representation of the neutron induced fission process. The fissile nucleus captures a neutron forming a compound nucleus. The compound nucleus will then deform until it reaches the scission point and splits into two fission fragments releasing neutrons in the process. The fission fragments populated in excited states deexcite via emission of prompt γ rays.

In a fission reaction, a nucleus splits into two or more lighter nuclei. The reaction can take place spontaneously for certain heavy nuclei, or be induced by particle capture such as neutrons. Fig. 1.8 schematically represents the neutron induced fission process. A fissile nucleus captures a neutron

[1] Preliminary results of the structure of ^{89}Br were presented in a conference proceeding [85], however no spectra or precise γ-ray energies were shown.

forming a compound nucleus that deforms and splits into two lighter fragments. In the fission process neutrons are released and the fission fragments are populated in excited states that deexcite via γ-ray emission. Despite the emission of neutrons, the two fission fragments formed are highly neutron rich. The reason for this can be understood looking at Fig. 1.9 that illustrates the deviation of the valley of stability from the $N = Z$ line for heavy nuclei towards a higher neutron-proton ratio. Consequently, the fission fragments will have an excess of neutrons and will decay towards the valley of stability via a series of β decays and delayed neutron emissions.

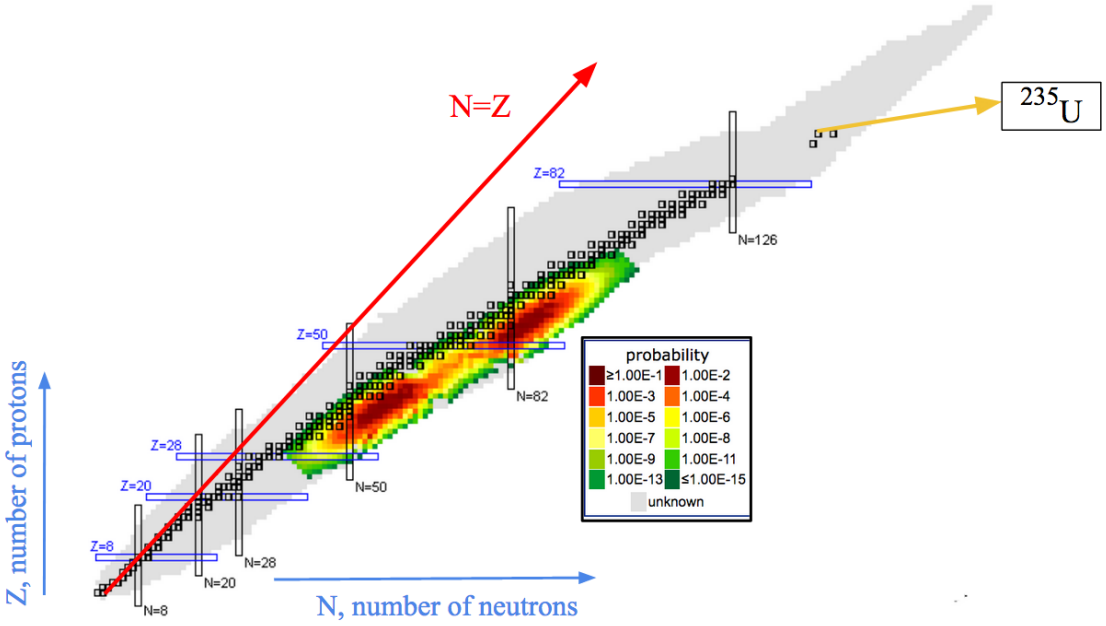

Figure 1.9: Nuclear chart showing fission yields of neutron induced fission of ^{235}U. The production of neutron rich nuclei grouped into a light and heavy fission fragment is observed. Image adapted from [7].

More than 140 isotopes can be produced with a probability larger than 0.1% [91]. The probability of being produced in the fission process is known as the fission yield. Fig. 1.9 shows the fission fragment yields corresponding to neutron induced fission of ^{235}U. The fission fragments can be grouped into a lighter fragment and a heavier fragment. This "two bump" behaviour appears not only for ^{235}U but for other neutron induced fission reactions and spontaneous fission sources, as can be seen from Fig. 1.10. It is Worth noting that the light mass peak shifts with increasing mass of the compound nucleus, while the heavy mass peak remains centred around 140. This is due to the particular stability of nuclei of this mass number, which have both number of protons and neutrons near a closed shell [92]. The mass distribution trend can be much more varied than one might think by simply looking at Fig. 1.10. Depending on the fissioning system, the symmetry of the distribution can change, as well as the number of fission fragments produced. Nowadays, being able to theoretically predict the diverse behaviour of fission yields remains a challenge for fission models [89].

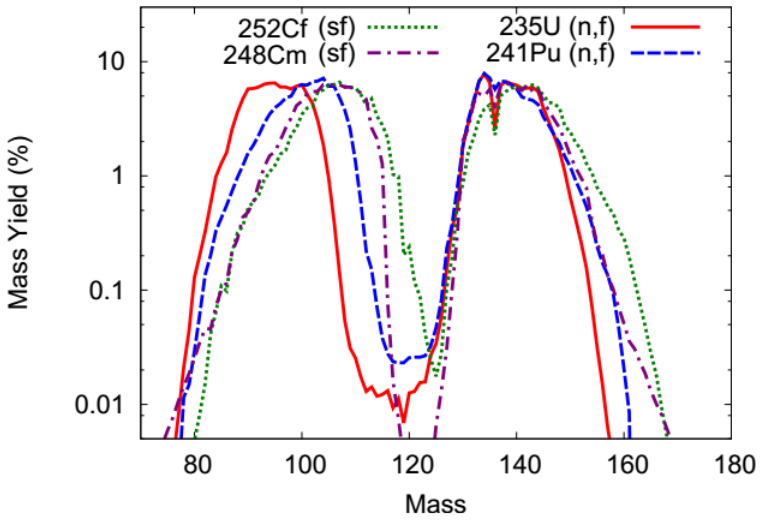

Figure 1.10: Fission yields for different fissioning systems, including spontaneous fission sources and the neutron induced reactions used during the EXILL campaign. Image taken from [90].

1.4.2 Past and present of γ-ray spectroscopy of fission fragments

The coupling of nuclear fission reactions, that produce nuclei far from stability, with large HPGe arrays has been used in the past decades to obtain valuable nuclear structure information on neutron rich nuclei. The first experimental campaigns were carried out in the 1990's and 2000's using spontaneous fission sources of ^{252}Cf and ^{248}Cm and employing arrays such as EUROGAM/EUROBALL [8] and GAMMASPHERE [9]. A wealth of fission data was obtained from these experimental campaigns. To extend and cross check the data obtained with spontaneous fission sources, neutron induced fission has been used in recent years. In 2012-2013 the EXILL campaign took place at the Institut Laue Langevin (ILL), using the EXOGAM array to study neutron induced fission of ^{235}U and ^{241}Pu [90]. As can be seen from the yields plotted in Fig. 1.10, neutron induced fission of ^{235}U gives access to nuclei in the $A \sim 90$ region which cannot be produced with large yields using spontaneous fission sources. Further details of the EXILL campaign will be given in section 2.2. In 2017-2018 experimental campaigns at the ALTO facility were carried out where the fast neutron source, LICORNE [93], was used to induce fission on ^{238}U and ^{232}Th targets. For these experiments the hybrid ν-Ball array, combining HPGe detectors and $LaBr_3$ detectors, was used [94, 95]. With respect to previous fission experiments the ν-ball fission campaign was able to produce more neutron rich isotopes due to the chosen fission reaction and presented the advantage of a fission time definition thanks to the use of a pulsed neutron beam.

In addition to spontaneous fission reactions and neutron induced fission, the development of radioactive ion beam facilities has opened the door to investigations into very neutron rich nuclei using beam induced fission reactions as well as post accelerated fission fragments. Noteworthy examples of such experiments include the EURICA campaigns carried out at RIKEN [96, 97] and measurements

performed at the Argonne National Laboratory with ATLAS and GRETINA [98, 99]. These types of experiments give access to excited states of fission products after beta decay or isomeric decay or employ Coulomb excitation. In contrast to the previously discussed campaigns (GAMMASPHERE, EXILL FIPPS etc.) which allow detailed prompt spectroscopy of fission fragments.

In recent years, prompt γ-ray spectroscopy of fission fragments has become an essential technique to study the structure of neutron rich nuclei. One of the main challenges faced in this sort of experiment is the large amount of γ rays being emitted in the deexcitation of the fission fragments, which complicate the assignment of a particular γ-ray transition to a particular nucleus. Traditionally, the identification is based on the γ-ray coincidence technique (see Chapter 3). In order to optimise the identification using γ-ray coincidences, the performance of the detector system (in terms of energy resolution, efficiency, peak-to-total ratio and granularity) is crucial. The evolution of performance of γ-ray detectors over the years is illustrated in Fig. 1.11. An enormous change in sensitivity is observed between the first single Ge(Li) detectors up to the γ-ray tracking array AGATA. Further details concerning the development of germanium detectors for γ-ray spectroscopy are reported in [100].

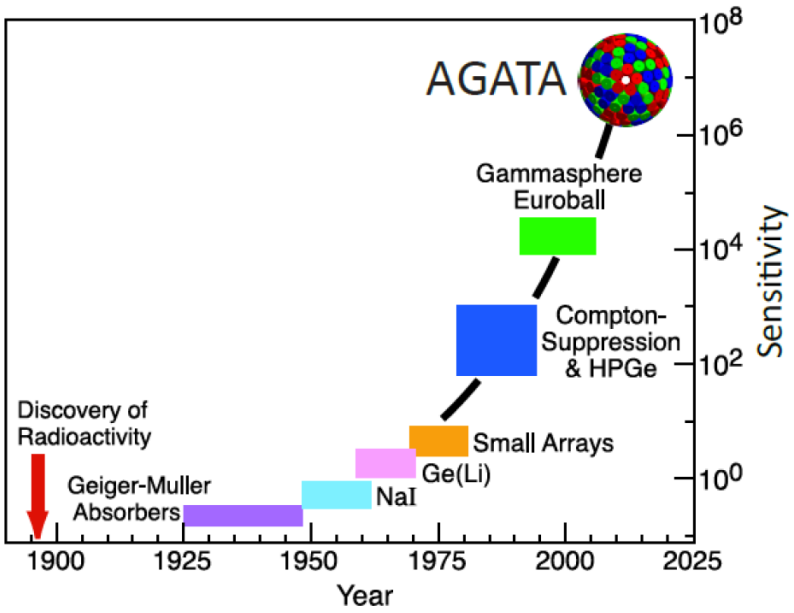

Figure 1.11: Evolution of sensitivity of γ-ray detectors from Geiger-Muller counters up to the Advanced GAmma Tracking Array (AGATA). The sensitivity is calculated using intensities in ^{156}Dy, and defined as the inverse of the fraction of the weakest channel reaction cross section which can be measured with respect to the total reaction cross section. Taken from [101].

In this work the analysis of two fission experiments, which are pushing the limits of sensitivity in γ-ray spectroscopy, was performed in order to investigate the structure of neutron rich Kr and Br isotopes. A first experiment (which took place in 2015, before the start of this thesis) was carried out at GANIL using fission of a ^{238}U beam on a Be target and combining the AGATA array with the VAMOS++ spectrometer. A second experiment, took place at the ILL in 2018 using neutron induced fission of ^{235}U and the FIPPS array with an active fission target. Both experiments present advantages with respect

to previous fission campaigns on three main fronts: the chosen fission reaction, the performance of the array and the fission detection setup. First of all, the chosen fission reactions exhibit higher fission yields for the isotopes of interest (see Fig. 1.10). Secondly, the performance of the HPGe detectors has been improved (in terms of energy resolution, efficiency etc.). Additionally, the γ-ray tracking capabilities of the AGATA array are nowadays the state of the art in γ-ray spectroscopy. The use of the VAMOS++ spectrometer during the GANIL experiment enabled an isotopic identification of the fission fragments, allowing the investigations of isotopes produced with low fission yields. The active fission target used during the FIPPS campaign, which provides a tag of the fission events, significantly improves the identification of prompt γ-ray transitions emitted by the fission fragments. A detailed description of both the FIPPS and AGATA-VAMOS++ experimental setups employed, as well as a discussion of their complementary, will be given in the following chapter.

Conclusion

This chapter has motivated the investigations into excited states of neutron rich Kr and Br isotopes, which give access to single-particle excitations as well as the development of collectivity between $N = 50$ and $N = 60$. Located just above the $N = 50$ shell closure, the odd-mass Br isotopes of interest are accessible through large-scale Shell Model calculations. Therefore, experimental spectroscopic information can be used to benchmark the nucleon-nucleon interaction outside of the ^{78}Ni core. Since the Kr isotopes studied in thesis are out of reach of standard Shell Model calculations, the mean field approach has been used in the past to predict the evolution of deformation in the Kr chain. MCSM calculations could perhaps give a microscopic explanation to the change of shape in the Kr isotopes with respect to neighbouring Sr and Zr chains. The current lack of experimental information on neutron rich Kr and Br isotopes has been discussed, highlighting the need for further experimental studies. In this work the use of fission reactions with ^{235,238}U, with respect to spontaneous fission sources used in the past, present the advantage of higher fission yields in the region of interest. To exploit the spectroscopic information of neutron rich nuclei produced in fission reactions, high efficiency and high resolution arrays (such as FIPPS and AGATA) are essential, as has been proved by previous campaigns.

CHAPTER 2

Experimental set-up

Contents

Nuclear structure information of neutron rich Kr and Br isotopes was obtained via fission experiments using state-of-the-art γ-ray arrays. This chapter describes the experimental aspects of both of the setups used: the FIPPS instrument and the AGATA-VAMOS++ setup at GANIL. An introduction to the research performed at the ILL, where both the FIPPS and EXILL campaign took place, is given in section 2.1. This is followed by an overview of the EXILL fission experiments, which laid the foundations for the FIPPS instrument, in section 2.2. In this chapter, particular focus is given to the ^{235}U fission campaign carried out at FIPPS (section 2.3), where for the first time at a neutron beam facility, an active fission target was used to identify the fission events. The evaluation of the performance of the FIPPS array in terms of energy resolution (section 2.3.5) and efficiency (section 2.3.6) is treated in detail, since it was an important part of this thesis work. A comprehensive description of the AGATA-VAMOS++ experimental campaign, data preparation and calibrations (which were performed prior to this thesis) can be found in [102]. The main characteristics of the AGATA-VAMOS++ experiment, needed for the analysis of the Kr and Br isotopic chains (Chapter 4 and Chapter 5), are presented in section 2.4.

2.1 Research at Institut Laue-Langevin

The Institut Laue-Langevin (ILL) is an international research facility situated in Grenoble, housing a high flux research reactor. Currently, the ILL reactor provides the world's most intense continuous neutron source. A flux of 1.5×10^{15} neutrons cm^{-2}s^{-1} can be achieved with the reactor at full power [103]. The neutrons can be used as a probe to study structure and dynamics in the fields of biology and material science. Neutrons are also used to address fundamental research questions in the fields of particle and nuclear physics, as is the case of this thesis.

The ILL high flux reactor uses a highly enriched (93%) ^{235}U fuel element of about 8.5 kg, and a heavy water moderator. The burn out of the fuel element defines a reactor cycle operation (about 50 days running at approximately 50 MW). The use of neutron guides allows the transport of neutrons from the reactor core to over 40 instruments. The neutron guides are formed of super mirror materials, where total internal reflection is exploited to transport the neutrons along $\sim$ 100 m with little losses. The energy and flux of the beam, as well as the geometry of the neutron guides, are customised according to the needs of each particular instrument. A schematic representation of the ILL experimental area and instruments is shown in Fig. 2.1. At the ILL, neutrons are mainly used for neutron scattering or diffraction experiments. However, slow neutrons can also be used to induce nuclear reactions such as neutron capture and neutron induced fission. Historically, high resolution nuclear structure studies of nuclei close to stability have been conducted using GAMS [104]. This instrument takes advantage of the high flux available using an *in-pile* target, to induce neutron capture reactions on stable targets. γ-ray spectroscopy of the reaction products was performed using a crystal spectrometer. The high energy resolution of the crystal spectrometer (1000 times better resolution than a conventional semiconductor detector), enabled precise γ-ray spectroscopy and lifetime measurements using the GRID technique [105].

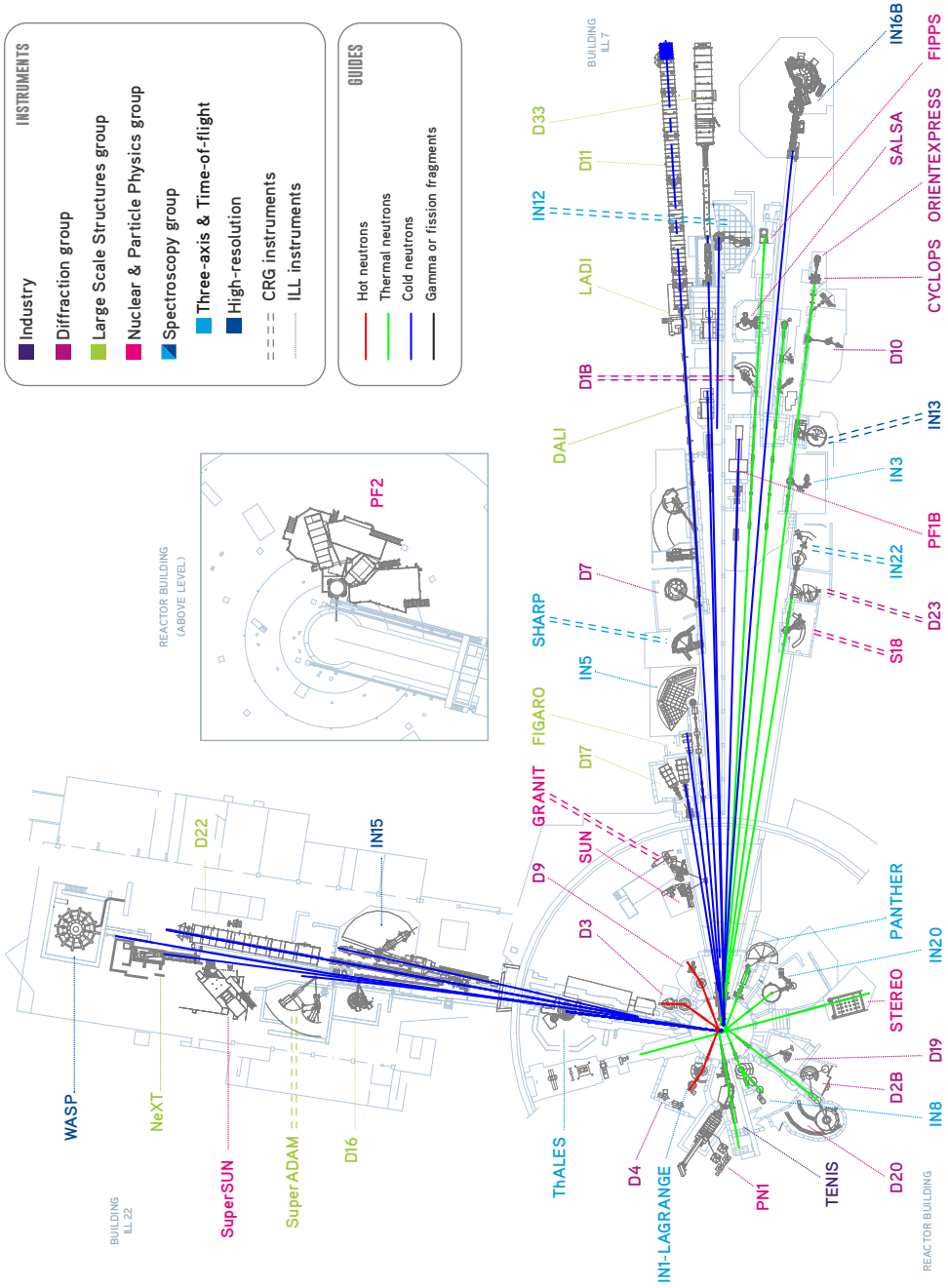

Figure 2.1: Plan of the ILL experimental facilities and instruments. The neutrons are conducted from the reactor core to the experimental area using neutron guides. Cold neutron guides are shown in blue while thermal neutron guides appear in green. The FIPPS instrument and the PFIB facility (where the EXILL campaign took place) are located in one of the guide halls and are labelled in pink. The LOHENGRIN instrument is located inside the reactor building, at the PN1 facility. Image taken from [103].

For more than 40 years, nuclear structure investigations of neutron rich nuclei, as well as fission studies, have been carried out at the ILL with the LOHENGRIN instrument [106]. The main component of the LOHENGRIN instrument is a mass spectrometer used for the separation of fission fragments produced by neutron induced fission at an in-pile target. γ-ray detectors can be installed at the focal plane of the spectrometer to perform γ-ray spectroscopy after isomeric decay or beta decay. The need for prompt γ-ray spectroscopy of fission fragments motivated the EXILL campaign, and later on the installation of the permanent instrument FIPPS. Both the EXILL campaign and the FIPPS instrument exploit *in-beam* target technologies to perform high efficiency and high resolution γ-ray spectroscopy of neutron induced fission and neutron capture reactions. Both setups, with particular focus on the FIPPS instrument extensively used in this thesis work, will be described in detail in the following sections.

2.2 The EXILL campaign

The EXILL campaign combined for the first time a high efficiency γ-ray detector array with an intense neutron beam, used for neutron induced reactions. The name of the campaign comes from the combination of the name of the detectors used (EXOGAM [107]) and the facility where the campaign took place (ILL). The main focus of the campaign was the study of prompt γ rays from fission products of neutron induced fission on ^{235}U and ^{241}Pu, to complement previous fission experiments carried out using spontaneous fission sources and in-beam fission (section 1.4). In addition, neutron capture reactions on a variety of stable targets with different physics cases were also carried out. The EXILL campaign is presented in [90], where the γ-ray spectroscopy analysis is discussed in detail. A description of the lifetime measurements using the fast timing technique performed during the EXILL campaign is given in [108].

The EXILL experimental campaign took place between the end of 2012 and the beginning of 2013. It consisted of 100 days of beam time corresponding to two reactor cycles. The high efficiency detector array was placed at the cold neutron beam facility PFIB. The setup included a collimation system, that achieved a pencil-like beam of approximately 1 cm in diameter and a thermal capture equivalent flux of 10^8 neutrons cm^{-2}s^{-1} at the target position [90]. Throughout the campaign, four different detector configurations were used, combining HPGe (10 EXOGAM clovers, 6 GASP detectors [109] and 2 clover detectors from the LOHENGRIN instrument) with $LaBr_3$ scintillator detectors. Except for the two LOHENGRIN clovers, all HPGe detectors were equipped with BGO Compton-suppression shields. The experimental setup, showing the two main configurations, can be seen in Fig. 2.2.

The EXILL campaign contributed to a better understanding of nuclear structure, both from the study of exotic neutron rich nuclei produced in fission and from nuclei close to stability produced via neutron capture [67, 110, 111, 112]. This motivated the installation of a permanent instrument with a similar design: FIPPS. The FIPPS project aims to combine a high efficiency γ-ray array with a mass spectrometer that allows identification of the fission fragments. More details about the FIPPS instrument, including improvements with respect to the EXILL campaign, its current state and future plans will be given in the following sections.

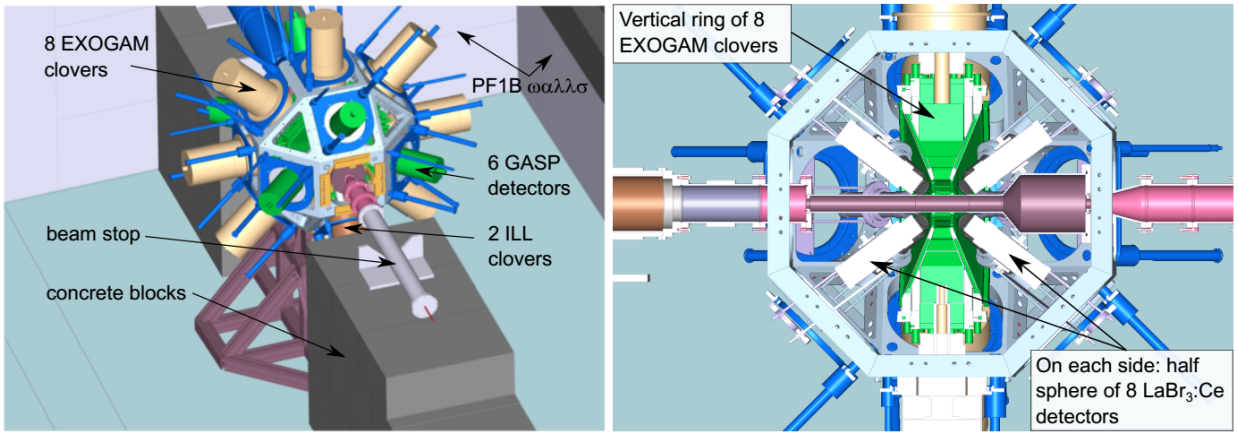

Figure 2.2: Schematic representation of the EXILL setup [90]. On the left, the configuration adopted for the γ spectroscopy experiments using only HPGe detectors is shown. On the right, the configuration used for lifetime measurements that consisted of a combination of HPGe detectors and $LaBr_3$ scintillator detectors (fast-timing setup) is shown.

2.3 The first fission campaign at FIPPS

The FIssion Product Prompt γ-ray Spectrometer (FIPPS) is dedicated to both γ-ray spectroscopy of neutron induced reactions and fission studies. The instrument was conceived as a continuation of the EXILL campaign, with the possibility to improve previous limitations in energy resolution, improve peak to background ratio and increase the selectivity of fission fragments for neutron induced fission experiments.

A significant part of the experimental results presented in this thesis were obtained from the experimental campaign carried out at the FIPPS instrument in September-October 2018. For this campaign, neutron induced fission of ^{235}U was used to produce neutron rich nuclei, whose structure has been studied using γ-ray spectroscopy. For the first time at a neutron beam, an active fission target was used for γ-ray spectroscopy studies, which allowed a tagging of the fission events and consequently a suppression of β-delayed γ-ray background.

The complete experimental campaign lasted a full reactor cycle ($\sim$ 50 days) which was divided into calibration and fission measurements. For the calibration of the array both radioactive sources and (n,γ) reactions were employed. Thermal neutrons were used to induced fission on ^{235}U, using both a 0.635 mg solid target ($\sim$ 7 days) and an active target with the uranium dissolved in a liquid scintillator ($\sim$35 days)

A description of the experimental setup used for this campaign is detailed in the following sections. Firstly, a general presentation of the FIPPS instrument will be given in section 2.3.1. This is followed by a description of the HPGe detector array formed by a combination of FIPPS detectors and detectors from the IFIN-HH collaboration in section 2.3.2. The active fission target will be presented in section 2.3.3. The acquisition system and data processing will be discussed in section 2.3.4. Finally, a

characterisation of the setup in terms of energy resolution and detection efficiency is given in sections 2.3.5 and 2.3.6.

2.3.1 The FIPPS instrument

The FIssion Product Prompt γ-ray Spectrometer [12] is one of the 3 ILL instruments dedicated to nuclear physics research. As already mentioned, the FIPPS project was conceived as a continuation of the EXILL campaign, and aims to perform γ-ray spectroscopy studies after neutron induced reactions. The instrument is situated at the end of the thermal neutron guide H22 (see Fig. 2.1). The FIPPS project is planned in two phases. The first phase has been operational since December 2016, consisting of a "pencil-like" thermal neutron beam coupled to a high resolution γ-ray spectrometer. In the second phase, a mass spectrometer formed by a gas filled magnet (currently under development), will be added to the setup.

The neutron beam exiting the H22 thermal neutron guide (50x30 mm^2) has a large divergence and needs to be collimated at the target position. A collimation is necessary to reduce the contribution to the γ-ray background produced by (n,γ) reactions on elements of the setup, such as the frame of the array or the detectors themselves. A schematic representation of the collimation system is shown in Fig. 2.3. The beam is collimated by a series of five apertures made of neutron absorbing materials placed in a tube coated with borated plastics. The first four apertures are made of boron carbide (B_4C) and the last one is made of ^{6}LiF. (n,α)-reactions take place in the ^{10}B and ^{6}Li with thermal neutron capture cross sections of 3840 b and 940 b respectively. In the case of the ^{10}B(n,α) reaction, α emission is followed by the emission of 0.48 MeV γ rays. In order to reduce the γ-ray background induced by the beam, 5 cm thick lead absorbers are placed after each aperture. A 20 cm thick lead wall is installed at the end of the collimation system for further background suppression. The neutron beam has 15 mm in diameter and a 1x10^8 neutrons $s^{-1}cm^{-2}$ flux at the target position. The collimation system is connected to a target chamber tube which is in turn connected to a beam stop. The whole system (collimation, vacuum chamber and beam stop) is kept under primary vacuum.

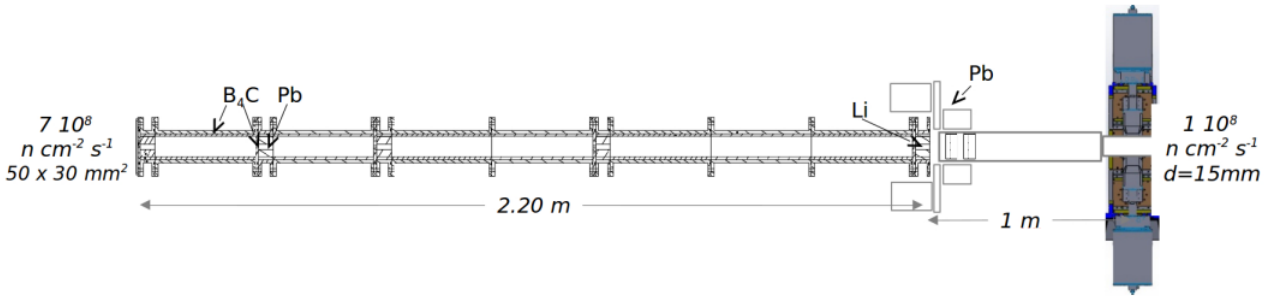

Figure 2.3: Schematic diagram of the FIPPS collimation system and detectors [12].

The FIPPS γ-ray detector array, shown in Fig. 2.4, is formed by a ring of 8 HPGe clover detectors mounted around the target position at 90° with respect to the beam direction. Each FIPPS clover is formed by four n-type HPGe tapered crystals with 50 mm diameter, 80 mm length. In its most

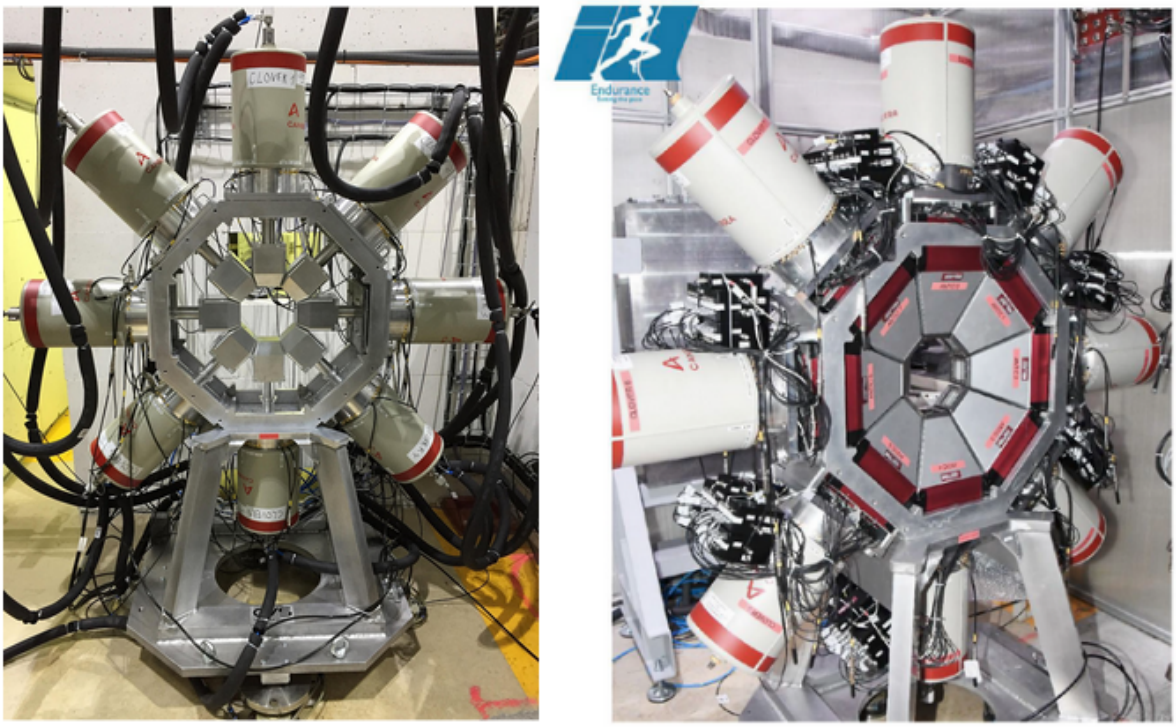

Figure 2.4: FIPPS array formed by 8 HPGe clover detectors mounted in a ring around the target position, shown without (left) and with (right) anti-Compton suppression shields. The FIPPS instrument is part of the Endurance program at the ILL.

compact configuration, the centre of each clover is at a distance of 9 cm from the target position. In March 2019, Compton suppression shields were installed [113]. In this configuration, the detectors are pulled back to a 13.4 cm clover-target distance. The FIPPS anti-Compton shields are segmented into three pieces: front, back and side. The back shield consists of CsI(Tl) detectors, while the front and side shields are made of BGO crystals. The 8 FIPPS HPGe clover detectors can be complemented with ancillary detectors such as $LaBr_3$ scintillator detectors, diamond detectors or additional HPGe detectors, depending on the experimental needs.

2.3.2 The FIPPS+IFIN-HH HPGe γ-ray array

The multiplicity of the γ rays produced in neutron induced fission, together with the need of multiple γ-ray coincidences for fragment identification, demand high efficiency and granularity of the detection system. For this reason, during the ^{235}U fission campaign in 2018, the 8 FIPPS detectors were complimented with an additional 8 HPGe clover detectors from the IFIN-HH collaboration. Each IFIN-HH clover is formed by four tapered crystals of 40.1 mm diameter and 70 mm length. All IFIN-HH clovers are equipped with Compton suppression shields. The FIPPS and IFIN-HH clovers were placed at a radial distance from the target position of 90.3 mm (no anti-Compton shields) and 152.5 mm respectively. The detector configuration is schematically shown in Fig. 2.5.

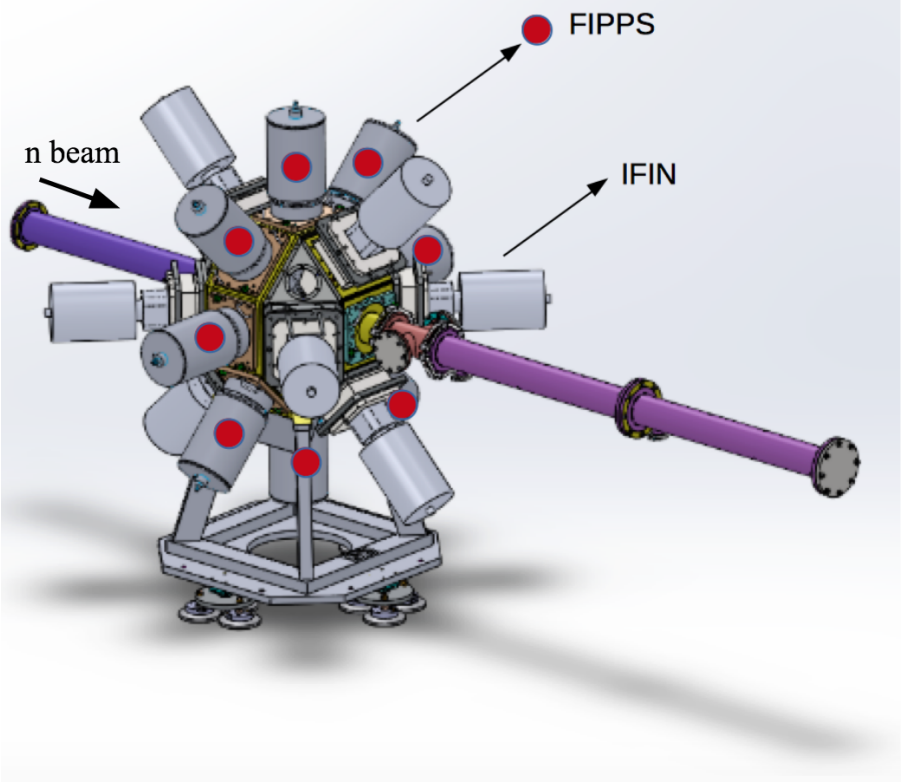

Figure 2.5: Diagram of the HPGe FIPPS+IFIN-HH array. The 8 FIPPS clovers, that form a ring around the target position, are marked in red. There are 4 IFIN clovers on each side of the FIPPS ring. The neutron beam direction is given by the beam tubes shown in purple.

2.3.3 The ^{235}U targets: standard target and active target

The neutron rich nuclei of interest were produced via thermal neutron induced fission of ^{235}U (σ_f=590.64 barns). In this reaction, more than 100 unstable isotopes are produced, who decay towards the valley of stability via β-decay with consequent γ-ray emission. The identification of a particular fission fragment is done via the γ-ray coincidence technique. To optimise the identification of the fission fragments, it is necessary to suppress the background coming from the β-delayed γ emission and improve the peak to total ratio of the HPGe array. For this purpose, for the first time at a high resolution γ-ray spectrometer, an active fission target was developed at the ILL [114]. The active target allows a tagging of the fission events, resulting in a distinction between prompt γ rays and β-delayed γ rays. During the experimental campaign both the newly developed active target and a standard solid $^{235}UO_2$ target were used. A higher fission rate was achieved using the standard fission target, providing higher statistics which were exploited in the analysis of nuclei where the β-decay component is not dominating. Furthermore, the use of the solid target allowed an evaluation of the performance of the active target.

"Standard" target

The same UO_2 target with a Be backing that was used during the EXILL campaign was used at the start of the FIPPS+IFIN-HH fission campaign (see Fig. 2.6). The target was enriched to 99.70% ^{235}U and had a mass of 0.635 mg. The target was mounted in a Li cylinder target holder. The measurement with the standard target lasted 7 days. A fission rate of 80 kHz was achieved.

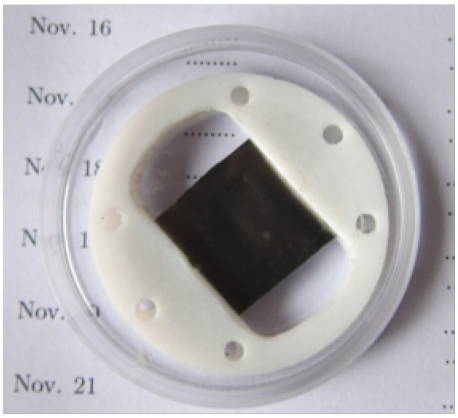

Figure 2.6: Photograph of the standard solid $^{235}UO_2$ used during the EXILL campaign. The same target in a different target holder was used at FIPPS for the fission experiment presented in this section. Image taken from [115].

Active target

The active fission target allows an identification of prompt γ rays and a suppression of the γ-ray background produced after β-decay of the fission fragments. The active target used in the ^{235}U fission campaign was developed specifically for the FIPPS instrument [114]. This new technology is based on dissolving the actinide, in this case the uranium, in a liquid organic scintillator [116]. The solution was prepared at the CEA DIF with nominally 650 μg of ^{235}U diluted in 370 μl of scintillator. This gives an indication of the uranium mass in the target, but unfortunately a precise value is not known due to uncertainties in the preparation of the solution and filling of the target cell.

The target design was optimised aiming for: a minimisation of (n,γ) reactions on the target material and a reduction of the γ-ray absorption between the target and the HPGe detectors, while ensuring an efficient collection of the scintillator light. The active target setup consisted of a target cell containing the scintillator and uranium (shown in Fig. 2.7) and a light guiding system. Both are placed inside a dedicated vacuum target chamber. The target cell is made of an aluminium frame, sapphire windows and PTFE (Polytetrafluoroethylene – $(C_2F_4)_n$) washers. The target cell was placed inside a vacuum chamber formed of carbon fibre and was surrounded by ^{6}Li loaded cylinders. The target cell was optically connected to a photomultiplier tube via a light guiding system formed by a reflective tube and mirror foil (Fig. 2.8).

When a fission reaction takes place inside the target cell, the fission fragments deposit their kinetic energy on the scintillator material that then emits light. The scintillator also emits light when detecting

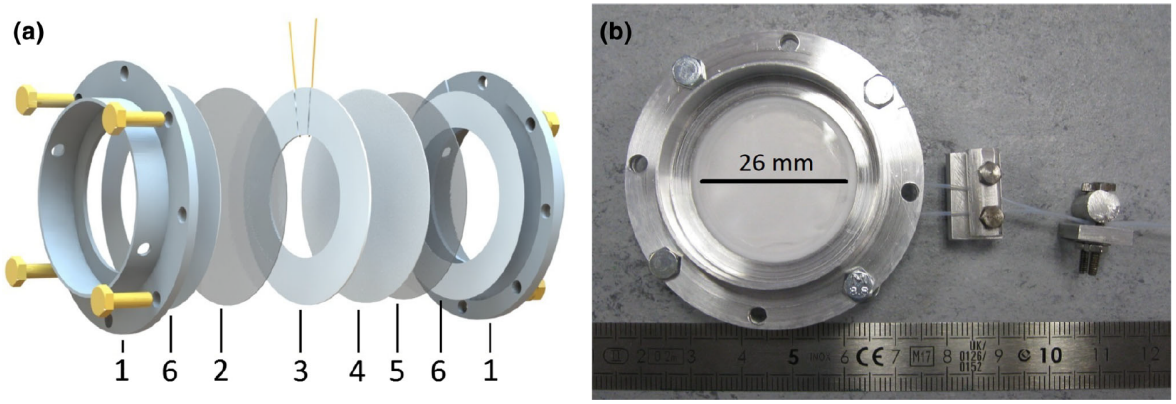

Figure 2.7: a) Diagram of the active target cell components. 1: aluminium frame; 2,5: sapphire window (thickness 0.2 mm); 3,4,6: PTFE (Polytetrafluoroethylene) washers. b) Photograph of target cell without scintillator. Image taken from [114].

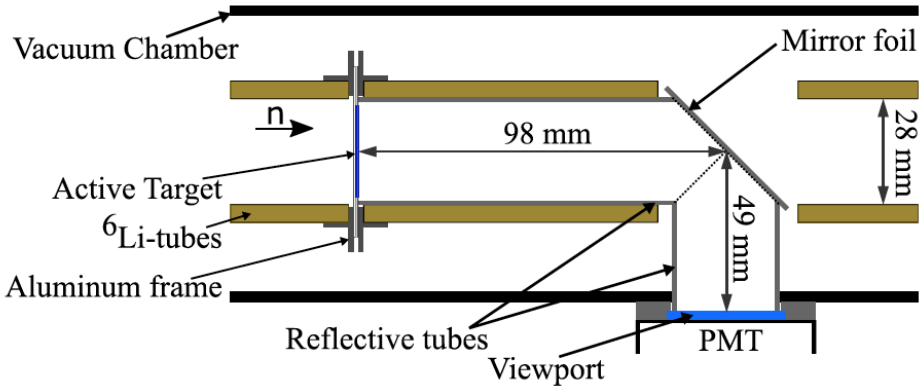

Figure 2.8: Schematics of the active target vacuum chamber and light guiding system. The light emitted by the scintillator of the active target is guided to a photomultiplier tube (PMT) via a reflective tube and mirror foil. Image taken from [114].

alpha particles or electrons. However, the intensity of the emitted light will depend on the ionising power of the emitted particle. Therefore, it is possible to distinguish the particles using pulse shape discrimination (PSD) (see Fig. 2.9). The PSD parameter is defined as the ratio between the total charge integration of the fast component over the slow component of the scintillator light emission: PSD=$(Q_{tot} - Q_{short})/Q_{tot}$. A PSD vs Q_{tot} plot allows an identification of different types of events. As can be seen from Fig. 2.9, a condition on the value of the total integrated charge ($1000 < Q_{tot} < 2000$) can be used to select the fission events.

The measurement using the active target setup lasted approximately 32 days. A fission rate up to 12 kHz was achieved, resulting in a total of 2×10^{10} fission tagged γ-γ coincidences [114]. The total count rate was limited in order to maintain the pileup fraction of the photomultiplier tube under 2%. A comparison of γ-ray spectra, showing the performance of the active target setup with respect to the standard solid target will be shown in the next chapter (see section 3.1.1).

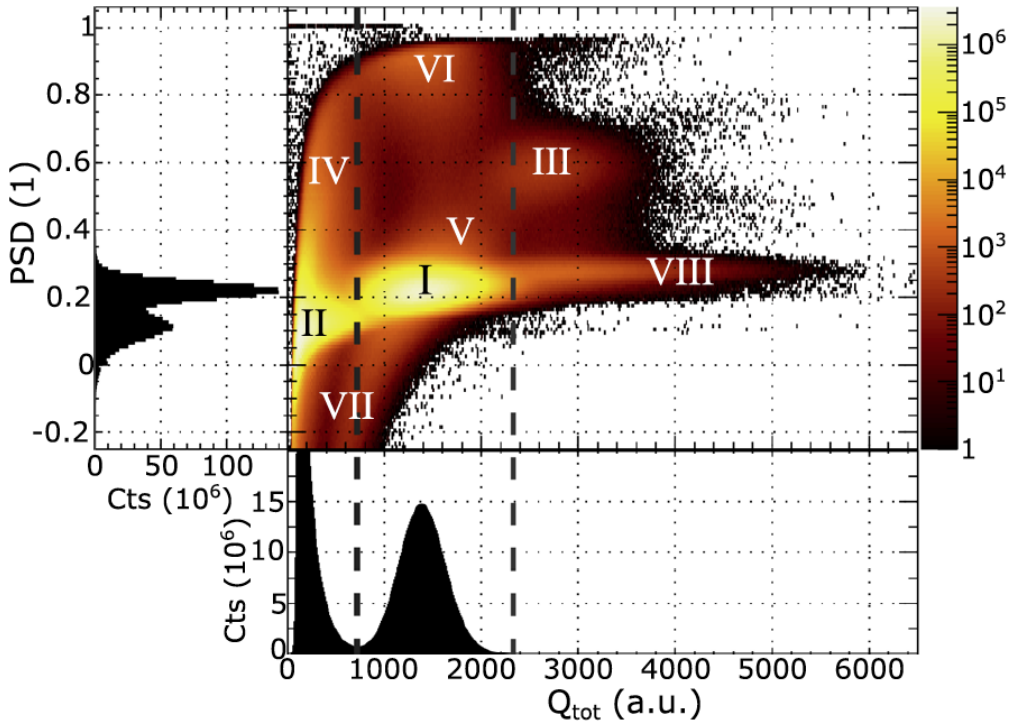

Figure 2.9: Pulse shape discrimination vs total charge detected in the active target after ^{235}U (n,f) reactions, with projections onto both axis shown in the side panels. The different regions define different events, a detailed explanation of each region can be found in [114]. The fission events correspond to region I. In order to select fission events, the condition $1000 < Q_{tot} < 2000$, indicated by the dashed lines, is imposed. Image taken from [114].

2.3.4 The acquisition system and data processing

Digital processing of the signals

The data of the experimental campaign were recorded using a digital acquisition system. The analog signals from the 64 HPGe crystals and anti-Compton shields were processed using V1725 CAEN digitizers with 16 channels of 14-bit resolution and 250 MS/s sampling rate.

The digitizer cards provide a signal processing thanks to an incorporated FPGA with an implemented Digital Pulse Processing (DPP) algorithm, that enables the extraction of the amplitude and time of the signal [117]. The information regarding the energy deposited on HPGe crystals and anti-Compton shields is obtained from the amplitude of the pulse. A trapezoidal filter is used in order to avoid the ballistic deficit caused by different collection times in the detectors [118], therefore optimising the energy resolution of the array. The working principle of this filter is illustrated in Fig. 2.10. The input signal shown in blue consists of the sum of two exponential decays, corresponding to the charge collection time of the detector and the RC of the preamplifier. This signal is then shaped into a trapezoid (shown in red), where the difference between the height of the flat top of the trapezoid and the

one of the baseline is proportional to the amplitude of the detector pulse. The following trapezoidal filter parameters were optimised for each channel in order to obtain the best energy resolution, the best linearity and avoid pileup.

- **Rise time**. The same value was used for all channels: 4 μs.
- **Baseline mean**. Corresponds to how many samples are taken to evaluate the value of the baseline. The higher the number of samples the more accurate the calculation will be. However, for high count rates a high number of samples can cause pileup. The same value was used for all channels: 1024 samples (corresponding to 4.096 μs).
- **Flat top**. Defined as the duration of the flat top. 1 μs was used in all cases.
- **Peak mean**. Number of samples used to calculate the value of the flat top of the trapezoid. The same value was used for all channels: 4 (corresponding to 16 ns).
- **Decay time** τ. Plays the role of the shaping time in an analog amplifier and needs to be adjusted for a proper pole zero cancellation [118]. It depends on the characteristics of the preamplifier and will therefore be detector dependent. The values used were of the order of $\sim$52 μs, tuned by evaluating the symmetry of the γ-ray peaks.

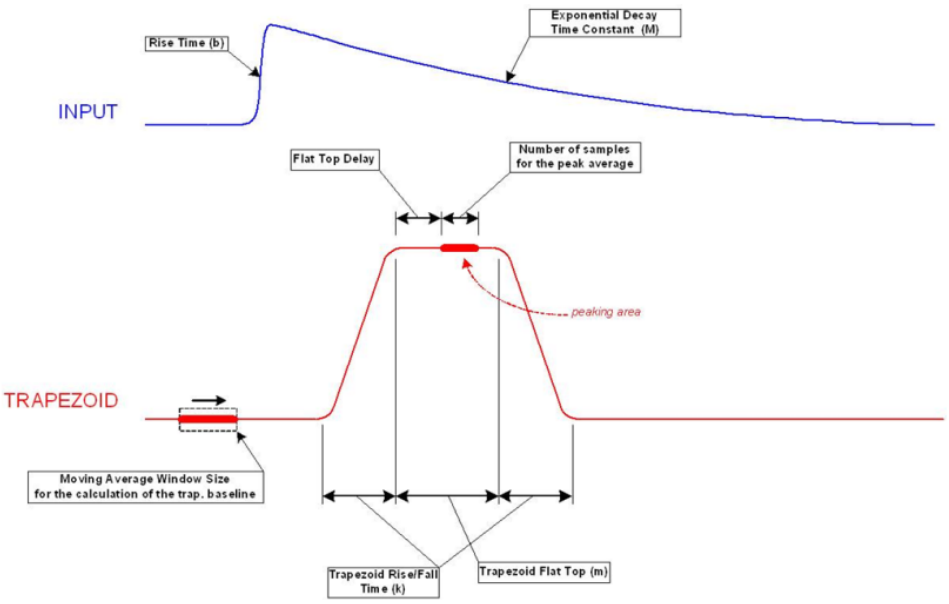

Figure 2.10: Schematic representation of the trapezoid filter applied in the pulse processing. In blue, a typical input signal from a preamplifier. Once the filter is applied, the output signal has a trapezoidal shape, as is shown in red. Image taken from [117].

.

The information regarding the time of arrival of the signal is determined using a leading edge timing on the signal second derivative.

For the case of the active target setup, the photomultiplier tube signal was processed using a V1751 CAEN card with 10-bit resolution and 1GS/s sampling rate. The energy of the scintillation signals is determined using charge integration, which is used to extract the PSD needed for the identification of fission events (for further details see [114]).

Event building

The data were acquired in trigerless mode, with the event building done off-line. For each γ ray detected, the following information was stored: amplitude, adc number and timestamp (in 4ns units). Both the calibration and fission data were saved in a series of 5 minute runs in two formats: ASCII and list-mode (binary). The ASCII format was used to produce γ-ray spectra for online analysis. The list-mode files were used for the event building.

The raw data were sorted using an event building code developed in ROOT [119]. The following steps were followed:

1. Time alignment. To compensate for a delay in the time signals introduced by differences in the cable lengths or electronic channels, the time response of all detectors is aligned to that of a reference detector.

2. Presorting into "clover events". γ rays detected in the same clover within a 280 ns window are grouped into a "clover event". This is done in order to keep flexibility in the choice of the time window on the event builder.

3. Event building. An event is defined in a 1 μs window with more than 1 clover fired. In the case of the active target setup a PMT signal is also required. At this point Compton suppression, cross-talk and energy gain drift corrections, and energy calibrations (discussed in section 2.3.5) are applied.

4. Relevant γ-ray spectra, matrices and cubes are produced for the extraction of the spectroscopic information.

2.3.5 Gain corrections and energy calibrations

In order to exploit the energy resolution of the FIPPS+IFIN-HH array and maximise the selectivity of fission fragments using the γ-coincidence technique (see section 3.1), a precise energy calibration is needed for each of the 64 HPGe crystals. Before an energy calibration could be determined, a correction for observed ADC gain shifts and cross-talk effects introduced by the electronics was applied. This data preparation was carried out by the ILL FIPPS group in collaboration with IP2I of Lyon. The main stages of the data preparation will be given in the following section, further details can be found in [120].

Gain drift correction

Comparing the γ-ray spectra collected in a series of runs, a drift in the peak positions of given γ rays over time was observed. This change in peak position is caused by a drift in the gain of the CAEN ADCs, thought to come from temperature variations (origin under investigation). An example of the change of peak position as a function of time for the case of a single FIPPS detector is plotted in Fig. 2.11.

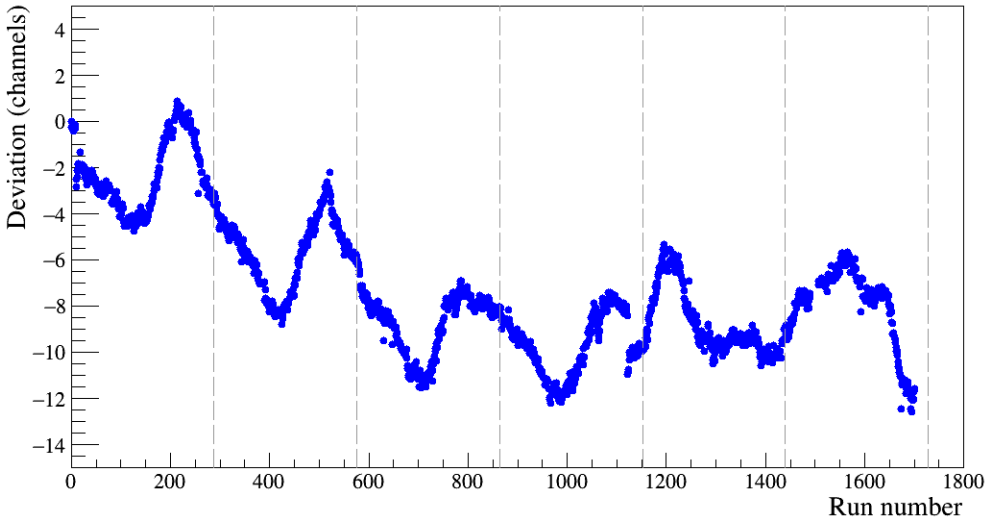

Figure 2.11: Typical gain drift observed in the peak position of the 1778.9 keV transition from the ^{27}Al(n,γ) reaction as a function of run number over a 6 day measurement (each run lasts 5 minutes). The vertical dashed lines indicate periods of 24 hours. A shift in one channel corresponds to a shift of approximately 0.35 keV in the peak centroid.

In order to correct for this gain drift, all runs are aligned to a reference run. The centroids of a series of prominent peaks in the spectra (coming from the fission reaction and neutron capture on aluminium) are tracked using an automatic fit routine. These channel positions are then used to calculate coefficients to realign the runs using a linear relationship.

Add-back procedure and cross-talk correction

As was discussed in section 2.3.2, the FIPPS-IFIN-HH array is formed of 16 HPGe clovers, each grouping 4 HPGe crystals in a single cryostat. Clover detectors, which were developed in the 1990's [121], offer the advantage of large active volumes while maintaining granularity.

The clover geometry allows for a gain in peak to total ratio and full-energy peak efficiency thanks to the add-back procedure, which adds the energies of γ rays detected in coincidence in neighbouring crystals of the same module. The increase of full-energy peak efficiency for a given energy E is quantified using the add-back factor f, defined as the ratio between the measured counts in add-back

mode and the measured counts in direct detection:

$$f(E) = \frac{(\mathrm{N_{counts}}(E))_{\mathrm{ADD-BACK}}}{(\mathrm{N_{counts}}(E))_{\mathrm{Direct}}}. \tag{2.1}$$

An add-back procedure was applied on the FIPPS and IFIN-HH clovers, where only neighbouring crystals from the same clover were considered. The obtained add-back factors as a function of the energy for the FIPPS+IFIN-HH array are shown in Fig. 2.12. A linear fit to the experimental data was performed, considering two separate regions. The different behaviour observed for energies greater than ∼1 MeV is due to the contribution of pair production. The add-back functions will be used in combination with the efficiency in order to evaluate experimental intensities.

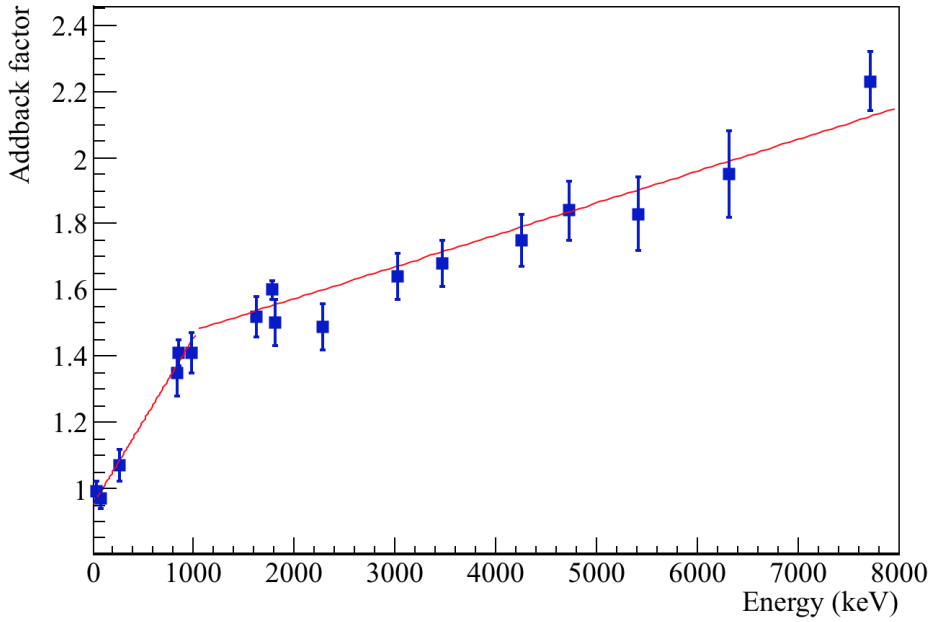

Figure 2.12: Add-back factor for the FIPPS+IFIN-HH array as a function of energy obtained using the ^{27}Al(n,γ) reaction. A linear fit, shown in red, was performed. Two regions were considered due to the contribution of pair production for energies greater than 1.022 MeV.

Comparing spectra before and after the application of the add-back procedure, a shift of the high energy peak positions was observed. This shift toward lower energy is caused by a crosstalk phenomenon that appears when multiple crystals in a clover are firing at the same time. The crosstalk effect is well known in segmented HPGe detectors, such as the ones of the AGATA array, and was found to be caused by current induction and electronic coupling [122]. When a γ ray interacts in one crystal the signal it produces will induce a smaller opposite-sign signal in the neighbouring crystal. If a second γ ray is detected simultaneously, its measured amplitude will decrease. Fig. 2.13 shows the effect on peak position and width, for the case of a 511 keV transition, as a function of clover multiplicity.

A ^{152}Eu source and the ^{27}Al(n,γ) reaction were used to quantify and develop a method to correct for the crosstalk [120]. The energy shift of the second γ ray firing in the clover was found to be

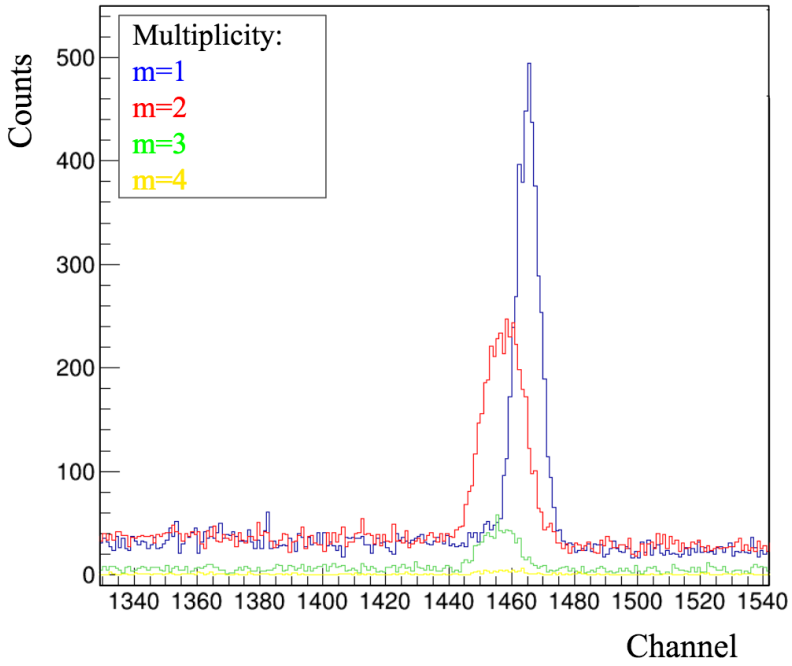

Figure 2.13: Uncalibrated spectra of one of the FIPPS clovers showing the 511 keV peak for different clover multiplicities. A broadening and shift towards lower energy is observed for events where more than one γ ray is detected in the clover.

proportional to the energy of the first detected γ ray. A linear correction was applied to each crystal pair for all the clover detectors. More details on the correction procedure and improvement of energy resolution after its implementation can be found in [120].

Energy calibration

The energy calibration of the FIPPS-IFIN-HH array was performed using known γ-ray transitions from the ^{27}Al(n,γ) reaction, with a cross section of 0.231 b, and the ^{55}Mn(n,γ) reaction, with a cross section of 13.3 b (contamination of the Al target). The transitions used, covering a range from 30 keV up to 7.7 MeV, are reported in Table 2.1.

Each of the 64 crystals of the array were calibrated individually. Strong ADC non-linearities introduced by the electronic cards were observed. The energy range was split into two regions, each calibrated using a 6th order polynomial. To avoid the influence of cross talk, the calibration coefficients were obtained selecting events with clover multiplicity equal to 1. The peak characteristics obtained for transitions in the ^{27}Al(n,γ) reaction after calibration, both with and without cross talk correction, of the full FIPPS+IFIN-HH array are shown in Fig. 2.14.

Energy (keV)	Reaction	Energy (keV)	Reaction
30.6382(7)	^{27}Al(n,γ)^{28}Al	2282.773(14)	^{27}Al(n,γ)^{28}Al
83.8990(15)	^{55}Mn(n,γ)^{56}Mn	3033.89(13)	^{27}Al(n,γ)^{28}Al
212.017(6)	^{55}Mn(n,γ)^{56}Mn	3465.07(10)	^{27}Al(n,γ)^{28}Al
271.175(9)	^{55}Mn(n,γ)^{56}Mn	4259.539(8)	^{27}Al(n,γ)^{28}Al
831.45(4)	^{27}Al(n,γ)^{28}Al	4733.847(12)	^{27}Al(n,γ)^{28}Al
846.764(2)	^{56}Mn β^-	6702.034(7)	^{27}Al(n,γ)^{28}Al
983.02(2)	^{27}Al(n,γ)^{28}Al	7213.034(7)	^{27}Al(n,γ)^{28}Al
1622.87(6)	^{27}Al(n,γ)^{28}Al	7693.398(11)	^{27}Al(n,γ)^{28}Al
1778.969(15)	^{28}Al β^-	7724.034(7)	^{27}Al(n,γ)^{28}Al
1810.726(4)	^{56}Mn β^-		

Table 2.1: Known γ-ray transitions from neutron capture of the ^{27}Al target used for energy calibrations.

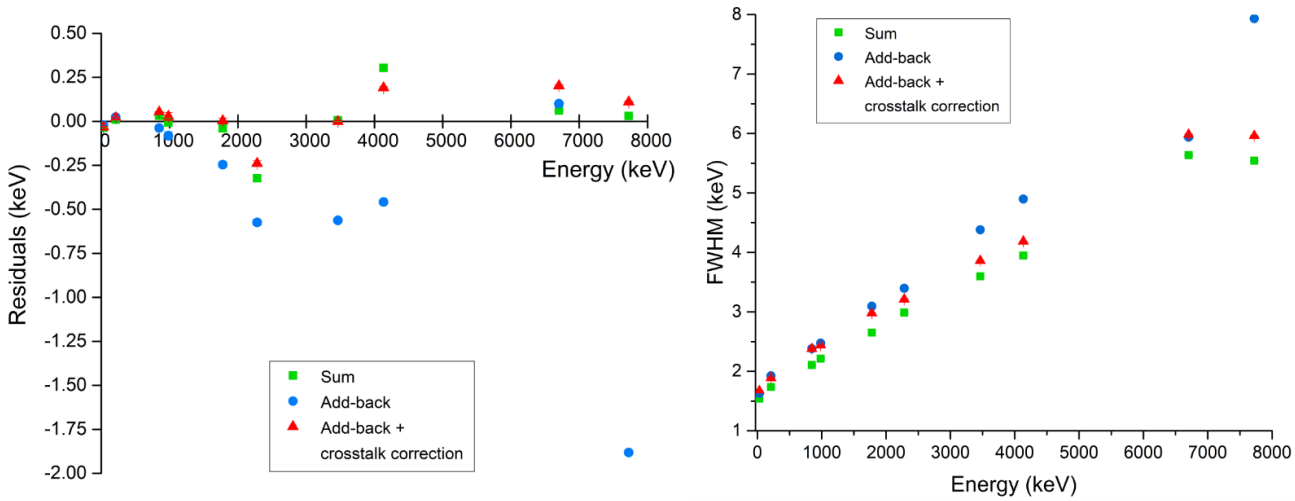

Figure 2.14: Performance of the energy calibration and cross talk correction showing: energy residuals (left) and FWHM (right) of γ transitions from ^{27}Al(n,γ). Image taken from [120].

An evaluation of the energy calibration of the full FIPPS+IFIN-HH array, applied to the standard solid fission target data, is reported in Fig. 2.15. This evaluation will be used as a reference in the multiple coincidence analysis of the fission data. Known γ-ray energies from high yield fission fragments in a 30 to 5000 keV range were used for the evaluation. An offset of 0.2 keV is observed at low energies. The large residuals observed at high energies are thought to be caused by an underestimation of the uncertainty in published energy values, due to the difficulty of a good high energy calibration using standard calibration sources. In this respect, the FIPPS setup offers the advantage of having the possibility to use well known neutron capture reactions for calibration purposes. The quality of the energy resolution of the FIPPS+IFIN-HH array is evident in the FWHM values obtained at high energies, which improve by 1.2 keV at 4 MeV with respect to the EXILL campaign [115].

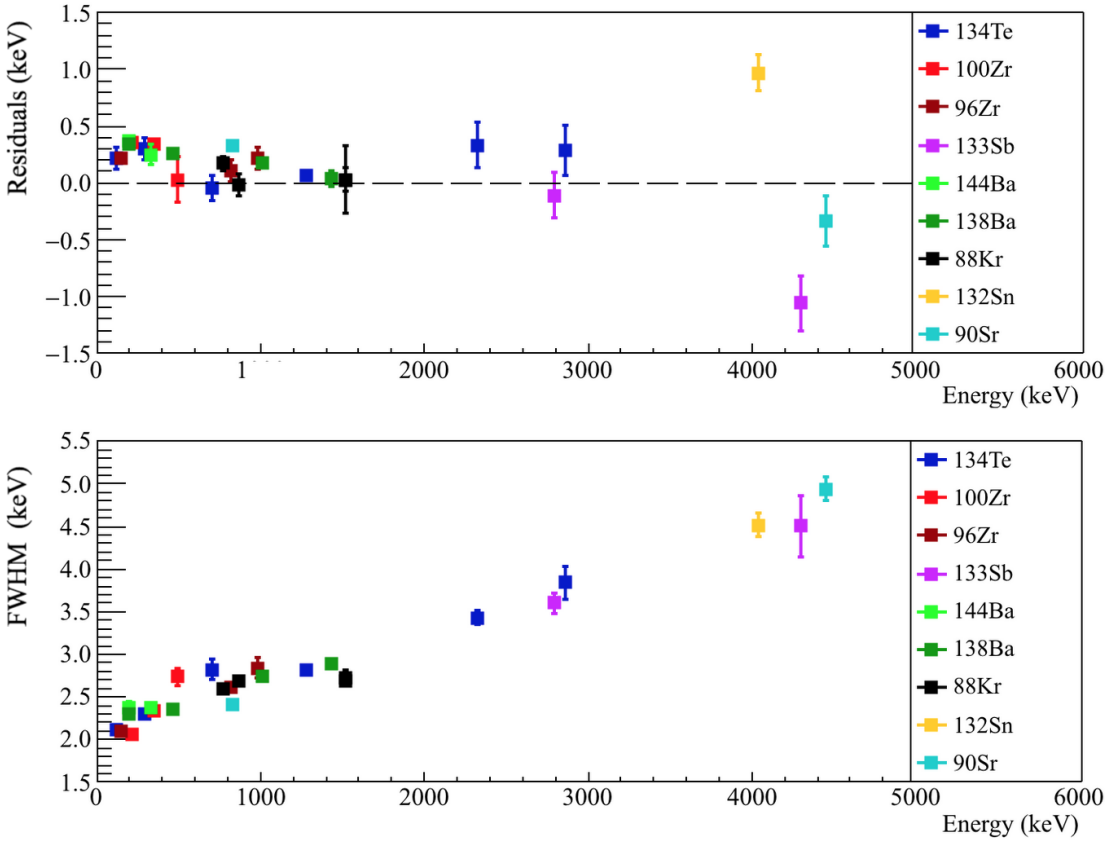

Figure 2.15: Evaluation of the quality of the energy calibration of the FIPPS+IFIN-HH array, performed using the main transitions observed in the fission data of the standard solid target. Deviation from the published energy values (top) as well as the FWHM of the fitted peaks (bottom) are shown as a function of energy.

2.3.6 Efficiency calibration

When using γ-ray spectroscopy for the construction of level schemes of nuclear excited states, it is essential to be able to assign intensity values to the observed γ-ray transitions, which are then used to determine branching ratios and transition probabilities. Since the detection efficiency of HPGe

detectors is strongly dependent on the energy, in order to compare counting rates at different energies, the observed rates need to be corrected for the detection efficiency. An evaluation of the efficiency of the FIPPS+IFIN-HH array was performed using both a ^{152}Eu source and neutron capture reactions on a ^{48}Ti target. γ-γ coincidences in cascades of ^{152}Gd and ^{152}Sm were employed to obtain absolute efficiency values independent of dead time effects, at energies of 121.7 keV and 344 keV. These values were in turn used to obtain an absolute efficiency curve. The experimental efficiency curve was then compared to Monte Carlo simulations.

Efficiency calibration using a ^{152}Eu source of known activity

As a first step in the efficiency calibration, a ^{152}Eu source of known activity was used to obtain absolute efficiency values of the FIPPS+IFIN-HH array using known transitions in a 100-1500 keV range (see Table. 2.2). The number of recorded counts in the 121.7817 keV and 1408.013 keV peaks are plotted for each individual crystal in Fig. 2.16. The histograms clearly show a higher number of counts in both cases for the FIPPS detectors, that are closer to the target position than the IFIN-HH detectors.

Energy (keV)	**Photons per 100 disint.**
40.03(4) (K_α)	58.5(6)
45.69(4) (K_β)	14.8(2)
121.7817(3)	28.41(13)
244.6930(8)	7.55(4)
344.2785(12)	26.59(12)
411.1165(12)	2.238(10)
444.00(3)	2.80(2)
778.905(2)	12.97(6)
867.380(3)	4.24(2)
964.057(5)	14.50(6)
1085.837(10)	10.13(6)
1112.076(3)	13.41(6)
1408.013(3)	20.85(8)

Table 2.2: Main γ-ray transitions and X-rays observed in the decay of a ^{152}Eu source. Energy and intensity values are taken from [123].

The known activity of the ^{152}Eu source was used to estimate the absolute efficiency of the FIPPS+IFIN-HH array at 121.7817 keV and 1408.013 keV. This method provides a first estimation, since it strongly depends on the accuracy of the value of the activity which is not known very precisely (a relative uncertainty value of $\sim 3\%$ is considered). In addition, this method is sensitive to the dead time of the system. Given the activity of a source, it is possible to determine the absolute efficiency, $\epsilon_{abs}(E_\gamma)$, of

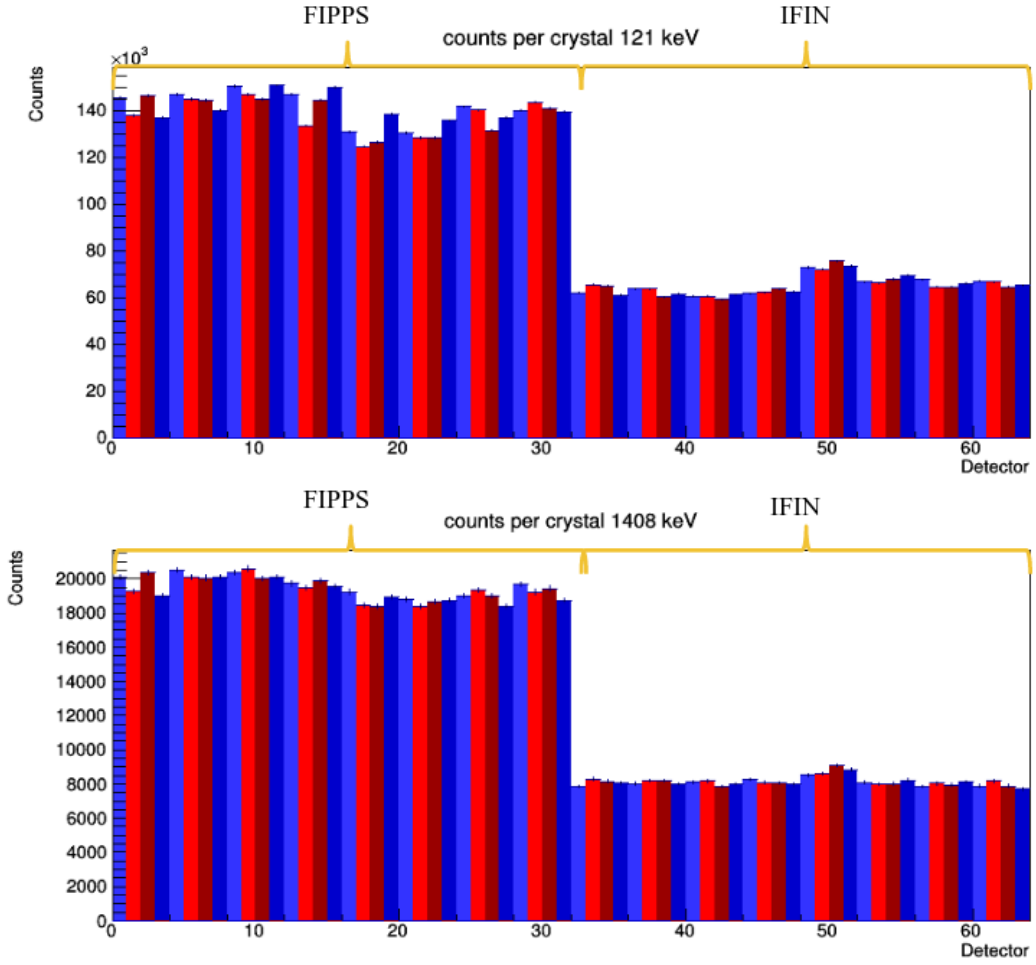

Figure 2.16: Number of counts in a 5 minute measurement of ^{152}Eu decay for each of the 64 crystals forming the FIPPS+IFIN-HH array . The number of counts are shown for two of the most intense transitions in ^{152}Eu: 121.779 keV (top) and 1408.013 keV (bottom). The ^{152}Eu source was placed at the centre of the array, without a target cell. For the case of the FIPPS clover detectors, the crystals shown in red are on the collimation side and the ones shown in blue are on the beam dump side.

an individual detector or the full detector array for a particular γ-ray energy E_γ:

$$\epsilon_{abs}(E_\gamma) = \frac{N^m(E_\gamma)}{I_\gamma A \Delta t}, \tag{2.2}$$

where $N^m(E_\gamma)$ is the number of counts measured at that energy, I_γ is the intensity of the transition, A is the activity of the source and Δt is the measuring time. The nominal activity of the source on the 1st of September 2012 was $4.20(13) \times 10^5$ Bq, giving an activity of $3.08(9) \times 10^5$ Bq on the day of the measurement (17th of September 2018). The absolute efficiency was measured for two γ-ray energies: 121.7817 keV and 1408.013 keV. The number of counts were obtained from the area of the corresponding peaks in the calibrated ADC projections. The efficiencies obtained using equation 2.2 are: $\epsilon_{abs}(121.7817) = 24.9(8)\%$ and $\epsilon_{abs}(1408.013) = 4.58(14)\%$. The main contribution to the

uncertainty of the efficiency comes from the uncertainty in the activity.

Since the measured activity of the source has a high uncertainty, it is worth using a method that is independent of this value and also independent of the dead time of the system. The absolute efficiency at the energies of 121.7817 keV and 344.2785 keV can be obtained using $\gamma - \gamma$ coincidences. For this method, one takes advantage of the fact that when ^{152}Eu decays to ^{152}Sm, the ^{152}Sm 1529.802 keV state can only be directly populated. To deexcite from this state two γ rays are produced in a cascade with the following energies: 121.7817 keV and 1408.013 keV (see in Fig. 2.17). Therefore, the number of 121.7817 keV γ rays emitted in that particular cascade will be equal to the number of 1408.013 keV γ rays emitted. When the ^{152}Eu decays to ^{152}Gd, a cascade formed by a 778.9045 keV γ ray and a 344.2785 keV γ ray with the same characteristics is observed. The same method can be applied to both cascades.

The number of measured γ rays of energy 1408.013 keV, $N_\gamma^m(1408.013)$, is given by:

$$N_\gamma^m(1408.013) = N_\gamma(1408.013)\epsilon_{abs}(1408.013), \tag{2.3}$$

where $N_\gamma(1408.013)$ is the number of 1408.013 keV γ-rays emitted by the source($= I_{1408.013}A$) and ϵ_{abs} is the absolute efficiency at that energy. The number of measured coincident events with 121.7817 keV and 1408.013 keV γ-rays, $N_{\gamma\gamma}^m(121.7817, 1408.013)$, can be expressed as:

$$N_{\gamma\gamma}^m(121.7817, 1408.013) = N_\gamma(1408.013)P_\gamma(121.7817)\Big(\frac{N-1}{N}\Big)\epsilon_{abs}(121.7817)\epsilon_{abs}(1408.013), \tag{2.4}$$

where $P_\gamma(121.7817)$ is the probability that once in the 2+ state, shown in Fig. 2.17, the ^{152}Sm nucleus will deexcite via gamma emission vs. internal conversion, and N is the number of crystals which is equal to 64 in this case.

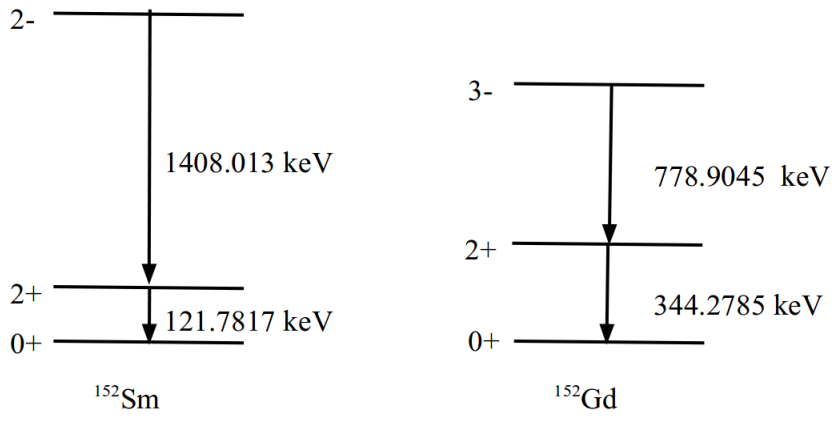

Figure 2.17: Cascades in ^{152}Sm and ^{152}Gd populated from the decay of ^{152}Eu.

Using equations 2.3 and 2.4 we obtain the following expression for $\epsilon_{abs}(121.7817)$:

$$\epsilon_{abs}(121.7817) = \frac{N_{\gamma\gamma}^m(121.7817, 1408.013)}{N_\gamma(1408.013)P_\gamma(121.7817)\Big(\frac{N-1}{N}\Big)}. \tag{2.5}$$

The number of 121.7817 keV and 1408.013 keV coincidences were obtained by gating on the 1408.013 keV peak in a $\gamma - \gamma$ matrix, no background substraction was done in the gating process. The value of $P_\gamma(121.7817)$ was calculated from the internal conversion coefficient, α, defined as the ratio between the number of deexcitations by electron emission and number of deexcitations by γ-ray emission for a given excited state. For the 121.7817 keV γ ray, a value of $\alpha = 1.165(35)$ [123] was used, resulting in $P_\gamma(121.7817) = 1/(1+\alpha) = 0.462(7)$.

The efficiencies obtained using equation 2.5 for both cascades were: $\epsilon_{abs}(121.7817) = 25.8(4)\%$ and $\epsilon_{abs}(344.2785) = 12.6(4)\%$. However, equation 2.4 is valid only if the efficiency of all the detectors is the same and needs to be corrected for the angular correlation between the two γ-rays of the cascade. To take into account the angular correlation of these transitions, as will be shown in section 3.3, one should consider:

$$W(\theta) = A_0[1 + a_2 P_2(cos(\theta)) + a_4 P_4(cos(\theta))], \tag{2.6}$$

where $W(\theta)$ is the probability that the two γ-rays are emitted with a relative angle θ. P_2 and P_4 are the Legendre polynomials. A_0 depends on the intensity of the cascade. For the 121.7817 keV and the 1408.013 keV cascade the coefficients are: $a_2 = 0.2179826$ and $a_4 = 0.0006026408$. For the 344.2785 keV and 778.9045 keV cascade the coefficients are: $a_2 = -0.07142857$ and $a_4 = 0$. The angular correlation functions are shown in Fig. 2.18.

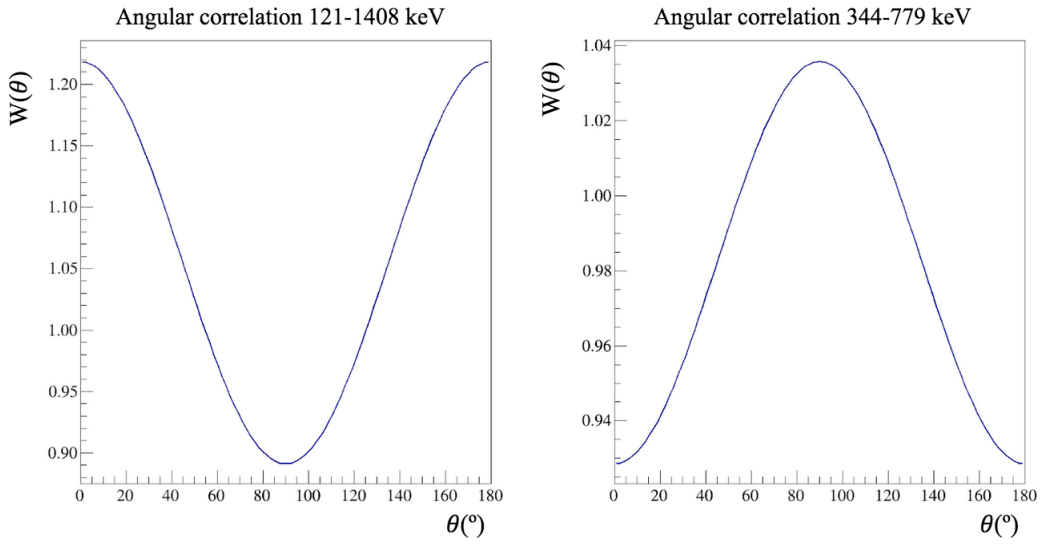

Figure 2.18: Angular correlation of the 121.7817 keV and 1408.013 keV 2→2→0 cascade in ^{152}Sm (left). Angular correlation of the 344.2785 keV and 778.9045 keV 3→2→0 cascade in ^{152}Gd (right).

The correction for angular correlation between two γ rays is applied event by event using the following procedure. A gate is applied on the 1408.013 keV γ-ray in a way that only the events that include this energy are considered. For each of these events, the value of $W(\theta_{ij})$ is computed for all pairs of detectors involved in the event. Each event with such a coincidence is weighted by $1/W(\theta)$, obtaining a corrected number of coincidences that can be used in equation 2.5.

The efficiency values obtained using the $\gamma - \gamma$ coincidence method are summarised in Table 2.3. The uncertainty on the efficiency at 121.7817 keV is dominated by the uncertainty of P_γ. The angular correlation correction contribution produces a decrease of 3.0 % in the efficiency at 121.7817 keV, and an increase of 8.8 % at 344.2785 keV.

Energy (keV)	**No correction**	**Event by event correction**
121.7817(3)	29.30(4)	28.41(4)
344.2785(12)	12.91(4)	14.16(5)

Table 2.3: Absolute efficiency (given in %) for the FIPPS+IFIN-HH array, obtained using a ^{152}Eu source and the $\gamma - \gamma$ coincidence method. Values without an angular correlation correction are compared to those obtained by applying an event by event correction.

Efficiency curve using a ^{152}Eu source and neutron capture reactions

Once an absolute efficiency value has been measured using γ-γ coincidences, an efficiency curve is determined using the ^{152}Eu source in addition to neutron capture reactions to extend the energy range. The γ-ray transitions used from the ^{48}Ti(n,γ) reaction are reported in Table 2.4.

^{48}**Ti(n,γ)**	
Energy (keV)	Intensity (%)
341.706(4)	24.8(8)
1381.745(5)	85(3)
1585.942(6)	10.2(4)
1761.97(6)	5.3(2)
3026.68(3)	2.07(9)
4881.38(3)	4.51(14)
6418.53(6)	30.5(9)
6760.12(4)	46.3(14)

Table 2.4: Main γ-ray transitions and corresponding intensities resulting from the ^{48}Ti(n,γ) reaction [124].

To measure absolute efficiency values using neutron capture reactions, the neutron capture rate can be used instead of the activity in equation 2.2. The capture rate, r, was calculated using:

$$r = \frac{mAbN_A}{M}\Phi\sigma, \tag{2.7}$$

where m is the mass of the target used, Ab is the isotopic abundance, N_A is Avogadro's constant, M is the molar mass, Φ is the neutron flux and σ is the neutron capture cross-section.

Fig. 2.19 shows the resulting experimental absolute efficiency curve of the FIPPS+IFIN-HH array obtained using both the ^{152}Eu source and the ^{48}Ti(n,γ) reaction. Due to uncertainties in the deter-

mination of the neutron flux[1], a flux was chosen in order to have consistent efficiency values between both data-sets. The data points were fitted using the following 8-parameter function [126]:

$$\epsilon(E) = Norm \exp\left\{\left[(A+B\ln(E/100)+C\ln^2(E/100))^{-G}+(D+E\ln(E/1000)+F\ln^2(E/1000))^{-G}\right]^{-1/G}\right\}. \quad (2.8)$$

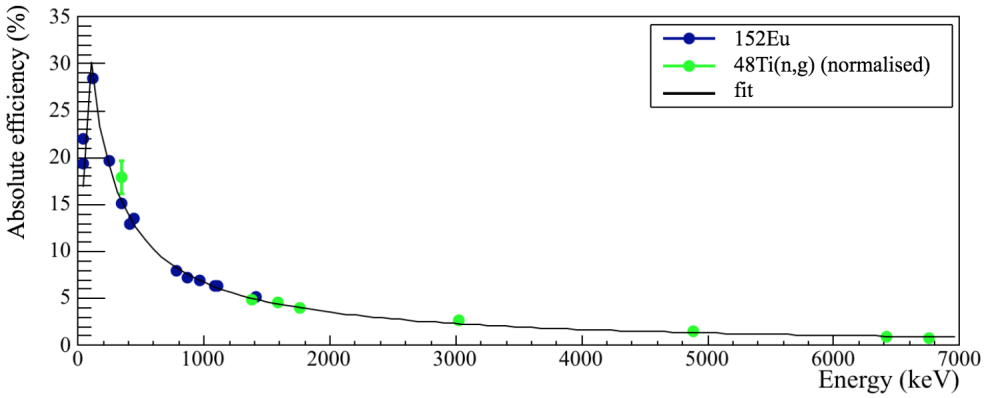

Figure 2.19: Experimental efficiency curve of the FIPPS+IFIN-HH array obtained using a ^{152}Eu source and a ^{48}Ti(n,γ) reaction.

In order to increase the number of available data points, and therefore the reliability of the obtained efficiency curve, GEANT4 simulations were used to calculate absolute efficiency values for γ-ray transitions observed in ^{55}Mn(n,γ) and ^{27}Al(n,γ) reactions. The accuracy of the Monte Carlo simulations was validated by comparing experimental and simulated efficiency values for the ^{152}Eu source. As can be seen in Fig. 2.20, experimental and simulated values are consistent except at low energies. The difference can be explained by threshold effects present in experimental data only.

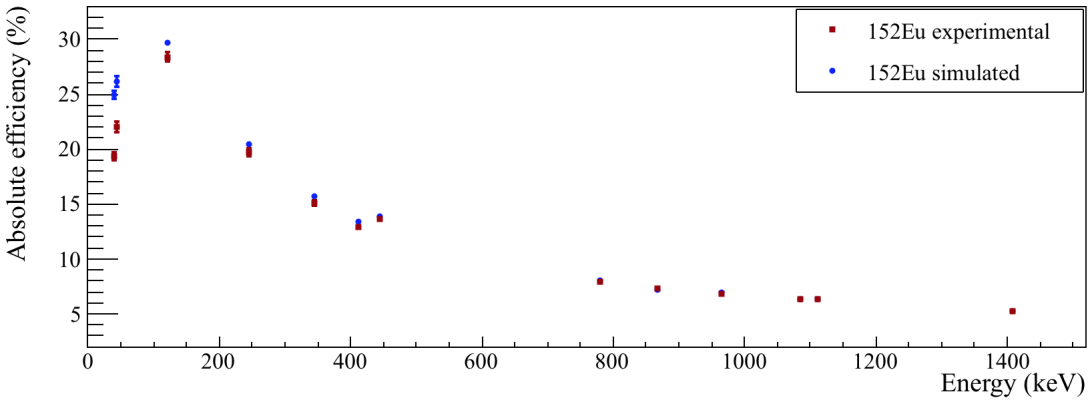

Figure 2.20: Simulated vs experimental absolute efficiency values for main transitions in ^{152}Eu.

[1]The flux can be determined using a gold foil measurement, which resulted in a value of $5.92(1) \times 10^7$ neutrons $cm^{-2}s^{-1}$ [125]. However, the flux at the target position of the FIPPS instrument is not stable due to neutron absorption caused by other instruments located upstream of the neutron guide.

The final efficiency curve was obtained using the combination of a simulated ^{152}Eu source, and ^{48}Ti(n,γ), ^{55}Mn(n,γ) and ^{27}Al(n,γ) reactions. The data points along with the fitted function and residuals of the fit are shown in Fig. 2.21. For the low energy range, the experimental data points are used. The fit parameters for the low energy range were fixed using the experimental data points. The obtained fit parameters are reported in Table 2.5. The efficiency values shown correspond to absolute efficiency values without taking into account the efficiency gain introduced by the add-back procedure. To determine unknown intensities in the Kr and Br isotopes of interest in the fission data, the add-back factor (Fig. 2.12) is taken into account.

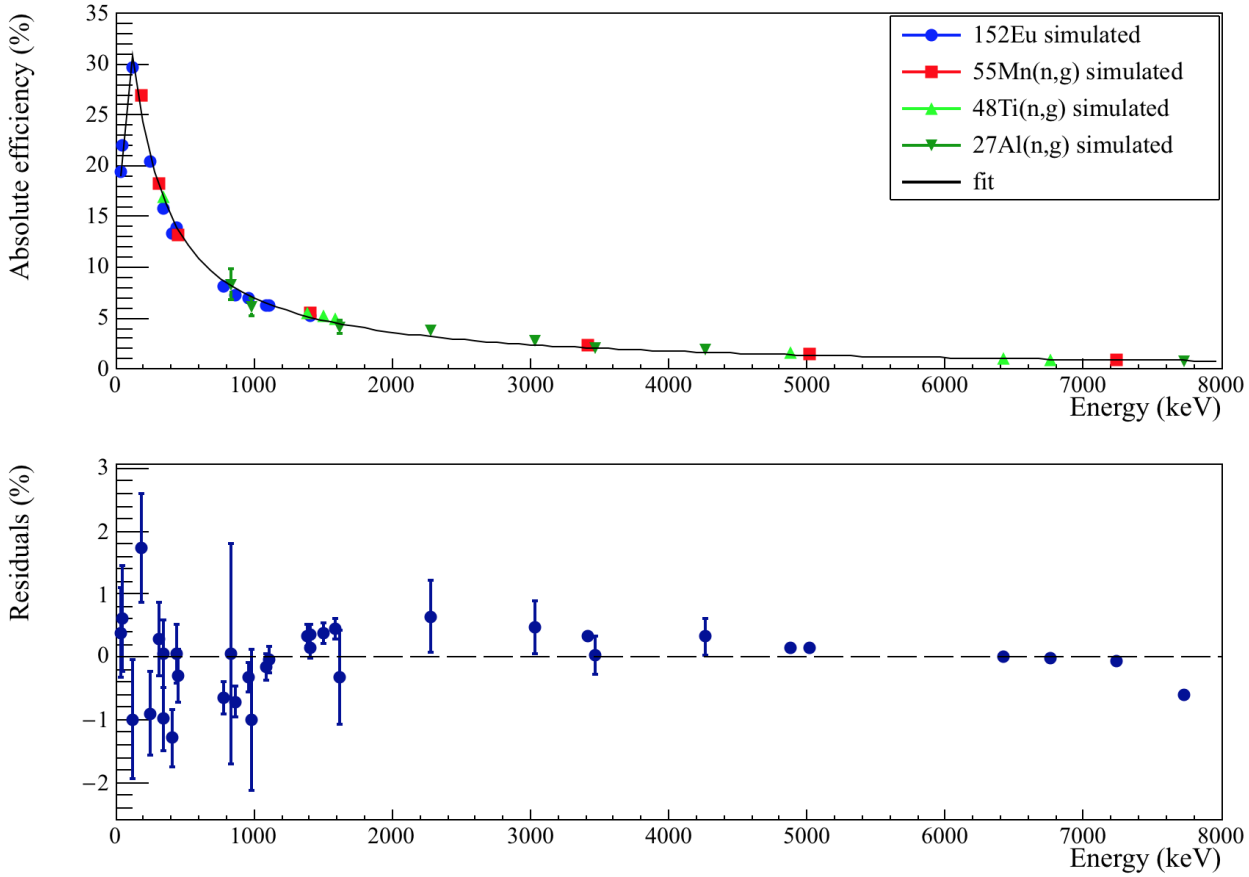

Figure 2.21: Simulated absolute efficiency curve for the FIPPS+IFIN-HH array. The simulated efficiency values for energies lower than 100 keV are corrected for threshold effects using experimental values (see text for more details).

$D = 7.064(18)$	$E = -0.897(2)$	$F = -7.19(17) \times 10^{-2}$
$G = 21.8(8)$	$Norm = 5.9(1)$	

Table 2.5: Fit parameters for the efficiency function (eq. 2.8) of the FIPPS+IFIN-HH array. Parameters A and B are fixed to 9 and 1 respectively, while parameter C is set to zero.

2.4 The AGATA-VAMOS++ setup at GANIL

The fission data collected at the ILL were complemented with data from a fission experiment where the HPGe array AGATA (Advanced GAmma Tracking Array) [11] was coupled to the mass spectrometer VAMOS++ (VAriable MOde Spectrometer) [10]. As previously discussed, one of the main challenges of γ-ray spectroscopy following a fission reaction, is identifying which fission fragment is emitting a particular γ-ray. The AGATA-VAMOS++ setup presents the advantage of a full identification in A and Z of the fission fragments. In this work, this characteristic was particularly exploited to investigate neutron rich Br isotopes for which no spectroscopic information was known, and that could therefore not be identified using the γ coincidence technique (section 3.1). The experimental fission campaign took place at GANIL in 2015, prior to the start of this work. In this section a brief overview of the characteristics of the experimental setup will be given.

The isotopes of interest were produced using a ^{238}U beam (with 6.2 MeV/u and 1 pnA intensity) impinging on a 10 μm ^{9}Be target. The forward focus of the fission fragments (with a recoil velocity of $\beta \sim 0.11$c), due to the inverse kinematics fission reaction, improves the detection efficiency and identification in the spectrometer. A schematic representation of the experimental setup used, showing the coupling of the AGATA array to the VAMOS++ spectrometer, can be seen in Fig. 2.22.

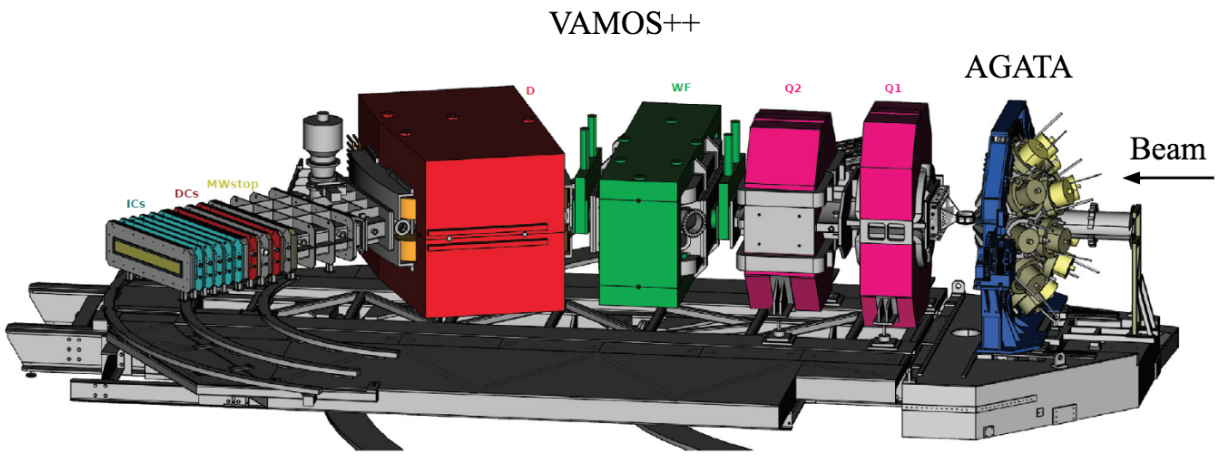

Figure 2.22: Schematic representation of the coupling of the HPGe array AGATA and the mass spectrometer VAMOS++, used for the fission campaign at GANIL. The VAMOS++ spectrometer is formed by two quadrupole magnets (Q_1,Q_2), a dipole magnet (D) and a detection system placed at the focal plane. The AGATA array can be seen in its 1π configuration. Image adapted from [102].

AGATA is the result of an international collaboration with the aim to construct the first γ-ray tracking array in Europe. The motivation behind such an array is to exploit the γ-ray tracking technique to maximise detection efficiency and energy resolution for in beam γ-ray spectroscopy. The AGATA array design was optimised to be used at the new generation of Radioactive Ion Beam (RIB) facilities such as SPES (Legnaro, Italy), FAIR (Darmstadt, Germany) and SPIRAL2 (Caen, France).

AGATA is formed by a set of triple clusters, housing three highly segmented HPGe detectors sharing the same cryostat. In its full configuration, AGATA is planned to have a 4π solid angle coverage. For the fission campaign at GANIL, in order to couple the array to VAMOS++, 24 detectors were used. Each HPGe detector is 36-fold segmented. The high segmentation enables an identification of the position of the γ-ray interactions, using pulse shape analysis techniques [127]. γ-ray tracking techniques [128] are then applied. The tracking allows a determination of the direction of the detected γ rays, which can be used in combination with the velocity obtained in VAMOS++ to guarantee the quality of the Doppler correction. An energy resolution of 5 keV FWHM at 1.2 MeV was achieved for recoiling fission fragments with $\beta \sim 0.11$c [52]. More technical details on the AGATA array and the coupling of AGATA to VAMOS++ can be found in [11, 129, 130].

For this experimental campaign, the AGATA 1π array was placed at the target position of VAMOS++ at backward angles with respect to the beam direction. The coupling of AGATA to a large acceptance magnetic spectrometer enabled a unique identification of each fission fragment. The spectrometer is formed of two large acceptance quadrupole magnets and a dipole magnet that guide the fission fragments. The identification is achieved through the determination of atomic number (Z), mass (A) and charge state (Q). For this purpose, a series of detectors were installed at the focal plain of the spectrometer: a multi wire parallel plane avalanche counter (MWPPAC), two drift chambers, segmented ionisation chambers and an array of Si detectors. The atomic number of the fission fragment Z is determined using the relationship between the energy loss ΔE and the total energy deposited in the ionisation chambers, as can be seen in Fig. 2.23. The mass selection is achieved using the correlation between the charge Q and the mass to charge ration M/Q. This results in a resolution of: $\Delta M/M \sim 0.6\%$ and $\Delta Z/Z \sim 1.5\%$. Further technical details regarding VAMOS++ and the particular settings for this experimental campaign can be found in [10] and [102] respectively.

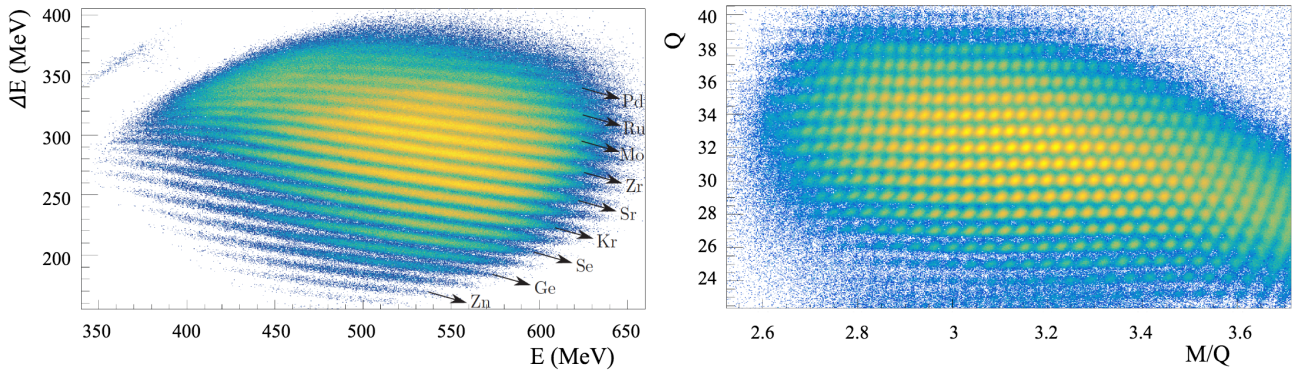

Figure 2.23: Relationship between energy loss ΔE and total energy E deposited in the ionisation chambers used for the determination of the atomic number of the fission fragment (left). Correlation between charge Q and M/Q ratio used for the determination of the mass of the fission fragments (right). Image adapted from [102].

For the construction of level schemes, it is essential to be able to assign intensities to the observed γ-ray transitions. The measured number of counts for each transition was corrected for the efficiency value at that particular energy using the relative efficiency curve. The efficiency curve was obtained using a ^{152}Eu source and GEANT4 simulations [131]. The same efficiency function is employed as

in the case of the FIPPS+IFIN-HH array (equation 2.8). The obtained parameters are reported in Table 2.6. For the analysis, an uncertainty of 5% is considered for the calculated efficiencies [132].

$A = 15.16$	$B = 2.99$	$C = -1.07$	$D = 11.45$
$E = -0.38$	$F = 0.020$	$G = 6.67$	$Norm = 1.47 \times 10^{-5}$

Table 2.6: Fit parameters for the efficiency function (eq. 2.8) of the AGATA array obtained from simulations. The error on the parameters is not included since it is purely statistical and does not take into account systematic uncertainties arising from differences between experimental and simulated efficiencies. For the analysis an uncertainty of 5% is considered for the calculated efficiencies [132].

Conclusion

In this chapter, the experimental characteristics of the setups used in this thesis work have been presented. A detailed account has been given of the first fission campaign carried out at the FIPPS instrument at the research reactor of the ILL, where an active fission target was used for the first time. The performance of the FIPPS+IFIN-HH HPGe array has been evaluated in terms of energy resolution and efficiency. Regarding energy resolution, a FWHM of ∼2.7 keV was obtained at 1.2 MeV using fission data, confirming a significant improvement with respect to the previous EXILL campaign. Concerning the absolute efficiency of the array, a value of 28.41 % at 121.7 keV was determined from measured γ-ray coincidences using a ^{152}Eu source. Future improvements of the experimental setup concern the electronic cards, in order to suppress the gain drift and implement a CFD to improve the time resolution. The key features of the AGATA-VAMOS++ setup were discussed. The main advantage of this setup with respect to FIPPS, is the identification in mass and proton number provided by the VAMOS++ spectrometer. However, a Doppler broadening is present since the fission fragments decay in flight, which results in a worse energy resolution of the AGATA array despite correction (FWHM 5 keV at 1.2 MeV). In addition, the higher statistics achieved during the FIPPS experiment allows the analysis of triple γ-ray coincidences. Furthermore, the FIPPS array can be used to perform angular correlation measurements and prompt-delayed coincidences which will be discussed in the next chapter.

CHAPTER 3

Experimental techniques

Contents

Since the introduction of germanium detectors in the 1960s, γ-ray spectroscopy has become a key method in experimental investigations of the nucleus. The continuous development of HPGe arrays and γ-ray spectroscopy techniques has led to discoveries of new phenomena and an increasing understanding of nuclear structure. γ rays emitted in the radioactive decay of a nucleus provide access to the main observables of nuclear excited states. On the one hand, the energy of excited states can be deduced from the energy and intensity of γ-ray transitions analysed with the γ-ray coincidence technique. On the other hand, transition probabilities can be calculated from measured lifetimes of the excited states. Furthermore, the angular distribution or angular correlation of a cascade of γ rays can be exploited to extract information on the spin and parity of excited states. These γ-ray spectroscopy techniques are well established. A detailed description can be found in the literature [1, 133, 134, 100].

The aim of this chapter is to describe the particular γ-ray spectroscopy techniques that can be exploited in the FIPPS+IFIN-HH array as well as the AGATA-VAMOS++ setup, presented in the previous chapter. This will serve as an introduction to the techniques used in the analysis of the bromine and krypton isotopic chains, which will be shown in Chapter 4 and Chapter 5. The γ-ray coincidence technique, and the procedure followed to identify new γ ray transitions and build new level schemes, will be presented in section 3.1. In order to demonstrate the effectiveness of this technique, as well as to evaluate the performance of the active fission target, a series of well known nuclei will be used as test cases. In section 3.3, the angular correlation capabilities of the FIPPS+IFIN-HH array will be discussed.

3.1 γ-ray coincidence techniques

In the past decades, the development of high resolution and high efficiency HPGe arrays opened the door to the study of complex γ-ray spectra, such as those resulting from fission experiments. As already presented in previous chapters, the neutron rich nuclei studied in this thesis work were produced in fission reactions, in which over 100 different nuclei are produced. The fission fragments, populated in excited states, deexcite via γ-ray cascades, giving rise to very complex γ-ray spectra. In the AGATA-VAMOS++ data, the γ-ray contribution of a particular nucleus is separated from the rest of the detected γ rays using the isotopic separation provided by the VAMOS++ spectrometer. In the FIPPS+IFIN-HH data, the identification of a particular fission fragment is achieved through multiple γ-ray coincidences. Two γ-ray transitions are considered in coincidence when they are detected in a time interval smaller than the detector time resolution. In this work the γ-coincidence technique is exploited both to identify the isotopes of interest and to place newly observed excited states in level schemes.

Due to the kinematics of the beam induced fission reaction used in the AGATA-VAMOS++ setup, only prompt γ rays are detected in the AGATA array. This characteristic along with further details of the analysis procedure used in the AGATA-VAMOS++ data-set will be discussed in section 3.2. The following sections will focus on the coincidence technique used for the analysis of the FIPPS+IFIN-HH

data-set.

Considering the time of γ-ray emission with respect to the fission reaction, combined with the resolution of the HPGe array (~ 80 ns FWHM [1]), *prompt* and *delayed* transitions are defined as:

- *Prompt γ-ray transitions:* are detected in coincidence with a fission event. A prompt time window of 300 ns was chosen.
- *Delayed γ-ray transitions:* are not measured in coincidence with the fission reaction, but in a time interval of the order of 300 ns to a few μs after a fission event. Delayed transitions allow the investigation of isomeric states. The particular delayed time window is chosen case by case, taking into account the lifetime of the isomeric state of interest.

Prompt and delayed γ-ray coincidence techniques can be applied to both the active fission target and the standard target data. However, for the study of short lived isomeric states (of the order of tens of ns) the active target setup presents a significant advantage, due to a more precise definition of the time of the fission event. In the standard target data-set, a fission event is defined imposing a minimum γ-ray multiplicity of 2. In this case the time of the fission reaction, or "time zero" is given by the timestamp of the first detected γ ray of the event.

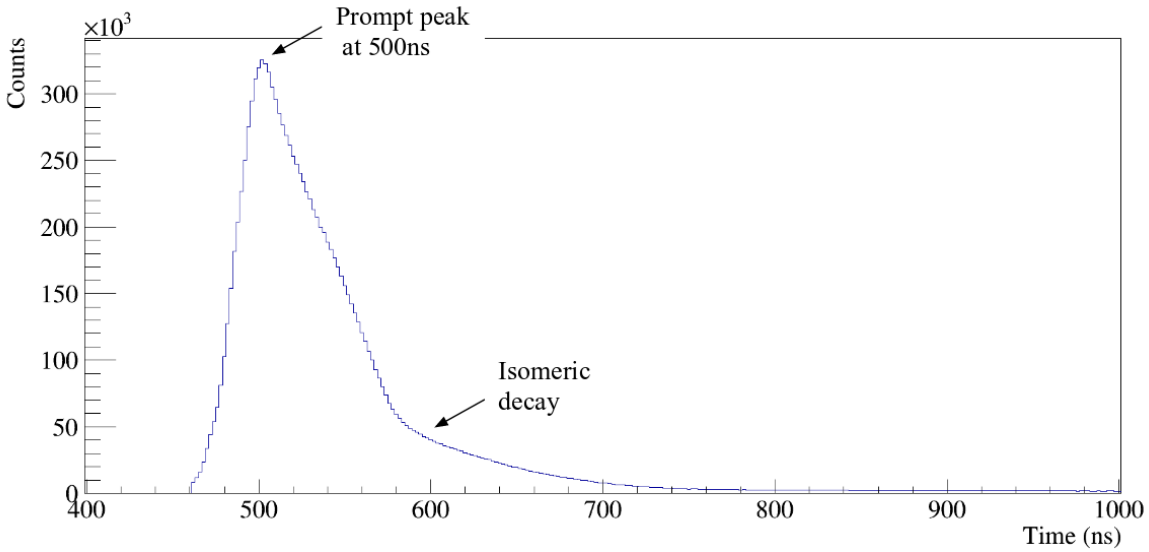

Figure 3.1: Time distribution of γ rays for the fission events recorded using the active fission target setup, for a FIPPS clover. The timestamp of the active target signal is used as reference. An arbitrary offset of 500 ns is applied.

In the case of the active fission target setup the timestamp of the scintillator signal is used as a reference. Fig. 3.1 shows an example of the time distribution of γ rays within a fission event, defined

[1] The typical time resolution of HPGe arrays results in ~ 30 ns FWHM. The FIPPS+IFIN-HH data suffer from the absence of a CFD at the front end electronics level, not foreseen with the commercial cards used (standard ILL).

using the event builder procedure which has been described in section 2.3.4. For each detected γ ray, a time t is assigned using the difference between the timestamp of the γ ray and the timestamp of the active target signal. In order to avoid negative time differences, an arbitrary offset is applied. The maximum of the time distribution defines the position of the prompt peak. Approximately 100 ns after the prompt peak a tail is observed corresponding to isomeric decays.

In order to extract the relevant spectroscopic information exploiting the γ-ray coincidence technique, the detected γ rays were sorted into 2-D and 3-D energy histograms. The multidimensional histograms, produced and analysed using the GASPWARE software package [135], will be referred to as coincidence matrices and cubes. The matrices and cubes were used to produce 1-D *gated spectra*, i.e. energy spectra observed in coincidence with a particular energy value (*gate*). The high energy resolution of the FIPPS+IFIN-HH array allows the application of narrow energy gates. Unless stated otherwise, a 3 keV gate width is used.

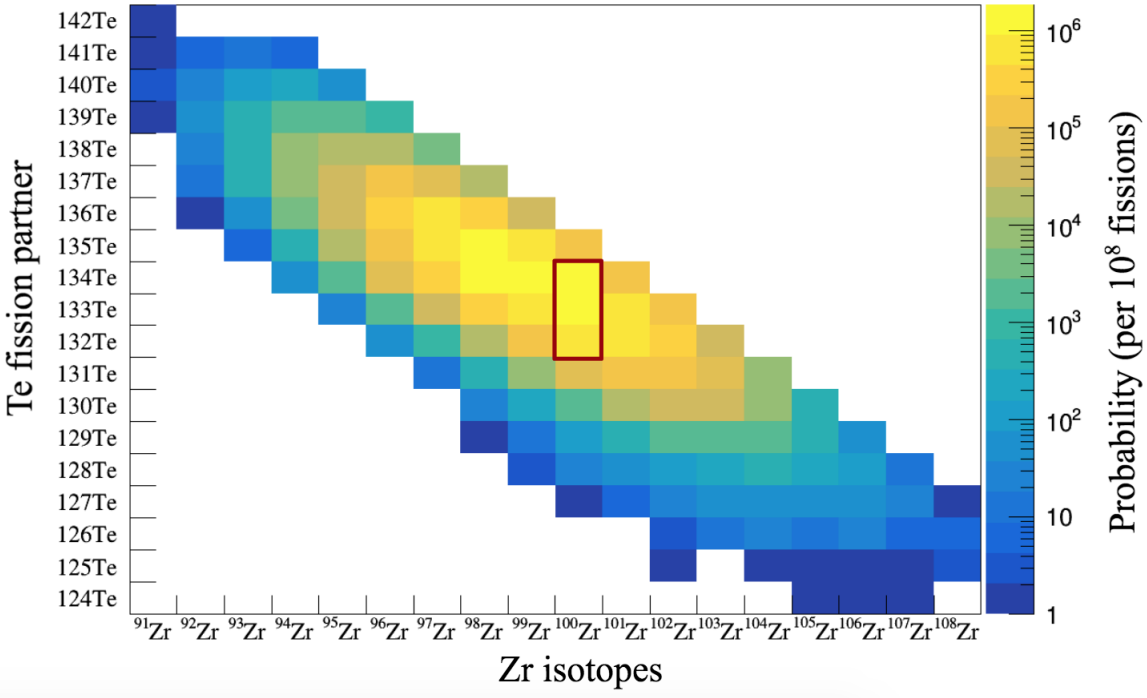

Figure 3.2: ^{235}U probability distribution for the Zr chain and corresponding Te complementary fragments. Values were obtained simulating 10^8 fission events with the GEF code [136]. The fission partners that were observed in coincidence in the FIPPS data-set with the ^{100}Zr nucleus, used as a test, are indicated with a red rectangle.

Using the coincidence technique, one can select a particular isotope by gating on known γ-ray transition energies. For the particular experimental setup used in this work, the high number of different isotopes produced in the fission reaction results in a high probability of detecting γ rays with the same energy ($\pm$1 keV) belonging to different nuclei. For this reason, in the analysis of fission spectra, the additional selectivity provided by a double gate on a triple coincidence cube is required. Consequently, it is necessary to know the energy of at least two transitions in the nucleus of interest

or its complementary fission partner (see section 3.1.1 for further details).

Both prompt and delayed γ-ray coincidences were used to identify new γ rays and build level schemes of excited states in the Kr and Br isotopic chains. A description of the adopted procedure will be detailed in the following sections using Te and Zr isotopes. These isotopes were chosen as a "test case" because of their high fission yields (see Fig. 3.2) and well studied nuclear structure.

3.1.1 Prompt γ-ray coincidences

The majority of the fission fragments in the region of interest are populated in excited states with typical lifetimes $<$ 1ns. Therefore, an analysis of prompt coincidences gives access to a thorough investigation of excited states in these nuclei. For this purpose, a prompt γ-γ coincidence matrix and a γ-γ-γ cube were constructed setting a 400 ns coincidence window using the active target data-set.

A total of 7.5×10^{10} γ coincidences were obtained, with γ-ray energies covering a range from 30 keV to 6 MeV. A total projection of the γ-γ matrix constructed using the active target data is shown in Fig. 3.3. A complex γ-ray spectrum is observed composed of γ-ray transitions of more than 100 fission products, as well as background transitions resulting from neutron capture reactions on ^{27}Al from the target cell. Coincidence spectra with single and double gates applied on the $2+ \rightarrow 0+$ (212.6 keV) and $4+ \rightarrow 2+$ (352.0 keV) transitions in ^{100}Zr are also shown in Fig. 3.3. As expected, using the γ-coincidence technique enhances γ-ray transitions belonging to the ^{100}Zr nucleus. When the uranium nucleus fissions and splits into two fragments, both fragments deexcite simultaneously. Therefore, one expects to see transitions from complementary fission fragments in prompt coincidence. Indeed, the coincidence spectra show the presence of γ-ray transitions belonging to the Te fission partners. As predicted by the GEF simulations (see Fig. 3.2), the most likely fission partner of ^{100}Zr is ^{134}Te. The $2+ \rightarrow 0+$(1279 keV) and $4+ \rightarrow 2+$(297 keV) in ^{134}Te are labelled in the coincidence spectra. A single gate on the 352 keV transition from ^{100}Zr already considerably enhances the physical coincidences. However, it is worth noting that in the single gated coincidence spectrum a high intensity transition at 204 keV is observed. This 204 keV transitions is identified as a $7/2+ \rightarrow 3/2+$ transitions in ^{95}Sr, which is present in the gated spectrum because of a 352 keV transition in ^{95}Sr. These "unwanted" transitions, not belonging to the nucleus of interest, introduced in the gated spectrum will be referred to as *contaminants*.

To further isolate transitions coming from ^{100}Zr and its fission partners, an additional gate is required. The selective power of the coincidence technique is demonstrated in the bottom spectrum. Nevertheless, the increase in selectivity comes at a cost of statistics. Taking as an example the strong 1279 keV transition that can be seen in the γ-γ projection, the number of counts in the total projection are $\sim 7.6 \times 10^7$, which decreases to $\sim 7.1 \times 10^5$ in the single gated spectrum and $\sim 7.2 \times 10^4$ in the doubly gated spectrum. Despite the loss in statistics, the additional selectivity provided by triple coincidences will prove essential in the identification of nuclei with low fission yields, as will be seen for the very neutron rich Kr and Br isotopes studied in this work.

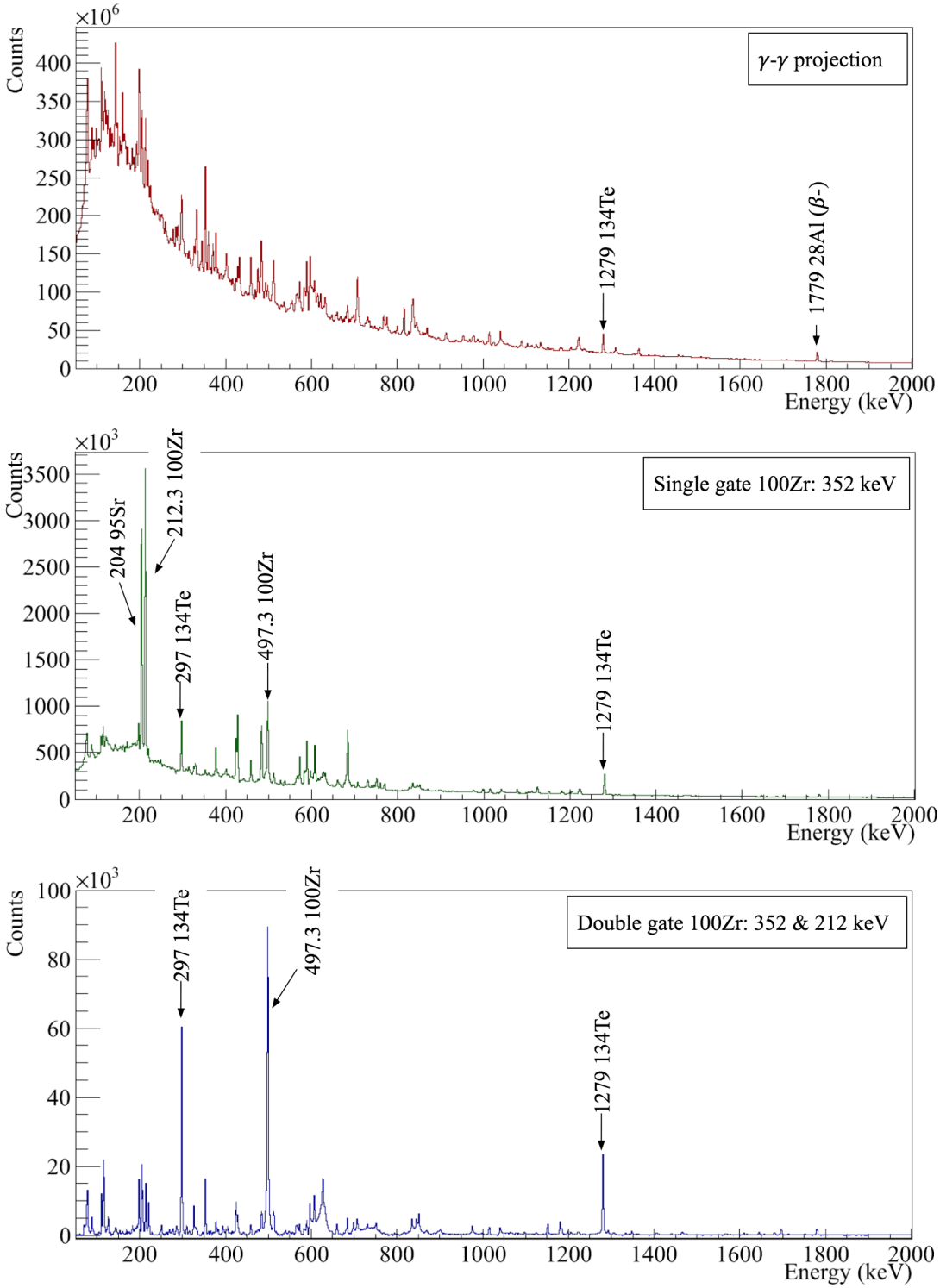

Figure 3.3: Prompt γ-ray spectra produced using the active target data-set. The total projection of a $\gamma - \gamma$ matrix is shown (top), along with single and double gated spectra applied on ^{100}Zr transitions. The main γ rays from ^{100}Zr and ^{134}Te (2n fission partner) are highlighted. An increase of selectivity along with a loss of statistics is observed when each gate is applied.

The active target provides an additional selectivity by considering only γ-ray transitions resulting from the fission reaction. In order to evaluate the performance of the active target setup, a multiple γ-ray coincidence analysis using the standard target data-set was performed. A factor of 3 more statistics was obtained ($\sim 2.1 \times 10^{11}$ γ-γ coincidences). The reduced statistics in the active target data-set is explained by a lower accessible fission rate due to count rate limitation in the PMTs (see section 2.3.3). Despite the lower statistics the active target data are characterised by better peak to background ratio that can help to distinguish γ rays coming from beta decay from those coming directly from fission. The use of the active target or standard target data was evaluated case by case.

The strength of the active target setup, compared to a standard fission target, is illustrated using γ-γ-γ coincidence spectra gated on transitions from ^{132}Te (see Fig. 3.4). γ-ray transitions from ^{132}Te as well as from the 2n (^{102}Zr), 3n (^{101}Zr) and 4n (^{100}Zr) complementary fission fragments are clearly identified in both spectra. A strong suppression of transitions coming form beta decay of ^{132}Sb is observed in the active target spectrum. The suppression is of particular importance at low energies, where two peaks coming from the Zr fission partners would otherwise not be resolved.

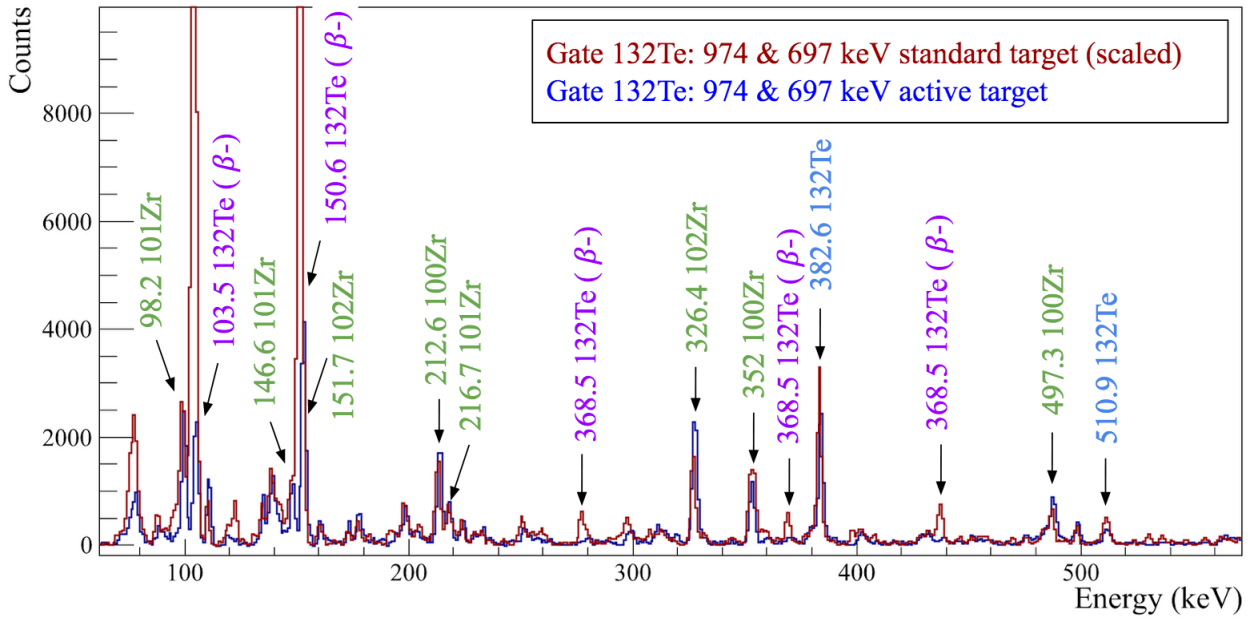

Figure 3.4: Comparison of prompt triple coincidence spectra obtained with the standard target and active target setup. The spectra are produced using a double gate on the 2+→0+ and 4+→2+ transitions in ^{132}Te. γ-ray transitions from ^{132}Te are labelled in blue. Transitions from the Zr complementary fission partners are marked in green. ^{132}Te transitions observed mainly in the beta decay of ^{132}Sb are highlighted in purple.

As previously mentioned (see section 2.3.3), the standard target data-set was produced using the same uranium target as in the EXILL campaign. Therefore, the γ-ray coincidence analysis of the standard solid target data not only allowed an evaluation of the performance of the active fission target, but also a comparison of the performance of the FIPPS+IFIN-HH array with respect to the EXILL setup. Such a comparison can be seen in Fig. 3.5, which shows coincidence spectra doubly gated on the 2+ → 0+ and 4+ → 2+ transitions in ^{134}Te. An increase in the statistics ($\sim \times 3.5$)

is observed, explained by higher efficiency of the FIPPS+IFIN-HH array and a better suppression of neutron induced γ-ray background. The improvement of the energy resolution is evident from the 2865 keV $8+ \rightarrow 6+$ transition in ^{134}Te, with a FWHM value of 5.35(8) keV in the EXILL data-set vs 3.86(2) keV in the FIPPS data-set. This improvement in energy resolution is essential for the coincidence analysis of complex γ-ray spectra produced in fission reactions.

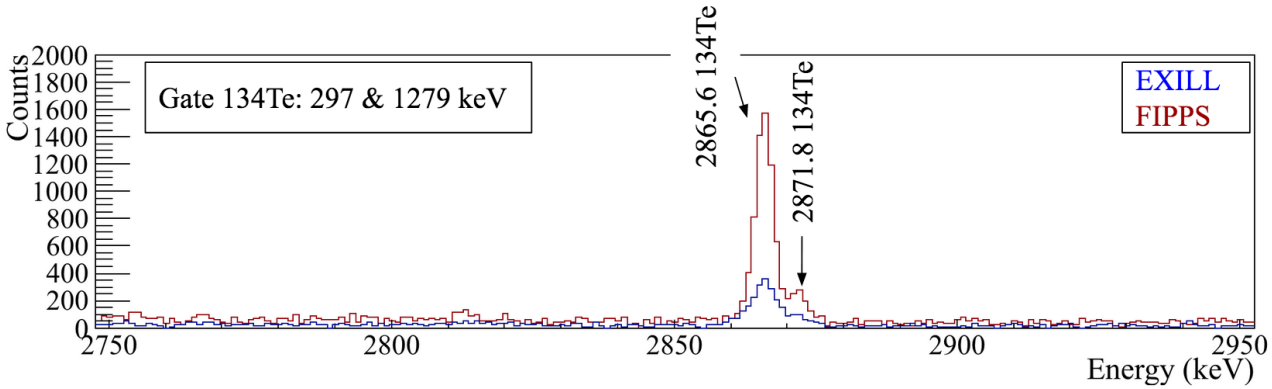

Figure 3.5: Coincidence spectra doubly gated on the $2+ \rightarrow 0+$(1279 keV) and $4+ \rightarrow 2+$ (297 keV) transitions in ^{134}Te. The spectrum in red is obtained using the standard solid target and the FIPPS+IFIN-HH array, while the spectrum in blue was obtained from the EXILL campaign using the same target. An increase in statistics, as well as an improvement of energy resolution can be seen.

The assignment of a new transition to a given nucleus is achieved by the comparison of coincidence spectra gated on known transitions of the nucleus of interest and its complementary fission partners. The typical procedure followed will be illustrated using transitions in ^{100}Zr and its most probable (see Fig. 3.2) complementary fission partners ^{134}Te (2n), ^{133}Te(3n) and ^{132}Te (4n). A coincidence spectrum doubly gated on the $2+ \rightarrow 0+$ (212 keV) and $4+ \rightarrow 2+$ (352 keV) transitions is shown in Fig. 3.6 a). Transitions belonging to the ^{100}Zr nucleus as well as the most intense transitions of the complementary fission fragments can be observed. When a double gate is applied with one transition in ^{100}Zr and another in ^{134}Te, as expected, transitions from the other complementary fission fragments are not present. In addition, it can be seen that the relative intensities of transitions in ^{100}Zr (such as the 497 keV) with respect to ^{134}Te (such as the 1279 keV) decrease.

If there is no available spectroscopic information on a given nucleus, but the complementary fission fragments are well known, it is still possible to obtain the strongest transitions in the nucleus of interest. These transitions are identified using different coincidence conditions on all of the complementary fission partners. This method will be referred to as the *cross coincidence technique* in Chapter 4 and Chapter 5.

When investigating low intensity γ-ray transitions, as is the case of nuclei populated with low fission yields or weak transitions in high yield nuclei, contaminants in the coincidence spectra can be dominant. An example of the appearance of contaminant peaks can be seen in the bottom spectrum of Fig. 3.6. The gate on the 706 keV transition in ^{134}Te introduces contaminant transitions from ^{90}Kr (yield 4.5×10^{-2}) and ^{91}Kr (yield 3.3×10^{-2}) due to a strong 707 keV transition in both nuclei. The contaminant peaks corresponding to ^{90}Kr, ^{91}Kr and their respective barium complementary fission

fragments are highlighted in yellow.

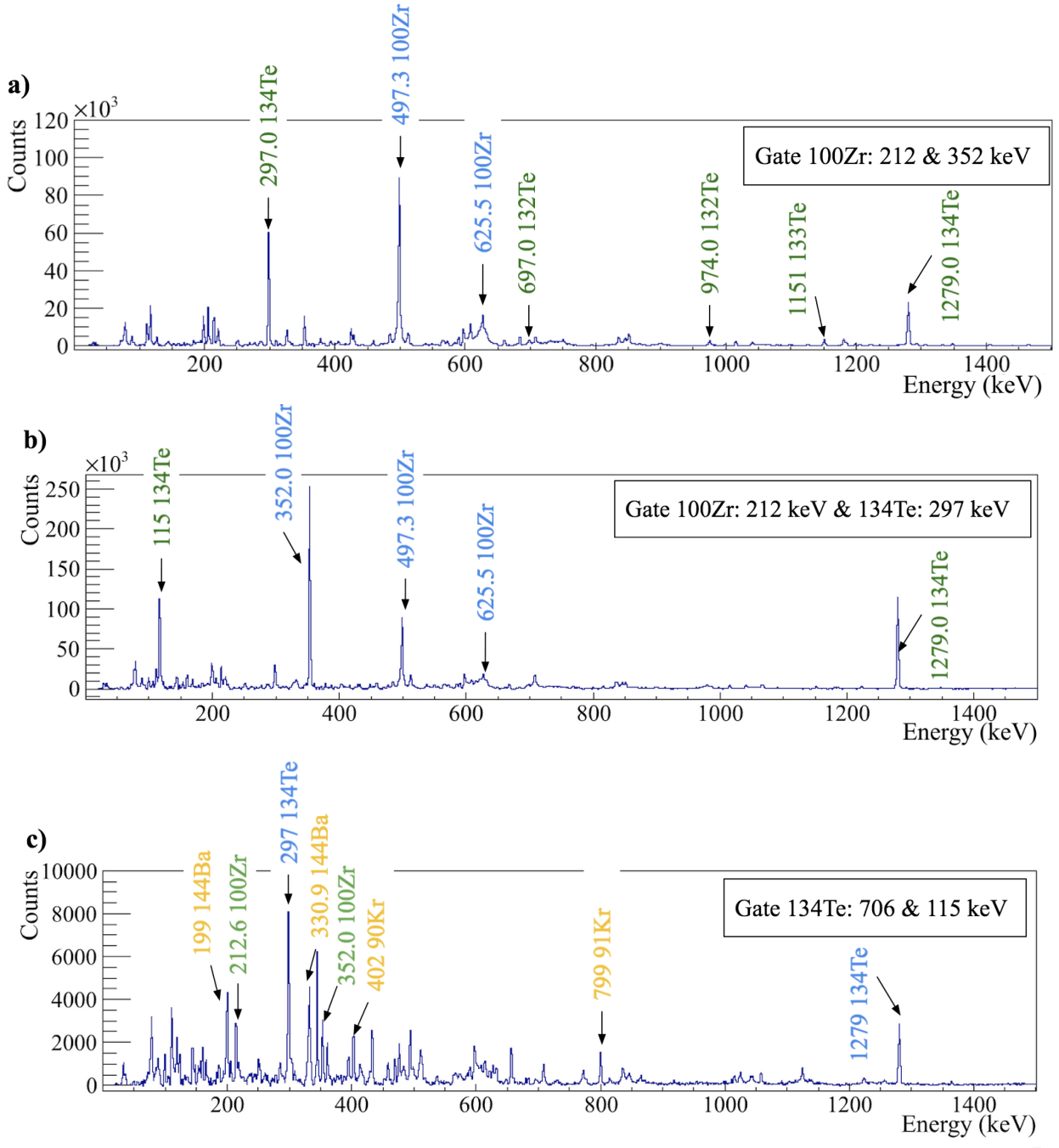

Figure 3.6: a) b) Coincidence spectra obtained using the active target prompt cube, doubly gated on the strongest transitions observed in ^{100}Zr (top) and a transition from ^{100}Zr and its 2n complementary fission partner ^{134}Te (bottom). As expected, transitions from ^{132}Te and ^{133}Te, seen in coincidence with ^{100}Zr, are not present in the ^{100}Zr-^{134}Te spectrum. c) Coincidence spectrum obtained using the active target prompt cube, doubly gated on two weak transitions from ^{134}Te. Contaminant transitions caused by a strong 707 keV transition in ^{90}Kr and ^{91}Kr are indicated in yellow.

To conclude, this section has demonstrated how multiple γ-ray coincidences can be exploited to select a particular isotope of interest and identify new transitions. The main limitation to the coincidence technique is that it requires previous knowledge of at least two transitions (assuming the use of triple coincidences) in the nucleus of interest or well known complementary fission partners. When investigating nuclei with relative low fission yields, as is the case of the neutron rich Br and Kr isotopes studied in this work, a systematic analysis of contaminants is necessary in order to assure correct assignment. The presented test cases have served to establish the improvements of the FIPPS+IFIN-HH fission campaign with respect to the EXILL campaign in terms of improved energy resolution and selectivity provided by the active target setup.

3.1.2 Prompt-delayed coincidences

Delayed coincidences give the opportunity to study the structure of nuclei characterised by isomeric states with lifetimes in the range of tens of ns to a few μs. The FIPPS+IFIN-HH array is particularly suited for the study of isomers in the 100 ns range. The characteristics of the FIPPS setup give the possibility to observe both prompt and delayed transitions. As will be discussed in section 3.2, only prompt transitions can be measured in the AGATA-VAMOS++ experiments. On the other hand, the LOHENGRIN instrument at the ILL gives access to delayed transitions for microsecond isomers, but short lived isomers and prompt γ-ray transitions cannot be studied. For the isotopes studied in this work, the prompt-delayed coincidence technique was used to study the structure of excited states situated both above and below isomeric states. In addition, the number of prompt-delayed coincidences observed using different time intervals can be used to estimate the lifetime of isomeric states [137].

In order to demonstrate the effectiveness of using prompt-delayed coincidences, the ^{134}Te isotope is chosen as a "test case". A partial level scheme of ^{134}Te, characterised by an isomeric state of 164 ns, is shown in Fig. 3.7. Taking into account this lifetime, a prompt window was defined from 0 to 150 ns while delayed transitions were considered in the 150-500 ns time interval. Delayed-delayed (DD) coincidence matrices as well as prompt-delayed-delayed (PDD) and delayed-delayed-delayed (DDD) coincidence cubes were constructed.

Prompt-delayed coincidence analysis was already performed during the EXILL fission campaign. However a significant improvement is achieved during the FIPPS campaign due to the use of the active fission target. In the prompt-delayed analysis of the EXILL data, a fission event is defined imposing a minimum of 3 γ rays detected in a 200 ns window with at least one delayed coincidence, which results in a reduction of statistics. In the case of the FIPPS data-set, no multiplicity conditions are required thanks to the precise time information provided by the active fission target. A comparison of the number of prompt-delayed coincidences observed in ^{134}Te using the active target setup vs the standard target are reported in Table 3.1. A significant gain in statistics ($\times 10, 15$) is obtained.

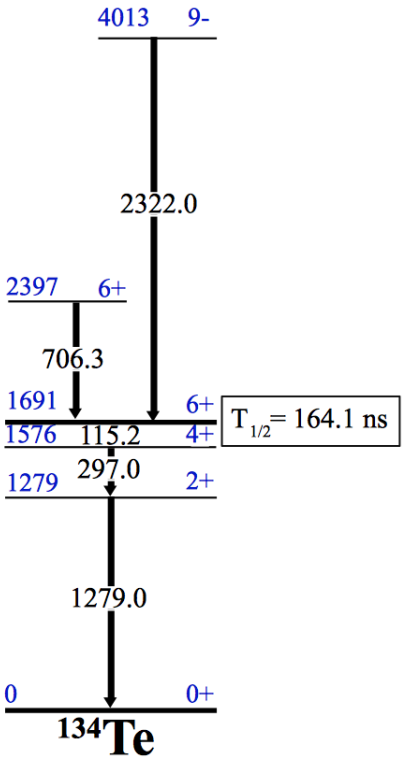

Figure 3.7: Partial level scheme of ^{134}Te, showing the short lived isomer ($T_{1/2} = 164$ ns) used as a test case of prompt-delayed coincidences.

Transition Energy (keV)	Active target	Standard solid target	Ratio (%)
2322 (^{134}Te)	6702(82)	1054(35)	15.7(6)
212.6 (^{100}Zr)	69229(263)	7361(92)	10.6(1)

Table 3.1: Number of prompt γ rays observed in coincidence with the 1279 keV delayed transition in ^{134}Te. A comparison between the number of coincidences observed using the active target setup or the standard solid target setup show the strength of using the fission trigger for prompt-delayed coincidence analysis. Adapted from [114].

The strength of the prompt-delayed coincidence technique using the active fission target is illustrated in Fig. 3.8. The additional selectivity provided by the time condition is reflected in the "clean" spectra obtained. In the delayed spectra, only transitions below the isomeric state are observed. Using the PDD cube, a drastic improvement is observed in the spectrum gated on the 706 keV and 115 keV transitions with respect to the coincidence spectrum obtained with the PPP cube (see Fig. 3.6). The prompt spectrum obtained by gating on two delayed transitions show both prompt ^{134}Te γ rays and transitions belonging to the Zr complementary fission partners.

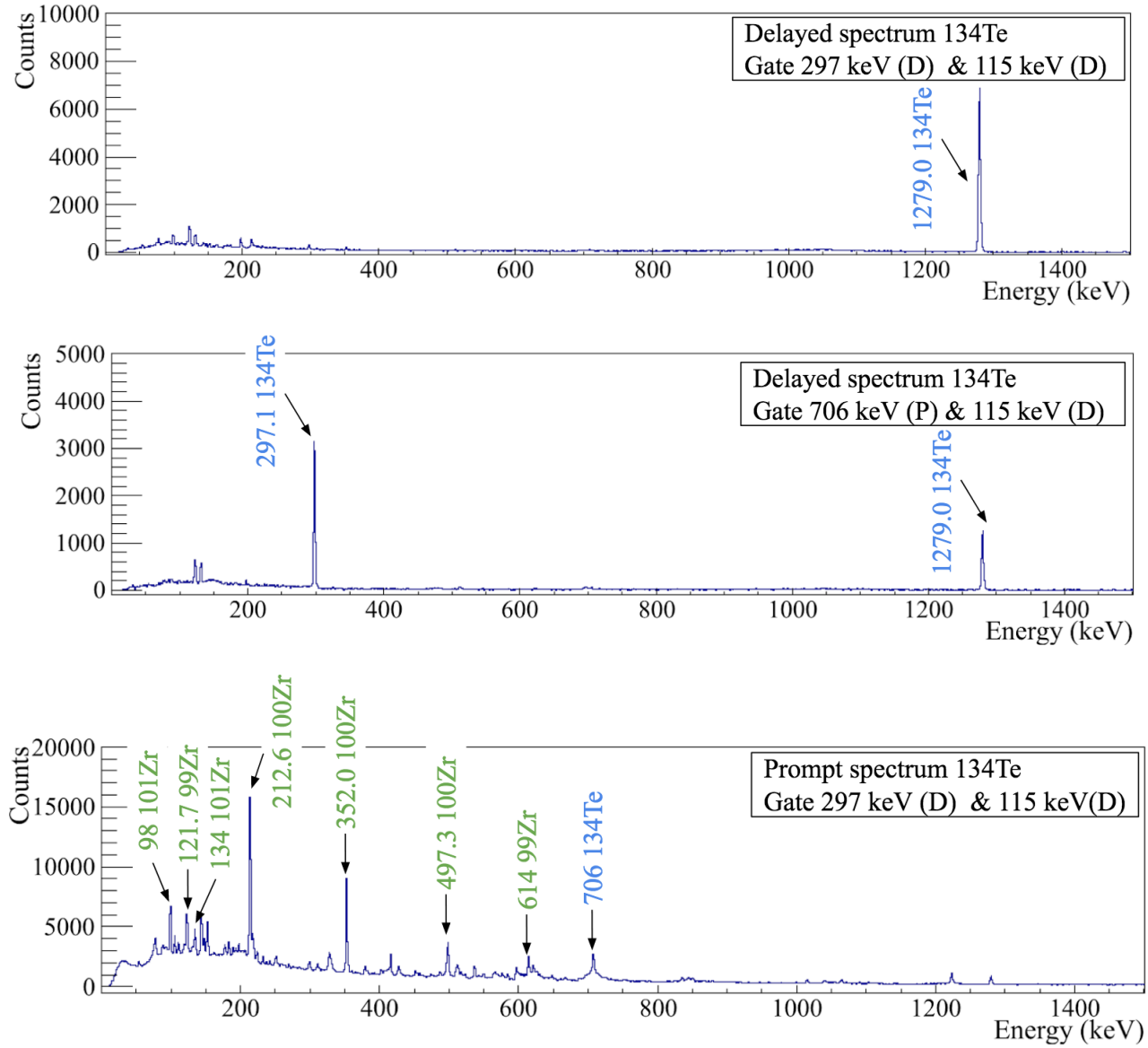

Figure 3.8: Prompt-delayed coincidences with ^{134}Te transitions, obtained using a DDD and PDD cubes considering a delayed interval of 150 ns - 500 ns. In the top two spectra only transitions under the 164 ns isomer are present. In the prompt spectrum shown at the bottom, prompt transitions from ^{134}Te and its corresponding fission partners can be seen.

3.2 γ-ray spectroscopy of isotopically identified fission fragments

In this section the procedure employed to perform γ-ray spectroscopy investigations of Kr and Br isotopes using the AGATA-VAMOS++ data-set will be presented. The ^{91}Br isotope will be used to illustrate the advantages and limitations of this setup. Excited states in the isotopes of interest were populated using fission of a ^{238}U beam on a Be target. Prompt γ-ray transitions from the fission fragments were measured using the AGATA advanced γ-ray tracking array. AGATA was coupled to the VAMOS++ spectrometer, which allowed an isotopic identification through the measurement of the mass number (M), atomic number (Z) and charge state (Q) of the fission fragments.

Once the calibration and Doppler corrections discussed in Chapter 2 were implemented, the following procedure was applied in order to extract the relevant γ-ray spectroscopy information:

- Production of prompt γ-ray spectra measured in coincidence with the isotope of interest detected in VAMOS++.
- Comparison of γ-ray spectra produced with different Z, M and Q gate conditions in order to identify potential contaminants.
- Construction of γ-γ coincidence matrices in order to place γ-ray transitions in a level scheme of excited states.

A typical prompt Doppler corrected γ-ray spectrum, obtained with AGATA and measured in coincidence with the ^{91}Br fission fragment, is shown in Fig. 3.9. Despite the high quality isotopic identification provided by the VAMOS++ spectrometer, for isotopes with low production yields with respect to neighbouring nuclei, contaminant transitions may be present in the γ-ray spectra. The atomic number selection performed using the ΔE vs E plot shown in Fig. 2.23, results in potential $Z \pm 1$ contamination. The mass selection is performed using the Q vs Q/M plot shown in Fig. 2.23, which may introduce contamination from nuclei with atomic masses $M \pm 1, \pm 2, \pm 3, \pm 4$.

In order to distinguish γ-ray transitions belonging to the nucleus of interest from those introduced by contaminants, a comparison of spectra produced with different gate conditions in the Z, Q and M selection is used. An example of such a comparison can be seen in Fig. 3.9. The gate condition on the experimental observed atomic number, Z_{exp}, defines the selection criteria. In this way, a $Z_{exp} = 0.5$ for the case of ^{91}Br ($Z = 35$) imposes a condition of $Z = 35 \pm 0.5$. In the comparison of a spectrum produced with this condition and another produced with more restrictive Z_{exp}, the contaminant peaks are suppressed while the peak to background ratio of transitions belonging to the isotope of interest improves. As expected from the atomic number distribution shown in Fig. 3.9, the main contaminant peaks observed in the ^{91}Br γ-ray spectrum belong to transitions in the ^{91}Kr isotope.

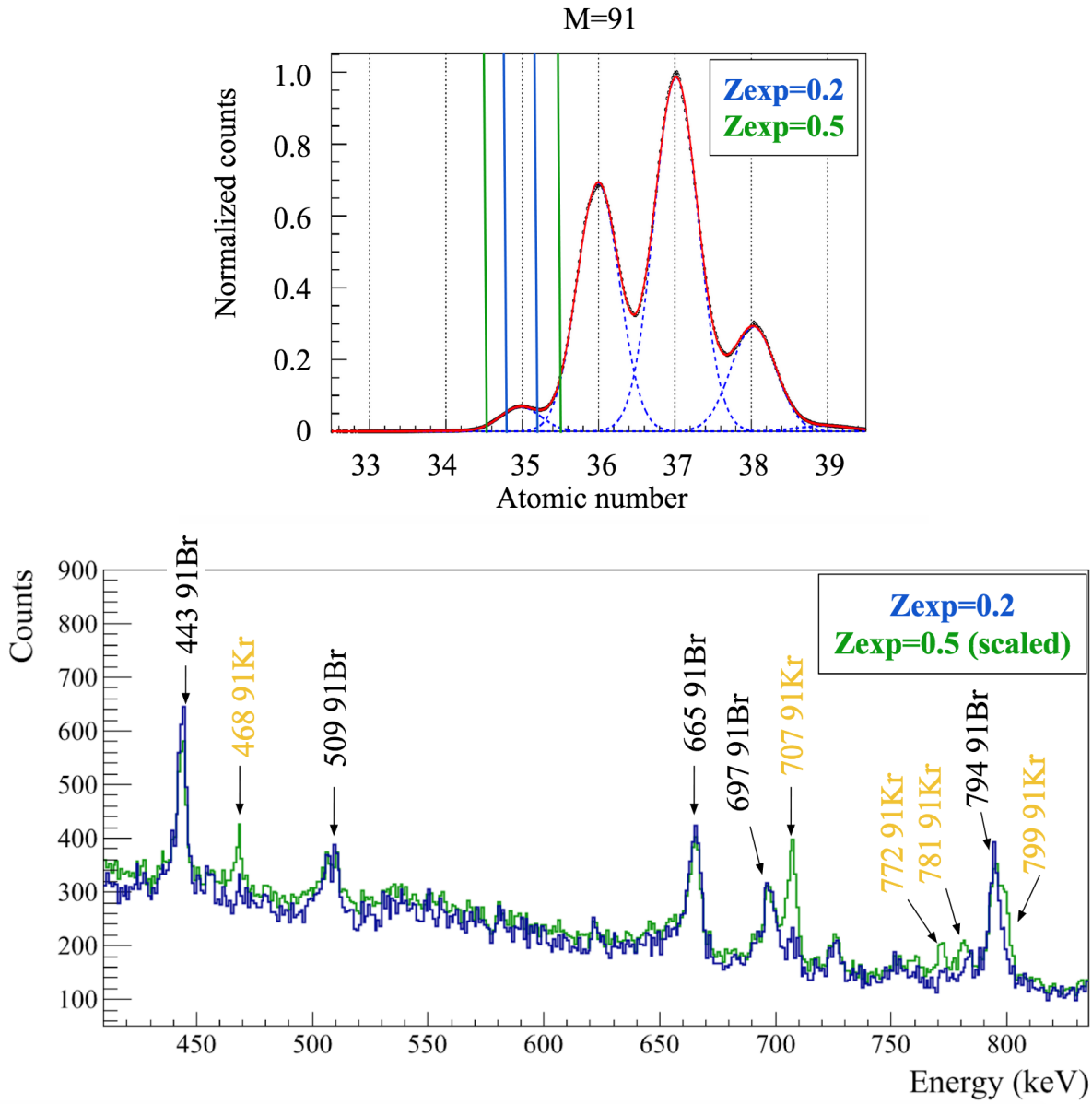

Figure 3.9: TOP: Normalised atomic number (Z) distribution observed after fission fragment identification in VAMOS++ for mass number $M = 91$. BOTTOM: Doppler corrected γ-ray spectra measured in AGATA in coincidence with the ^{91}Br fission fragment. The spectra are produced with different quality factors on the Z selection. To facilitate the comparison the spectra generated with a quality factor of $Z_{exp} = 0.5$ (green) has been scaled to match the statistics in the spectra produced with a quality factor of $Z_{exp} = 0.2$ (blue). A comparison of both spectra allows an identification of contaminant transitions introduced by neighbouring nuclei with higher production yields. In the case of ^{91}Br($Z = 35$), contaminant γ-ray transitions belonging to ^{91}Kr ($Z = 36$) are identified and labelled in yellow.

Once all γ-ray peaks have been identified, newly observed transitions are placed in the level scheme of the nucleus of interest using the γ-coincidence technique. γ-γ coincidence matrices are constructed using a 200 ns coincidence window. For some cases, due to statistical limitations on the fission yields of some of the studied isotopes, γ-γ coincidences could not be used. This will be discussed for each krypton and bromine isotope case by case in Chapters 4 and 5.

The γ-ray spectroscopy information gathered and placed in a nuclear level scheme allows a determination of the energies of excited nuclear states. Additional information can be extracted from the AGATA-VAMOS++ data-set, which allows the determination of an upper limit to the lifetime of the observed excited states. The inverse kinematics of the fission reaction employed, produced forward focused fission fragments with typical v/c values in the range of 0.095 to 0.135 [52]. Since the fission fragments deexcite in flight, γ-ray emission after isomeric decay will occur further from the target position, resulting in low detection efficiency for the AGATA array. Consequently, an upper limit of $\sim$5 ns can be established for the lifetime of the excited states depopulated by the observed transitions.

3.3 γ-ray angular correlation analysis

In order to have a good description of an excited nuclear state, it is necessary to know not only its energy but also its spin and parity. The experimental determination of the spin of a level is essential for the comparison with theoretical models and the determination of the microscopic origin of a given excitation. There are different experimental methods to obtain the spin of a nuclear state. In particular in γ-ray spectroscopy, the angular correlation between γ rays emitted in a cascade have been exploited since the 1950s. Angular correlation measurements enable the determination of multipolarity and mixing ratios of the γ-ray transitions involved in the cascade, thus providing information on nuclear spins of the excited states.

A brief introduction to the angular correlation between γ-rays will be given in section 3.3.1. Further details of this well established technique can be found in [138, 139, 140]. The procedure followed to obtain nuclear structure information from angular correlation measurements using the FIPPS data-set will be given in section 3.3.2. The challenges of performing angular correlation measurements in fission experiments with a composite array will be discussed. For the case of the AGATA-VAMOS++ setup, the detection of the fission fragment establishes a direction, therefore angular distribution measurements are possible. However, for the fission campaign presented in this work, the collected statistics were not enough for such an analysis.

3.3.1 The angular correlation function

When a nucleus de-excites via emission of a cascade of γ rays, a correlation exists between the relative angle of emission, θ, of the γ rays of the cascade. The case of two γ rays, γ_1 and γ_2, connecting three levels of spin J_1, J_2 and J_3, and emitted with a relative angle θ is illustrated in Fig. 3.10. The

probability of emission of two γ rays at a particular relative angle is given by the angular correlation function $W(\theta)$:

$$W(\theta) = \sum_k A_k P_k(\cos(\theta)), \tag{3.1}$$

where A_k are the angular correlation coefficients and P_k are the Legendre polynomials [140]. The index k is an even integer that can take values from zero up to the smallest value between $2J_2$, $2L_1$ or $2L_2$ where L_1 and L_2 are the maximum multipolarities of γ_1 and γ_2 respectively. The angular correlation coefficients A_k depend on the spin of the levels involved and multipolarity of the γ radiation of the cascade. In the case of non-stretched transitions the mixing ratio δ of the cascade, defined as the ratio of intensities I_L and I'_L of the L-pole and L'-pole radiation, needs to be taken into account.

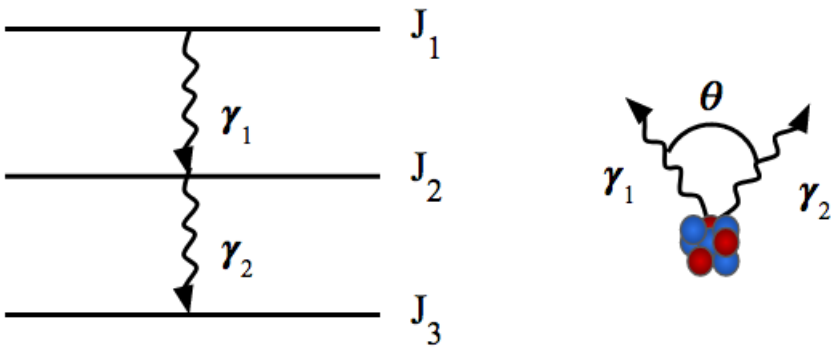

Figure 3.10: Schematic diagram of two γ rays in a cascade, emitted with relative angle θ.

If the maximum multipolarity value considered is equal to 2, as will be the case for most transitions studied in this work, equation 3.1 can be written as:

$$W(\theta) = A_0[1 + a_2 P_2(\cos(\theta)) + a_4 P_4(\cos(\theta))], \tag{3.2}$$

where A_0 takes into account the intensity of the cascade and $a_k = A_k/A_0$. The corresponding Legendre polynomials are:

$$P_2(\cos(\theta)) = \frac{1}{2}(3\cos^2(\theta) - 1), \quad P_4(\cos(\theta)) = \frac{1}{8}(35\cos^4(\theta) - 30\cos^2(\theta) + 3). \tag{3.3}$$

The theoretical angular correlation function, plotted for cascades involving different values of spin of the excited states, is shown in Fig. 3.11. The a_2 and a_4 coefficients are reported in Table 3.2.

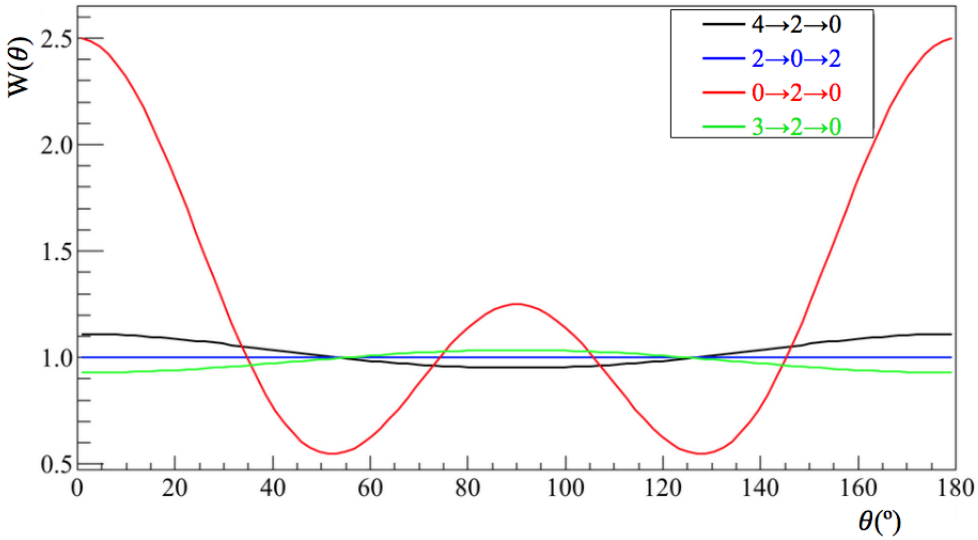

Figure 3.11: Theoretical angular correlation function for cascades involving different spin values.

Cascade	a_2	a_4
$4 \rightarrow 2 \rightarrow 0$	0.10204	0.00907
$2 \rightarrow 0 \rightarrow 2$	0	0
$0 \rightarrow 2 \rightarrow 0$	0.35714	1.14286
$3 \rightarrow 2 \rightarrow 0$	-0.07143	0

Table 3.2: Theoretical a_2 and a_4 values for different cascades. Values taken from [141].

3.3.2 Angular correlation capabilities of the FIPPS+IFIN-HH array

The geometry and granularity of the FIPPS array is ideal for angular correlation measurements. The different pair combinations between the individual FIPPS crystals give access to 24 different angles, reported in Table 3.3. Angular correlations measurements have been carried out using the FIPPS instrument in the analysis of neutron capture reactions [142, 143]. In the case of the fission experiment performed with the FIPPS+IFIN-HH array, the analysis of angular correlations is more complex. On the one hand, the large number of different detected γ rays and the low statistics of the isotopes of interest make the coincidence analysis and background substraction more challenging. On the other hand, the difference in geometry and efficiency between the FIPPS and IFIN-HH detectors requires different corrections. It is worth noting that the angular correlation measurements performed during the EXILL campaign, also produced with a composite array, took into account only one kind of detector [90, 144]. The FIPPS collaboration developed a dedicated code and established a procedure for the analysis of the FIPPS+IFIN-HH data, with the aim of optimising the performance in terms of angular correlation measurements. An outline of the procedure will be given below, further details will be published in [145].

FIPPS crystals			
Angle (º)	**Nº pairs**	**Angle (º)**	**Nº pairs**
0	16	92	32
19	32	107	16
25	16	111	16
28	16	113	16
32	16	116	16
44	32	131	32
49	32	136	32
64	16	148	16
67	16	152	16
69	16	155	16
73	16	161	32
88	32	180	16

Table 3.3: Relative angles and number of combinations (pairs) between FIPPS crystals.

For the analysis of angular correlations, a series of γ-γ coincidence matrices are sorted according to the relative angle between the pair of detectors that fired. In order to extract the relevant structure information from the observed distribution of coincidences, experimental effects need to be taken into account. First of all, the number of coincidences measured at a particular angle depends on the number of detector combinations contributing to that angle, which varies from angle to angle (see Table 3.3). Secondly, the number of observed coincidences depends on the efficiency of each detector. Consequently, a correction or *normalisation* angle by angle needs to be applied. Furthermore, the measured distribution is attenuated due to the finite size of the detectors.

Regarding the normalisation procedure, the standard approach is to obtain normalisation coefficients using the measured coincidences between two γ rays emitted isotropically [143]. For example, the emission of γ rays in a $2 \rightarrow 0 \rightarrow 2$ cascade is isotropic (see Fig.3.11). Another option for fission experiments, is to exploit γ-ray transitions belonging to complementary fission fragments. During the EXILL campaign both $2 \rightarrow 0 \rightarrow 2$ cascades from calibration data and γ rays emitted by two fission fragments were employed [144]. The main limitation of this method is that it does not take into account the efficiency variation as a function of energy, which translates to an energy dependence of the normalisation coefficients. A recent study by the GRIFFIN collaboration tackled this problem by introducing a new normalisation technique based on a mixing of events [146]. The basic idea behind this method is to construct normalisation matrices for each angle by mixing γ rays of different events, therefore corresponding to the decay of different nuclei and thus emitted isotropically. In this way, one can correct the coincidences measured between two γ rays of energy E_1 and E_2 for a given relative angle by the number of coincidences that would be detected for those same energies if the emission was isotropic. With this method a normalisation is applied angle by angle for each particular γ-γ coincidence of interest. This event mixing technique was adopted for the angular correlation analysis

of the FIPPS+IFIN-HH data-set. Fig. 3.12 shows a comparison of the normalisation coefficients, $n(\theta)$, obtained for the FIPPS crystals using both the "standard" normalisation technique and the event mixing technique. The standard normalisation coefficients (indicated in blue) were calculated by averaging the $n(\theta)$ values obtained for three different fission partner couples: ^{100}Zr-^{134}Te (352-1279 keV), ^{94}Sr-^{40}Xe (1309-458 keV) and ^{92}Kr-^{142}Ba (769-360 keV). Two examples of the event mixing normalisation, corresponding to transitions from ^{100}Zr-^{134}Te (352-1279 keV) and ^{102}Zr-^{132}Te (151-102 keV), are included in the plot. The resulting $n(\theta)$ values are compatible using both methods for angles larger than 60°. However, larger differences are observed at lower angles, where efficiency differences and Compton background corrections are more critical. This supports the need of a normalisation procedure that takes into account the γ-ray energies of the transitions in the cascade.

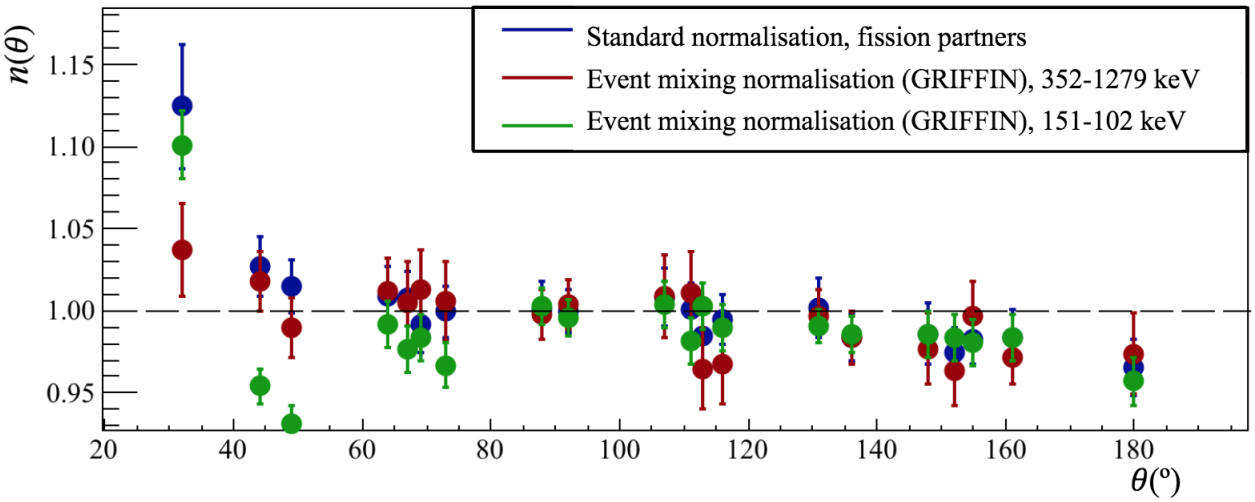

Figure 3.12: Normalisation coefficients for the FIPPS detectors, obtained using $\theta = 88°$ as a reference. The data points in blue were obtained using a series of γ-ray transitions from complementary fission partners. The data points in red and green were obtained applying the event mixing technique. See text for further details.

In order to correct for the finite size of the detectors, attenuation coefficients or *q-values* are introduced in eq. 3.1. Consequently, the experimental angular correlation function, $W(\theta)_{exp}$, will take the form of:

$$W(\theta)_{exp} = A_0[1 + q_2 a_2 P_2(cos(\theta)) + q_4 a_4 P_4(cos(\theta))], \tag{3.4}$$

where the attenuation coefficients q_2 and q_4 depend on the detector size, target size and target-to-detector distance. Both experimental measurements and Monte Carlo simulations showed that to combine the information from the different detector types, q-values need to be calculated independently for the FIPPS-FIPPS, FIPPS-IFIN and IFIN-IFIN combinations due to large differences in geometry and efficiency. The q values were evaluated using a ^{152}Eu source, as well as cascades in ^{136}Ba and ^{116}Sn populated using neutron capture reactions. The experimental values were used to validate GEANT4 simulations, which were then adapted to different detector configurations. Further details can be found in [145]. With the purpose of maximising the statistics at each point of the angular correlation distribution (essential for low fission yield nuclei), instead of using the individual crystals the clovers are considered as a single detector. The angles and different combinations accessible through the

FIPPS and IFIN-HH clovers are shown in Fig. 3.13, while the evaluated q-values are reported in Table 3.4.

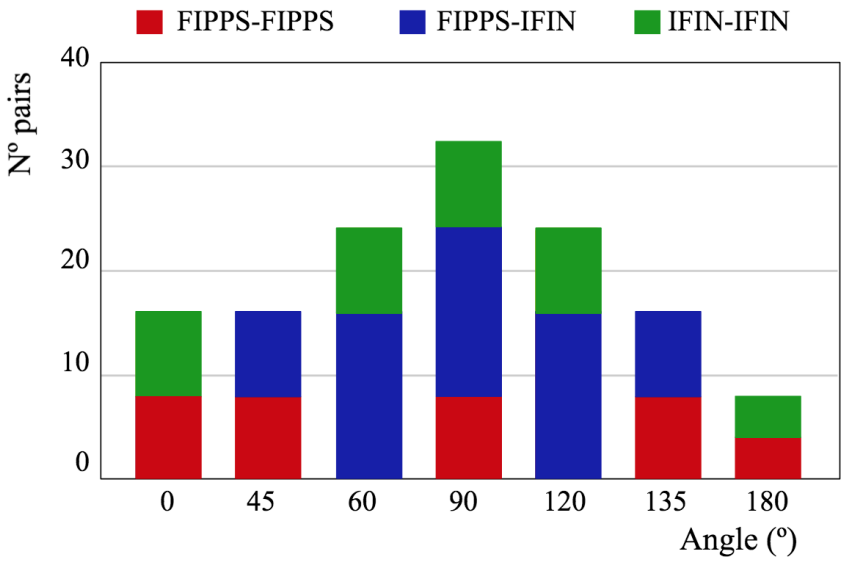

Figure 3.13: Number of available combinations as a function of the angle for the FIPPS+IFIN-HH array, considering clover detectors. The different detector combinations are shown in different colours: FIPPS-FIPPS (red) FIPPS-IFIN (blue) and IFIN-IFIN (green).

	q_2	q_4
FIPPS-FIPPS	0.822(4)	0.495(2)
FIPPS-IFIN	0.845(9)	0.641(3)
IFIN-IFIN	0.923(14)	0.732(6)

Table 3.4: Q-values for each detector type combination of the FIPPS+IFIN-HH array [145].

The procedure for extracting the relevant spin, multipolarity and mixing ratio from the angular correlation distribution will be presented using known nuclei with high fission yields as test cases. For example, the angular correlation obtained measuring the number of coincidences between the 1176 keV and the 359 keV transitions belonging to the $0+ \rightarrow 2+ \rightarrow 0+$ cascade in ^{142}Ba (fission yield $= 2.9 \times 10^{-2}$) is shown in Fig. 3.14. A simultaneous fit of the three FIPPS-FIPPS, FIPPS-IFIN and IFIN-IFIN distributions is performed to eq. 3.4 using the q-values reported in Table 3.4. The resulting experimental a_2 and a_4 coefficients are compatible with theoretical values of a $0+ \rightarrow 2+ \rightarrow 0+$ cascade, as shown in Table 3.5. In order to determine whether there is a mixing of multipolarities δ for a given spin hypothesis, a χ^2 test is performed using the following expression:

$$\chi^2 = \left(\frac{a_2 - a_2^{theory}(\delta)}{\Delta a_2}\right)^2 + \left(\frac{a_4 - a_4^{theory}(\delta)}{\Delta a_4}\right)^2. \tag{3.5}$$

The obtained experimental a_2 and a_4 values compared to the theoretical values corresponding to the calculated mixing ratio are shown in the bottom panels of Fig 3.14.

Nucleus	Cascade	$\gamma_1 - \gamma_2$ (keV)	$a_2(exp)$	$a_4(exp)$	$a_2(th)$	$a_4(th)$
^{142}Ba	$0 \rightarrow 2 \rightarrow 0$	359.0-1176	0.35(5)	1.24(7)	0.357	1.143
^{94}Sr	$4 \rightarrow 2 \rightarrow 0$	836.9-1309.1	0.097(8)	-0.001(11)	0.102	0.009
^{94}Sr (g. 1010 keV)	$4 \rightarrow 2 \rightarrow 0$	836.9-1309.1	0.13(11)	0.04(16)	0.102	0.009
^{94}Sr (g. 377 keV)	$4 \rightarrow 2 \rightarrow 0$	836.9-1309.1	0.13(9)	0.02(13)	0.102	0.009

Table 3.5: Experimentally obtained angular correlation coefficients for cascades in ^{142}Ba and ^{94}Sr, compared to theoretical values. The results corresponding to additional gates on transitions in the ^{94}Sr or its ^{140}Xe fission partner are also shown.

Some of the γ-ray cascades of interest have energies very close to dominating transitions in the total fission spectrum, in particular the Br isotopes studied in this work (see section 5.1.7). In order to increase the selectivity, an additional coincidence gate can be applied. However, the question arises of whether a gate on a third γ-ray transition could affect the correlation between the other two. This was tested using the $4+ \rightarrow 2+ \rightarrow 0+$ cascade in ^{94}Sr. The measured distributions for three cases: no additional gate, gate on the $6+ \rightarrow 4+$ transition in ^{94}Sr and gate on the $2+ \rightarrow 0+$ transition in the ^{140}Xe fission partner, are shown in Fig. 3.15. For the first case, the experimental a_2 and a_4 are consistent with theoretical values (see Table 3.5). The shape of the distribution is not significantly affected by either of the additional gates. However, the reduced statistics (by approximately a factor of 45) produce $a_{2,4}$ coefficients with large uncertainties. Further work is required to establish the effect of additional gates and apply the method to transitions of unknown multipolarity.

Conclusion

The strength of the well established γ-ray coincidence technique has been illustrated using known γ-ray transitions in high fission yield Zr and Te isotopes. The improvements of the FIPPS campaign with respect to the EXILL campaign, in terms of energy resolution and suppression of the γ-ray background produced by β-decay of fission fragments, has been demonstrated. In addition, investigations of excitations in nuclei with isomeric states in the tens of ns range using prompt-delayed coincidences have been examined. The procedure for the identification of contaminant γ-ray transitions has been shown for the analysis of both FIPPS and AGATA-VAMOS++ data-sets. The γ-ray angular correlation capabilities of the FIPPS+IFIN-HH array have been discussed, as well as the challenges in the analysis of angular correlations for fission fragments.

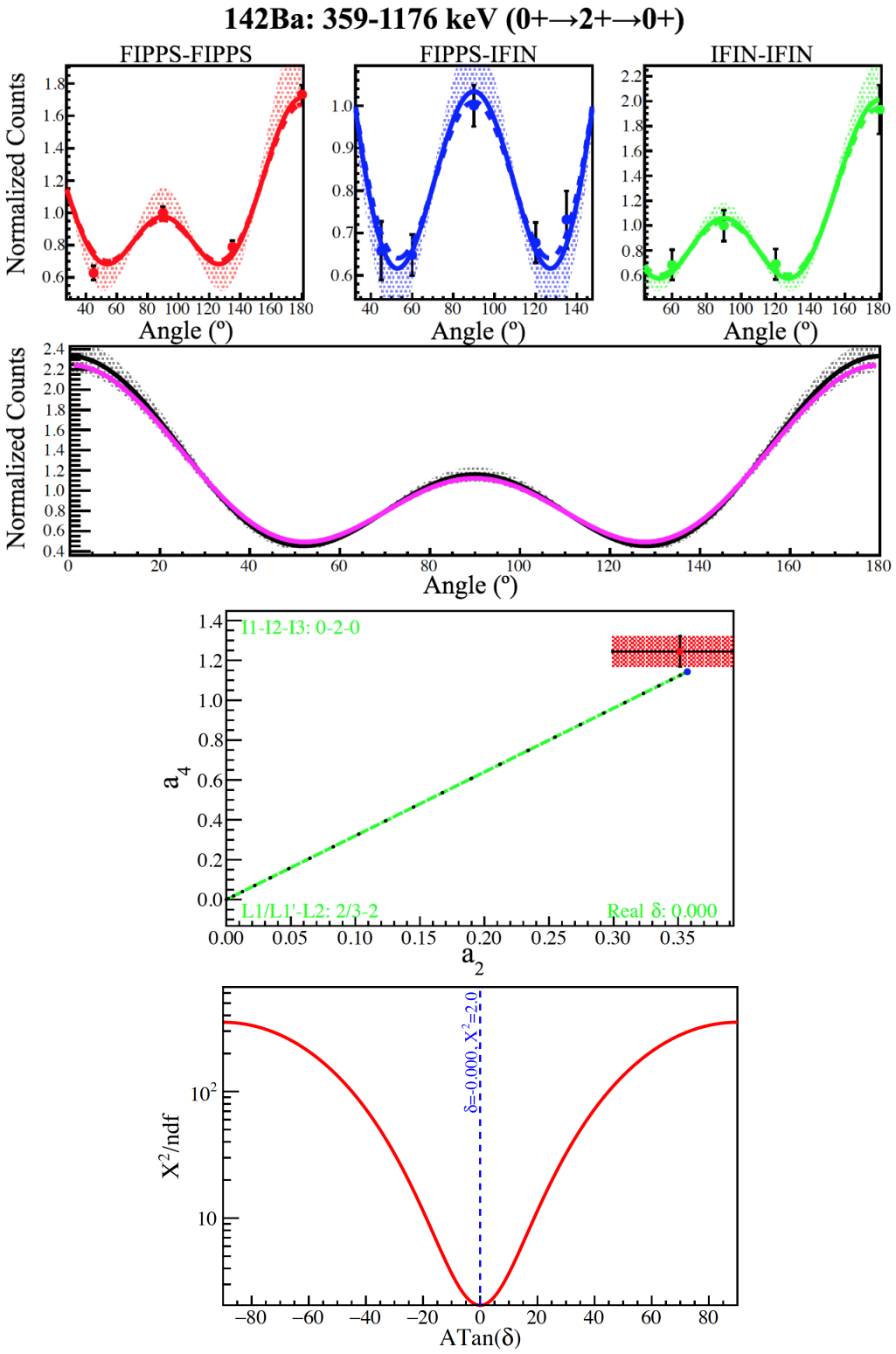

Figure 3.14: Angular correlations obtained for the $0+ \rightarrow 2+ \rightarrow 0+$ cascade in ^{142}Ba. The top plots show the measured angular correlation distribution for each type of detector combination. The experimental distribution combining all clover detectors is shown in black, and compared to the theoretical distribution in pink. The experimental a_2 and a_4 values as well as the χ^2 minimisation used to obtain the δ are shown in the bottom.

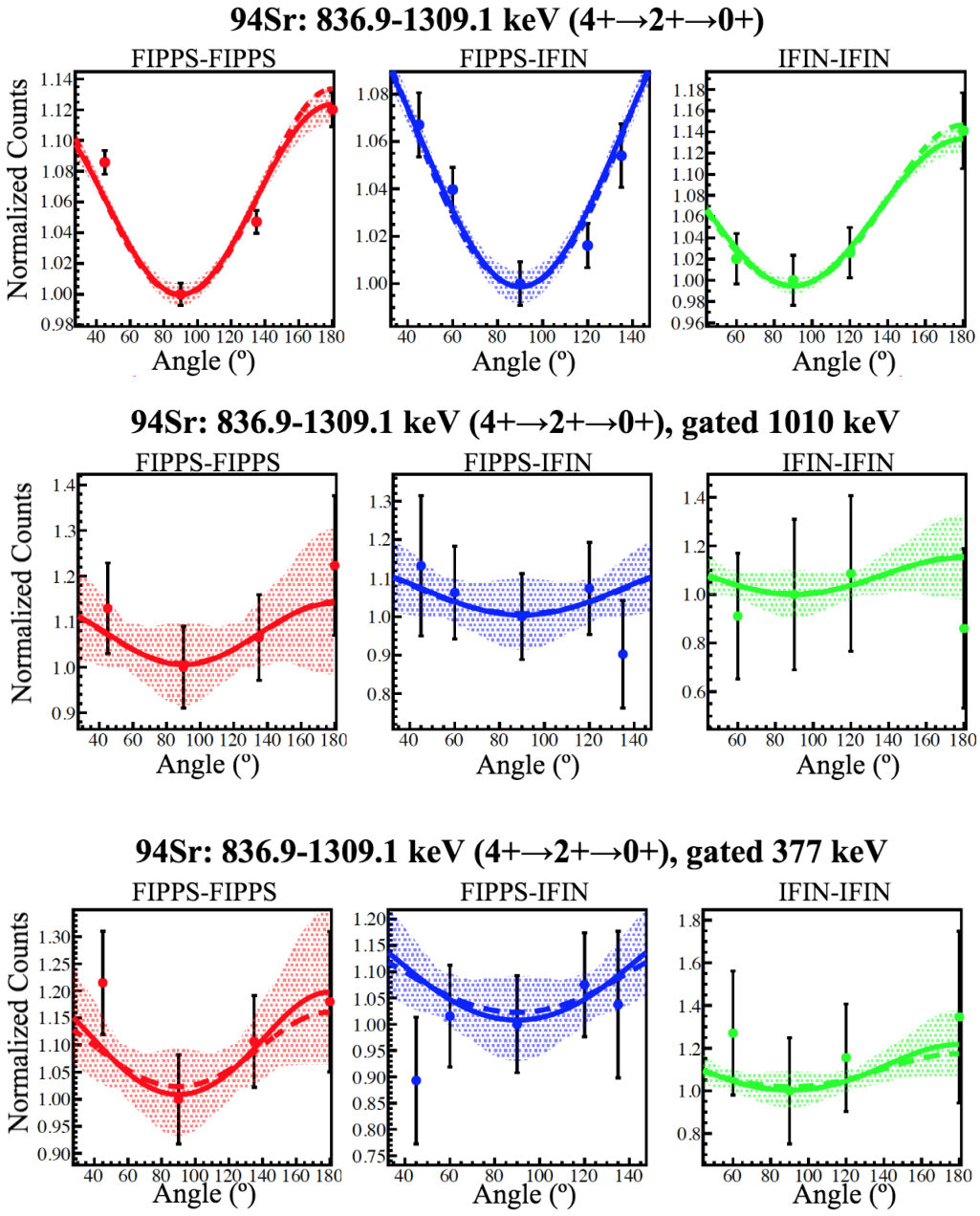

Figure 3.15: Angular correlations obtained for the 4+ → 2+ → 0+ cascade in ^{94}Sr. The second and third panel show the distribution obtained when applying an additional gate, either on the 6+ → 4+ transition in ^{94}Sr (1010 keV) or the 2+ → 0+ transition (377 keV) in the ^{140}Xe complementary fission partner.

CHAPTER 4

γ-ray spectroscopy of neutron rich Kr isotopes

Contents

In this chapter the analysis of neutron rich $^{90-95}$Kr isotopes will be presented. The analysis was performed combining the FIPPS active data with the data acquired in the AGATA-VAMOS++ fission experiment. The known level schemes of the Kr isotopes of interest were extended by exploiting the γ-ray spectroscopy techniques presented in Chapter 3.

Neutron rich krypton isotopes are located in the $A \sim 100$ region. Nuclei situated in this region exhibit among the most drastic shape changes as a function of neutron number observed across the nuclear chart (see section 1.2). Even though some nuclei in this region such as Zr, Sr, and Mo have been well studied, more experimental information is needed for isotopes located in the low Z limit of the $A \sim 100$ region, such as the Kr isotopes.

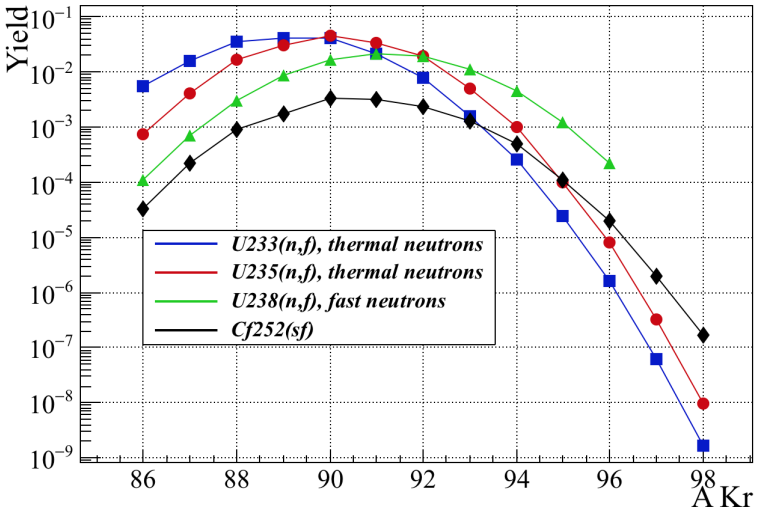

Figure 4.1: Fission yields of the Kr isotopic chain resulting from different fissioning systems. Fission yield values are taken from [7, 147, 148].

As previously discussed, the high number of different isotopes than can be produced using fission reactions make them particularly suited to carry out a systematic study of the evolution of structure along an isotopic chain. The neutron rich Kr isotopes of interest have previously been studied using spontaneous fission sources, as well as neutron induced fission during the EXILL campaign. The fission yields of the Kr isotopic chain for various fissioning systems are plotted in Fig. 4.1. A maximum in the fission yield distribution can be observed for $^{89-92}$Kr isotopes. In all fissioning systems, the fission yields decrease drastically with increasing neutron number. This translates into less known spectroscopic information for nuclei approaching $N = 60$, focus of this work. The highest yields in this region are obtained using fast neutron induced fission of ^{238}U (reaction used during the ν-ball campaign [95]). However, the higher yields come at the cost of a lower fission cross section (0.53 b [149]) in comparison with thermal neutron induced fission of ^{235}U (590 b [149]). The highest production rate can be achieved using the ^{235}U(n,f) reaction employed for the FIPPS fission campaign presented in this work. This fact combined with the fission tag, the higher efficiency, and improved energy resolution achieved during the experiment (with respect to EXILL) allowed an extraction of new spectroscopic information.

The quality of the isotopic separation achieved for Kr isotopes using the VAMOS++ spectrometer in the AGATA-VAMOS++ data is reported in Fig. 4.2. Isotopes $^{84-96}$Kr were detected, with a maximum production yield corresponding to ^{90}Kr. This work will focus on the data analysis of neutron rich $^{90-95}$Kr isotopes. Located at the $N = 60$ boundary of shape transition, and with only the $4+ \rightarrow 2+$ and $2+ \rightarrow 0+$ known transitions, the ^{96}Kr nucleus is a particularly interesting isotope to be studied. The results obtained from the AGATA-VAMOS++ analysis of ^{96}Kr ($N = 60$) can be found in [52]. As presented in the previous chapter, γ-ray spectra gated on the isotopes of interest with more or less restrictive conditions were employed to identify new transitions. In the cases with enough statistics, γ-γ coincidences were exploited to place the newly observed transitions in a level scheme.

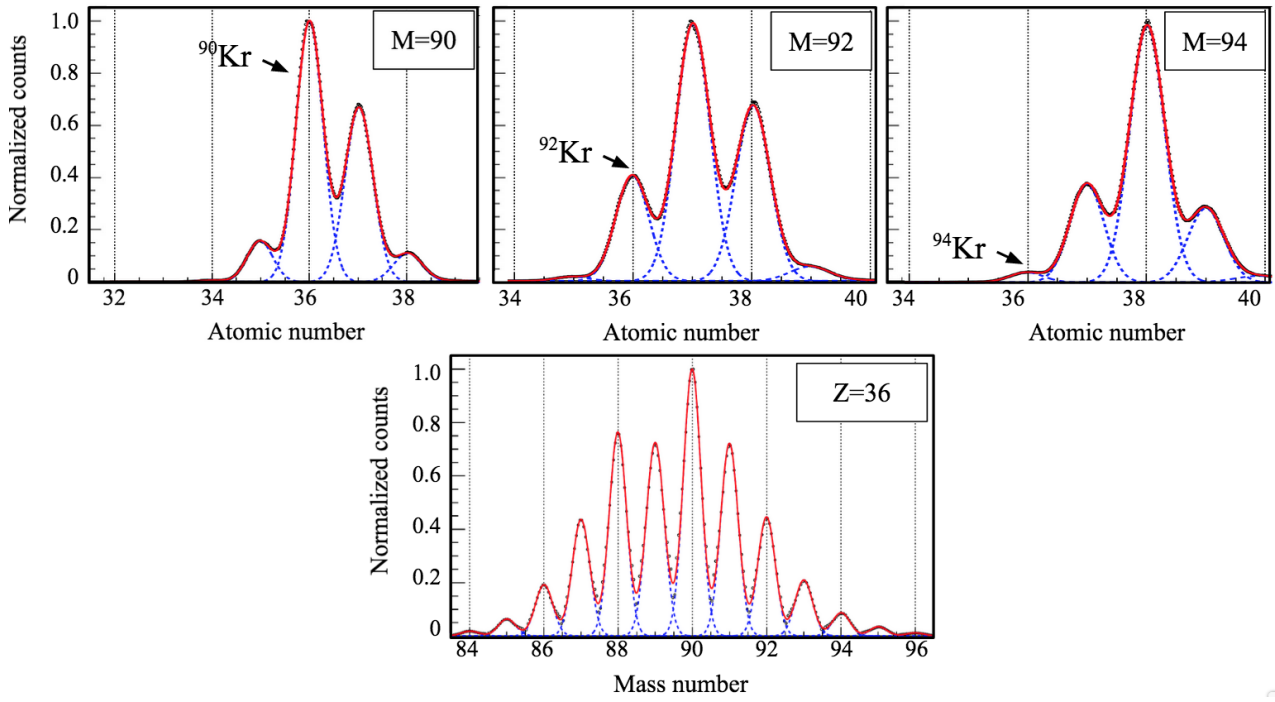

Figure 4.2: Atomic and mass distributions obtained with VAMOS++, employed for the analysis of the Kr isotopes. The distributions are normalised to the maximum value [132].

For the analysis of the FIPPS data-set γ-γ-γ coincidences were employed. New γ-ray transitions were identified using known transitions in the isotopes of interest, as well as the complementary Ba fission partners. The main prompt γ-ray transitions of the Ba isotopes observed in neutron induced fission of ^{235}U are well known and can be found in Ref. [150]. The Kr-Ba fission partner distributions are shown in Fig. 4.3. In addition to triple prompt coincidences, the prompt-delayed coincidence technique was exploited to investigate the structure across isomeric states in $^{93-95}$Kr. Both prompt coincidences on the two known transitions and prompt delayed coincidences in ^{138}Ba (2n complementary fragment), revealed that the extremely neutron rich ^{96}Kr isotope was out of reach in the present FIPPS setup. This is explained by the sudden decrease in fission yield after ^{94}Kr. The low fission yield of ^{96}Kr, along with a comparison of the probability of production of the ^{96}Kr-^{138}Ba pair and the ^{94}Kr-^{140}Ba pair is shown in Fig. 4.4.

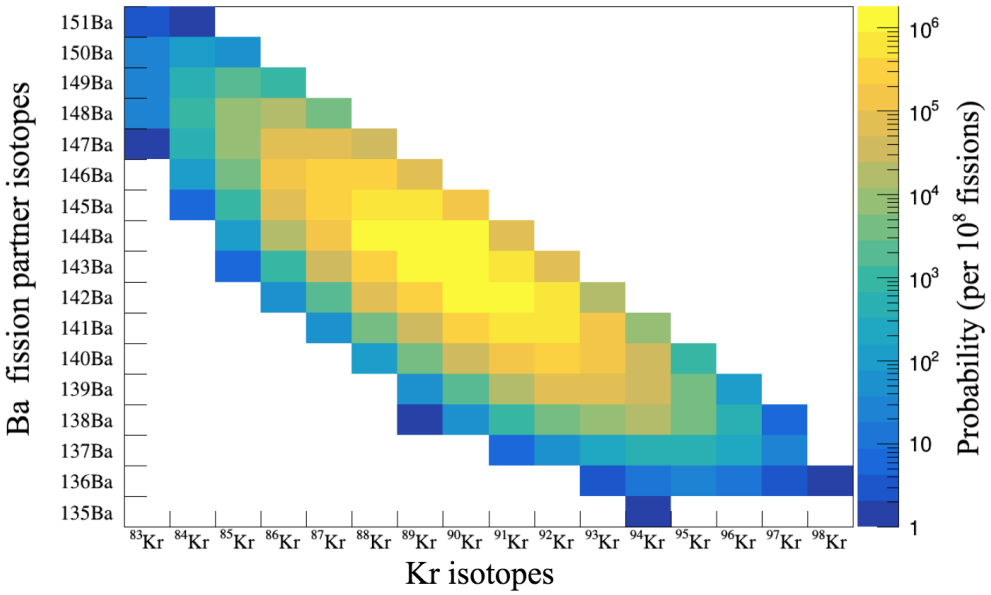

Figure 4.3: Kr-Ba fission yields for thermal neutron induced fission of ^{235}U. Values were obtained simulating 10^8 fission events with the GEF code [136].

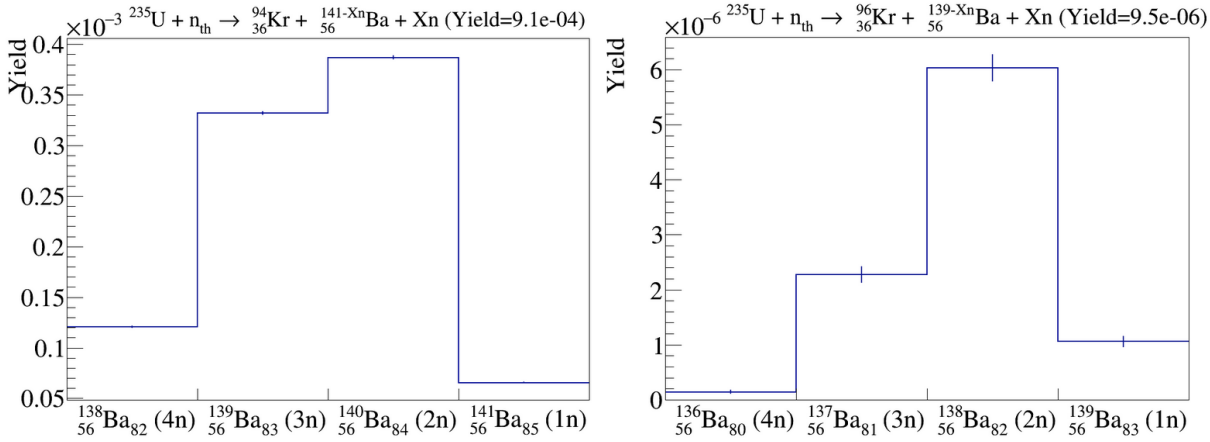

Figure 4.4: Fission partner distributions of ^{94}Kr and ^{96}Kr produced in thermal neutron induced fission of ^{235}U, obtained using the simulation code GEF [136]. A comparison of the ^{94}Kr-^{140}Ba yield with the ^{96}Kr-^{138}Ba yield reveals a difference of two orders of magnitude.

The obtained γ-ray spectroscopy results for each of the Kr isotopes studied will be presented in the following sections, starting from the well known ^{90}Kr isotope up to ^{95}Kr. With increasing mass number, the challenges of studying highly neutron rich nuclei will be seen in the decrease of statistics and increase of γ-ray peaks from contaminant isotopes. An interpretation of the obtained level schemes and a comparison with neighbouring nuclei will be given in section 4.2.

4.1 Experimental results

4.1.1 Spectroscopy of $^{90-91}$Kr

Due to their high fission yields (see Fig. 4.1), excited states in ^{90,91}Kr have been previously studied in fission experiments, resulting in well known level schemes. First investigations were performed using spontaneous fission sources [62, 63, 65]. More recently, their structure was studied during the EXILL campaign [67, 66]. The isotopic identification provided by the VAMOS++ spectrometer combined with larger statistics and higher energy resolution of the FIPPS+IFIN array allowed the addition of less intense transitions to the known level schemes of these nuclei.

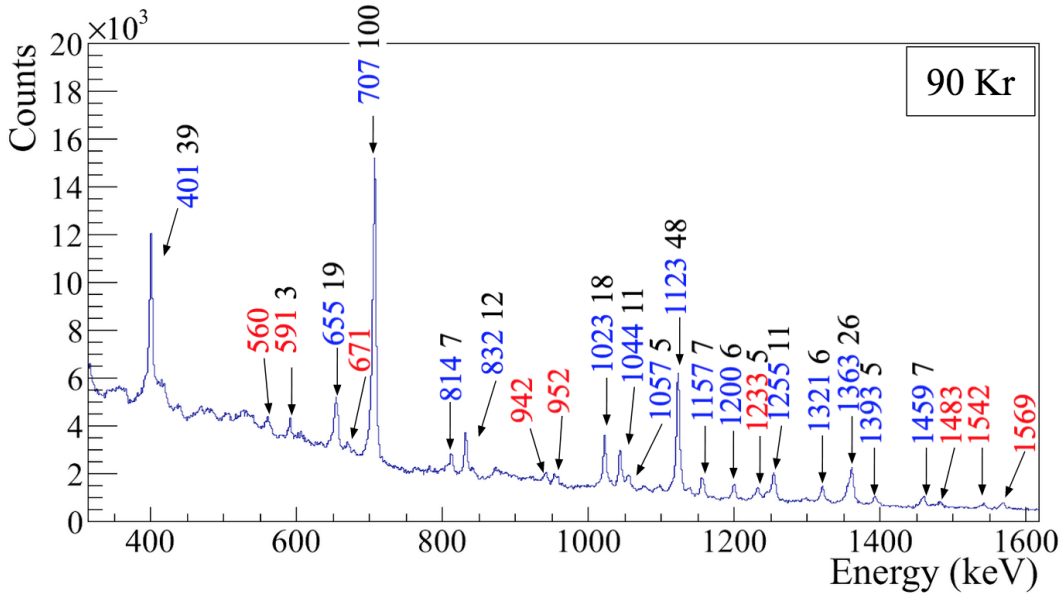

Figure 4.5: Doppler corrected prompt γ-ray spectrum measured in AGATA in coincidence with the ^{90}Kr ions detected in VAMOS++. Previously known transitions are marked in blue. Newly observed transitions are marked in red. Intensities relative to the strongest transition (707 keV) are indicated in black.

The Doppler corrected γ-ray spectrum observed in AGATA, measured in coincidence with the ^{90}Kr fission fragment identified in VAMOS++, is shown in Fig. 4.5. Newly observed transitions are highlighted in red. γ-γ coincidences applied to the AGATA-VAMOS++ data as well as γ-γ-γ coincidences observed in the FIPPS data-set were used to reconstruct excited levels from the new transitions. Fig. 4.6 shows typical prompt coincidence spectra obtained using the active target FIPPS data. Coincidence spectra gated on the $4+ \rightarrow 2+$ (1123 keV) transition and the $2+ \rightarrow 0+$ (707 keV) transition as well as the $5 \rightarrow 4+$ (1023 keV) are shown. The low energy part of the spectrum is dominated by γ-ray transitions corresponding to the Ba fission partners. A comparison of such gated spectra enables an identification and placement of the newly observed γ rays (for example the 671 keV and 1569 keV transitions).

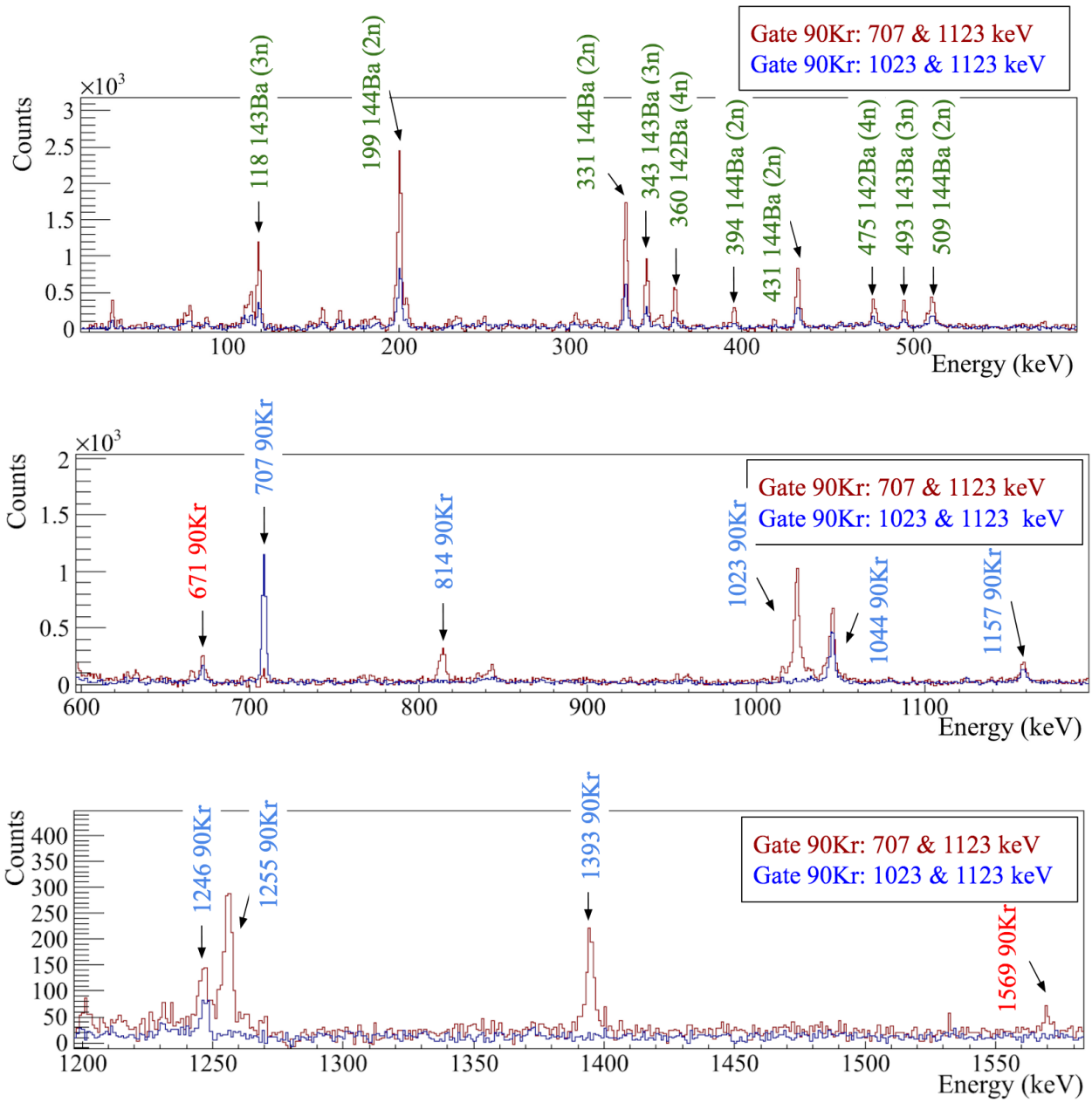

Figure 4.6: Coincidence spectra obtained using the active fission target data collected at FIPPS. The shown comparisons of doubly gated spectra on known transitions in the ^{90}Kr nucleus were used to identify new transitions and confirm the placement of known transitions in a level scheme. The low energy spectrum is dominated by γ-ray transitions belonging to the Ba complementary fission partners (indicated in green). Known transitions in ^{90}Kr are labelled in blue, while newly identified transitions are marked in red.

All the γ-ray transitions assigned to ^{90}Kr, with their corresponding measured intensities, are reported in Table 4.1. The final level scheme obtained for the ^{90}Kr nucleus is shown in Fig. 4.9. A total of 10 new γ-ray transitions and 7 new excited levels were observed. The intensities shown in the level schemes of the Kr isotopes are the ones measured with the FIPPS data-set.

Energy (keV)	**Intensity** (%)	$J_i \rightarrow J_f$	E_i **(keV)**	E_f **(keV)**	**Data-set**
401.3(2)	39(3)	$(3+, 4+) \rightarrow 2+$	1764	1363	F+A
560.2(4)*	< 5	-	4098	3538	F+A
655.1(2)	19.2(14)	$2+ \rightarrow 2+$	1363	707	F+A
671.1(2)*	< 5	-	4568	3897	F+A
706.9(2)	100.0	$2+ \rightarrow 0+$	707	0	F+A
813.6(3)	6.7(5)	-	4037	3223	F+A
832.3(3)	11.9(9)	-	2596	1764	F+A
842.0(5)*	< 5	-	5127	4285	F+A
942.0(3)*	< 5	-	3538	2596	F+A
952.0(4)*	< 5	-	4037	3085	F+A
1022.6(2)	18.4(14)	$(5) \rightarrow 4+$	2853	1830	F+A
1031.0(5)*	< 5	-	6085	5054	F
1043.7(2)	11.1(8)	-	3897	2853	F+A
1056.9(2)	4.5(4)	$(3+, 4+) \rightarrow 2+$	1764	707	F+A
1098.2(3)	4(2)	-	3694	2596	F+A
1123.3(2)	48(3)	$4+ \rightarrow 2+$	1830	707	F+A
1156.7(2)	6.8(5)	-	5054	3897	F+A
1199.5(4)	5.7(5)	-	4285	3085	F
1232.5(2)*	4.9(4)	-	2596	1363	A
1245.7(3)	5.2(5)	-	4099	2853	F+A
1254.7(2)	11.2(8)	$5+ \rightarrow 4+$	3085	1830	F+A
1320.6(2)	6.1(5)	$5+ \rightarrow (4+, 3+)$	3085	1764	F+A
1362.5(2)	26.7(2)	$2+ \rightarrow 0+$	1363	0	F+A
1393.2(2)	5.3(4)	-	3223	1830	F+A
1459.7(2)	7.3(6)	$(5+, 6+) \rightarrow (3+, 4+)$	3223	1764	F+A
1483.0(4)	< 5		4079	2596	F+A
1568.8(2)*	3.5(3)	-	3399	1840	F+A
Unplaced transitions					
590.9(2)*	3.1(3)	-	-	-	A
1542.0(2)*	< 5	-	-	-	A

Table 4.1: Properties of the γ-ray transitions assigned to ^{90}Kr in this work. Newly observed transitions are marked with (*). In the last column, information is given on whether they were observed in both the FIPPS and AGATA-VAMOS++ data-sets (F+A), only in the FIPPS data (F) or only in the AGATA-VAMOS++ data (A). Efficiency corrected intensity values are given relative to the strongest transition (706.9 keV). The reported intensities were obtained from the AGATA-VAMOS++ data, except for transitions observed only in the FIPPS data-set. The indicated spin and parity values of excited states were adopted from [66].

The structure of ^{91}Kr was previously studied in fission experiments using spontaneous fission sources [65] and neutron induced fission [66]. The strongest observed transition in this nucleus corresponds to a transition from the first 7/2+ state at 707 keV to the ground state. This 707 keV transition, as well as a group of transitions built on top of the 707 keV state, were initially wrongly assigned to ^{90}Kr [62], because of the 2+ $\rightarrow$ 0+ transition of the same energy. A careful analysis of the EXILL data using the intensities of the transitions from the Ba complementary fission fragments in coincidence with the 707 keV peak and other intense transitions, allowed the confirmation of a 707 keV transition in ^{91}Kr [62]. This assignment is firmly established in this thesis thanks to the isotopic identification provided by the VAMOS++ spectrometer. The Doppler corrected γ-ray spectrum observed in AGATA, measured in coincidence with the ^{91}Kr fission fragment identified in VAMOS++, is shown in Fig. 4.7. Four new transitions were identified and are marked in red in the figure. An example of a gated spectrum obtained with the FIPPS data-set, used to place one of the newly observed transitions, can be seen in Fig. 4.8. The properties of all the observed transitions assigned to ^{91}Kr are reported in Table 4.2. The final level scheme is shown in Fig. 4.9.

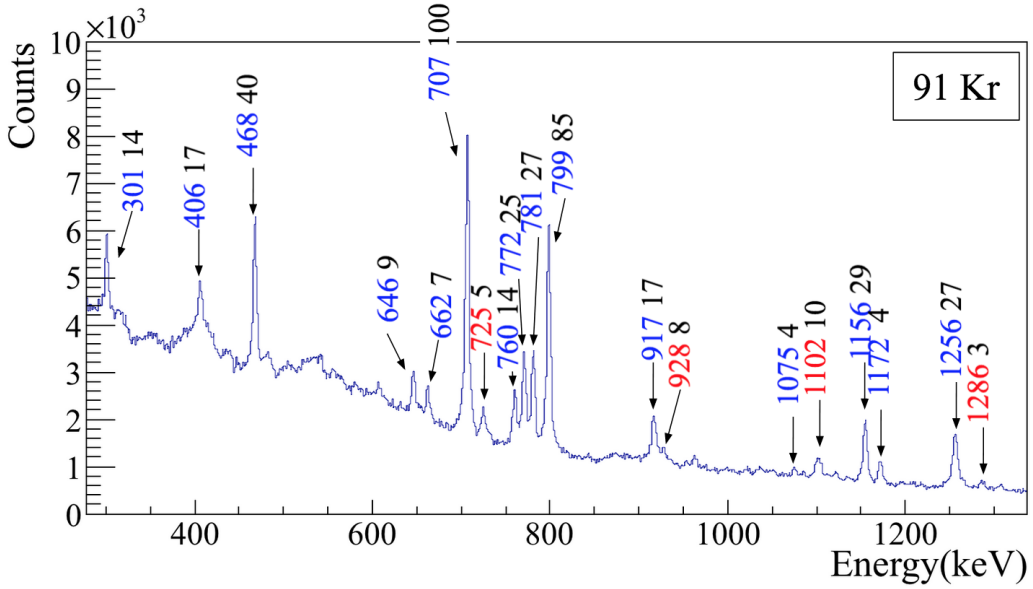

Figure 4.7: Doppler corrected prompt γ-ray spectrum measured in AGATA in coincidence with the ^{91}Kr ions detected in VAMOS++. Previously known transitions are marked in blue. Newly observed transitions are marked in red. Intensities relative to the strongest transition (707.2 keV) are indicated in black.

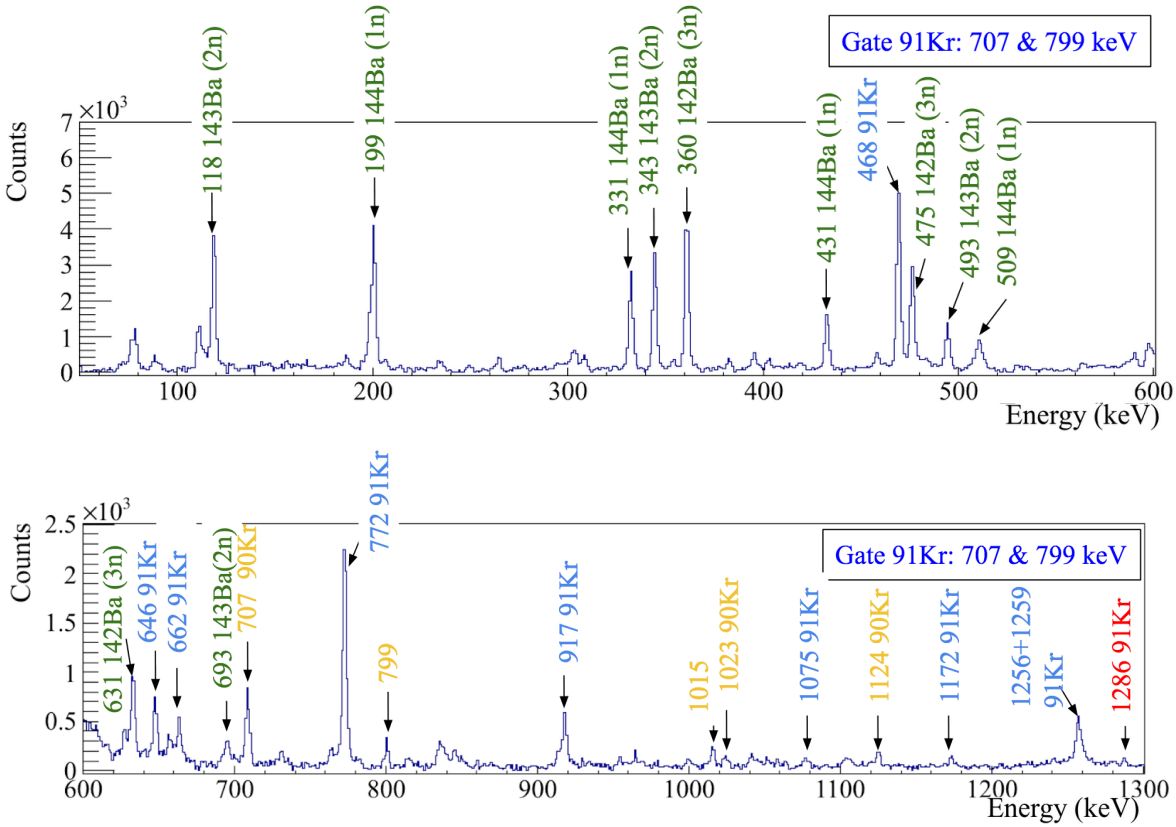

Figure 4.8: Coincidence spectra obtained using the active fission target data collected at FIPPS gated on the strongest transitions in ^{91}Kr. The low energy spectrum is dominated by γ-ray transitions belonging to the Ba complementary fission partners, indicated in green. Known transitions in ^{91}Kr are labelled in blue while newly identified transitions are marked in red. Contaminant peaks belonging to ^{90}Kr and strong transitions observed in the total projection are labelled in yellow.

Energy (keV)	**Intensity** (%)	$J_i \rightarrow J_f$	E_i **(keV)**	E_f **(keV)**	**Data-set**
301.0(2)	14.9(11)	$(5/2+, 3/2+) \rightarrow 5/2+$	301	0	F+A
406.2(2)	17.4(11)	$7/2+ \rightarrow (5/2+, 3/2+)$	707	301	F+A
468.0(2)	40(3)	$(11/2, 13/2) \rightarrow 11/2+$	1974	1506	F+A
646.1(2)	9.2(7)	-	3407	2762	F+A
662.2(2)	6.9(6)	-	3407	2746	F+A
707.2(2)	100.0	$7/2+ \rightarrow 5/2+$	707	0	F+A
725.3(2)*	5.2(5)	-	1506	781	F+A
730.0(2)	< 5	-	3407	2678	F+A
760.20	14.0(11)	$13/2+ \rightarrow 9/2+$	1916	1156	F+A
771.5(2)	25(2)	-	2745	1974	F+A
781.2(2)	27(2)	-	781	0	F+A
798.9(2)	85(6)	$11/2+ \rightarrow 7/2+$	1506	707	F+A
916.7(2)	17.3(14)	-	4324	3407	F+A
1075.4(3)	4.2(8)	-	5079	4004	F+A
1155.5(2)	29(2)	$9/2+ \rightarrow 5/2+$	1156	0	F+A
1171.9(2)	8.2(7)	-	2678	1506	F+A
1255.8(2)	27(2)	-	2762	1506	F+A
1258.7(2)	5.1(4)	-	4004	2745	F+A
1286.0(2)*	2.8(3)	-	2792	1506	F+A
Unplaced transitions					
928.0(4)*	8.4(9)	-	-	-	A
1101.7(4)*	10.2(8)	-	-	-	A
1308.0(4)*	1.7(2)	-	-	-	A

Table 4.2: Properties of the γ-ray transitions assigned to ^{91}Kr in this work. Newly observed transitions are marked with (*). In the last column, information is given on whether they were observed in both the FIPPS and AGATA-VAMOS++ data-sets (F+A), only in the FIPPS data (F) or only in the AGATA-VAMOS++ data (A). Efficiency corrected intensity values are given relative to the strongest transition (707.2 keV). The reported intensities were obtained from the AGATA-VAMOS++ data. The indicated spin and parity values of excited states were adopted from [66].

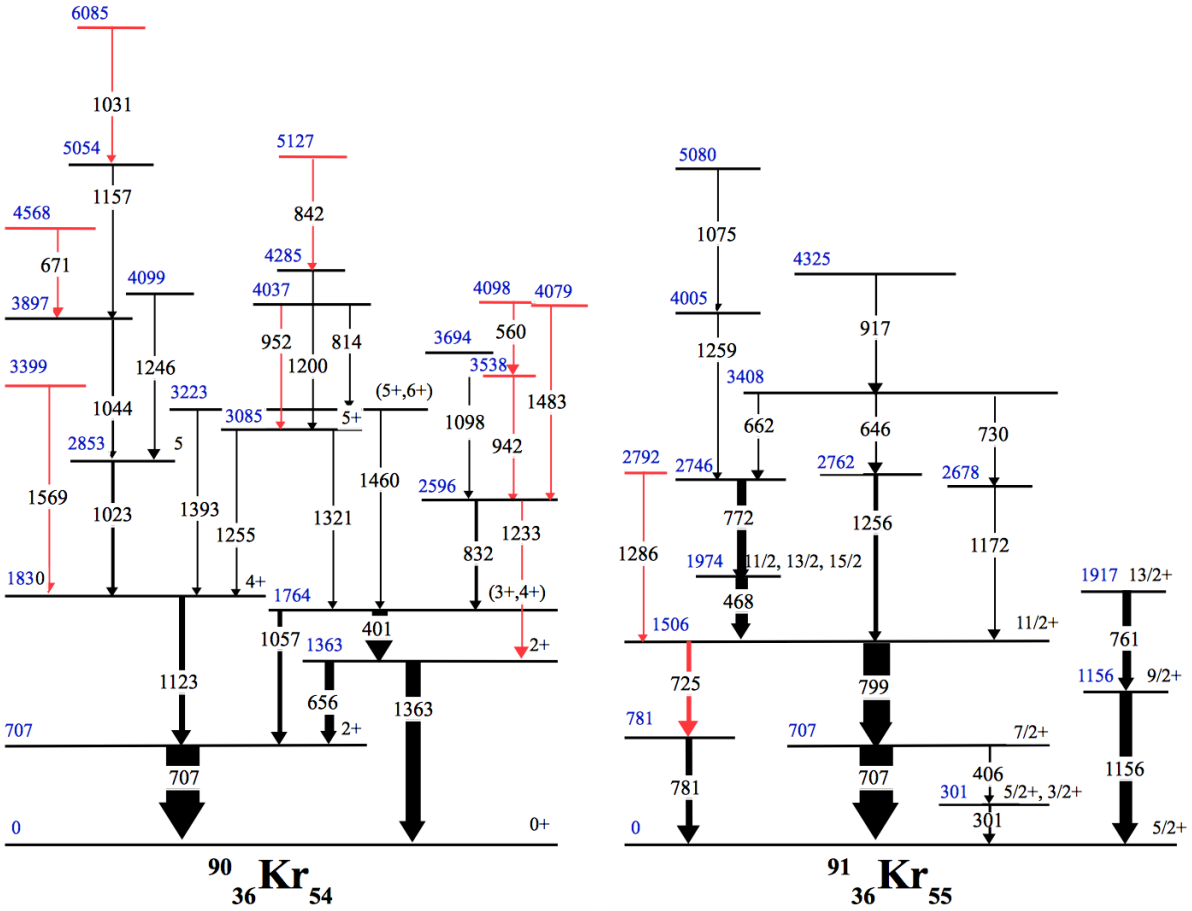

Figure 4.9: Level schemes of ^{90}Kr and ^{91}Kr obtained in this work. Known transitions are shown in black and newly found transitions in red. The width of the arrows reflect the observed intensity in the FIPPS data-set. Spin and parity values are taken from [66].

4.1.2 Spectroscopy of ^{92}Kr

Excited states of ^{92}Kr, populated using a spontaneous fission source, have been extensively studied in [65]. The γ-ray spectrum measured in AGATA is shown in Fig. 4.10. Most of the already known transitions were observed. New transitions were identified from the analysis of the FIPPS data-set. An example of a coincidence spectrum can be seen in Fig. 4.11. The relevant information of all the observed γ-ray transitions is given in Table 4.3. The obtained level scheme of ^{92}Kr is shown in Fig. 4.12. Three new transitions and two new excited states were added to the known level scheme.

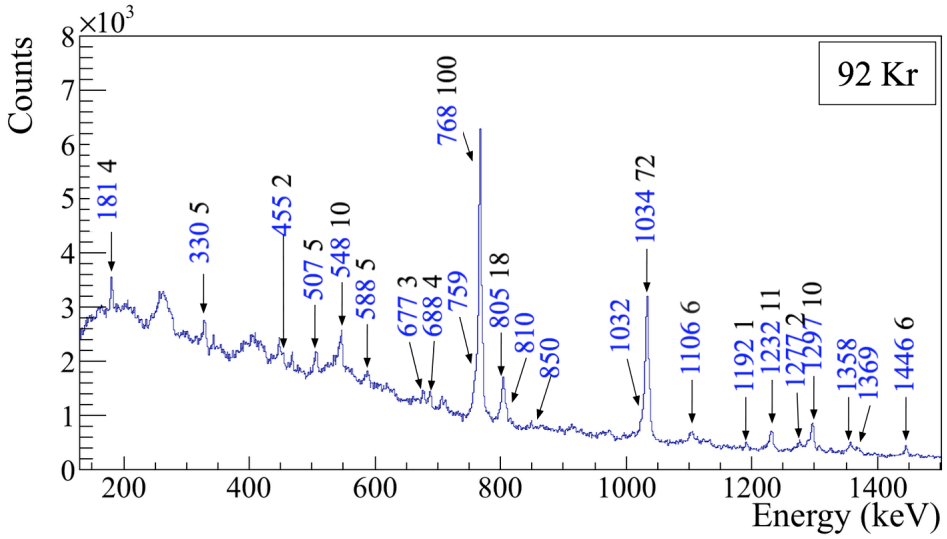

Figure 4.10: Doppler corrected prompt γ-ray spectrum measured in AGATA in coincidence with the ^{92}Kr ions detected in VAMOS++. All observed transitions were previously known [65]. Intensities relative to the strongest transition (768 keV) are written in black.

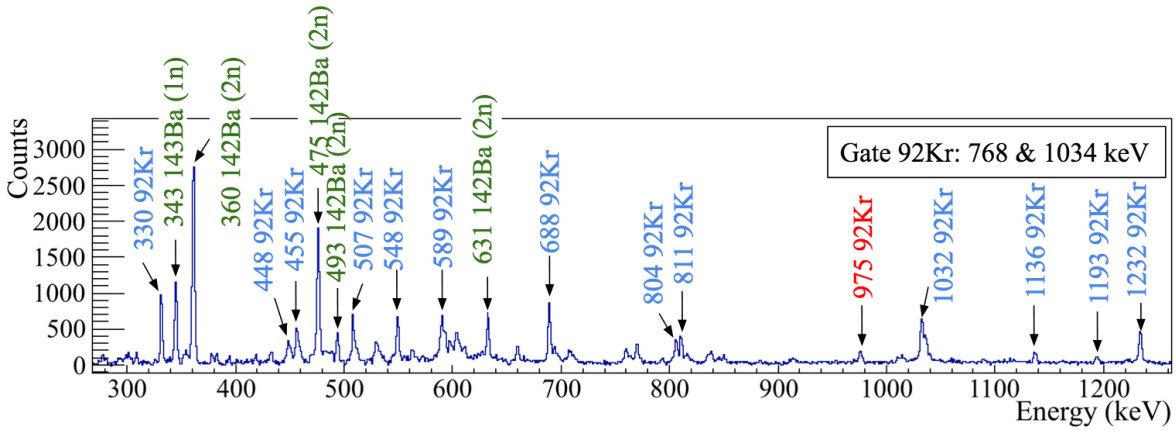

Figure 4.11: Coincidence spectrum obtained using the active fission target data collected at FIPPS, gated on the 4+ $\rightarrow$ 2+ and 2+ $\rightarrow$ 0+ transitions in ^{92}Kr. γ-ray transitions belonging to the Ba complementary fission partners are indicated in green. Known transitions in ^{92}Kr are labelled in blue while newly identified transitions are marked in red.

Energy (keV)	**Intensity** (%)	$J_i \rightarrow J_f$	E_i **(keV)**	E_f **(keV)**	**Data-set**
181.1(2)	3.9(3)	(4+) → (4+)	1983	1802	F+A
329.7(2)	4.5(4)	(10+) → (8+)	4174	3844	F+A
425.5(3)*	< 5	-	2419	2065	F
449.0(2)	< 5	-	3626	3177	F+A
455.4(2)	1.60(17)	-	3626	3171	F+A
506.5(3)	4.8(4)	(6+) → (4+)	2490	1983	F+A
548.1(2)	10.2(8)	-	4174	3626	F+A
587.4(2)	5(3)	-	1355	768	F+A
592.0(2)	5(4)	-	3626	3034	F
677.4(2)	2.9(3)	(1, 2+) → 2+	1445	768	F+A
688.0(2)	3.8(4)	(6+) → (4+)	2490	1802	F+A
759.5(2)	< 5	-	3594	2834	F+A
768.2(2)	100.00	2+ → 0+	768	0	F+A
793.0(3)*	< 5	-	3626	2834	F
804.7(2)	17.8(14)	(12+) → (10+)	4979	4174	F+A
809.6(2)	< 5	-	3844	3034	F+A
850.0(2)	4(3)	-	2652	1802	F+A
974.8(2)*	3(2)	-	2777	1802	F
1031.8(2)	10(3)	-	2834	1802	F+A
1034.4(2)	60(5)	(4+) → 2+	1802	768	F+A
1106.0(2)	5.9(5)	(6+) → (4+)	3171	2065	F+A
1112.0(2)	4.0(5)	(6+) → (4+)	3177	2065	F
1135.7(2)	< 5	-	3626	2490	F
1192.8(2)	1.36(17)	-	3844	2652	F+A
1232.4(2)	10.9(8)	(6+) → (4+)	3034	1802	F+A
1276.6(4)	2.2(2)		2045	768	F+A
1297.4(2)	10.1(8)	(4+) → 2+	2065	768	F+A
1358.1(2)	< 5	-	4392	3034	F+A
1368.9(2)	2.5(2)	(6+) → (4+)	3171	1802	F+A
1374.0(5)	< 2	(6+) → (4+)	3177	1802	F
1445.5(3)	6.0(5)	(1, 2+) → 0+	1445	0	F+A

Table 4.3: Properties of the γ-ray transitions assigned to ^{92}Kr in this work. Newly observed transitions are marked with (*). In the last column, information is given on whether they were observed in both the FIPPS and AGATA-VAMOS++ data-sets (F+A) or only in the FIPPS data (F). Efficiency corrected intensity values are given relative to the strongest transition (768.2 keV). The reported intensities were obtained from the AGATA-VAMOS++ data, except for transitions observed only in the FIPPS data-set. The indicated spin and parity values of excited states were adopted from [65].

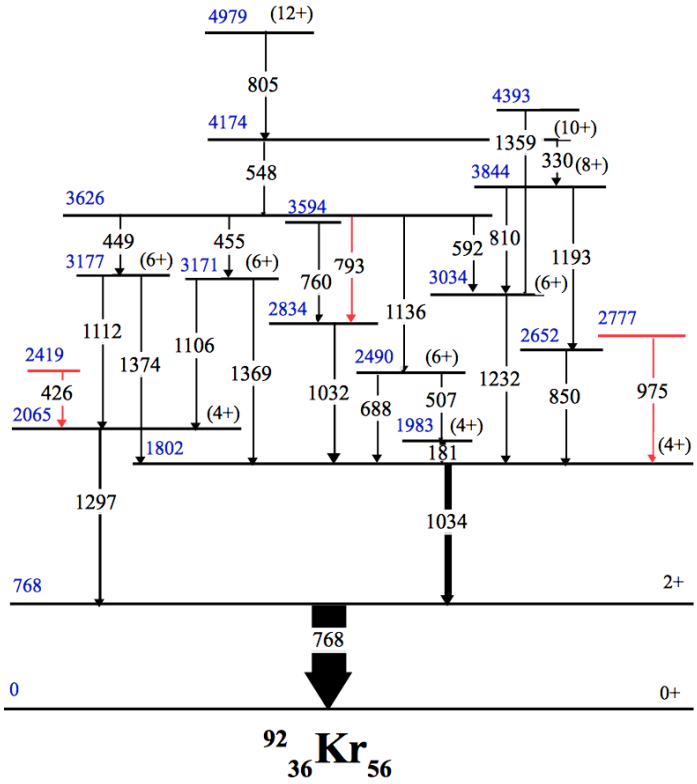

Figure 4.12: Level scheme of ^{92}Kr obtained in this work. Known transitions are shown in black and newly found transitions in red. The width of the arrows reflect the observed intensity in the FIPPS data-set. Spin and parity values are taken from [65].

4.1.3 Spectroscopy of ^{93}Kr

The ^{93}Kr nucleus was first studied after β-decay of ^{93}Br [151] and then using spontaneous fission of ^{252}Cf [64]. In both experiments a (7/2+) state at 355 keV excitation energy was found to have isomeric character. The determined half-life of this state was 22(12) ns and 10(2) ns respectively. More recently, the ^{93}Kr isotope was investigated with the EXILL setup. A preliminary half-life of 6.3(10) ns for the (7/2+) state was measured using fast timing techniques [152].

In this work, the precise time information provided by the active fission target was exploited in the FIPPS data-set to increase the selectivity in prompt-delayed coincidences. A delayed time window of 40-300 ns was used in order to study prompt-delayed coincidences across the 354 keV state. The prompt spectrum doubly gated on the 117 keV and 237 keV delayed transitions is shown in Fig. 4.13. The three transitions highlighted in red correspond to new γ rays assigned to the ^{93}Kr nucleus on the basis of a series of prompt-delayed coincidences. This assignment is confirmed by their presence in the AGATA-VAMOS++ data, as can be seen from Fig. 4.14. An additional 3 new γ-ray transitions were identified in this data-set. All observed transitions, with their corresponding intensities, are reported in Table 4.4. The resulting level scheme is shown in Fig. 4.15.

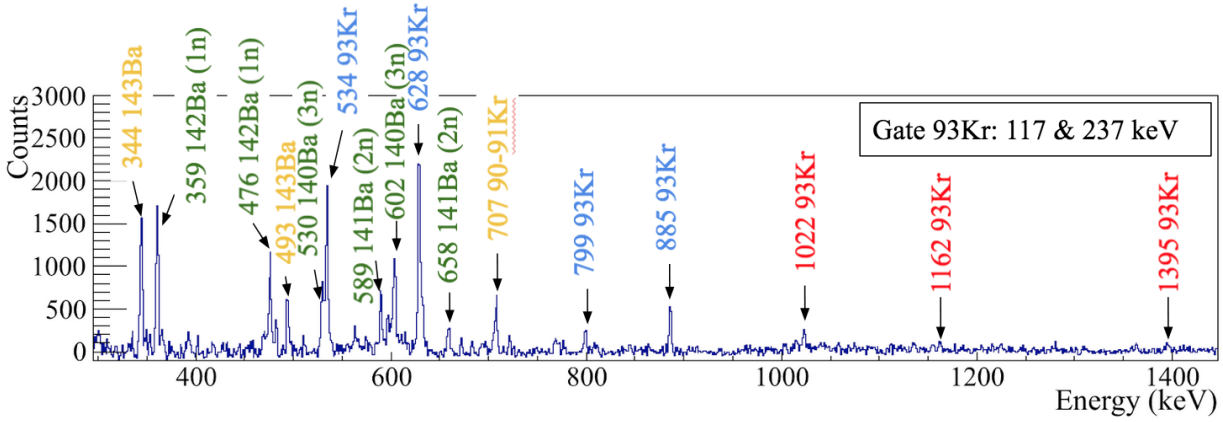

Figure 4.13: Prompt coincidence spectrum of ^{93}Kr doubly gated on the 117 keV and 237 keV delayed transitions, obtained using the active target data at FIPPS. Prompt coincidences are defined in a 0-40 ns window while delayed coincidences are defined in a 40-300 ns interval. Up to 700 keV the spectrum is dominated by γ-ray transitions belonging to the Ba complementary fission partners (green). Contaminant transitions introduced by the 117 keV gate, due to a 118 keV transition in ^{143}Ba, are highlighted in yellow. Known transitions in ^{93}Kr are indicated in blue, while new transitions are marked in red.

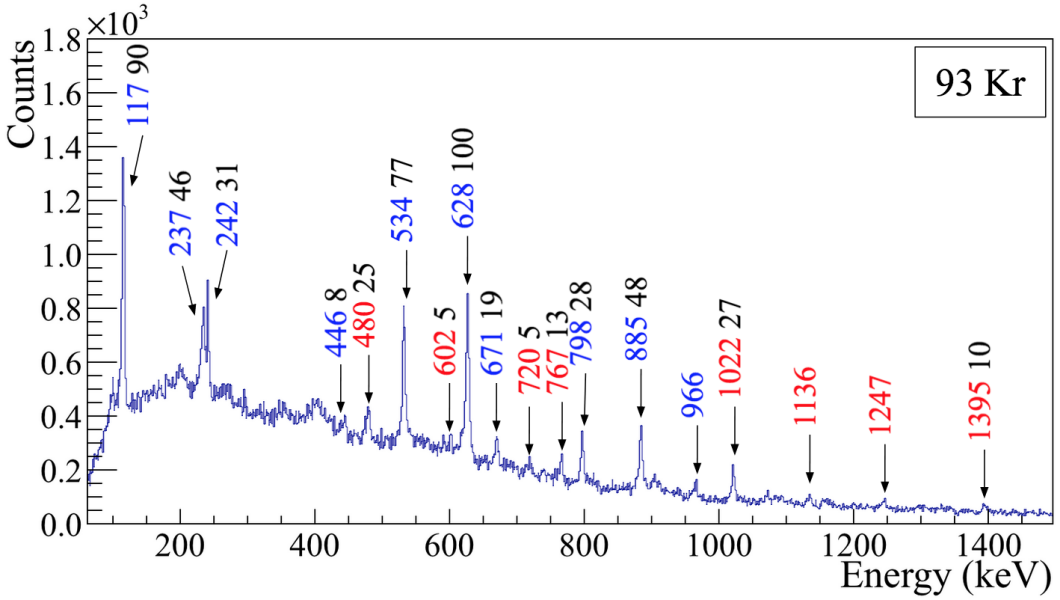

Figure 4.14: Doppler corrected prompt γ-ray spectrum measured in AGATA in coincidence with the ^{93}Kr ions detected in VAMOS++. Previously known transitions are marked in blue. Newly observed transitions are marked in red. Intensities relative to the strongest transition (628 keV) are indicated in black.

Energy (keV)	**Intensity** (%)	$J_i \rightarrow J_f$	E_i **(keV)**	E_f **(keV)**	**Data-set**
116.9(2)	90(7)	$(3/2)+ \rightarrow 1/2+$	117	0	F+A
237.1(2)	46(4)	$(7/2+) \rightarrow (3/2)+$	354	117	F+A
241.8(2)	31(2)	$(< 5/2+) \rightarrow (3/2)+$	359	117	F+A
445.7(2)	7.9(7)	-	805	359	F+A
533.5(3)	77(6)	$(15/2+) \rightarrow (11/2)+$	1516	982	F+A
627.8(2)	100.0	$(11/2+) \rightarrow (7/2)+$	982	354	F+A
670.5(5)	12.8(15)	-	1029	359	F+A
688.0(3)	4.2(5)	-	805	117	F+A
720.1(3)*	5(2)	-	2469	1749	F+A
798.1(2)	28(2)	$(23/2+) \rightarrow (19/2)+$	2199	2401	F+A
884.8(2)	48(4)	$(19/2+) \rightarrow (15/2)+$	2401	1516	F+A
966.0(3)	10(2)	-	1325	359	F+A
1022.3(2)*	27(2)	-	1376	354	F+A
1161.6(2)*	5(3)	$(15/2+) \rightarrow (7/2)+$	1516	354	F
1394.8(2)*	10(1)	-	1749	354	F+A
Unplaced transitions					
481.3(3)*	25(2)	-	-	-	A
602.3(4)*	5.0(5)	-	-	-	A
767.4(4)*	13.0(11)	-	-	-	A
1136.0(4)*	< 5	-	-	-	A
1247.0(4)*	< 5	-	-	-	A

Table 4.4: Properties of the γ-ray transitions assigned to ^{93}Kr in this work. Newly observed transitions are marked with (*). In the last column, information is given on whether they were observed in both the FIPPS and AGATA-VAMOS++ data-sets (F+A), only in the FIPPS data (F) or only in the AGATA-VAMOS++ data (A). Efficiency corrected intensity values are given relative to the strongest transition (628 keV). The reported intensities were obtained from the AGATA-VAMOS++ data, except for transitions observed only in the FIPPS data-set. The indicated spin and parity values of excited states were adopted from [64].

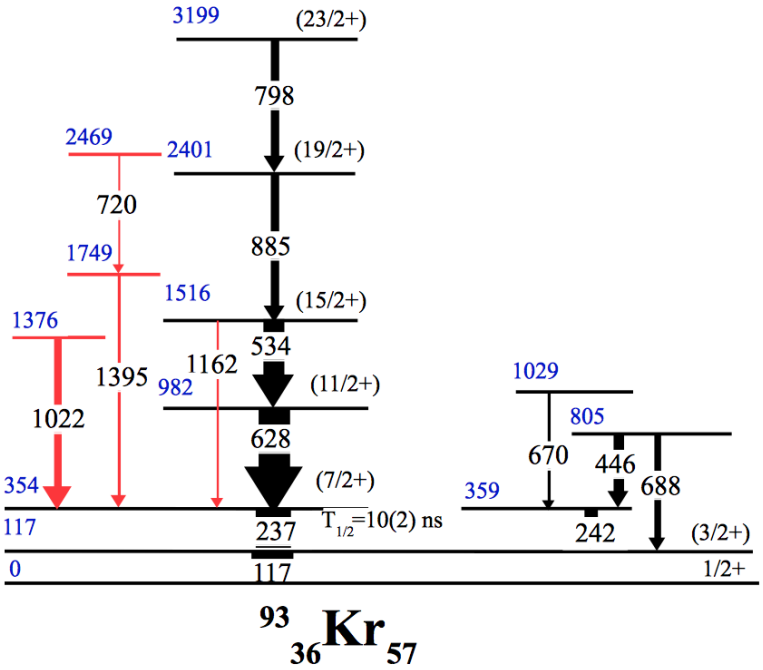

Figure 4.15: Level scheme of ^{93}Kr obtained in this work. Known transitions are shown in black and newly found transitions in red. The width of the arrows reflect the observed intensity in the FIPPS data-set. Spin and parity values, as well as the half-life of the 354 keV state are adopted from [64].

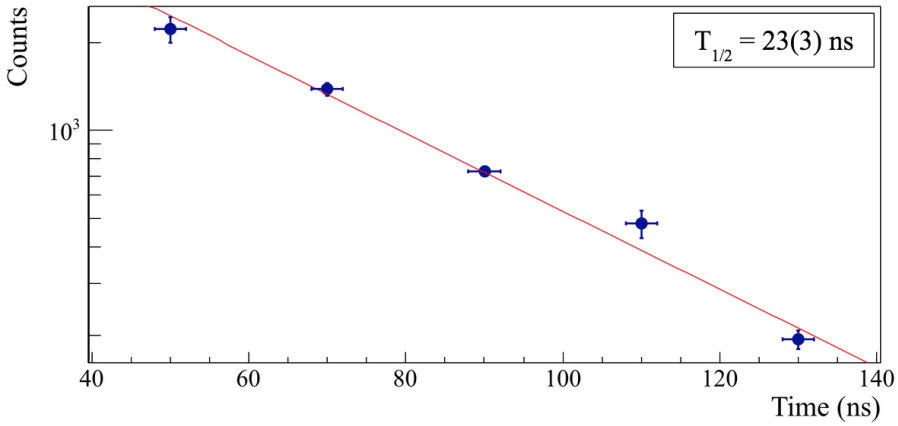

Figure 4.16: Number of coincidences observed between the 237 keV and 117 keV transitions in different time intervals. A fit to an exponential decay is used to estimate the half-life of the 354 keV state in ^{93}Kr.

Using the FIPPS data-set an estimation of the lifetime of an isomeric state in the range from 15 ns up to a few hundred ns is possible, based on the number of observed coincidences between transitions depopulating the isomeric state for different time intervals. This technique will be referred to as the *intensity balance technique* [137]. Using the number of coincidences measured between the 237 keV and 117 keV transitions in 20 ns time intervals in a range from 30 to 130 ns a preliminary value of 23(3) ns was obtained for the half-life of the (7/2+) state in ^{93}Kr (Fig. 4.16). This value is consistent with the value measured in β-decay studies [151], while it is not consistent with the value obtained

in fission studies [64]. The observation of the 237 keV transition in the AGATA-VAMOS++ data-set suggests indeed a shorter lifetime, consistent with the preliminary value measured in EXILL [152]. The disagreement with the value obtained in this thesis with the intensity balance technique is likely due to systematic errors in this kind of analysis when applied to low statistics channels.

4.1.4 Spectroscopy of ^{94}Kr

Moving further away from the valley of stability, less spectroscopic information is known on the neutron rich Kr isotopes. Before the start of this thesis project, only three excited states were known in ^{94}Kr. These excited states were populated following spontaneous fission of ^{248}Cm and measured using the EUROGAM2 array [62]. The three detected γ-rays were assigned to the (6+) $\rightarrow$ 4+ (1001 keV), 4+ $\rightarrow$ 2+ (854 keV) and 2+ $\rightarrow$ 0+ (666 keV) transitions, based on observed intensities and angular correlation measurements. Later on, the reduced transition probability $B(E2; 2+ \rightarrow 0+)$ was determined using Coulomb excitation at the REX-ISOLDE facility [70, 71]. In this work, the combination of the FIPPS data-set and the AGATA-VAMOS++ data was used to extend the known level scheme of ^{94}Kr with the identification of more than 13 new γ-ray transitions and 10 new excited states [153]. Parallel to this work similar results were obtained by the ν-ball collaboration using fast neutron induced fission of ^{238}U [154].

The ^{94}Kr γ-ray spectrum measured in AGATA is shown in Fig. 4.17. The most intense peaks correspond to the previously known 2+ $\rightarrow$ 0+ (665 keV), 4+ $\rightarrow$ 2+ (854 keV) and (6+) $\rightarrow$ 4+ (1001 keV) transitions (blue). An additional 8 newly observed γ rays were assigned to ^{94}Kr (red).

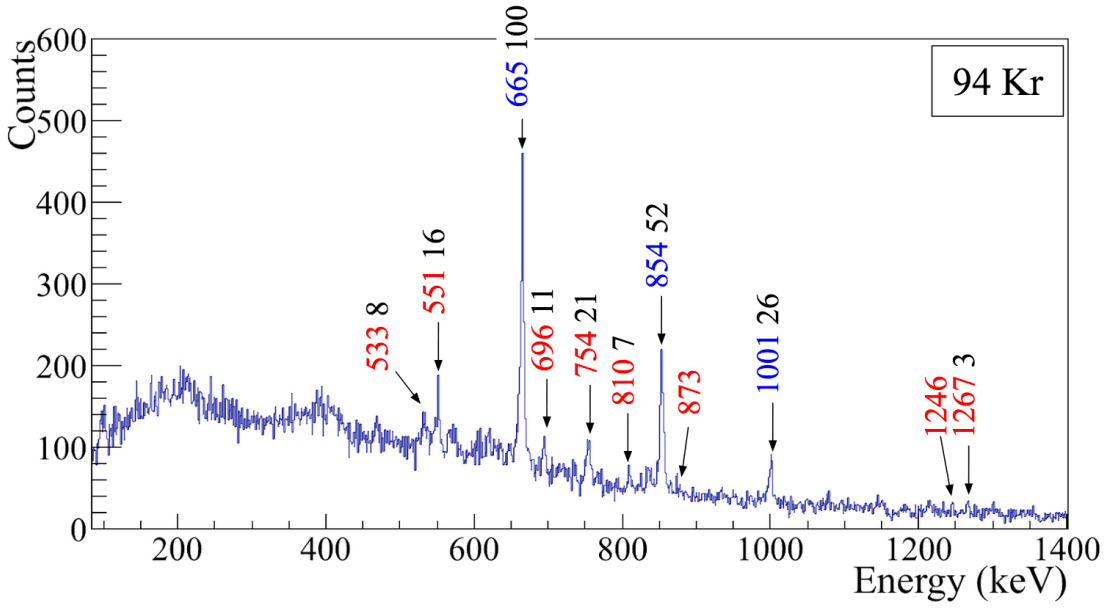

Figure 4.17: Doppler corrected prompt γ-ray spectrum measured in AGATA in coincidence with the ^{94}Kr ions detected in VAMOS++. Previously known transitions are marked in blue. Newly observed transitions are marked in red. Intensities relative to the 665 keV (2+ $\rightarrow$ 0+) transition are indicated in black.

An analysis of prompt transitions was performed using γ-γ-γ coincidences in the FIPPS data-set, with the purpose of placing the new transitions identified in the AGATA-VAMOS++ data and searching for additional transitions. The ^{94}Kr isotope, with a ^{235}U fission yield of 9.8×10^{-4}, was the most neutron rich Kr isotope that could be studied with the FIPPS data-set.

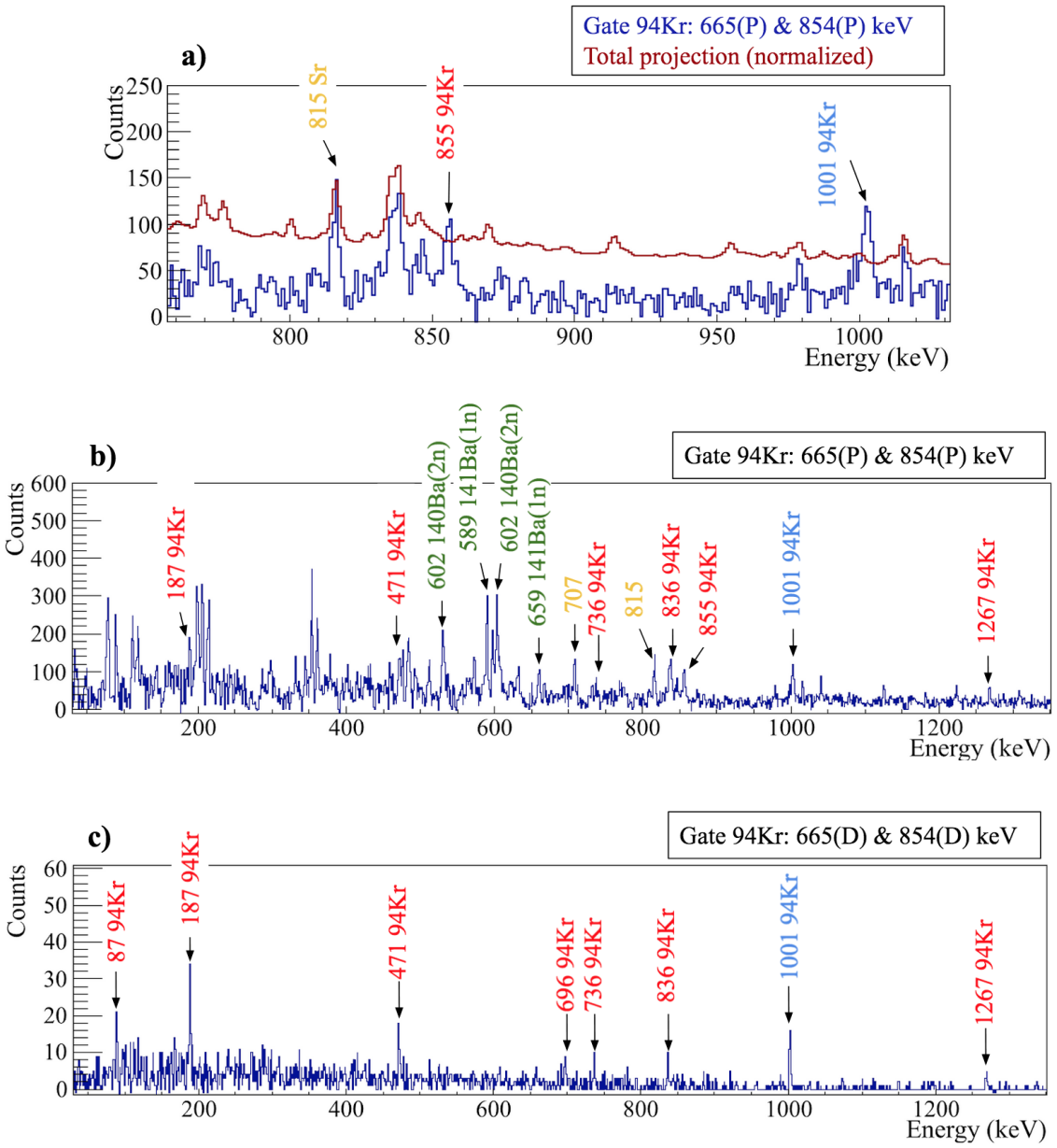

Figure 4.18: ^{94}Kr coincidence spectra obtained using the active target FIPPS data-set. The 1001 keV transition previously assigned to ^{94}Kr is marked in blue. New transitions assigned to ^{94}Kr are highlighted in red. Transitions from the Ba complementary fission partners are labelled in green while contaminant peaks are labelled in yellow. Prompt coincidences with the $2+ \rightarrow 0+$ (665 keV), $4+ \rightarrow 2+$ (854 keV) transitions are shown in a) b) for two different energy ranges. c) Delayed transitions observed in a 60-600 ns time window in coincidence with the 665 keV and 854 keV delayed transitions.

Due to its low fission yield, the FIPPS coincidence spectra show the presence of the strongest fission channels as contaminant transitions. In order to distinguish the contaminant peaks from those belonging to transitions in ^{94}Kr, a careful comparison between the coincidence spectra and the total projection was necessary. This method is illustrated in Fig. 4.18 a), which shows the prompt coincidence spectrum in a 700-1000 keV range obtained by gating on the 2+ $\rightarrow$ 0+ (665 keV) and 4+ $\rightarrow$ 2+ (854 keV) transitions. The most prominent peaks in this energy range correspond to the 815, 836, 855 and 1001 keV γ rays. The 1001 keV peak, known to belong to ^{94}Kr, is predominant with respect to the normalised total projection. The fact that the 855 keV transition dominates with respect to the total projection was used in combination with doubly gated spectra on the 855-854 keV to assign this γ ray to ^{94}Kr. Since the 855 keV transition is not seen in the coincidence spectrum gated on 854 and 1001 keV, it was placed populating the 4+ state at 1519 keV. This placement and energy is not consistent with the level scheme published by the $\nu-$ball collaboration, where a 852.9 keV transition is placed populating the (8+) 3356 keV state [154]. From a similar procedure, comparing gated spectra with the total projection, the assignment of the 836 keV to ^{94}Kr was not conclusive. This particular transition will be discussed later on, when the prompt-delayed analysis will be presented. The 815 keV transition is strongly seen in the total projection and was identified as a contaminant peak.

Fig. 4.18 b) shows the prompt coincidence spectrum doubly gated on the 665 and 854 keV transitions in a 100-1300 keV energy range. For clarity purposes the total projection is not superimposed, even though it was used to identify potential ^{94}Kr transitions. The most intense γ-ray transitions observed belong to the ^{141,142}Ba complementary fission partners. In addition to the previously known 1001 keV transition, 6 new γ-ray transitions were assigned to the ^{94}Kr isotope and placed in the level scheme. The 1267 keV transition was also observed in the AGATA data-set and was placed parallel to the 1001 keV transition.

A search for ns isomeric states in ^{94}Kr was performed by studying delayed coincidences in a 60-600 ns time window. Fig. 4.18 c) shows the transitions observed in delayed coincidence with the 665 and 854 keV transitions. In such a delayed spectrum, the fission partner transitions dominating the prompt coincidences (see 4.18 b)) as well as contaminant peaks disappear, extremely simplifying the spectrum. Triple delayed coincidences among these transitions were used to firmly assign them to ^{94}Kr and place them in a level scheme depopulating an isomeric state at 3445 keV. Similarly to the ^{93}Kr short lived isomeric state, the half-life of the 3445 keV state was determined using the number of coincidences between transitions resulting from the isomeric decay for different time intervals. A preliminary value of 38(6) ns was obtained (see Fig. 4.19). The fact that the 187 and 87 keV transitions were not measured in the AGATA array confirms that they depopulate the isomeric state. The presence of the 1001 keV and 1267 keV transitions in the AGATA-VAMOS++ data-set indicates that the levels that they depopulate can also be populated directly in the fission process or by decay paths that bypass the isomeric state.

Some of the prompt transitions assigned to the ^{94}Kr, were placed in the level scheme using γ-γ coincidences in the AGATA-VAMOS++ data-set. An example of a coincidence spectrum gated on the 551 keV transition is shown in Fig. 4.20. The 551 keV transition was found to be a part of a cascade of 874-696-551 keV transitions populating the 665 keV state. The order of these transitions was assigned

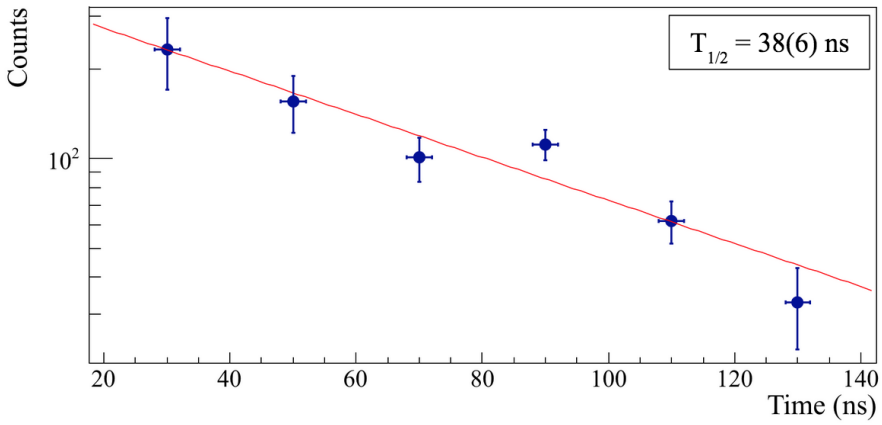

Figure 4.19: Number of coincidences observed between a series of delayed transitions (665, 854, 1267, 471 keV) in different time intervals. A fit to an exponential decay is used to estimate the half-life of the 3445 keV state in ^{94}Kr.

using intensity arguments. Due to low coincidence statistics in the 874 keV transition, the position in the level scheme is tentative. Only prompt coincidences between the 754 and 808 keV were observed, indicating that they could possibly populate the isomeric state.

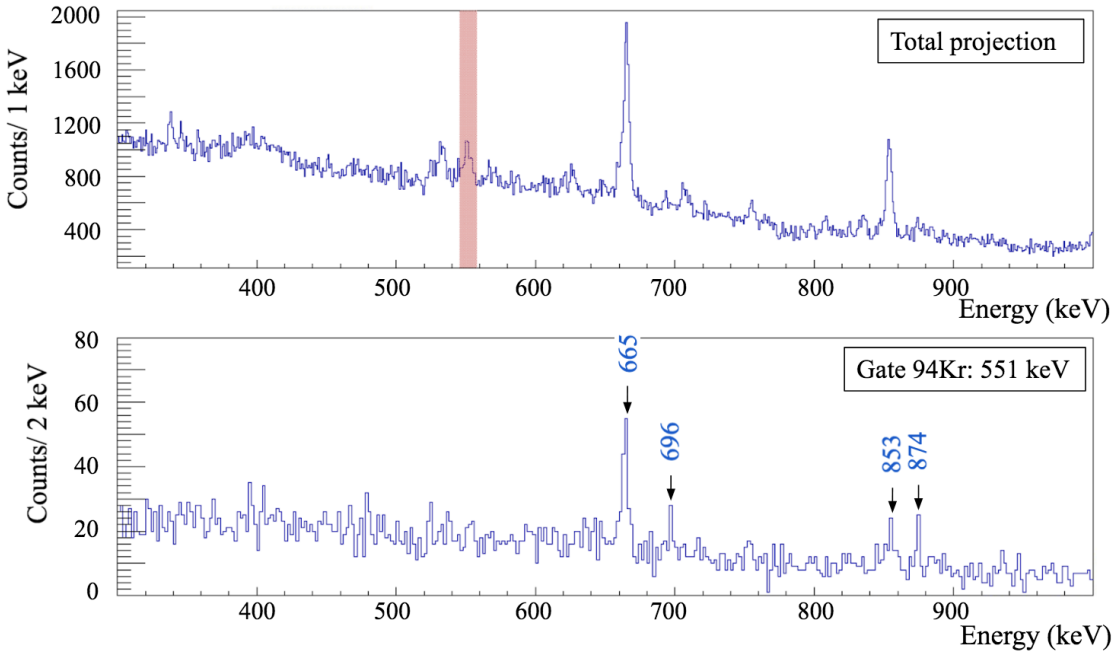

Figure 4.20: TOP: total projection of γ-γ matrix for ^{94}Kr constructed using the AGATA-VAMOS++ data-set. The applied energy gate on the 551 keV transition is shown in red. BOTTOM: coincidence spectra with the 551 keV transition in ^{94}Kr without a background substraction. The relative intensity of γ rays in true coincidence with the 551 keV transition (696 and 874 keV) increase with respect to dominant transitions in the total projection (665 and 853 keV).

The efficiency corrected intensities of all the transitions assigned to ^{94}Kr are reported in Table 4.5. The final level scheme obtained for ^{94}Kr in this work is shown in Fig. 4.21, where 13 new transitions and 10 new states were identified. With respect to recently published ^{94}Kr results obtained by the ν-ball collaboration [154], three additional transitions could be placed in the level scheme. Among these transitions worth mentioning is the 87 keV transition which could not be experimentally observed in the nuball experiment due to low detection efficiency in this energy range. The observation of the 87 keV transition, which depopulates the 3445 keV isomeric state allowed a determination of the branching ratio of this level. Spin and parity assignments to the newly observed levels could not be made using angular correlations because of limited statistics (see section 4.1.6). However tentative assignments can be made using a systematic study of excited states in neighbouring nuclei, which will be discussed in section 4.2.

Energy (keV)	**Intensity** (%)	$J_i \rightarrow J_f$	E_i **(keV)**	E_f **(keV)**	**Data-set**
87.4(3)*	8(3)	$(9-) \rightarrow (7-)$	3445	3356	F
186.9(2)*	15(5)	$(9-) \rightarrow (8+)$	3445	3257	F
471.0(2)*	11(2)	$(7-) \rightarrow (5,6+)$	3257	2786	F
551.2(4)*	16.2(14)	-	1216	665	A
665.4(2)	100.0	$2+ \rightarrow 0+$	665	0	F+A
696.2(5)*	11(1)	-	1911	1216	A
735.8(2)*	8(3)	$(7-) \rightarrow (6+)$			F
754.4(4)*	20.7(17)	-	4199	3445	A
809.6(5)*	7.3(7)	-	5009	4199	A
835.7(2)*	12(3)	$(8+) \rightarrow (6+)$	3356	2520	F
853.8(2)	52(5)	$2+ \rightarrow 0+$	1519	665	F+A
855.0(5)*(t)	8(3)	-	2375	1518	F+A
873.5(4)*(t)	< 5	-	2786	1911	A
1001.3(2)	26(2)	$2+ \rightarrow 0+$	2520	1519	F+A
1245.5(8)*	< 5	-	4690	3445	A
1267.2(2)*	3.6(5)	$(5,6+) \rightarrow 4+$	2786	1519	F+A
Unplaced transitions					
533.3(4)*	8.4(8)	-	-	-	A

Table 4.5: Properties of the γ-ray transitions assigned to ^{94}Kr in this work. Newly observed transitions are marked with (*). Tentative placements are indicated with (t). In the last column, information is given on whether they were observed in both the FIPPS and AGATA-VAMOS++ data-sets (F+A), only in the FIPPS data (F) or only in the AGATA-VAMOS++ data (A). Efficiency corrected intensity values are given relative to the strongest transition (665 keV). The reported intensities were obtained from the AGATA-VAMOS++ data, except for transitions observed only in the FIPPS data-set. The indicated spin and parity values of excited states were adopted from [154].

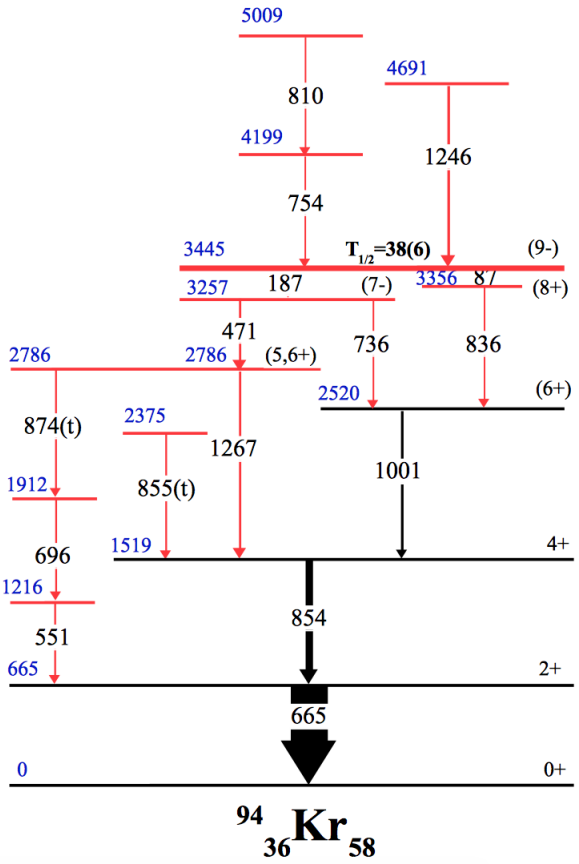

Figure 4.21: Level scheme of ^{94}Kr obtained in this work. Known transitions are shown in black and newly found transitions in red. The width of the arrows reflect the observed intensity in the FIPPS data-set. Spin and parity values are taken from [154].

4.1.5 Spectroscopy of ^{95}Kr

For the case of ^{95}Kr, only two transitions are known (with 82 keV and 114 keV energies). These two transitions were observed after the isomeric decay of its (7/2+) state with a half-life of 1.4 μs. The ^{95}Kr isotope was produced using thermal neutron induced fission of ^{241}Pu and studied using the LOHENGRIN instrument at the ILL [72].

A search of new transitions was carried out using the AGATA-VAMOS++ data-set. As previously discussed, in this setup the fission fragments decay in flight, moving away from the target position "seen" by the AGATA array. For this reason, only prompt transitions can be investigated. The ^{95}Kr isotope is at the limit of what could be studied in the AGATA-VAMOS++ experiment. In order to identify the γ rays emitted by the ^{95}Kr nucleus, a comparison of γ-ray spectra selecting the ^{95}Kr ions with more or less restrictive gates was performed. The comparison is shown in Fig. 4.22. Contaminant transitions from ^{94}Kr and ^{95}Rb were observed. A 735 keV transition appears even with more restrictive gates and can be tentatively assigned to ^{95}Kr.

In order to confirm this transition and identify new prompt transitions, a prompt-delayed-delayed cube was constructed using the FIPPS data-set. However, due to the low fission yield of the ^{95}Kr isotope (1×10^{-4} [147]) not enough statistics was available. The tentative level scheme obtained is shown in Fig. 4.23.

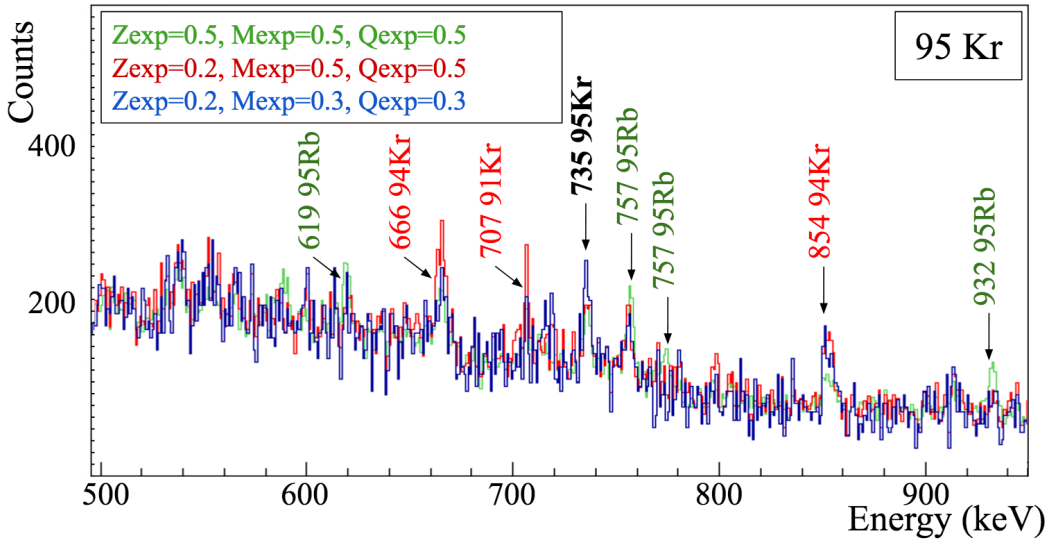

Figure 4.22: Doppler corrected prompt γ-ray spectra measured in AGATA in coincidence with the ^{95}Kr ions detected in VAMOS++. Three different gates were applied in order to distinguish contaminant transitions (marked in green and red) from γ rays emitted by the ^{95}Kr nucleus.

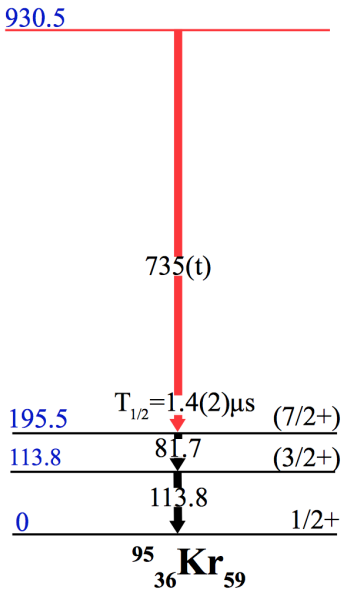

Figure 4.23: Level scheme of ^{95}Kr obtained in this work. The two previously known transitions are indicated in black. The newly identified prompt transition shown in red is tentatively placed (t) populating the isomeric state but could also populate the ground state. Spin and parity values are taken from [72].

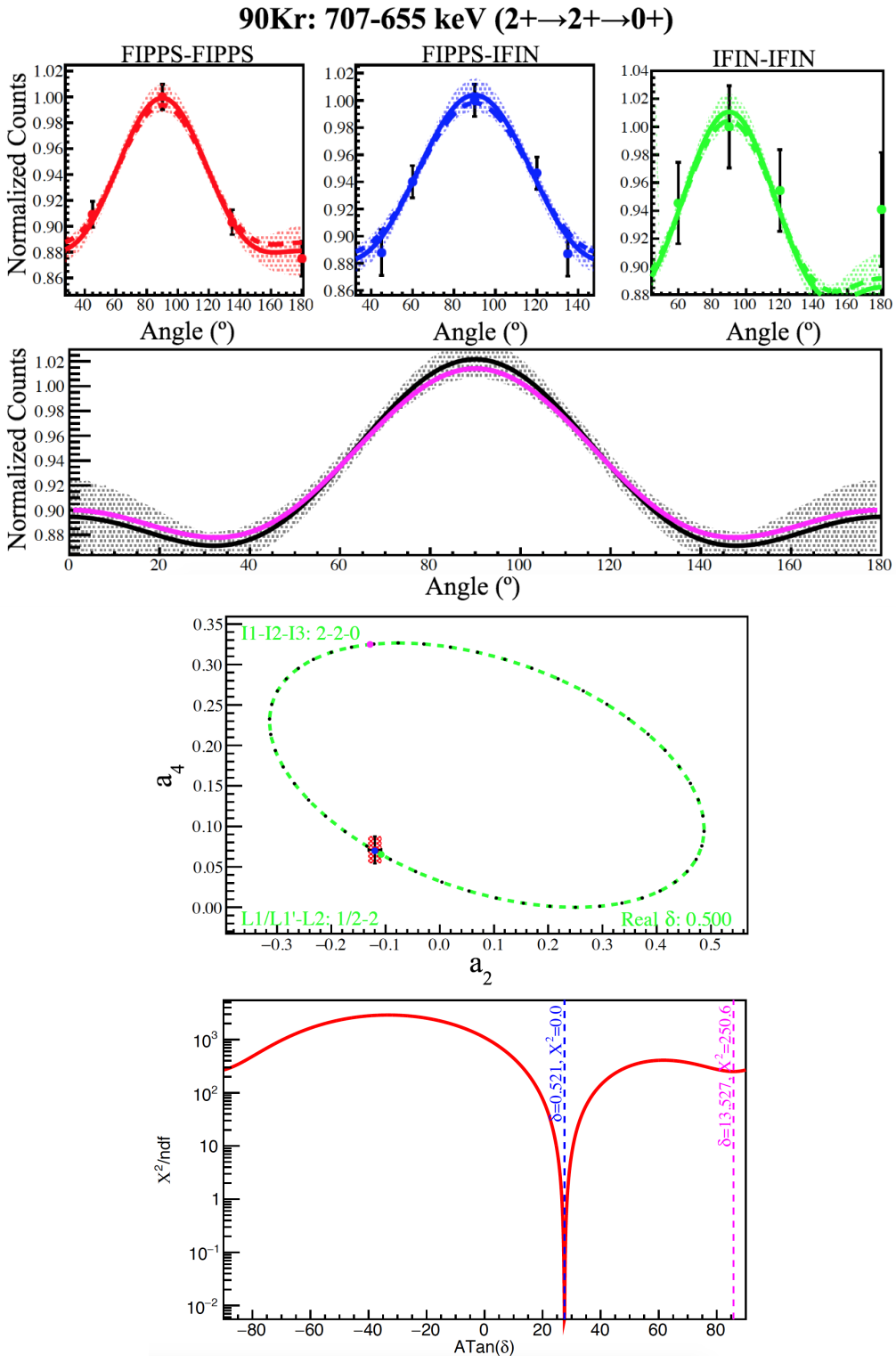

Figure 4.24: Angular correlations obtained for the $2+ \rightarrow 2+ \rightarrow 0+$ cascade in ^{90}Kr. The top panel shows the measured coincidences as a function of angle for all clover combinations. The resulting fitted curve is shown in black and compared to the theoretical function for a $2 \rightarrow 2 \rightarrow 0$ cascade (pink). The bottom panel shows the χ^2 analysis used to determine the mixing ratio δ for a spin hypothesis of $2 \rightarrow 2 \rightarrow 0$.

4.1.6 Angular correlation measurements

Angular correlation analysis was carried out in order to determine the spins of excited states in the studied neutron rich Kr isotopes, using the procedure detailed in section 3.3.2. As previously discussed, angular correlation measurements are strongly limited by statistics and proper background substraction, which makes angular correlation measurements in fission experiments particularly challenging. As a result, the angular correlation analysis of the Kr isotopic chain was used to confirm previously measured spins of the strongest cascades, but could not be employed to obtain new information.

The angular correlation analysis of the $2+ \rightarrow 2+ \rightarrow 0+$ cascade in ^{90}Kr is shown in Fig. 4.24. The fit to the three different clover combinations is shown, together with the overall angular correlation function obtained by combining the three. The experimental a_2 and a_4 values and mixing ratio δ obtained for the most intense cascades in ^{90,92,94}Kr are reported in Table 4.6. The coefficients as obtained in this work for cascades in ^{90,92}Kr are consistent with previously reported experimental values, supporting previous spin assignments. Statistics limitations in the $4 \rightarrow 2 \rightarrow 0$ cascade in ^{94}Kr resulted in large uncertainties in the coefficients.

	Cascade	$\gamma_1 - \gamma_2$ (keV)	$a_2(exp)$	$a_4(exp)$	$\delta(exp)$	$a_2(lit)$	$a_4(lit)$	$\delta(lit)$
^{90}Kr	$2 \rightarrow 2 \rightarrow 0$	707-665	-0.119(12)	0.071(17)	0.52(2)	-0.129(14)	0.090(27)	0.507(20)
^{90}Kr	$4 \rightarrow 2 \rightarrow 0$	707-1123	0.118(29)	-0.008(40)	0.1(1)	0.095(15)	-0.012(33)	0
^{92}Kr	$4 \rightarrow 2 \rightarrow 0$	768-1034	0.109(22)	-0.025(32)	1.59(3)	0.12(1)	0.03(1)	-
^{94}Kr	$4 \rightarrow 2 \rightarrow 0$	665-854	0.16(16)	-0.018(230)	-	-0.11(1)	0.09(3)	-

Table 4.6: Measured angular correlation coefficients of the most intense cascades in even-even neutron rich Kr isotopes. Latest published values are included for comparison and taken from [66, 62].

4.2 Discussion

The characterisation of nuclear properties in the $A \sim 100$ region, where the neutron rich krypton isotopes investigated in this work are located, presents a challenge to state-of-the-art nuclear models. The neutron rich krypton isotopes of interest ($^{90-95}$Kr) have eight valence protons filling the $\pi 1f_{5/2}$, $\pi 2p_{3/2}$, $\pi 2p_{1/2}$ and $\pi 1g_{9/2}$ Shell Model orbitals. The valence neutrons occupy the $\nu 2d_{5/2}$, $\nu 3s_{1/2}$, $\nu 1g_{7/2}$, and $\nu 2d_{3/2}$ orbitals. The structure of ^{90,91}Kr was recently investigated using Large-Scale Shell Model calculations [66]. Nonetheless, the more neutron rich Kr isotopes studied in this work remain out of reach for this type of calculations. Different theoretical approaches have been used to describe the krypton isotopic chain in the past decades, mostly using beyond mean field methods [70, 44, 155, 156, 157]. However these same calculations have not been able to reproduce the drastic shape change at $N = 60$ observed in the Zr and Sr neighbouring chains. Recently, a first microscopic description of the rapid onset of collectively in the Zr isotopes was achieved using the Monte Carlo Shell Model [21, 24]. MCSM calculations for the Kr and Sr chains will be crucial to explain the difference of behaviour, in terms of shape evolution, in the Kr chain compared to the Sr and Zr chains (see Fig. 1.5).

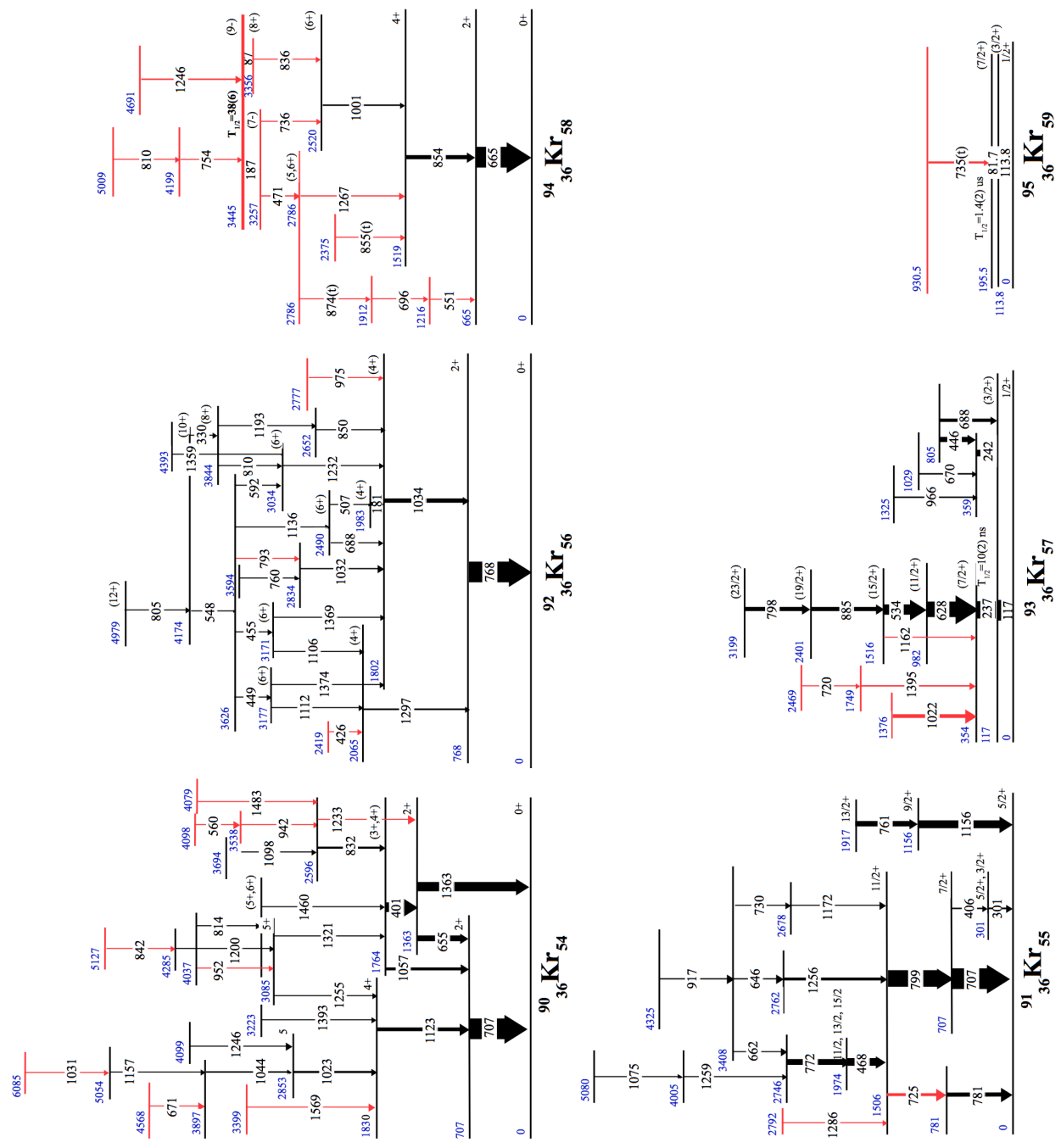

Figure 4.25: Level schemes of $^{90-95}$Kr isotopes obtained in this work. Previously known transitions are indicated in black while newly found transitions are shown in red. The observed intensities are reflected in the width of the arrows. Transitions indicated with (t) are tentatively placed. Spin and parity values are taken from [62, 72, 64, 154]. Half-lives in ^{93,95}Kr are adopted from [64, 72], while in the ^{94}Kr case the value measured in this work is given.

Despite the current limitations of available theoretical approaches, insight into the nature of nuclear states in neutron rich krypton isotopes could still be gained in this thesis through the comparison of experimental data with available theoretical predictions. In addition, a systematic study of the energies and spin parity values of excited states in the Kr ($Z = 36$) chain, as well as neighbouring Sr ($Z = 38$) and Zr ($Z = 40$) chains will be conducted. In order to facilitate the discussion, the spectroscopic results obtained in this work are summarised in the level schemes of $^{90-95}$Kr isotopes shown in Fig. 4.25.

For the case of the even-mass krypton isotopes, a smooth evolution of the excitation energy of the 2_1+ and 4_1+ states can be seen in the level schemes of ^{90,92,94}Kr. This information is complemented with published values of excitation energies of the yrast band in other even-even krypton isotopes and plotted in Fig. 4.26. After a sharp decrease when going from a closed shell at $N = 50$ to $N = 52$, the 2_1+ energy remains constant for $^{88-94}$Kr ($52 \leq N \leq 58$). The gradual decrease of the 2_1+ energy observed in $^{96-100}$Kr indicates a smooth increase of collectivity for $N \geq 60$, in contrast to other nuclei in the $A \sim 100$ region. This interpretation is confirmed by the increase of the $B(E2; 2+ \rightarrow 0+)$ values reported in Fig. 4.26. However, the measured $R_{4/2}$ show a contradictory trend, which is still unresolved. The shape evolution in the neutron rich Kr isotopes, that can be deduced from spectroscopic information, was first experimentally established in measurements of charge radii [158] and later on by mass measurements [69]. From a theoretical point of view, the early Nilsson-Strutinksy calculations [159] pointed towards a gradual transition from spherical to deformed nuclei in $^{88-94}$Kr. The latest Hartree-Fock-Bogoliubov (HFB) calculations based on the Gogny-D1M [156], predict a smooth evolution in $^{86-94}$Kr shapes from nearly spherical to γ-soft, up to a γ-soft oblate minimum in ^{94}Kr. A prolate-oblate shape coexistence is predicted for $^{96-100}$Kr by the same model.

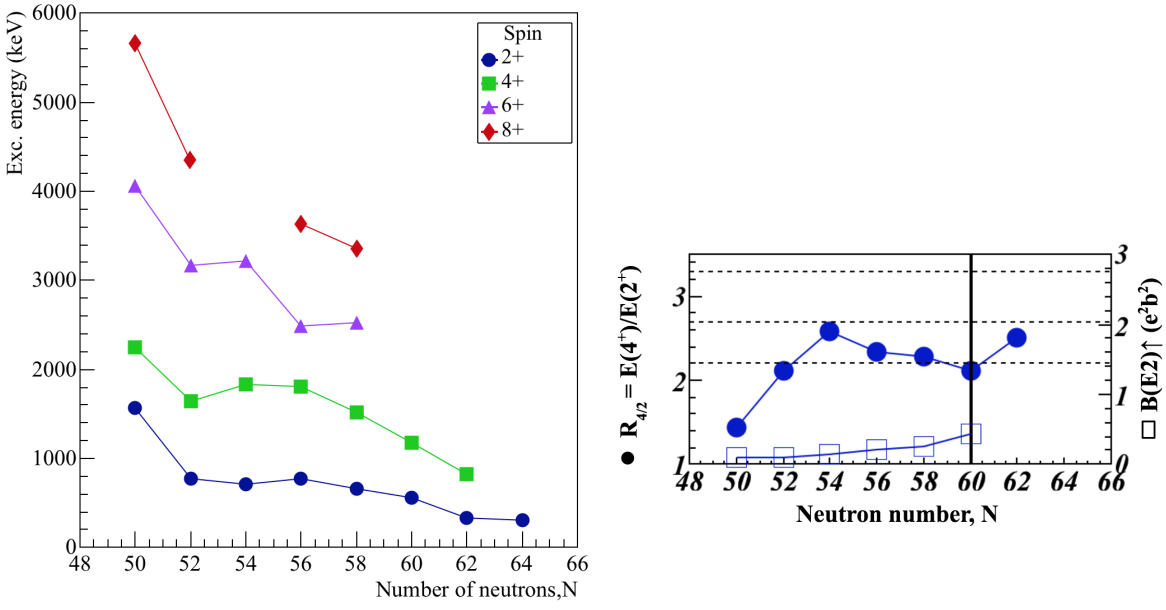

Figure 4.26: Systematics in even-even Kr isotopes. LEFT: Energies of the yrast band as a function of neutron number. RIGHT: Ratio of the excitation energies of the 4+ and 2+ states and reduced transition probabilities ($B(E2) \uparrow$).

Going higher in excitation energy, the nature of the ^{94}Kr isomeric state at 3445 keV is of special interest. In this work a preliminary half-life of 38(6) ns was obtained using the number of coincidences between γ-ray transitions depopulating the isomer for different delayed time windows. The obtained value is consistent with the 32(3) ns half-life measure by the ν-ball collaboration [154]. In this publication a tentative spin and parity of (9-) was assigned to this state in $^{94}_{36}Kr_{58}$ based on the existence of known isomers with similar characteristics in the neighbouring $N = 58$ Se [160] and Sr [161] nuclei. The $^{92}_{34}Se_{58}$ was found to have a 9- isomeric state at 3072 keV excitation energy with a half-life of 15.7(7) μs. In $^{96}_{38}Sr_{58}$ the 9- isomeric state has a half-life of 40(8) ns and an excitation energy of 3523 keV . These 9- states were interpreted as originating from the $\nu[(g_{7/2}h_{11/2})]_{9-}$ coupling in the spherical ^{96}Sr nucleus and a two neutron quasi particle configuration 9-($\nu 7/2 + [404]11/2 - [404]$) in a oblate deformed ^{92}Se. In this case, the Nilsson orbitals were obtained using Hartree-Fock-Bogoliubov (CHFB) calculations with the Gogny D1S interaction [44]. A plot of the neutron orbitals obtained with the same calculation for the case of the ^{94}Kr isotope is shown in Fig. 4.27. In ^{92}Se the 9- state was observed to decay to a 7- state via an E2 transition of 67 keV. Assuming a similar behaviour in ^{94}Kr, an E2 character can be assigned to the 187 keV transition depopulating the 9- isomer [154]. This results in a reduced transition probability of $B(E2) = 1.6(5)$ W.u. [1]. This value is consistent with the previously published value ($B(E2) = 1.8(5)$ W.u.) [154], and supports the single particle interpretation of the isomeric state at 3445 keV, whose decay can be explained by a transition of a neutron from the 7/2+[404] to the 3/2+[402] Nilsson orbital.

For the case of the odd-mass ^{91,93,95}Kr isotopes, a lower number of excited states could be experimentally observed, with respect to the neighbouring even-even Kr isotopes. This is a consequence of lower fission yields, but also of a higher fragmentation of the γ strength in the level schemes (see Fig. 4.25). The ^{91,93,95}Kr isotopes present very different structure, despite occupying the same neutron orbitals in the context of the spherical shell model. The most striking difference is the change of ground state spin value, which has been firmly established in laser spectroscopy measurements [158]. The change takes place when going from $N = 55$ to $N = 57$, from a 5/2+ to a 1/2+ ground state. This same change is also observed in the Zr and Sr chains. A possible explanation for this change of ground state is a reordering of the single particle orbitals with small changes of deformation, as can be seen from Fig. 4.28.

From a theoretical point of view, the nuclear structure of odd mass nuclei in this mid shell region is more complex to investigate. The reason behind the complexity is the need to take into account both single particle and collective behaviours. A first theoretical study of the ground state and first excited states properties of odd mass krypton isotopes has been recently conducted, within the framework of the interacting boson-fermion model (IBFM) based on the Gogny-D1M energy density functional (EDF) [157]. These calculations were able to reproduce the change of ground state spin, as can be seen from Fig. 4.29, showing a comparison of experimental and theoretical excitation energies. The wave function for the ground state of ^{91}Kr was found to be mainly composed of the $\nu 2d_{5/2}$ configuration.

[1] W.u. stands for "Weisskopf units", which provide an estimation of the single particle transition probability for each multipolarity [162, 26].

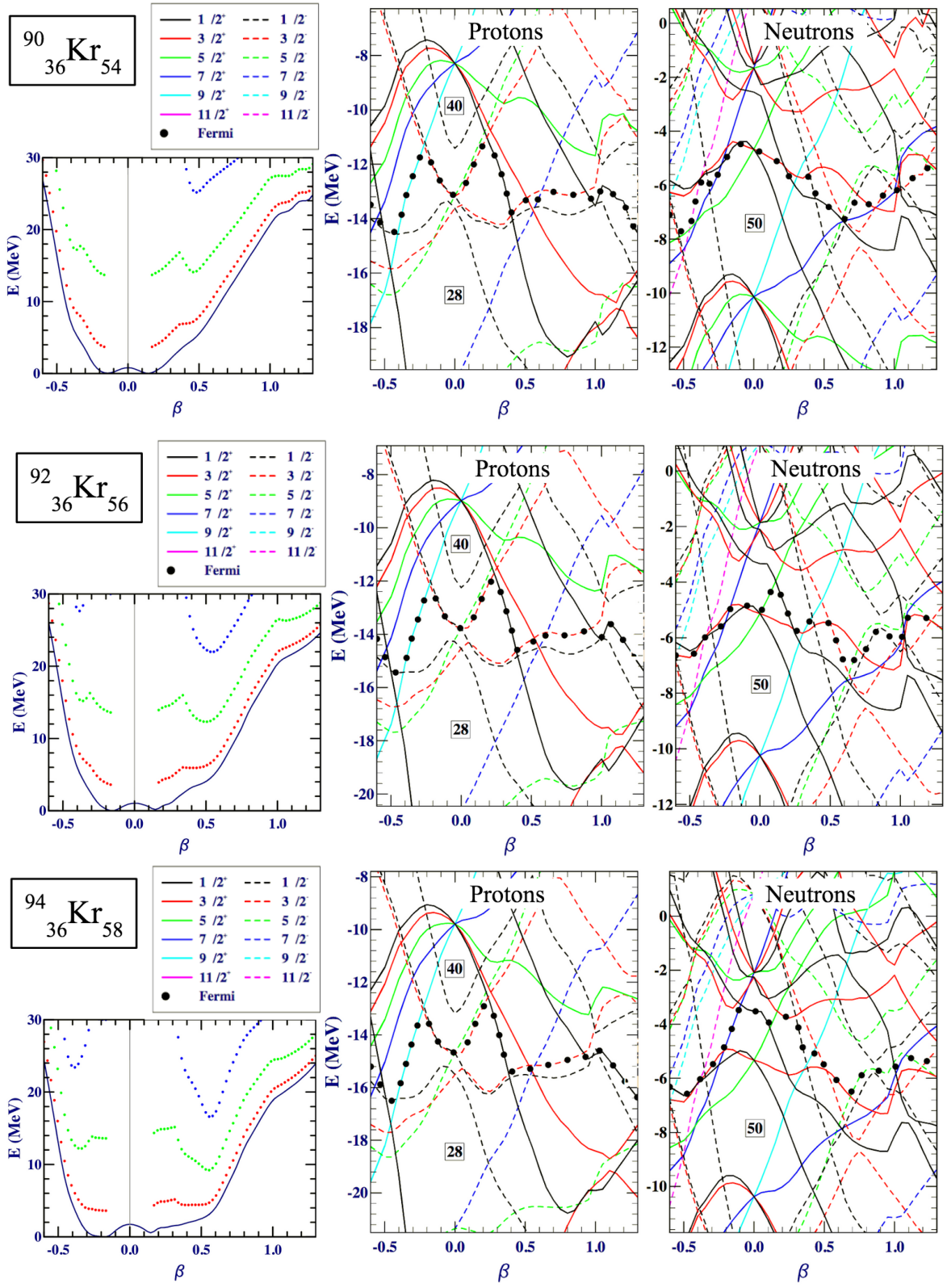

Figure 4.27: Potential energy plots and single-particle orbitals obtained by Hartree-Fock-Bogoliubov calculations based on the Gogny force for the even-even Kr isotopes studied in this work. Adapted from [43].

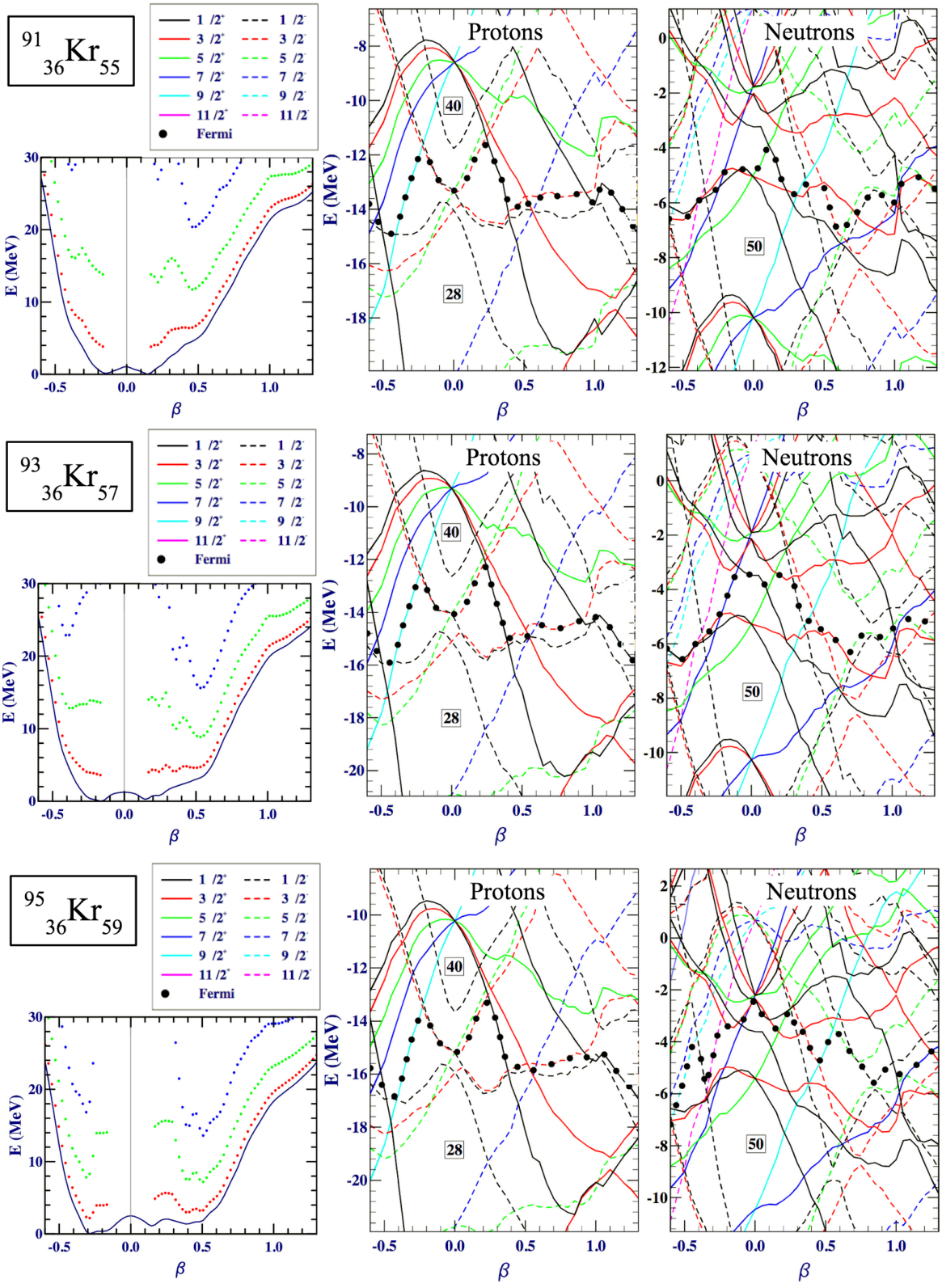

Figure 4.28: Potential energy plots and single-particle orbitals obtained by Hartree-Fock-Bogoliubov calculations based on the Gogny force for the even-odd Kr isotopes studied in this work. Adapted from [43].

In contrast, the ground state wave function in ^{93,95}Kr was composed of a mixture of the $\nu 2d_{3/2}(\approx 50\%)$ and $\nu 2d_{5/2}(\approx 30\%)$ configurations. Concerning the evolution of deformation in the odd-mass Kr isotopes, the above mentioned theoretical study revealed a gradual increase of collectivity, consistent with results in even-even Kr isotopes.

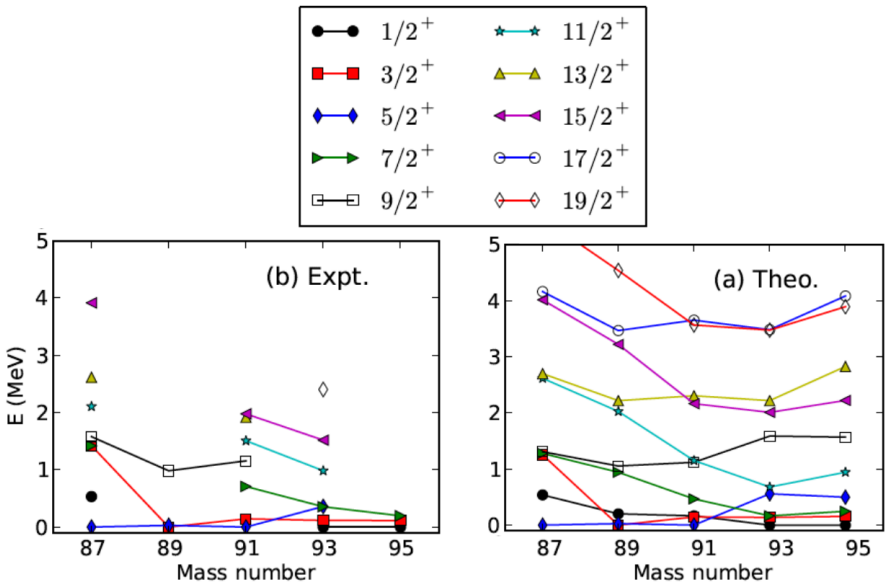

Figure 4.29: Comparison of experimental and theoretical values of excitation energies in odd-mass Kr isotopes as a function of mass number. Theoretical predictions were obtained in the framework of the the interacting boson-fermion model based on the Gogny-D1M energy density functional, adapted from [157].

Both ^{93}Kr and ^{95}Kr present a 7/2+ isomeric state at low excitation energy. Similar isomeric states have been identified in neighbouring Zr and Sr isotopes and attributed to single neutron excitations to the $g_{7/2}$ orbital [72]. Partial level schemes of the Zr, Sr and Kr isotopes of interest are shown for the $N = 57$ and $N = 59$ isotonic chains in Fig. 4.30. A constant excitation energy is observed for the 7/2+ state in the $N = 59$ chain, in contrast to the decreasing trend exhibited by the $N = 57$ isotones. A possible explanation is the change in energy of the $\nu g_{7/2}$ orbit as a function of deformation. Concerning transition probabilities, for the $N = 57$ isotopes B(E2) values of 1.55(5), 2.64(6) and 2.9(6) W.u. were obtained for ^{97}Zr, ^{95}Sr, and ^{93}Kr respectively. For the case of the ^{93}Kr, the B(E2) value of 2.9(6) W.u. was calculated using the latest published half-life of 10(2) ns. For the $N = 59$ isotopes B(E2) values of 1.33(5), 1.75(10) and 1.47(27) W.u. were obtained for ^{99}Zr, ^{97}Sr, and ^{95}Kr [72]. The similar values obtained for transition probabilities support the hypothesis of similar nature for the corresponding isomeric 7/2+ states.

Conclusion

The combination of the FIPPS and AGATA-VAMOS++ data-sets resulted in the observation of new γ-ray transitions in neutron rich $^{90-95}$Kr. The new transitions were placed in the level schemes using γ-ray coincidence techniques. The known level scheme of ^{94}Kr was significantly extended. The

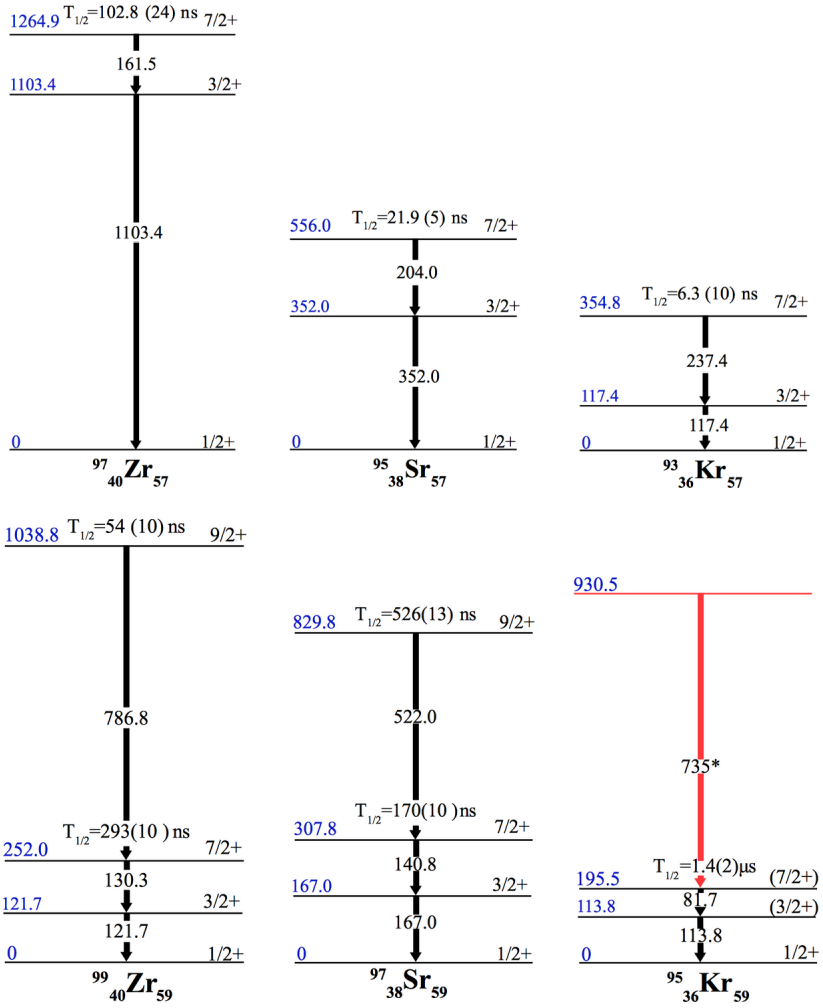

Figure 4.30: Partial level schemes showing isomeric states populated in fission for $N = 57$ and $N = 59$ isotones in the ^{93,95}Kr region. Adapted from [72].

timing information provided by the active fission target was exploited to investigate structure across isomeric states in ^{93,94}Kr. The selectivity of the VAMOS++ spectrometer allowed a tentative placement of a new transition in the highly neutron rich ^{95}Kr isotope.

Both experimental measurements of low lying excited states and theoretical predictions point towards a smooth evolution of nuclear shape in the $^{90-95}$Kr isotopes. The interpretation of high energy excited states newly observed in this work, is quite difficult due to the lack of theoretical predictions. Further insight will be provided by spin-parity measurements and lifetime measurements. Nevertheless, the experimental results achieved in this work can be used to benchmark future theoretical calculations. The microscopic explanation of isomeric states in the Kr region also remains a challenge. Future MCSM calculations could eventually determine the nature of the observed isomeric states and give a microscopic interpretation to the evolution of shape in the Kr chain.

CHAPTER 5

γ-ray spectroscopy of neutron rich Br isotopes

Contents

In this chapter, the results found on the spectroscopy of odd-mass neutron rich bromine isotopes $^{87-93}$Br will be reported. These bromine isotopes are located in the vicinity of the doubly magic nucleus $^{78}_{28}Ni_{50}$, which has been the subject of numerous theoretical studies in recent years (section 1.3). The odd-mass Br isotopes studied in this work, situated just above the $N = 50$ shell closure, provide an ideal testing ground for Large Scale Shell Model calculations. Of particular interest in odd-mass nuclei in this region is the evolution of the 9/2+ state, associated to a proton excitation to the $\pi g_{9/2}$ orbital [163, 79]. From an experimental point of view, these nuclei are difficult to access due to low production yields in the nuclear reactions typically used in the past. This has resulted in a lack of experimental information of excited states in $^{87-93}$Br, which were mostly unknown before this work.

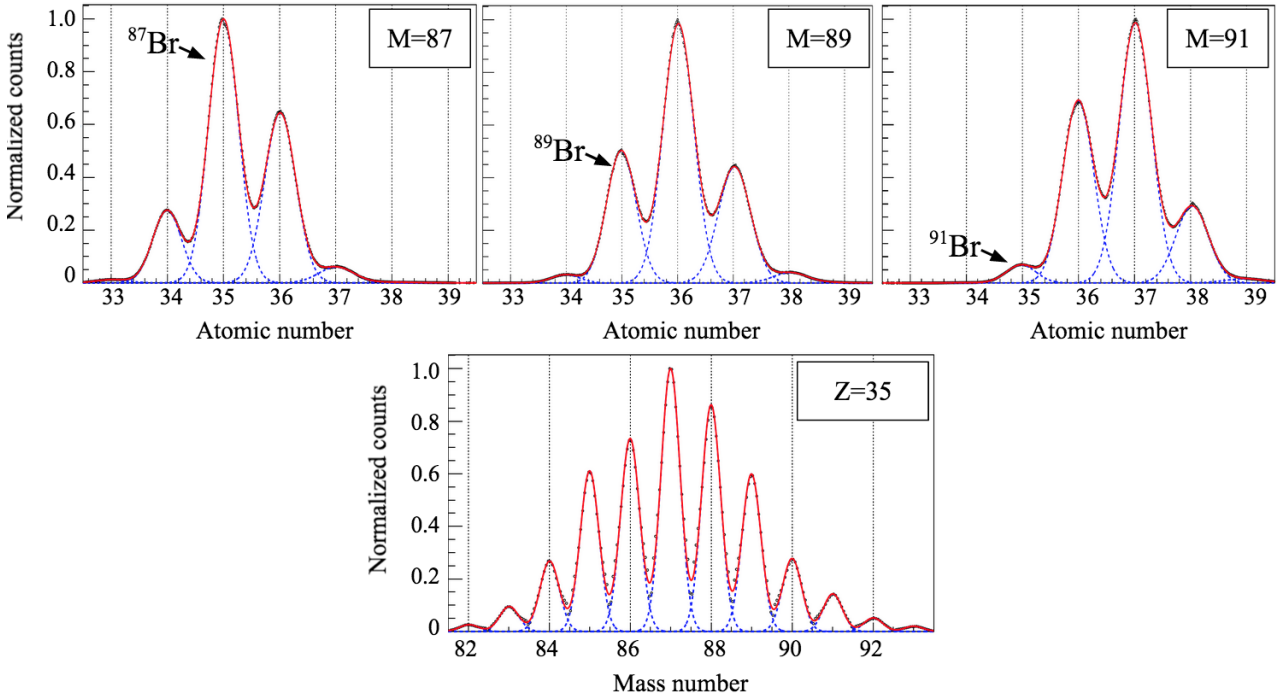

Figure 5.1: Normalised atomic and mass distributions obtained with VAMOS++, in the region of the Br isotopes studied in this work. The distributions are normalised to the maximum value [132].

The neutron rich Br isotopes of interest were produced using two complementary fission experiments, as described in section 2.4. Firstly, the AGATA-VAMOS++ setup was used in combination with beam induced fission of ^{238}U on ^{9}Be to study the neutron rich fission fragments of interest. The isotopic selection provided by VAMOS++ was used to identify the Br fission fragments detected in coincidence with the measured γ rays in the AGATA array. The quality of the isotopic and mass separation along with the normalised production yields of the bromine isotopes studied are illustrated in Fig. 5.2. The isotopic separation was of particular importance for the cases of ^{89,91,93}Br where no spectroscopic information was previously known. For the cases with enough statistics, γ-γ coincidences in a 200 ns time window were used to construct level schemes of the corresponding Br nuclei.

As for the case of the Kr isotopes, the AGATA-VAMOS++ data-set was complemented with the data collected at the ILL during the FIPPS fission campaign, detailed in section 2.3. The ^{235}U(n,f)

reaction used during the campaign provides high fission yields in the Br region of interest (see Fig. 5.2). The high statistics of the FIPPS data-set was exploited to construct level schemes of neutron rich Br isotopes based on triple γ-ray coincidences. Both known transitions in the Br chain and transitions in the $^{143-148}$La complementary fragments, extensively studied after fission reactions [164, 165, 166, 167], were employed. The simulated Br-La fission partner distributions, shown in Fig. 5.3, were used to determine the most probable complementary fragment in each case. γ-ray transitions belonging to ^{91,93}Br were not accessible in the FIPPS data-set due to low fission yields and *"fragmented level schemes"* typical of odd-mass nuclei [1].

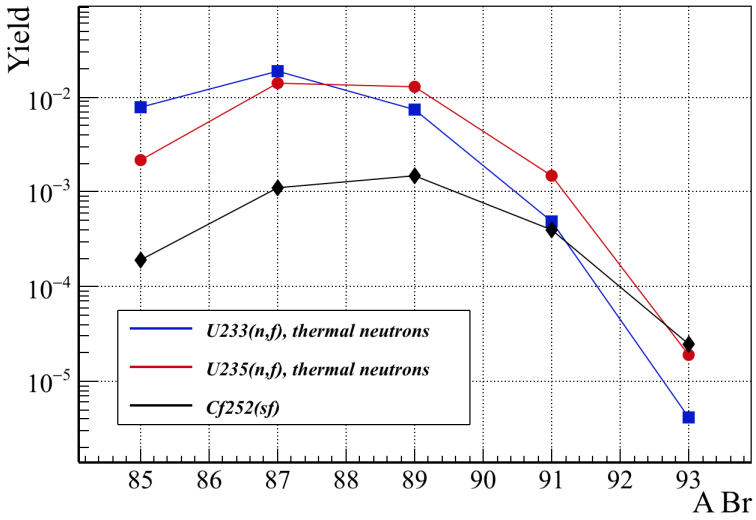

Figure 5.2: Fission yields of odd mass Br isotopes for different fissioning systems, including neutron induced fission and spontaneous fission. Values taken from [7, 147].

The following sections of this chapter will present the new spectroscopic information obtained by combining the FIPPS and the AGATA-VAMOS++ data for each of the neutron rich Br isotopes of interest. A study of excited states in ^{85}Br is included as a "test case". New transitions were added to complete the level scheme of ^{87}Br while for the case of ^{89,91,93}Br all information is new. A study of the systematics of excited states in the Br chain as well as neighbouring nuclei enabled tentative spin parity assignments and an interpretation of the observed excitations, which will be discussed in 5.2. Finally, a comparison of the experimental results with preliminary Large Scale Shell Model calculations is presented.

[1] In odd-mass nuclei the multitude of excited states give rise to different decay paths, in contrast to even-even nuclei where the γ-decay intensity is concentrated in the yrast $2J+$ band.

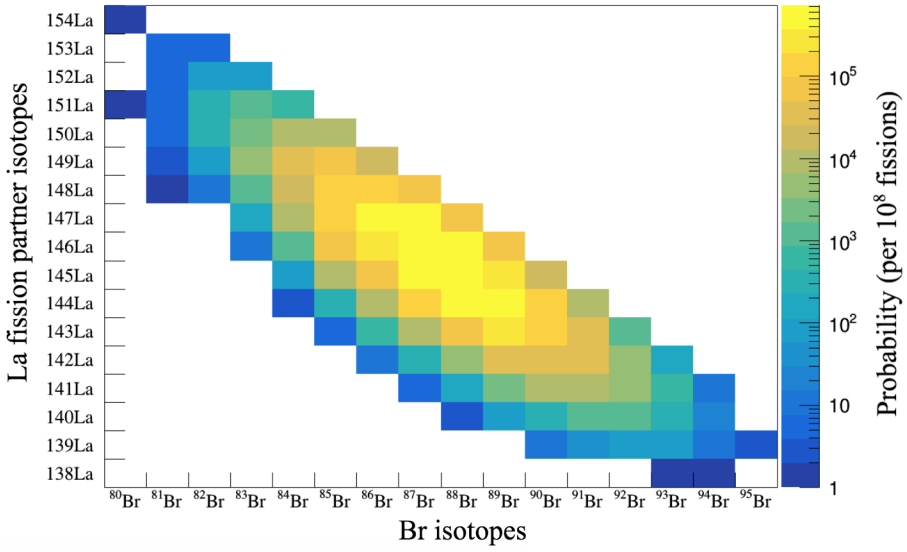

Figure 5.3: Br-La fission yields for thermal neutron induced fission of ^{235}U. Values were obtained simulating 10^8 fission events with the GEF code [136].

5.1 Experimental results

5.1.1 Spectroscopy of ^{85}Br,"test case"

Situated at the the $N = 50$ shell closure, the ^{85}Br isotope has been studied after β-decay [168] and more recently after fusion-fission reactions [81, 80]. Even though no new transitions could be observed in this work, the γ spectroscopy analysis of ^{85}Br is included as a "test case". The obtained level scheme was used to validate previously known information and to facilitate a comparison with neutron rich Br isotopes with $N > 50$. In addition, coincidence spectra produced with the FIPPS data are included to discuss the limitations of using the cross coincidence method for low yield nuclei with highly fragmented level schemes.

Excited states in ^{85}Br were investigated in the FIPPS data-set using γ-γ-γ coincidences. Due to a low fission yield (2.2×10^{-3}), only the most intense transitions were observed. Examples of coincidence spectra doubly gated on known intense transitions in ^{85}Br are shown in Fig. 5.4. Transitions belonging to ^{85}Br can be seen in the coincidence spectra, and are labelled in blue. As already introduced in section 3.1.1, when analysing coincidence spectra of nuclei with a low fission yield, such as the ^{85}Br (yield=2.2×10^{-3}), contaminant transitions from nuclei with higher fission yields and similar γ-ray energies are present in the gated spectra. For this case, contaminant transitions are observed belonging to ^{143}Ba (yield=4×10^{-2}) and ^{96}Sr (yield=3.9×10^{-2}), and are labelled in yellow. Transitions emitted by the lanthanum fission partners are expected to be seen in prompt coincidence with the bromine transitions. The γ-γ-γ coincidence spectrum gated on the ^{85}Br 345-1227 keV transitions shows the 167 keV and 212 keV from the ^{147}La fission partner. However, these transitions are not seen in the 1227 keV and 1161 keV gate. This is explained by the presence of a 346 keV transition in ^{147}Ba,

enhancing its contribution to the spectrum. The fact that in the 1227-1161 keV gate, transitions that have been firmly established to belong to the ^{85}Br isotope, no significant peaks belonging to any of the fission partners can be seen shows the problematic appearing in odd-odd and odd-even isotopes with highly fragmented level schemes. Consequently, new transitions cannot be confirmed by the presence of fission partner lines. The cross coincidence method, which has been used in the past in fission experiments to identify the strongest γ-ray transitions in a nucleus with no previous known information, will be limited in the case of the odd-mass Br isotopes.

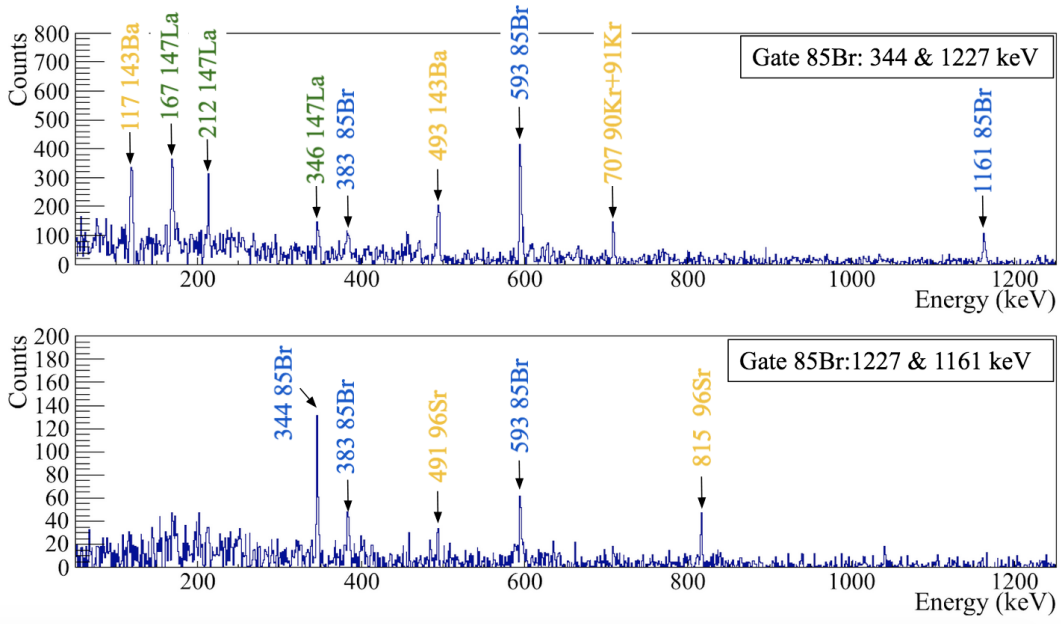

Figure 5.4: Doubly gated spectra on known transitions from ^{85}Br obtained with FIPPS active target data. Known transitions belonging to ^{85}Br are marked in blue, transitions from the ^{147}La fission partner are marked in green. Contaminant transitions are indicated in yellow.

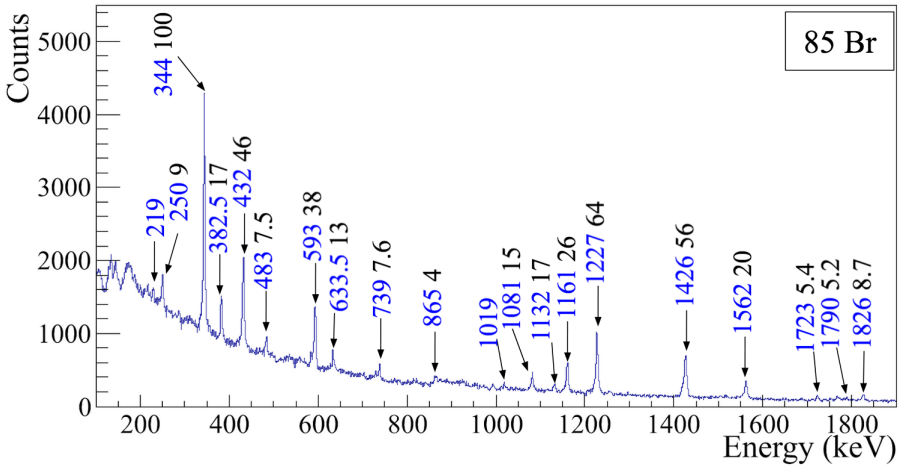

Figure 5.5: Doppler corrected γ-ray spectrum obtained for ^{85}Br in the AGATA-VAMOS++ experiment. All transitions were previously observed in [80]. Intensities relative to the strongest transition are shown in black.

The FIPPS data were complemented with the AGATA-VAMOS++ data-set. The Doppler corrected γ-ray transitions observed in AGATA in coincidence with the ^{85}Br fission fragment identified in VAMOS++ are shown in Fig. 5.5. A total of 20 γ-ray transitions were observed and are reported in Table 5.1. For the ^{85}Br isotope (and all other Br isotopes), the intensity values are calculated relative to the strongest transition and using the measured number of counts in the AGATA-VAMOS++ data-set. The number of counts are corrected for efficiency values using the efficiency curve presented in section 2.4. Differently from the Kr case, the intensities extracted from the AGATA-VAMOS++ data are considered for the construction of the Br level schemes, instead of the measured intensities from the FIPPS data-set due to statistics limitations.

Energy (keV)	**Intensity** (%)	$J_i \rightarrow J_f$	E_i **(keV)**	E_f **(keV)**	**Data-Set**
219.0(5)	<5	(17/2+) → (17/2+)	4658	4439	A
250.2(4)	9.1(8)	(19/2+) → (17/2+)	4908	250	A
344.4(2)	100	5/2− → 3/2−	344	0	F+A
382.6(2)	17(2)	15/2(−) → 3/2(−)	3707	3325	F+A
432.2(3)	46(4)	9/2+ → 7/2−	1859	1427	F+A
483.5(4)	7.5(7)	(21/2−) → (19/2+)	5391	4908	A
593.4(2)	38(3)	11/2− → 9/2−	2164	1571	F+A
633.8(4)	13(1)	(17/2−) → 9/2−	4341	3707	A
738.8(2)	7.6(7)	11/2− → 7/2−	2164	1427	F+A
865.0(4)	4.0(4)	(15/2+) → (11/2+)	3856	2991	A
1019.0(4)	<5	(17/2+) → (13/2+)	4439	3420	A
1081.9(2)	15(1)	7/2− → 3/2−	1427	344	F+A
1132.0(4)	17(2)	11/2(+) → 9/2+	2991	1859	A
1160.8(2)	26(2)	13/2(−) → 11/2−	3325	2164	F+A
1227.4(2)	64(5)	9/2− → 5/2−	1571	344	F+A
1419.0(4)	7(2)	11/2(+) → 9/2−	2991	1571	A
1427.2(2)	56(4)	9/2− → 5/2−	1427	0	F+A
1562.4(3)	20(2)	(13/2+) → 9/2+	3420	1859	F+A
1790.0(4)	5.2(6)	-	3954	2164	A
1826.2(4)	8.7(9)	(13/2+) → 9/2+	3685	1859	A

Table 5.1: Properties of the γ-ray transitions assigned to ^{85}Br in this work. In the last column, information is given on whether they were observed in both the FIPPS and AGATA-VAMOS++ data-sets (F+A) or only in the AGATA-VAMOS++ data (A). Efficiency corrected intensity values are given relative to the strongest transition (344.4 keV). The reported intensities were obtained from the AGATA-VAMOS++ data. The indicated spin and parity values of excited states were adopted from [80].

Fig. 5.6 shows the final level scheme obtained for ^{85}Br in this work, compared with the results obtained in fusion-fission experiments [80]. Although low lying γ-ray transitions and their intensities are consistent with previous results, some high excitation transitions could not be confirmed due to low statistics.

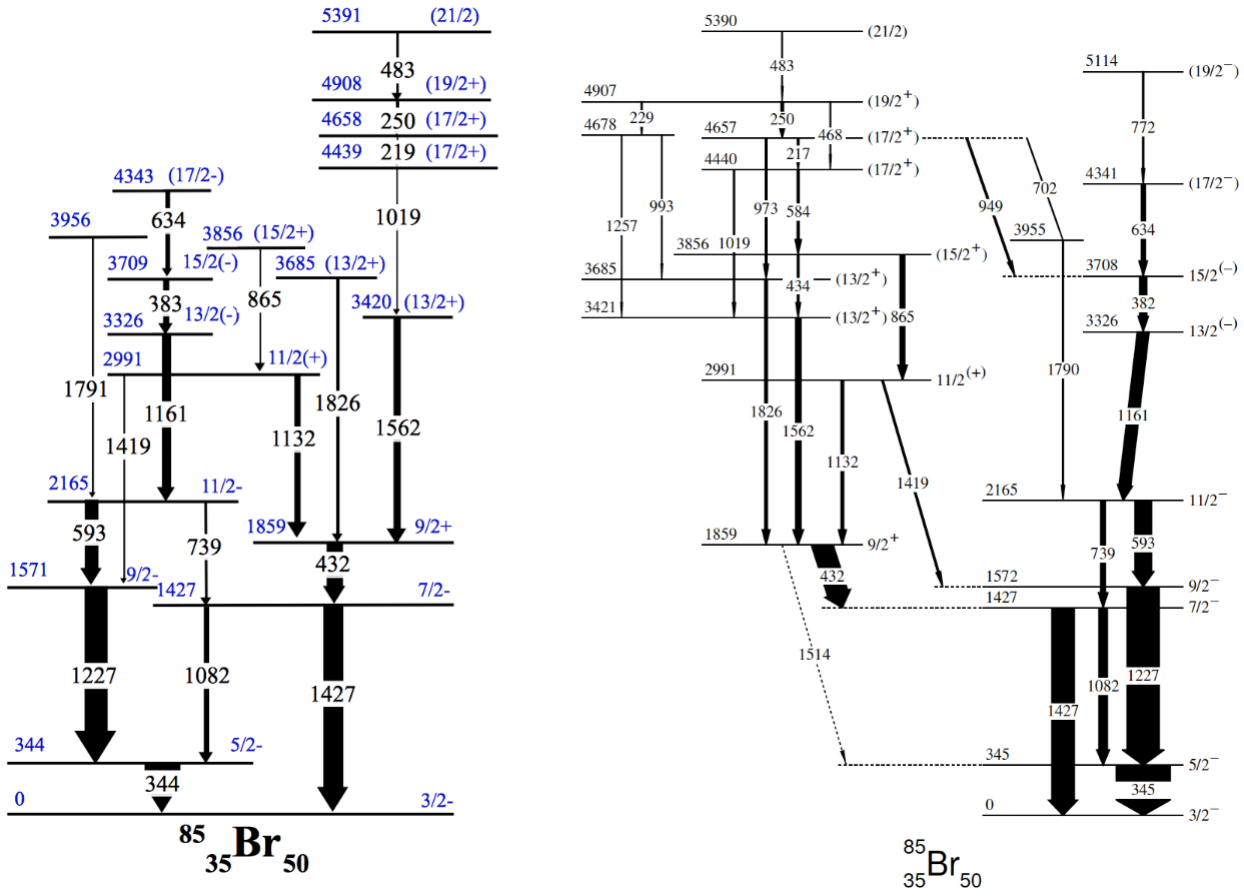

Figure 5.6: Comparison of the partial level scheme of ^{85}Br obtained in this work (left) with the level scheme obtained after fusion-fission reactions (right) [80]. The width of the arrows are proportional to the observed experimental intensities. Spin and parity values are taken from [80].

5.1.2 Spectroscopy of ^{87}Br

Excited states of the $^{87}_{35}Br_{52}$ nucleus, situated just above the N=50 shell closure, were studied following fission reactions during the EXILL campaign [85, 82]). More recently, excited states populated in the β-decay of ^{87}Se were extensively studied [79]. From the combined analysis of the AGATA-VAMOS++ and FIPPS data-sets, the known level scheme of ^{87}Br was confirmed and further information obtained.

The γ-ray spectrum obtained for ^{87}Br with the AGATA-VAMOS++ setup is shown in Fig. 5.7. Previously known transitions are indicated in blue, while the six newly found transitions are highlighted in red. The efficiency corrected intensities are reported in black. Worth noting is the existence of a broad peak at 874 keV, corresponding to two previously known transitions with energies of 872 and 876 keV which cannot be resolved in AGATA (due to resolution limitations related to the Doppler correction). The doublet was confirmed with the higher resolution available from the FIPPS data, which was used to assign relative intensities to these two transitions.

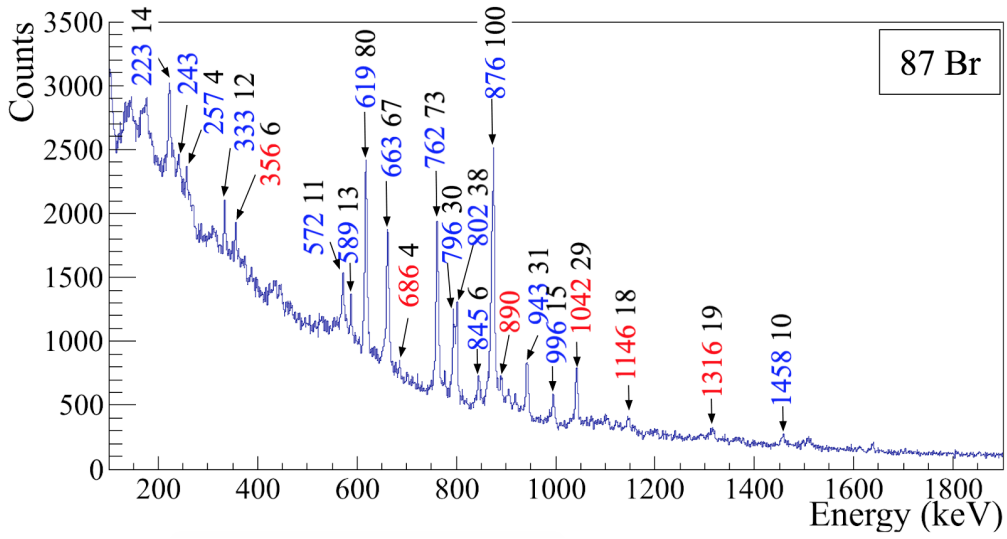

Figure 5.7: Doppler corrected prompt γ-ray spectrum measured in AGATA in coincidence with the ^{87}Br ions detected in VAMOS++. Previously known transitions are marked in blue. Newly observed transitions are marked in red. Intensities relative to the strongest transitions are indicated in black.

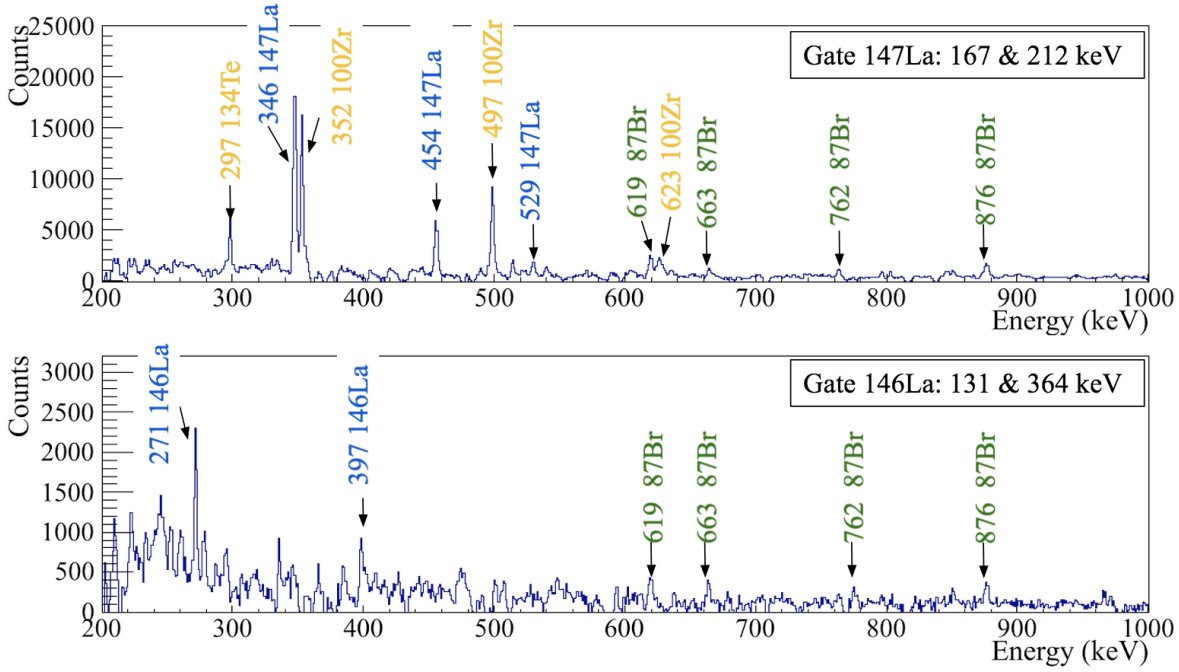

Figure 5.8: Coincidence γ-ray spectra doubly gated on transitions from the main complementary fission fragments of ^{87}Br obtained with the active ^{235}U fission target at FIPPS. Transitions belonging to ^{147}La and ^{146}La are shown in blue. Transitions present in both gates belonging to ^{87}Br are marked in green. Contaminant transitions are indicated in yellow.

The FIPPS data-set was used in order to confirm the placement of the known transitions, place the new transitions in a level scheme and search for transitions belonging to ^{87}Br not observed in AGATA. The high ^{235}U fission yield of ^{87}Br (1.4×10^{-2}) resulted in high statistics in the doubly gated spectra. Prompt coincidence spectra gated on transitions from the complementary fission fragments: ^{146}La (131-364 keV) and ^{147}La (167-212 keV) are shown in Fig. 5.8. The fact that the 619, 663, 762 and 876 keV transitions are present in both the ^{146}La (3-neutron partner) gate and the ^{147}La (2-neutron partner) gate supports the assignment to ^{87}Br and establishes these transitions as the strongest populated in fission. In addition to La and Br peaks, contaminant peaks are observed in the spectra belonging to ^{100}Zr and its fission partner ^{134}Te. The contamination is introduced via the 212 keV gate due to a strong 212.6 keV 2+ $\rightarrow$ 0+ in ^{100}Zr (yield = 4.9×10^{-2}).

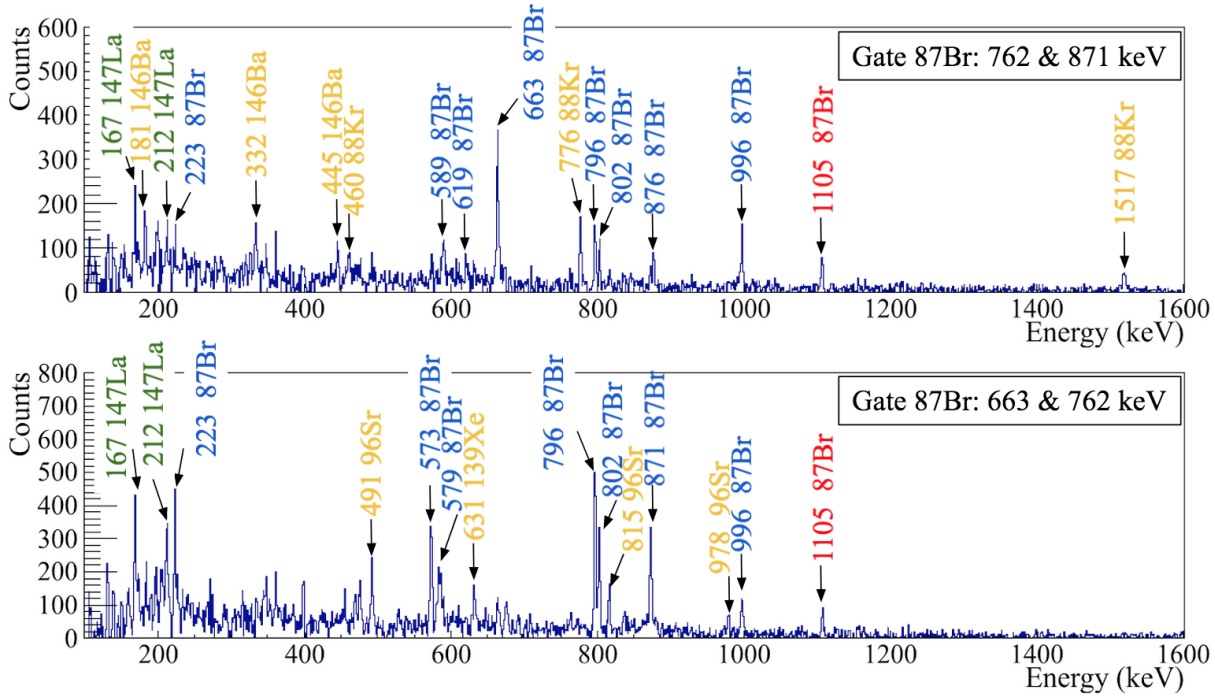

Figure 5.9: Coincidence γ-ray spectra doubly gated on the most intense transitions observed in ^{87}Br, obtained with the active ^{235}U fission target at FIPPS. Known ^{87}Br transitions are marked in blue, while the newly observed 1105 keV transition is marked in red. Transitions belonging to the complementary fission partner ^{147}La are indicated in green. Contaminant peaks are labelled in yellow.

Once the main transitions have been established, a series of coincidence spectra were produced and used to build a level scheme of ^{87}Br. An example of coincidence spectra obtained with the FIPPS active target data gated on the main transitions in ^{87}Br can be seen in Fig. 5.9. The transitions depopulating the (9/2+) level with an excitation energy of 1465 keV are observed in the top spectrum, gated on the (17/2+) $\rightarrow$ (13/2+) transition (762 keV) and the (17/2+) $\rightarrow$ (13/2+) (871 keV). In addition, two intense transitions belonging to the complementary fission partner ^{147}La as well as contaminant transitions belonging to ^{146}Ba (yield = 9.2×10^{-3}) are present. A γ ray at 1105 keV was seen in coincidence with the 762-871 keV transitions as well as the 663-762 keV transitions (bottom spectrum of Fig. 5.9) and was assigned to ^{87}Br populating the state at 4095 keV. This transition was

not observed in the AGATA-VAMOS++ data due to the lack of γ coincidence efficiency.

The FIPPS data-set was further exploited to distinguish excited states populated in fission from those populated after β-decay [79]. A comparison of coincidence spectra produced with the active target data and the standard target data revealed a series of γ rays only emitted after beta decay. The coincidence spectra, along with a partial level scheme of these states, are shown in Fig. 5.10.

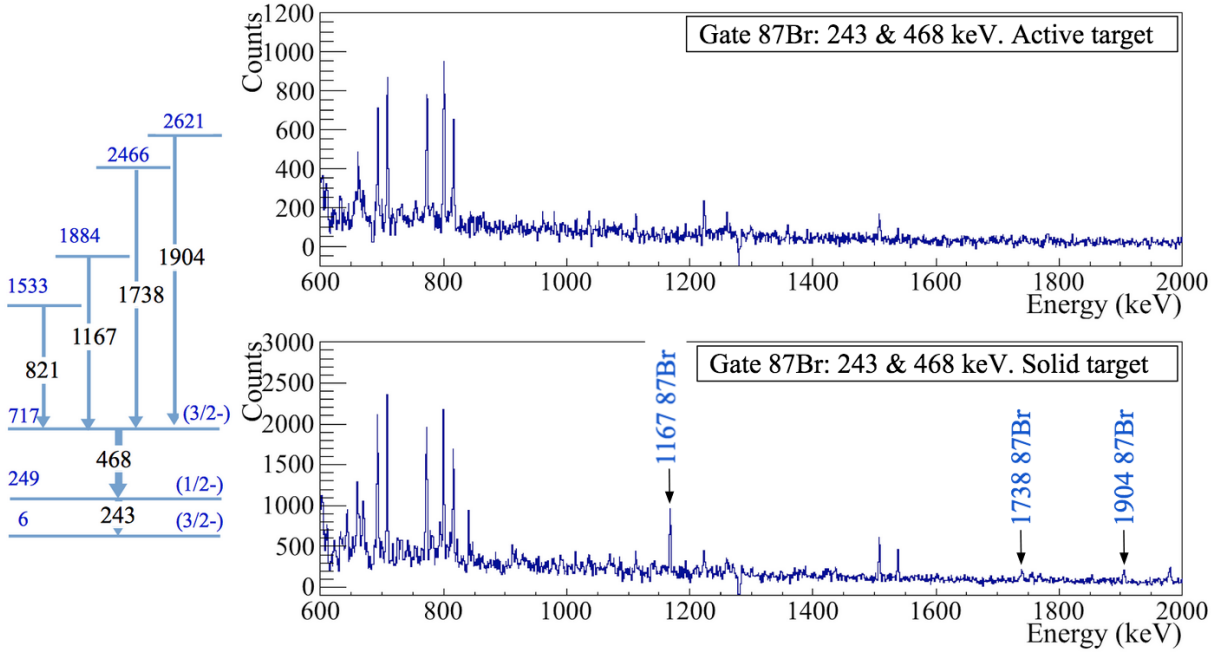

Figure 5.10: LEFT: partial level scheme of ^{87}Br excited states populated in the beta decay of ^{87}Se not seen in fission. RIGHT: γ-ray coincidence spectra doubly gated on 243 keV and 468 keV transitions, two of the most intense transitions observed in ^{87}Br after β decay [79]. The top spectrum is obtained using the active fission target. The bottom spectrum is obtained using the standard solid target.

Due to strong contamination in the FIPPS coincidence spectra, some of the newly identified transitions were placed in the level scheme using γ-γ coincidences in the AGATA data. Such was the case of the 1042 keV transition, found to be in clear coincidence with the 876 keV transition (see Fig. 5.11) and placed populating the 876 keV level. Coincidences between the 356 keV, 686 keV and the 876 keV transitions were observed. Since the energies of the 356 keV and 686 keV transitions add up to 1042 keV and were not seen in coincidence with this transition, they were placed parallel to the 1042 keV transition. An additional 890 keV transition was observed in coincidence with the 876 keV transition and placed populating this state. Coincidences between the 1316 keV, 943 keV and 619 keV transitions allowed the placement of the new transition at 1316 keV populating the 1562 keV state. Although the 333 keV transition decaying to the ground state is observed with high intensity in β-decay [79] and was observed in the AGATA γ-ray spectrum (see Fig. 5.7), it was not not seen in coincidence with any other transitions. This is explained by a combination of lower population of the 333 keV state in fission as well as high fragmentation in the transitions populating this state.

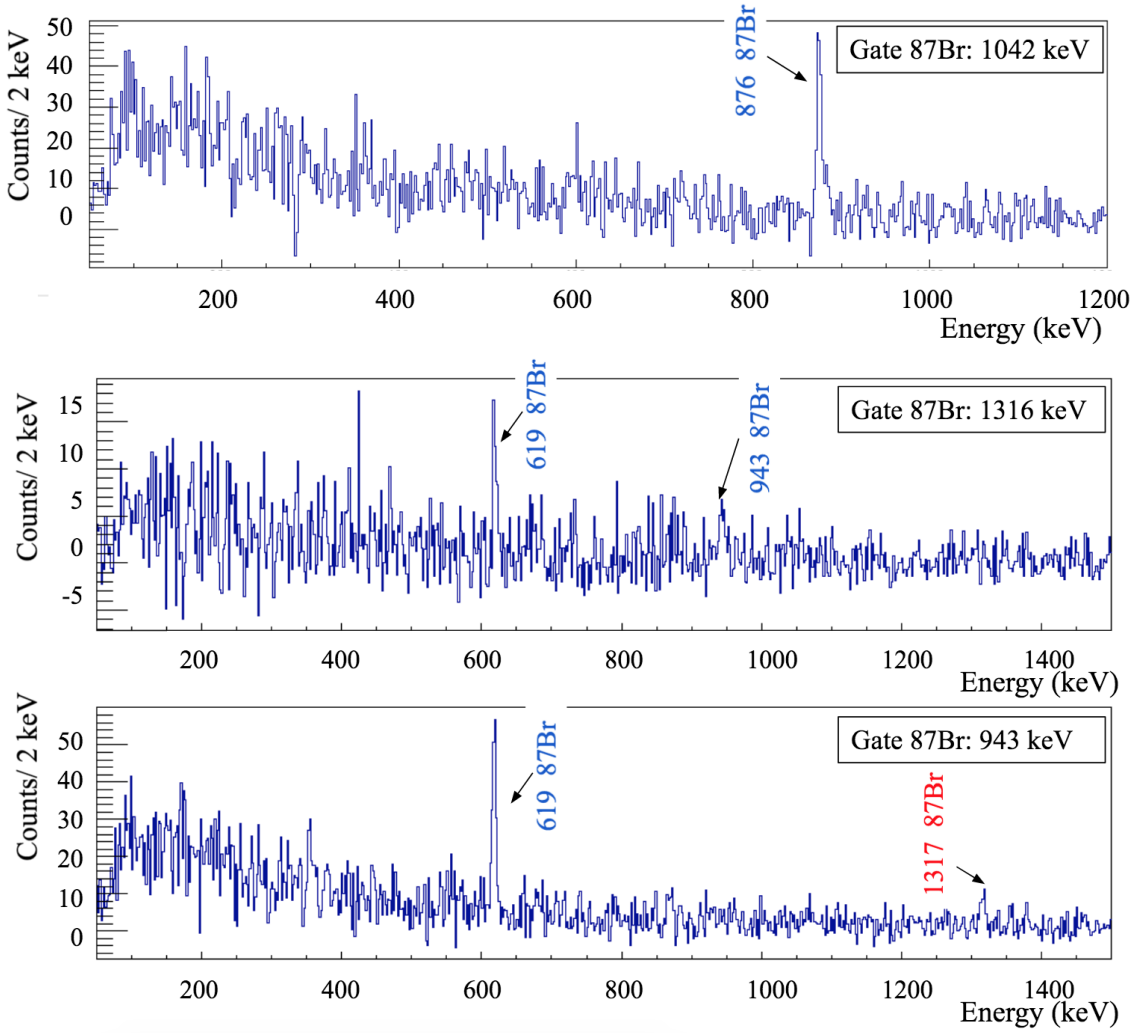

Figure 5.11: γ-γ coincidence spectra gated on known and newly observed transitions (red) in ^{87}Br, obtained with the AGATA-VAMOS++ data-set.

The combination of the FIPPS and AGATA-VAMOS++ data-sets resulted in the observation of 24 γ-ray transitions corresponding to the ^{87}Br nucleus, out of which 7 are newly observed. During the writing of this manuscript the results of the EXILL campaign were published in [82], which are in agreement with the results presented in this work. The information of all the observed transitions, including spin values of the excited states and calculated intensities, is reported in Table 5.2. The final level scheme obtained for ^{87}Br is shown in Fig. 5.12.

Energy (keV)	**Intensity** (%)	$J_i \rightarrow J_f$	E_i **(keV)**	E_f **(keV)**	**Data-set**
222.6(2)	14(2)	$(7/2-) \rightarrow (5/2-)$	802	579	F+A
257.1(3)	4(2)	$9/2- \rightarrow (7/2-)$	876	619	F+A
333.4(4)	12(2)	$(3/2-) \rightarrow 5/2-$	333	0	A
356.0(5)*	6(1)	-	1918	1562	A
572.6(2)	11(1)	$(5/2-) \rightarrow (3/2-)$	579	6	F+A
579.2(2)	< 5	$(5/2-) \rightarrow 5/2-$	579	0	F
588.8(2)	13(2)	$9/2+ \rightarrow 9/2-$	1465	876	F+A
618.6(2)	80(10)	$(7/2-) \rightarrow 5/2-$	619	0	F+A
662.8(2)	67(8)	$9/2+ \rightarrow (7/2-)$	1465	802	F+A
686.0(5)*	4(1)	-	1562	876	A
761.8(2)	73(9)	$(13/2+) \rightarrow 9/2+$	2227	1465	F+A
795.6(3)	30(4)	$(7/2-) \rightarrow (3/2-)$	802	6	F+A
801.5(2)	38(4)	$(7/2-) \rightarrow 5/2-$	802	0	F+A
845.8(2)	6(1)	$9/2+ \rightarrow (7/2-)$	1465	619	F+A
871.5(3)	68(8)	$(17/2+) \rightarrow (13/2+)$	3099	2227	F+A
875.5(2)	100	$9/2- \rightarrow 5/2-$	876	0	F+A
890.4(3)*	< 5	-	1766	876	F+A
943.1(2)	31(4)	-	1562	619	F+A
996.0(2)	15(2)	$(21/2+) \rightarrow (17/2+)$	4095	3099	F+A
1042.2(4)*	29(4)	-	1918	876	A
1105.0(2)*	8(3)	-	5200	4095	F
1316.4(4)*	19(2)	-	2878	1562	F+A
1458.2(3)	10(1)	$9/2+ \rightarrow (3/2-)$	1465	6	A
Unplaced transitions					
1146.0(5)*	16(2)	-	-	-	A

Table 5.2: Properties of the γ-ray transitions assigned to ^{87}Br in this work. Newly observed transitions are marked with (*). In the last column, information is given on whether they were observed in both the FIPPS and AGATA-VAMOS++ data-sets (F+A), only in the FIPPS data (F) or only in the AGATA-VAMOS++ data (A). Efficiency corrected intensity values are given relative to the strongest transition (875.5 keV). The reported intensities were obtained from the AGATA-VAMOS++ data, except for transitions observed only in the FIPPS data-set. The indicated spin and parity values of excited states were adopted from [82].

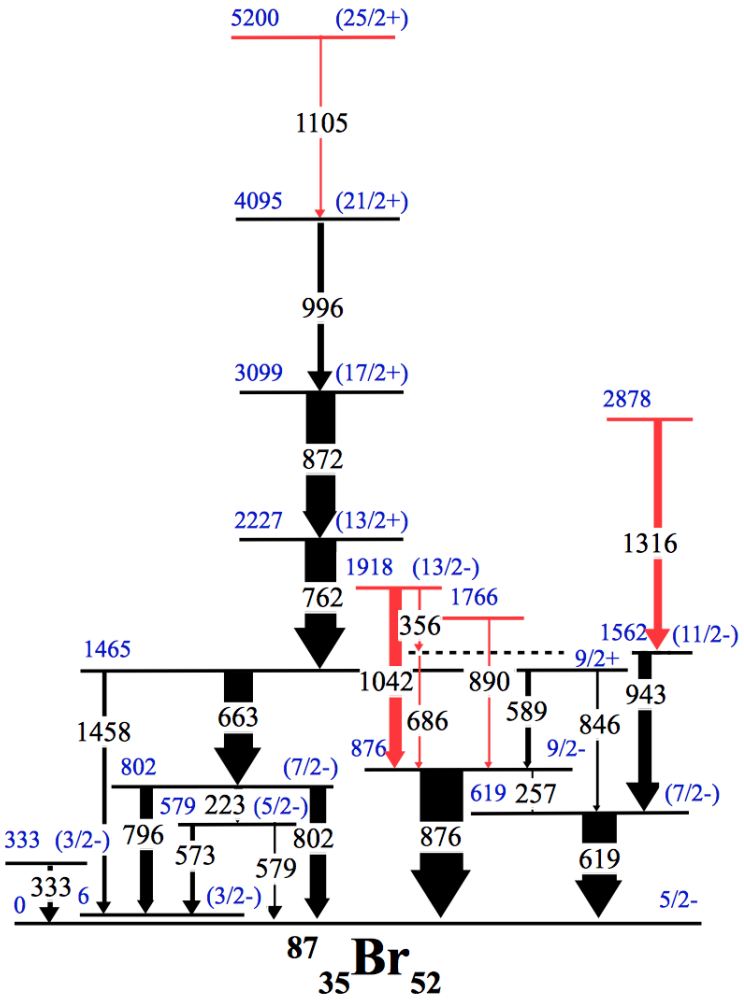

Figure 5.12: Level scheme of ^{87}Br obtained in this work. Known transitions are shown in black and newly found transitions in red. Spin and parity values are taken from [79, 82].

5.1.3 Spectroscopy of ^{89}Br

No spectroscopic information was known of ^{89}Br ($N = 54$) before this study. Although preliminary results from the EXILL campaign suggested a similar structure to the ^{87}Br, no transition energies or spectra were shown [85]. In this work, the first level scheme of excited states of ^{89}Br will be presented.

γ-ray transitions corresponding to deexcitations in the ^{89}Br nucleus were identified using the AGATA-VAMOS++ data-set. The Doppler corrected γ-ray spectrum detected with AGATA and measured in coincidence with the isotopically identified ^{89}Br fission fragment is shown in Fig. 5.13. As discussed in section 3.2, different conditions on Z, M and Q are used to identify contaminant peaks. For the case of ^{89}Br, a contaminant peak at 954 keV belonging to ^{89}Kr was observed. A total of 20 new transitions belonging to ^{89}Br were identified.

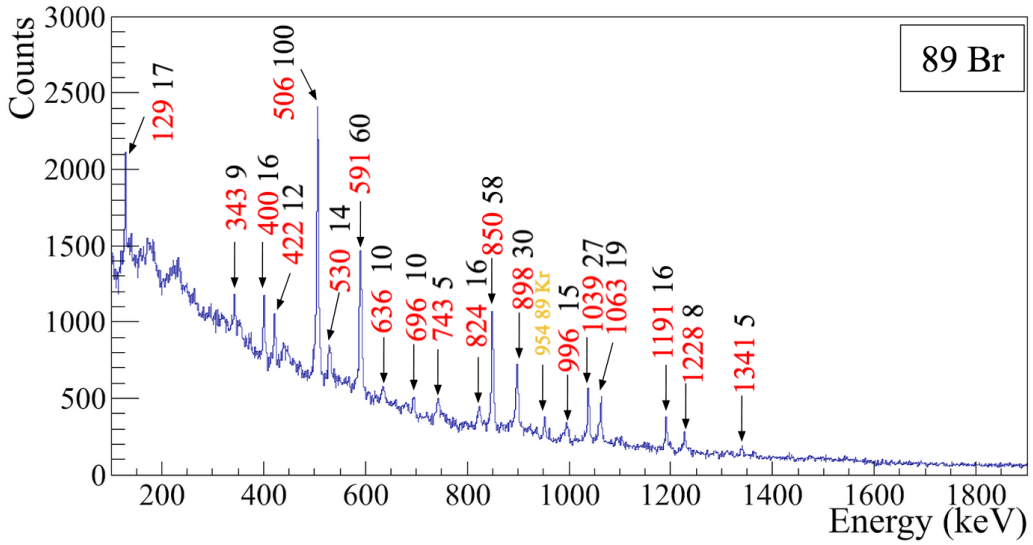

Figure 5.13: Doppler corrected prompt γ-ray spectrum measured in AGATA in coincidence with the ^{89}Br ions detected in VAMOS++. All new transitions are labelled in red. A contaminant transition belonging to ^{89}Kr is indicated in yellow. Intensities relative to the strongest transition are indicated in black.

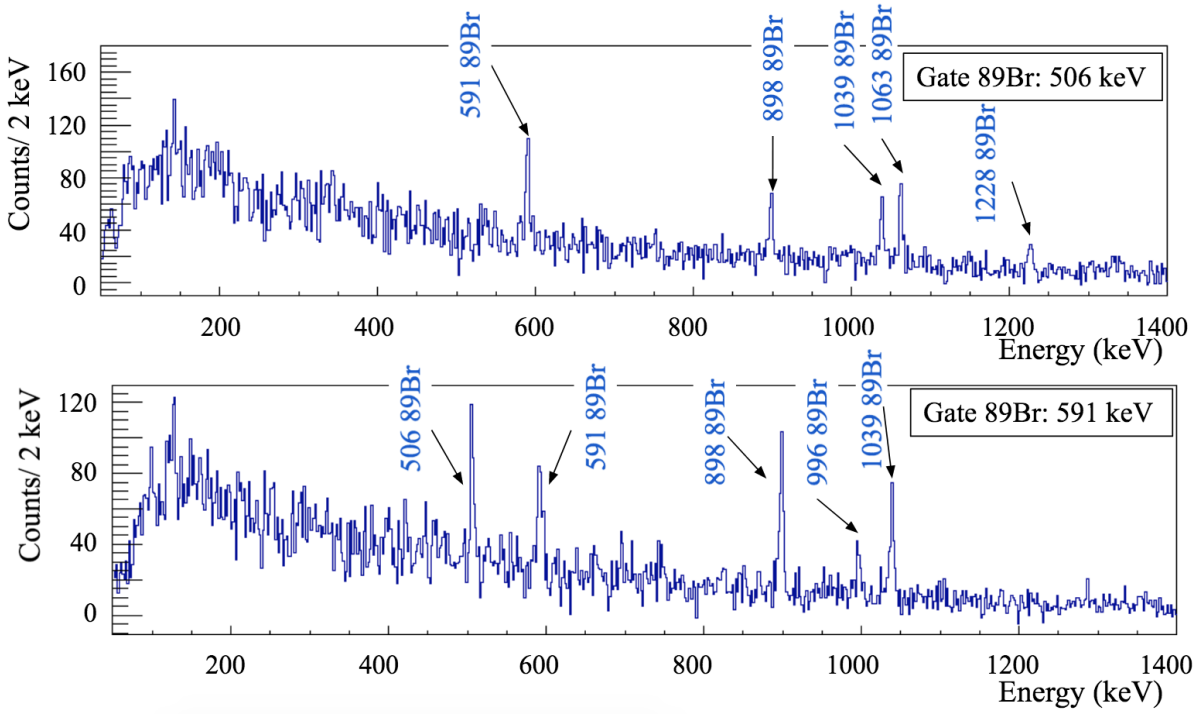

Figure 5.14: γ-γ coincidence spectra gated on the 506 keV and 591 keV transitions assigned to ^{89}Br produced with the AGATA-VAMOS++ data-set.

Once the γ-ray transitions had been identified, γ-γ coincidence matrices were produced using the AGATA data-set in order to build a level scheme of ^{89}Br. The most intense transition (506.3 keV) was used as a starting point and was placed feeding the ground state. Coincidence spectra gated on the 506.3 keV and 591 keV transitions are plotted in Fig. 5.14. Worth noting is the presence of auto coincidences in the spectrum gated on the 591 keV transition (see Fig. 5.14), indicating a doublet. Even though the two peaks cannot be resolved the doublet is confirmed using relative intensities on gated spectra. These spectra reveal clear coincidences between the 506, 591, 898 and 1039 keV transitions, forming a cascade. The order of these transitions was established using triple γ-ray coincidences in the FIPPS data-set and will be discussed later on in this section. Coincidence spectra gated on the 898 keV and 1039 keV transitions are shown in Fig. 5.15. A 996 keV transition is seen in coincidence with the 898 keV and 591 keV transitions.

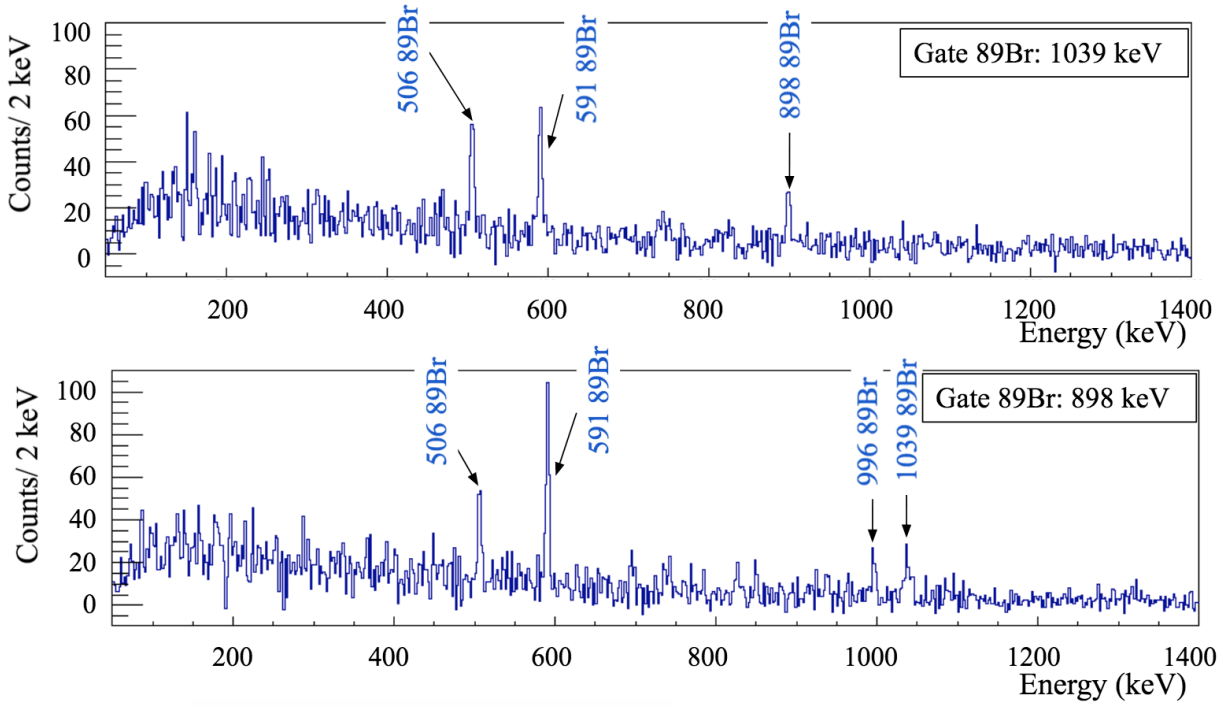

Figure 5.15: γ-γ coincidence spectra gated on the 1039 keV and 898 keV transitions assigned to ^{89}Br produced with the AGATA-VAMOS++ data-set.

The spectrum gated on the 506 keV transition shows the presence of 1227 and 1063 keV γ rays. Spectra gated on both transitions, shown in Fig. 5.16, are used to place them populating the 506.3 keV level. The 636 keV transition, already observed in the total γ-ray spectrum is seen in coincidence with the 1063 keV transition and is placed populating the 1569 keV state.

Coincidences measured with the intense low energy transition observed at 129 keV are used to place this transition in the level scheme. The spectrum gated on the 129 keV transition, shown in Fig. 5.17, indicates coincidences with the 401, 422, 824 and 591 keV transitions. This group of transitions are placed parallel to the 506.3 keV transition. The order inside the group is determined using observed intensities.

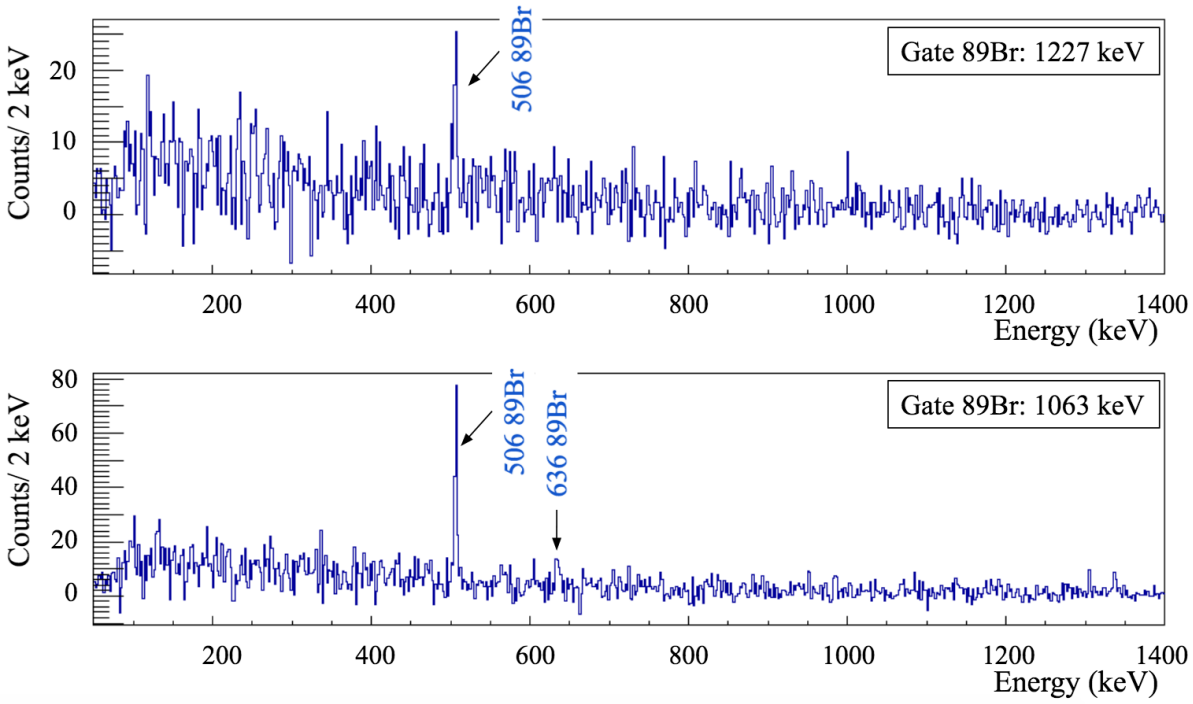

Figure 5.16: γ-γ coincidence spectra gated on the 1227 keV and 1063 keV transitions assigned to ^{89}Br produced with the AGATA-VAMOS++ data-set.

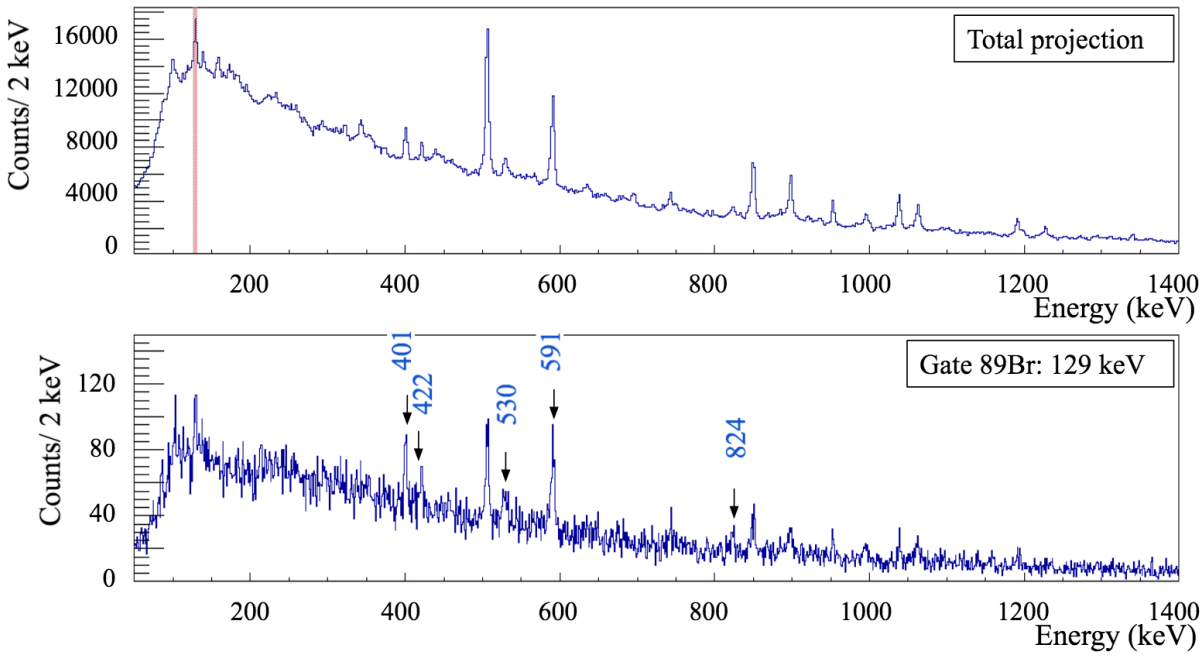

Figure 5.17: ^{89}Br coincidence spectra gated on the 129 keV transition obtained with the AGATA-VAMOS++ data-set. Due to low statistics, no background substraction was performed to produce the gated spectrum. The relative intensity of transitions in true coincidence with the 129 keV are enhanced with respect to intense transitions seen in the total projection (top), and are indicated in blue.

The results obtained with the AGATA-VAMOS++ data-set were complemented with the FIPPS data, which was primarily used to place transitions in a level scheme using prompt triple γ-ray coincidences. As can be seen from Fig. 5.3, the most probable complementary fragments of ^{89}Br are ^{144}La (3n) and ^{145}La (2n). Coincidence spectra gated on transitions in ^{145}La are shown in Fig. 5.18. A series of γ rays from ^{145}La dominate the coincidence spectra, however a strong presence of contaminant transitions from ^{146}Ba (yield $= 9.2 \times 10^{-3}$) and ^{93}Kr (yield $= 5.3 \times 10^{-3}$) is observed. The 506 keV peak present in both gates is identified as a γ ray from ^{89}Br, as already established with the AGATA-VAMOS++ data-set. In order to confirm the assignment of the 506 keV to ^{89}Br in the FIPPS data-set, it would be necessary to see this transition in prompt coincidence with transitions in ^{144}La as well as ^{145}La. However, no transitions from ^{144}La could be identified in the FIPPS data-set.

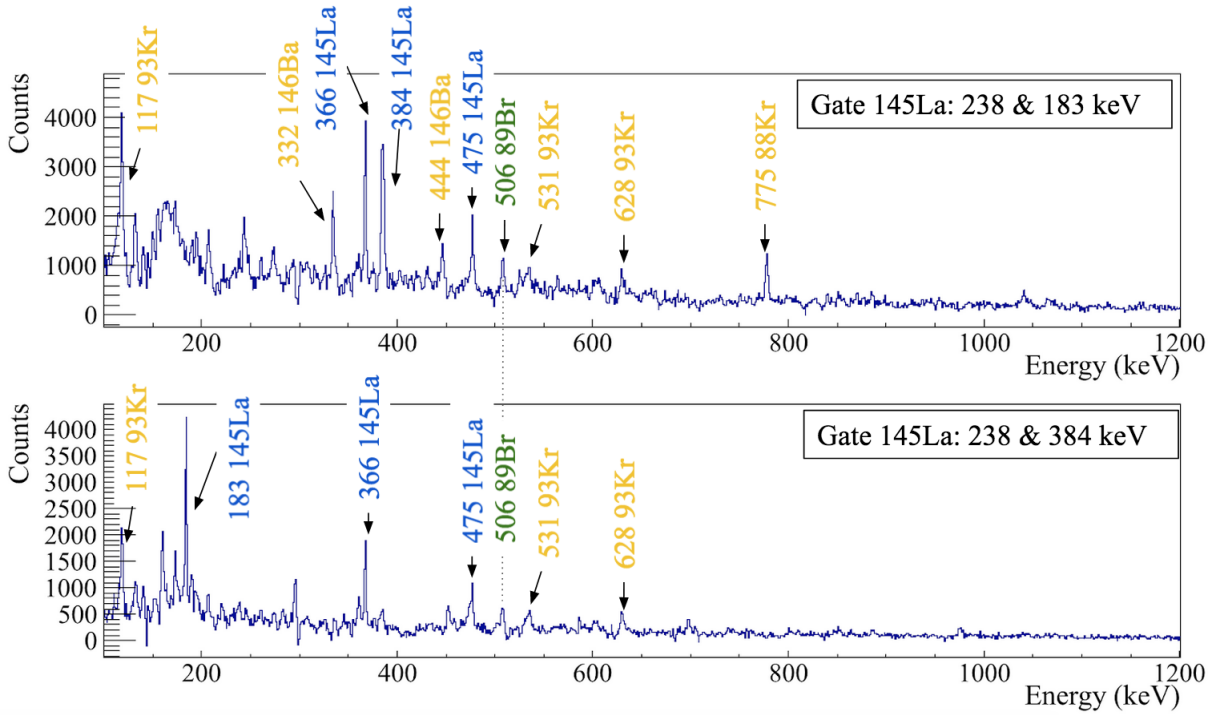

Figure 5.18: Coincidence spectra gated on transitions from ^{145}La, obtained using the active fission target FIPPS data. γ rays from ^{145}La are labelled in blue, while contaminant transitions are labelled in yellow. The 506 keV transition, labelled in green and present in both spectra, is assigned to ^{89}Br.

Fig. 5.19 shows coincidence spectra obtained with the standard uranium target data-set gated on ^{89}Br transitions. A very "clean" coincidence spectrum is obtained gating on the 1038-898 keV pair. These coincidences are used to assign an order to the cascade of 506, 591, 898 and 1039 keV transitions already observed in AGATA, as well as to place the 996 keV transition. It is worth noting that similarly to the ^{85}Br case, no fission partner transitions are observed in the spectra. This is explained as originating from high fragmentation of the γ-ray intensity in the lanthanum complementary fission fragments.

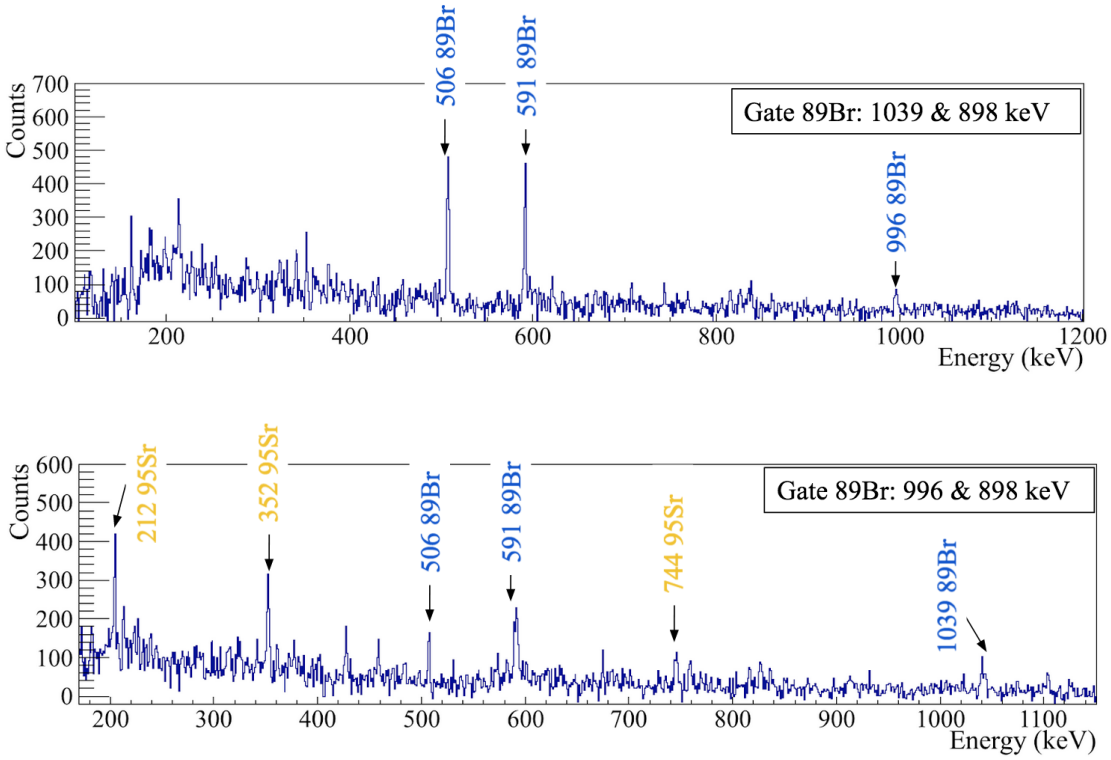

Figure 5.19: Coincidence spectra gated on newly found transitions in ^{89}Br, obtained using the standard target FIPPS data. The top spectrum is dominated by γ-ray transitions form ^{89}Br, indicated in blue. γ-ray transitions form the La fission partners are not observed in either spectra. Contaminant peaks are labelled in yellow.

The relevant information of all the γ-ray transitions assigned to ^{89}Br is reported in Table 5.3. Intensity values are given relative to the 506 keV transition. A total of 20 transitions were observed, 19 of which were placed in a level scheme (see Fig. 5.20), resulting in 14 newly observed levels. It is worth mentioning that the sequence of transitions depopulating the 1545 keV consisting of the 591, 422, 401, 824 and 129 keV transitions were not observed in the FIPPS data-set. The identification of such transitions in γ-γ or γ-γ-γ coincidences might have been compromised by the occurrence of contaminant peaks and the low intensity of the considered decay path. The ^{89}Br level scheme exhibits a very similar structure to that of ^{87}Br. These similarities as well as spin assignments based on systematics of the Br chain will be discussed in section 5.2.

Energy (keV)	**Intensity** (%)	$J_i \rightarrow J_f$	E_i **(keV)**	E_f **(keV)**	**Data-set**
129.2(4)*	17(2)	$(3/2-) \rightarrow (5/2-)$	129	0	A
343.34(4)*	9(2)	$(9/2-) \rightarrow (7/2-)$	850	0	A
400.5(4)*	16(2)	$(9/2-) \rightarrow (7/2-)$	531	129	A
421.8(4)*	12(2)	$(7/2-) \rightarrow (5/2-)$	953	531	A
506.3(2)*	100	$(7/2-) \rightarrow (5/2-)$	506	0	F+A
529.9(4)*	14(3)	$(5/2-) \rightarrow (5/2-)$	531	0	A
590.5(2)*	32(5)	$(13/2+) \rightarrow (9/2+)$	2136	1545	F+A

591.0(4)*	27(5)	(9/2+) → (7/2−)	1545	953	A
635.9(2)*	10(3)	-	2206	1569	F+A
695.5(4)*	10(3)	(9/2+) → (9/2−)	1545	850	A
823.8(4)*	16(6)	(7/2−) → (3/2−)	953	129	A
849.8(4)*	58(4)	(9/2−) → (5/2−)	850	0	A
898.3(2)*	30(3)	(17/2+) → (13/2+)	3034	2136	F+A
995.7(2)*	15(2)	(21/2+) → (17/2+)	4030	3034	F+A
1038.6(2)*	27(2)	(9/2+) → (7/2−)	1545	506	F+A
1062.8(3)*	19(2)	-	1569	506	F+A
1191.2(2)*	16(2)	-	2041	850	A
1227.4(4)*	8(1)	-	1734	506	A
1341.0(4)*	5(1)	-	2910	1569	F+A
Unplaced transitions					
743*	5(1)	-	-	-	A

Table 5.3: Properties of the γ-ray transitions assigned to ^{89}Br in this work. All transitions were observed for the first time and marked with (*). In the last column, information is given on whether they were observed in both the FIPPS and AGATA-VAMOS++ data-sets (F+A) or only in the AGATA-VAMOS++ data (A). Efficiency corrected intensity values are given relative to the strongest transition (506.3 keV). The reported intensities were obtained from the AGATA-VAMOS++ data. The indicated spin and parity values of excited states were assigned on the basis of the systematics (see section 5.2).

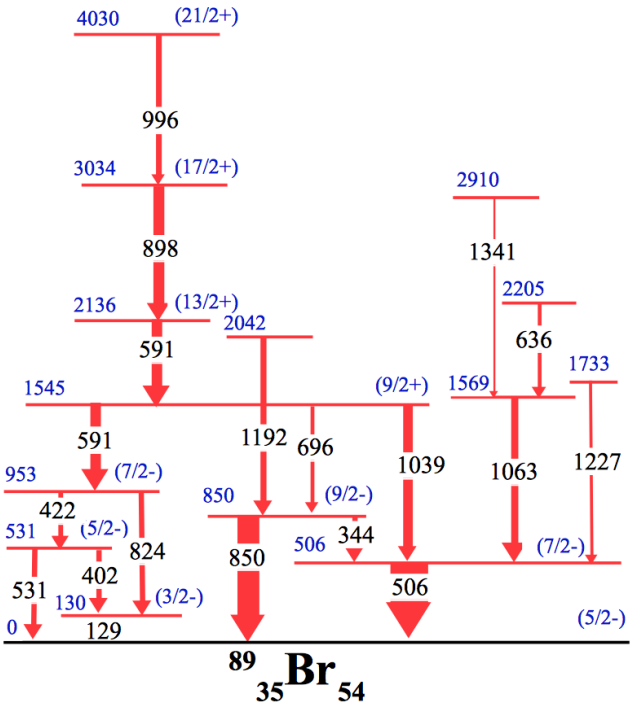

Figure 5.20: Level scheme of ^{89}Br obtained in this work. The width of the arrows reflects their relative intensity as seen in the AGATA-VAMOS++ data.

5.1.4 Spectroscopy of ^{91}Br

No spectroscopic information was known for ^{91}Br prior to this work. Due to its low fission yield, an order of magnitude smaller than the ^{89}Br (see Fig. 5.2), this isotope was not observed in the FIPPS data-set. Nevertheless, the isotopic selectivity provided by VAMOS++ enabled an identification of the main γ-ray transitions in ^{91}Br.

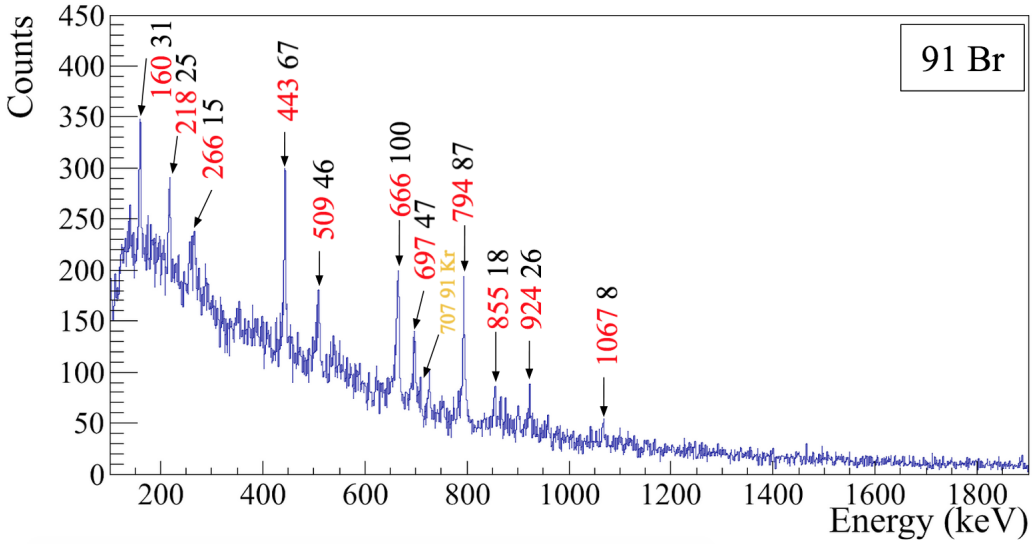

Figure 5.21: Doppler corrected prompt γ-ray spectrum measured in AGATA in coincidence with the ^{91}Br ions detected in VAMOS++. Intensities relative to the strongest transition (666 keV) are indicated in black.

The Doppler corrected γ-ray spectrum obtained with the AGATA-VAMOS++ experiment is shown in Fig. 5.21. The 11 new transitions assigned to ^{91}Br are marked in red, while a contaminant peak from ^{91}Kr is labelled in yellow.

$\gamma - \gamma$ coincidences matrices were produced in order to construct a level scheme. For this isotope, the coincidence analysis presented the challenge of limited statistics. As a result, not all the observed transitions could be placed and some placements can only be tentative. Coincidence spectra gated on the most intense transitions are shown in Fig. 5.22. The clearest coincidences were observed between the 444-697, 444-509 keV and the 666-923 keV transitions which are placed in parallel in the level scheme. A hint of the 923 keV transition can be seen in the 444 keV gate, indicating a connection between the 666 keV and 444 keV levels. Even though a 221 keV transition was not seen in coincidence with the 444 keV transition a 218 keV transition was observed in the singles γ-ray spectrum and can be tentatively placed populating the 444 keV state. The 160 keV transition is seen in coincidence with the 509 keV, however higher statistics are needed to make a conclusive placement.

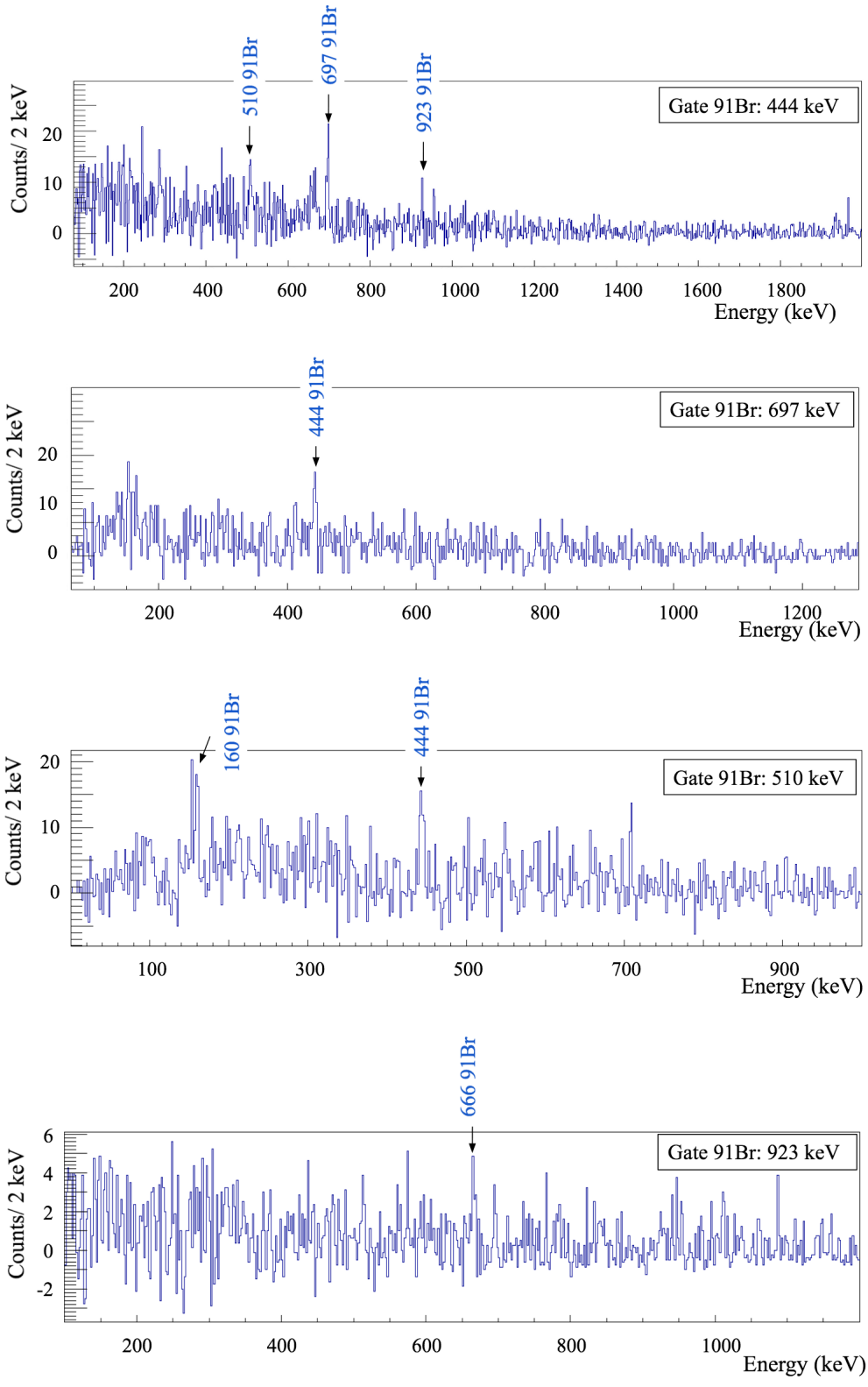

Figure 5.22: Coincidence spectra gated on ^{91}Br transitions, obtained with the AGATA-VAMOS++ data-set.

Details on the γ-ray transitions assigned to ^{91}Br are reported in Table 5.4. Intensity values are given relative to the 666 keV transition. Seven transitions could be placed in a level scheme, while statistics limitations prevented the placement of four of the observed transitions. The final level scheme obtained for ^{91}Br is shown in Fig. 5.23. The structure of the excited states and spin assignments will be discussed in section 5.2.

Energy (keV)	**Intensity** (%)	$J_i \rightarrow J_f$	E_i **(keV)**	E_f **(keV)**	**Data-set**
159.9(4)*(t)	47(5)	-	1114	954	A
217.5(4)*(t)	37(5)	(9/2−) → (7/2−)	666	444	A
444.1(4)*	100	(7/2−) → (5/2−)	444	0	A
509.9(4)*	68(8)	-	954	444	A
665.6(4)*	64(10)	(9/2−) → (5/2−)	666	0	A
697.4(4)*	70(8)	-	1141	444	A
923.0(7)*	39(5)	(9/2+) → (9/2−)	1589	666	A
Unplaced transitions					
267.1(5)*	23(3)	-	-	-	A
794.9(4)*	87(11)	-	-	-	A
854.6(4)*	26(4)	-	-	-	A
1067.9(4)*	12(3)	-	-	-	A

Table 5.4: Properties of the γ-ray transitions assigned to ^{91}Br in this work. All transitions were observed for the first time and marked with (*). Transitions which are tentatively placed are marked with (t). All the transitions were observed only in the AGATA-VAMOS++ data (A). Efficiency corrected intensity values are given relative to the strongest transition (444.1 keV). The indicated spin and parity values of excited states were assigned on the basis of the systematics (see section 5.2).

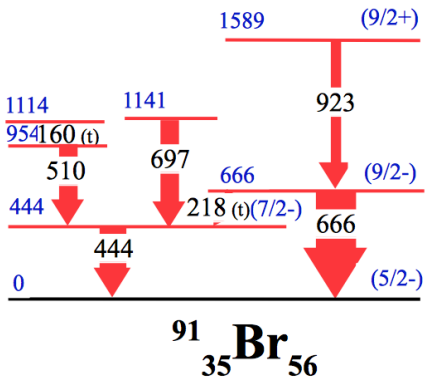

Figure 5.23: First level scheme of ^{91}Br, obtained in this work using the AGATA-VAMOS++ data. The width of the arrows represents efficiency corrected intensities relative to the 666 keV transition. The placement of the 160 and 218 keV transitions, indicated with (t), is tentative. Spin and parity values were assigned on the basis of the systematics in the Br chain and will be discussed in section 5.2.

5.1.5 Spectroscopy of ^{93}Br

Located well above the $N = 50$ shell closure, the ^{93}Br isotope is the most neutron rich Br nucleus that could be studied with the AGATA-VAMOS++ data-set. Due to its low ^{235}U fission yield (1.9×10^{-5}) the FIPPS data-set could not be exploited. Despite the isotopic selectivity provided by VAMOS++, the γ-ray spectrum gated on the ^{93}Br nucleus is dominated by contaminants, due to its low production yield relative to neighbouring nuclei. As can be seen from Fig. 5.24, even though a condition of $Z = 35 \pm 0.5$ is imposed the strongest γ-ray transitions belong to ^{93}Kr. When more restrictive conditions are applied to the Z_{exp}, M_{exp} and Q_{exp} values the ^{93}Kr transitions are suppressed. Despite the limited statistics, a peak is observed at an energy of 531 keV. Worth noting is that the ^{93}Kr nucleus has a 534 keV transition. However, in this nucleus the 534 keV transition is less intense than the 628 keV which is significantly suppressed when applying more restrictive conditions. Using these arguments the 531(1) keV transition is tentatively assigned to ^{93}Br, and placed populating the ground state.

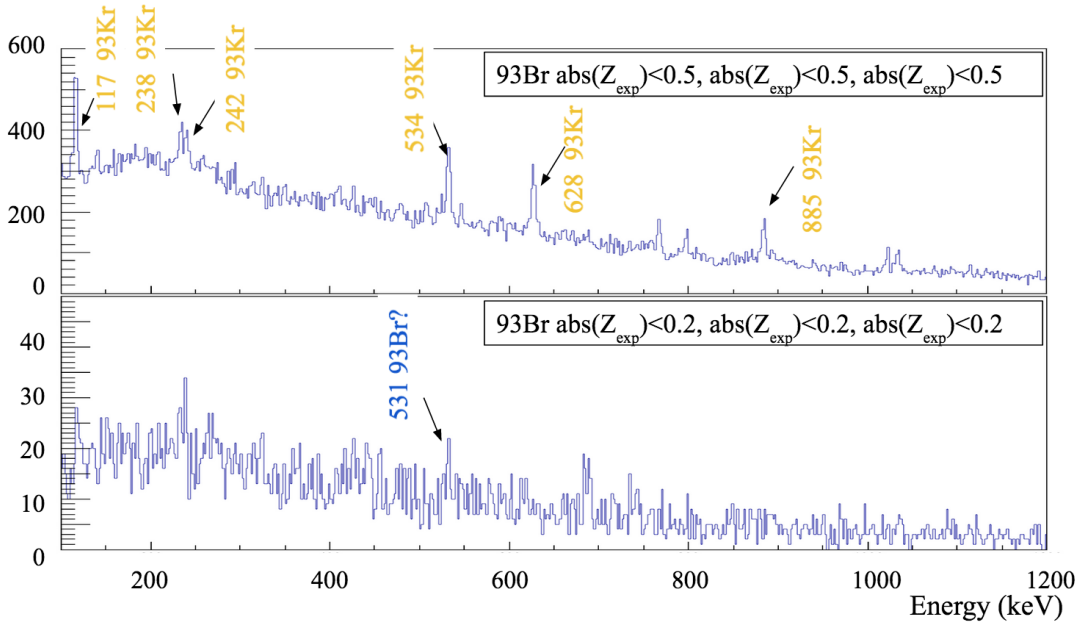

Figure 5.24: Doppler corrected prompt γ-ray spectrum measured in AGATA in coincidence with the ^{93}Br ions detected in VAMOS++ obtained imposing different selection conditions.

5.1.6 Search for isomeric states

In addition to providing information on excitation energies of the Br nuclei of interest, both the FIPPS and the AGATA-VAMOS++ data-sets can be used to extract information regarding the lifetime of excited states. On the one hand, the prompt-delayed coincidence analysis of the FIPPS data-set (introduced in section 3.1.2) allows the identification of short lived isomers and an estimation of their

lifetime. On the other hand, the characteristics of the AGATA-VAMOS++ setup can be exploited to set a limit on upper of ~ 5 ns to the lifetime of the observed states.

A search for isomeric states in neutron rich odd-mass Br isotopes was carried out. It was concluded that none of the observed excited states had a lifetime > 5 ns. This result is of particular importance for $9/2+$ states associated with a proton excitation to the $\pi g_{9/2}$ orbit (discussed in the following section), which have an isomeric character in neighbouring Rb nuclei. In the case of ^{85}Br, a previous upper limit of 10 ns was set [80]. In the case of the ^{87}Br, a lifetime of 20 ns was suggested [79].

5.1.7 Note on angular correlations

The angular correlation analysis techniques presented in section 3.3 were applied to cascades in the odd-mass neutron rich isotopes using the FIPPS data-set. However, no information on spin values could be extracted. For most cascades, angular correlation measurements could not be performed due to statistics limitations. For the case of intense transitions in ^{87}Br and ^{89}Br (with $\approx 10^5$ $\gamma - \gamma$ coincidences) the difficulty was introduced by the presence of strong contaminants. For example the coincidences between the 762-872 keV transitions in ^{87}Br are contaminated by coincidences between 760-869 keV transitions from ^{88}Kr. A similar situation was found in the case of the 506-1039 keV cascade in ^{89}Br. These constraints motivated the investigations into increasing the selectivity by applying an additional gate and measuring triple γ-ray coincidences (see section 3.3.2). The recent EXILL publication on ^{87}Br [82] presented angular correlation measurements for some of the most intense cascades. Angular correlation measurements using the FIPPS data-set, with similar statistics to EXILL, resulted in large uncertainties in the a_2 and a_4 values for the same cascades. Further investigations are needed to finalise the γ-ray angular correlation analysis of the FIPPS data for the case of the Br isotopic chain.

5.2 Discussion

The nuclear Shell Model predicts a smooth evolution of nuclear properties across the nuclear chart for nuclei whose protons and neutrons occupy the same orbitals. This smooth evolution was exploited to deduce the nature of excited states in the Br isotopes studied in this work. A systematic analysis of the energy of excited states and known spin and parity values of the Br isotopic chain and neighbouring nuclei was carried out. All spectroscopic results obtained from combining the FIPPS experiment with the AGATA-VAMOS++ data-set are summarised in Fig. 5.25, showing the obtained level schemes for odd-mass $^{85-91}$Br. The spin values of excited states in ^{85,87}Br, which were studied prior to this work, are taken from the most recent publications [80, 79, 82]. For the case of the ^{89,91,93}Br isotopes, where all the excited states are measured for the first time, spin and parity values are tentatively assigned using the systematics analysis.

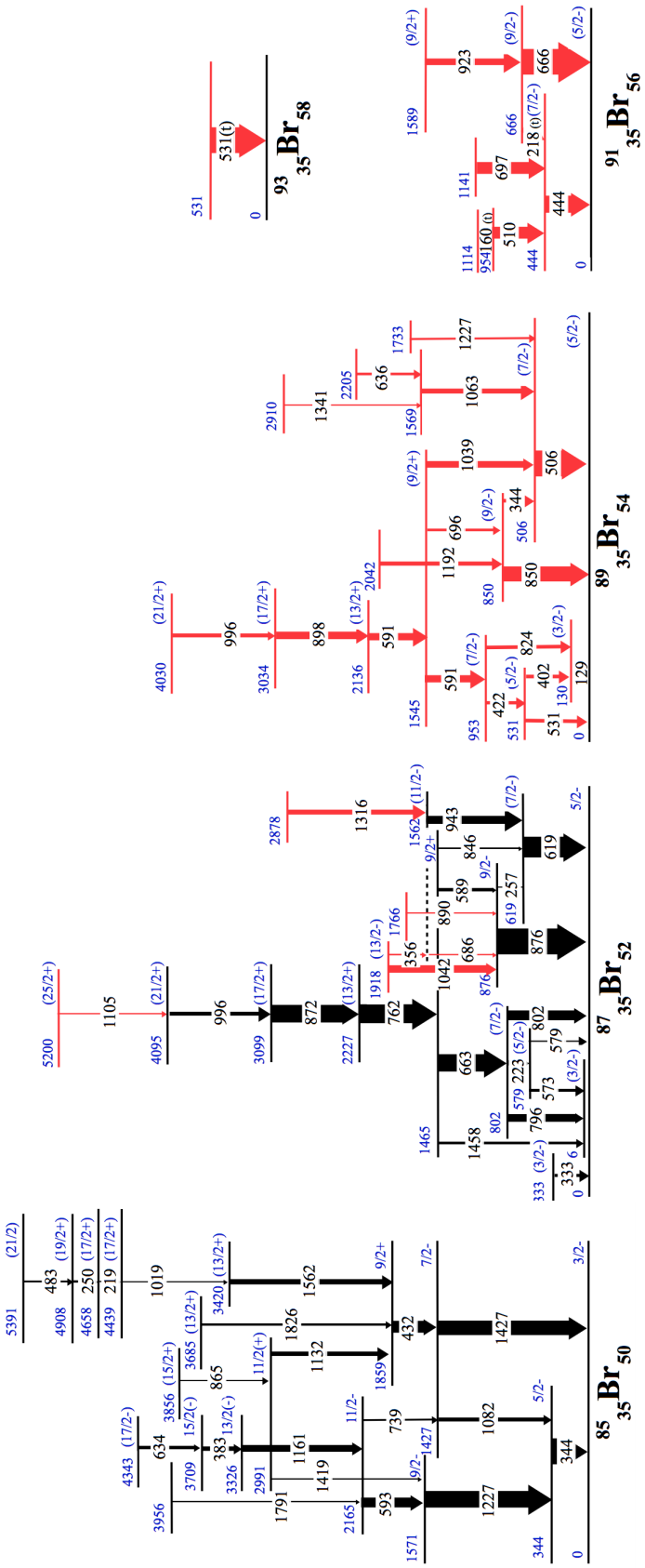

Figure 5.25: Level schemes of odd-mass Br isotopes obtained in this work. Known transitions are indicated in black, newly observed transitions are shown in red. Tentative placements are indicated with (t). The width of the arrows correspond to observed intensities in the AGATA-VAMOS++ data. For ^{85}Br and ^{87}Br, spin values are adopted from the literature [80, 79, 82]. Tentative spin assignments in ^{89}Br and ^{91}Br are performed through a systematic study of excited states in the Br chain and neighbouring nuclei (see text for details).

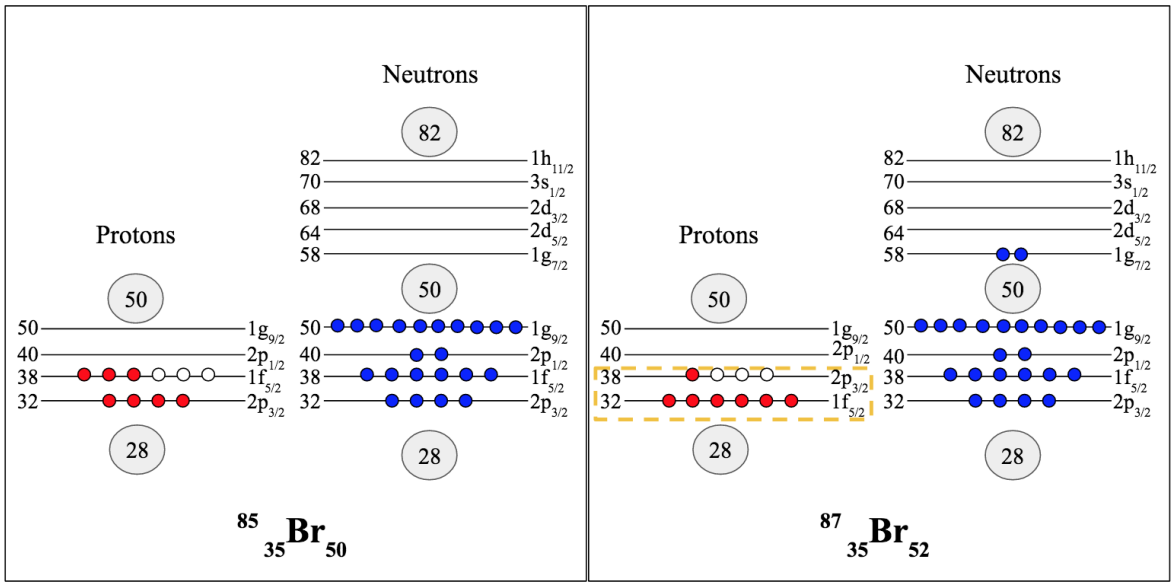

Figure 5.26: Schematic diagram of proton and neutron orbital occupation in ^{85,87}Br. The inversion of the $\pi f_{5/2}$ and $\pi p_{3/2}$ orbitals is marked in yellow.

In the Br region, with $28 < Z < 50$, the proton orbitals involved in nuclear excitations are the $\pi p_{3/2}$, $\pi f_{5/2}$, $\pi p_{1/2}$ and $\pi g_{9/2}$ orbitals. A simplified representation of the proton and neutron valence space in the context of the Shell Model is shown in Fig. 5.26. As can be seen from Fig. 5.25, in the bromine isotopic chain there is a general change in the structure of excited states when going from the $N = 50$ shell closure (^{85}Br) to $N = 52$ (^{87}Br). A first feature to notice is a change in the ground state spin from $3/2^-$ to $5/2^-$. A $3/2^-$ spin parity value was experimentally determined for the ground state of ^{85}Br using angular distributions in (d,^{3}H) reactions [169]. The $5/2^-$ ground state spin and parity value was experimentally established using $\log(ft)$ values in a β decay study of ^{87}Se [79]. The change of ground state spin can be explained by an inversion of the $\pi p_{3/2}$, $\pi f_{5/2}$ orbitals with respect to the standard Shell Model configuration. This inversion of the orbitals has already been observed experimentally in the copper isotopes and reproduced using Large Scale Shell Model calculations [170, 171]. Another noteworthy characteristic is the regular structure built on top of the 9/2+ state in ^{87}Br, not present in ^{85}Br. The distribution of excited states in ^{87}Br into 3 band-like structures was already described in [82] and will be discussed below.

Contrary to the difference in structure of excited states observed between ^{85}Br and ^{87}Br, a similarity was found between the populated excited states of the ^{87}Br and ^{89}Br isotopes. The resemblance is to be expected, since both nuclei have the same proton and similar neutron configurations with neutron pairs occupying the $\nu g_{7/2}$ orbital. The similarity between the level schemes is exploited to assign spin values of excited states in ^{89}Br. As illustrated in Fig. 5.27, both nuclei exhibit excited states distributed into 3 band structures, labelled *Band I, Band II* and *Band III* in the figure. The band head of each band corresponds to a single particle configuration. A series of excited states are built on top of each band head originating from a coupling of the single particle state to collective vibrations of the even-even cores of ^{86}Se and ^{88}Se isotopes [172, 173], which will be demonstrated in detail case by case.

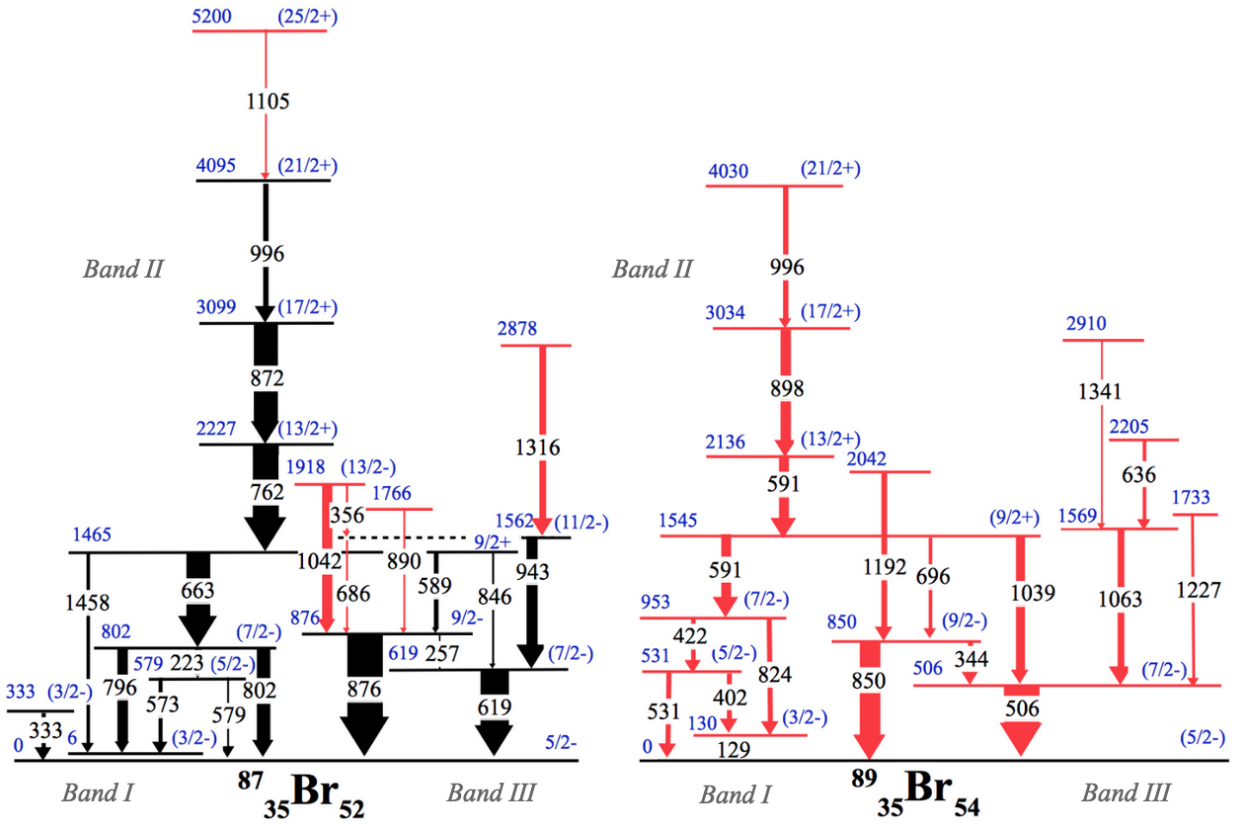

Figure 5.27: Comparison of obtained level schemes of ^{87}Br and ^{89}Br with excited states distributed into 3 band-like structures.

The band head of *Band I* is the low lying 3/2- state. This state was argued to originate from the anomalous coupling of the $(\pi f_{5/2})^3$ multiplet to a core vibration [79, 174]. This state is situated at 6 keV in ^{87}Br and 130 keV in ^{89}Br. A coupling of this state with the 2+ state of the ^{86}Se/ ^{88}Se core gives rise to 7/2- and 5/2- states located at 802 keV and 579 keV for ^{87}Br and 954 keV and 532 keV for ^{89}Br.

In ^{87}Br the 5/2- ground state is the band-head of *Band III* and is interpreted as arising from a proton in the $\pi f_{5/2}$ orbital. Assuming the same ordering of the proton orbitals for bromine isotopes with $N > 52$ the ground states of ^{89}Br and ^{91}Br can tentatively be assigned 5/2- spin and parity. The coupling of the single particle state to a core excitation $\pi f_{5/2} \otimes 2+$ gives rise to 9/2- and 7/2- states which correspond to the 876 and 619 keV states in ^{87}Br, and to the 850 keV and 507 keV states in ^{89}Br. Spin and parity assignments can also be made for ^{91}Br, assuming that the strongest two transitions observed in ^{87}Br and ^{89}Br also correspond to the strongest transitions in ^{91}Br. This results in a spin parity assignment of 9/2- and 7/2- to the 665 keV and 444 keV states in ^{91}Br. The energies of the 9/2- and 7/2- states in ^{87,89,91}Br are compared to the energies of the 2+ states in the Se chain in Fig. 5.28. The behaviour of these states after $N = 50$ supports the spin assignments for *Band III* observed in both ^{89}Br and ^{91}Br isotopes. The band-head state of *Band II* is identified as the 9/2+ state, corresponding to a promotion of a proton to the $\pi g_{9/2}$ orbital. A 9/2+ spin and parity value of

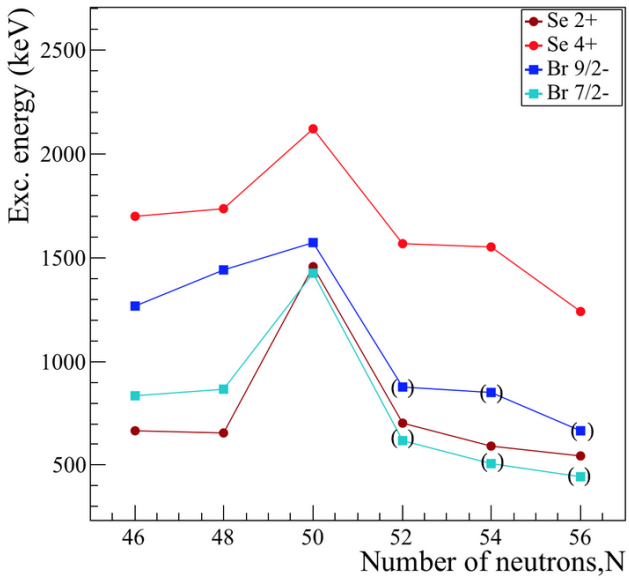

Figure 5.28: Comparison of the energies of the 2+ and 4+ excited states in Se with the 9/2- and 7/2- states in the Br isotopic chain.

the 1465 keV state in ^{87}Br was assigned in both β decay and fission studies [79, 82]. From the observed similarities in structure with respect to ^{87}Br, a spin parity assignment of 9/2+ can be made for the 1545 keV state in ^{89}Br and the 1588 keV state in ^{91}Br. This assignment is supported by the evolution of the energy of the 9/2+ state in neighbouring nuclei. The energy difference between the 9/2+ and 5/2- states is plotted for the Br isotopic chain ($Z = 35$), as well as the As ($Z = 33$), Rb ($Z = 37$) and Y ($Z = 39$) chains in Fig. 5.29 a). A very similar behaviour is observed between the Rb and Br isotopic chains consisting of an increase of the difference between $N = 42$ and $N = 50$, due to the interaction between the proton in the $\pi g_{9/2}$ orbital and the neutrons filling the $\nu g_{9/2}$ orbital [79], with a flattening of the 9/2+ energy for $N > 50$. No experimental information on the energy of the 9/2+ state is available for the As chain. The different behaviour in the Y chain can be explained taking into account the different proton occupation, since at $Z = 37$ the $\pi p_{3/2}$ and $\pi f_{5/2}$ are completely filled. Therefore the proton excitations result in different states and contribute differently to the monopole part of the tensor interaction. The lifetime of the 9/2+ state in this region covers a broad range, as can be seen in Fig. 5.29 b). From the comparison with the Rb chain, a lifetime of the order of a few ns is expected for Br isotopes with $N \geq 50$. A comparison of the reduced transition probabilities would lead to more precise conclusions. However, an evaluation of reduced transition probabilities is difficult due to large uncertainties in published multipolarities and branching ratios.

In the ^{87}Br and ^{89}Br isotopes, a regular structure is built on top of the 9/2+ state, labelled *Band II* in Fig. 5.27. Since the 9/2+ state in ^{87}Br (or ^{89}Br) can be interpreted as a coupling of a proton in the $\pi g_{9/2}$ with the ^{86}Se (or ^{88}Se) core, the excitations observed above this level can be explained as a coupling of the $\pi g_{9/2}$ proton with the 2+ and 4+ excited states of the core. This coupling gives rise to states with spin parity of 13/2+ and 17/2+, which can be assigned to the two excited states on top of the 9/2+ state. A comparison of the energies of these states with energies of the ground state band of

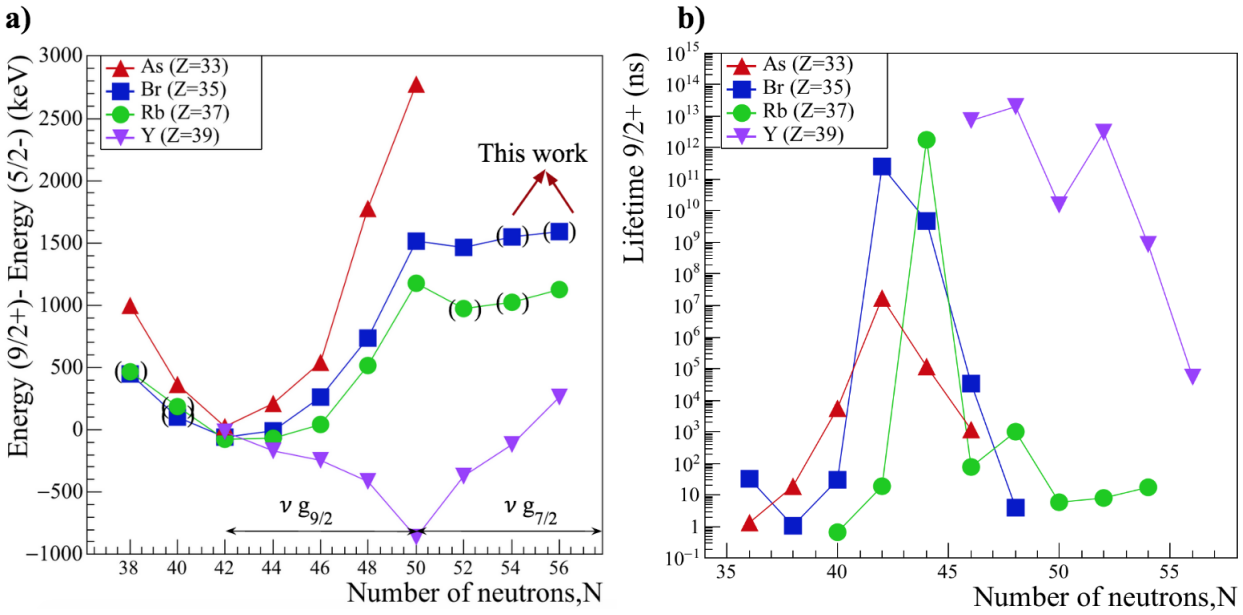

Figure 5.29: a) Systematics of the energy difference between the 9/2+ and 5/2- states for the Br isotopic chain and neighbouring nuclei [7]. b) Lifetime values of the 9/2+ state in the Br chain and neighbouring nuclei [7].

even-even isotopes for $N = 50$, $N = 52$ and $N = 54$ is shown in Fig. 5.30. A smooth evolution of the energy of the 2+ and 13/2+ states is observed for all isotonic chains. This behaviour is in agreement with the spin assignment of 13/2+ to the 2137 keV state in ^{89}Br. A smooth evolution of the 4+ and 17/2+ states is seen in the $N = 52$ chain, while a more "scattered" behaviour is observed for the $N = 50$ and $N = 54$ chains. Despite larger differences in energies observed between the 4+ states of the isotonic chains, the 3036 keV level assigned a spin parity value of 17/2+ in ^{89}Br remains close in energy to the 4+ of ^{88}Se. Consequently supporting the interpretation of a coupling of the $\pi g_{9/2}$ proton to the ^{88}Se core excitation. The ratio of the energies of the 17/2+ and 13/2+, in analogy to the 4+/2+ ratio even-even nuclei, can give an indication on the type of collective excitation and the shape for the nucleus. For ^{87}Br this ratio is equal to 2.14, suggesting a vibrational nucleus. The ratio of 2.5 found for ^{89}Br suggests an increase of deformation. As was pointed out in [82], Large Scale Shell Model Calculations carried out using the NATHAN code are not successfully reproducing the positive parity band built on top of the 9/2+ state. This is possibly due to an increase in collectivity. The Nilsson Model can provide an alternative interpretation of the 9/2+ state and band that is built on top of it. Considering a prolate deformation, the 9/2+ state arises from a proton in the 1/2[440] Nilsson orbital (see Fig. 1.4), with a sequence of rotational states built on the single particle state.

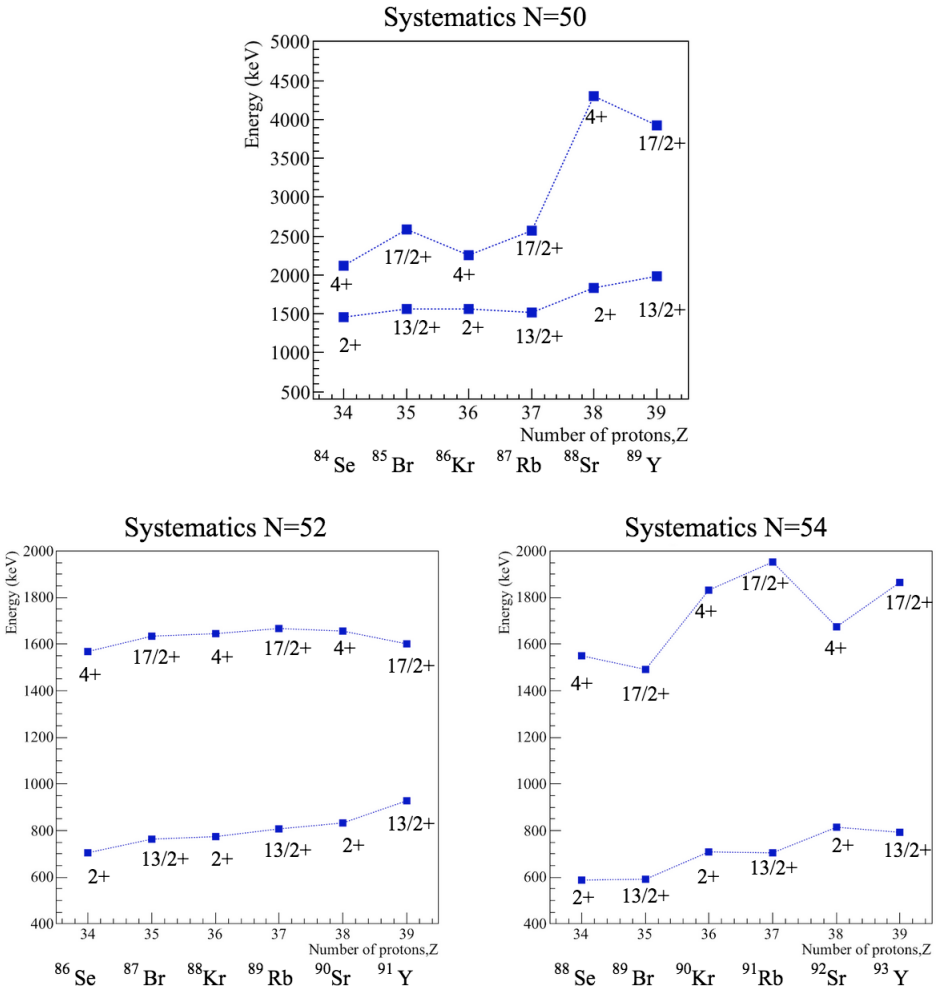

Figure 5.30: Systematics of the energies of the 2+ and 4+ excited states in even-even nuclei compared to the energies of the 13/2+ and 17/2+ states for neighbouring odd-even isotopes. The reported energies of the 13/2+ and 17/2+ states of each isotope are given in reference to the 9/2+ state energy. This comparison is shown for the $N = 50$, $N = 52$ and $N = 54$ isotopes in the Br region.

5.2.1 Comparison with Shell Model calculations

In order to gain further insight into the nature of the excitations and confirm the spin and parity assignments of the observed excited states, a comparison with theoretical predictions was carried out. The experimentally obtained excited states were compared with preliminary results from Large Scale Shell Model calculations performed with the ANTOINE code [16]. Following earlier works [175, 176], a valence space with a ^{78}Ni core and the $f_{5/2}, p_{3/2}, p_{1/2}, g_{9/2}$ proton orbitals and $g_{7/2}, d_{5/2}, d_{3/2}s_{1/2}h_{11/2}$ neutron orbitals was assumed. The set of Two-Body Matrix Elements (TBME) is composed of: the JUN45 interaction [177] for the proton-proton interaction, the GCN5082 interaction [178] for the neutron-neutron interaction, and the Kahana-Lee-Scott interaction [179]. For the neutron-neutron matrix elements originally defined for a ^{100}Sn core, a pairing reduction to incorporate the core polar-

isation mechanism differences between ^{78}Ni and ^{100}Sn [180] was assumed. The cross-shell monopole matrix elements have been constrained to reproduce the spectroscopy evolution with neutron filling up to $N = 56$. In particular, constraints were obtained from the evolution of the 9/2+ and 13/2+ states in Rb and Y isotopes, as well as for the spectroscopy of ^{96}Zr.

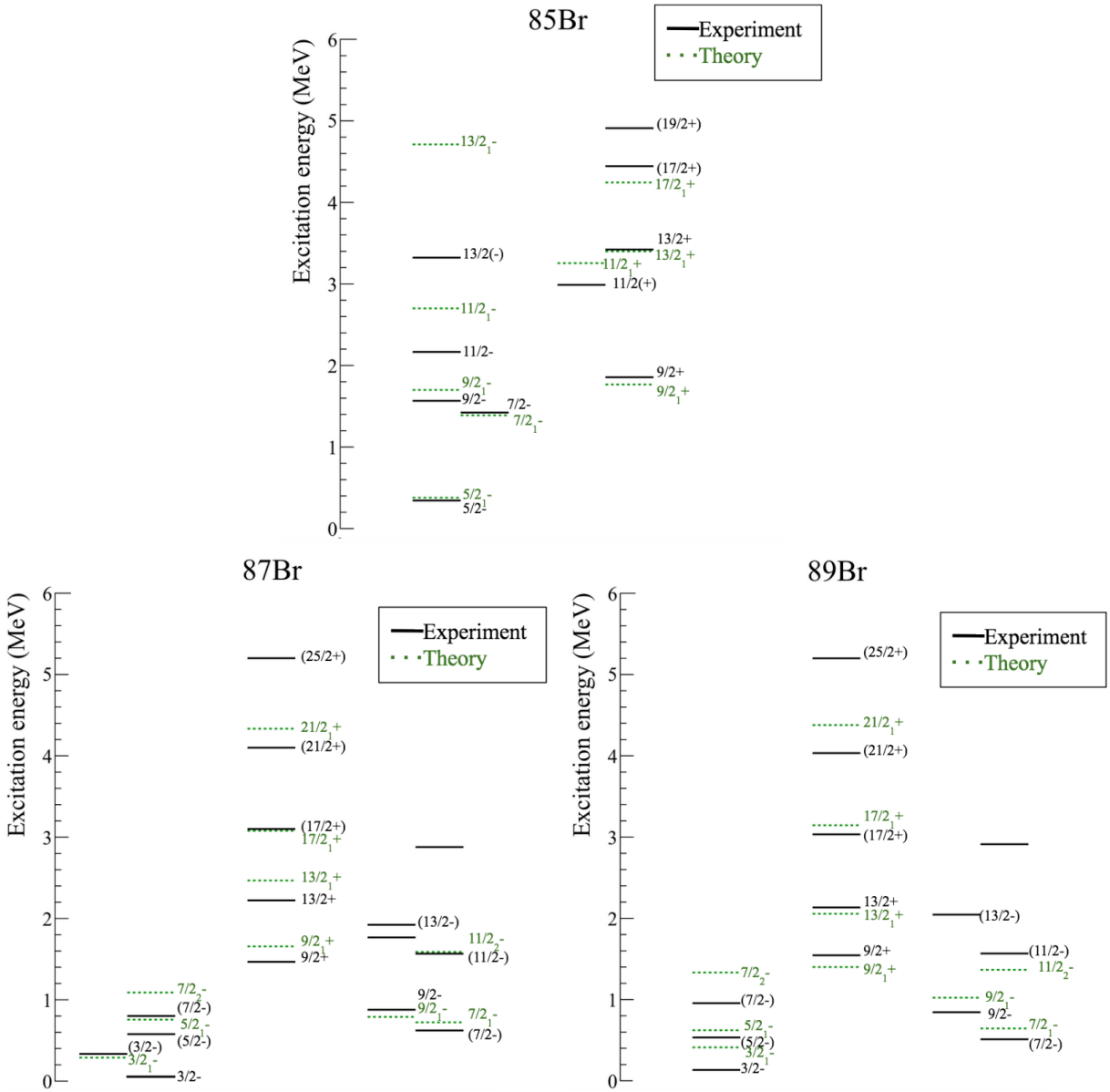

Figure 5.31: Comparison of experimentally measured excited states in ^{85,87,89}Br with SM predictions.

The performed SM calculations predict the change of ground state spin from 3/2- to 5/2- observed between ^{85}Br and ^{87}Br. A comparison of experimental excitation energies and theoretical predictions for excited states in ^{85,87,89}Br is shown in Fig. 5.31. In general, a good agreement between theoretical calculations and experimental values is observed, in particular for the ^{87,89}Br isotopes. The energy of the 9/2+ state in ^{87}Br and ^{89}Br is predicted with an accuracy of $\sim$ 180 keV and $\sim$ 150 keV

respectively. With respect to previous Shell Model calculations performed for the ^{87}Br nucleus [79, 82], the agreement between the excitation energies of the positive parity band built on the 9/2+ state is improved. The disagreement observed for the low lying negative parity states may indicate that they are mainly arising from the coupling of the valence proton with the deformed Se core. New mean field calculations for the neighbouring even-even Se isotopes are ongoing in order to investigate the effect of triaxial deformation in this mass region.

The neutron and proton orbital occupation for selected states, are reported in Table 5.5. The SM calculations predict a strong mixing between the $\pi f_{5/2}$ and $\pi p_{3/2}$ orbitals in the ground state and first excited states. The resulting proton occupation for the $9/2^+_1$ state confirms the interpretation of this state as a proton excitation to the $\pi g_{9/2}$ orbital.

^{85}Br									
	Neutrons					Protons			
State	$d_{5/2}$	$s_{1/2}$	$g_{7/2}$	$d_{3/2}$	$h_{11/2}$	$f_{5/2}$	$p_{3/2}$	$p_{1/2}$	$g_{9/2}$
$3/2^-$(gs)			-			5.38	1.29	0.11	0.22
$5/2^-_1$			-			4.64	1.84	0.19	0.32
$7/2^-_1$			-			4.66	1.96	0.19	0.19
$9/2^-_1$			-			4.80	1.95	0.09	0.17
$9/2^+_1$			-			4.91	0.78	0.12	1.19
^{87}Br									
	Neutrons					Protons			
State	$d_{5/2}$	$s_{1/2}$	$g_{7/2}$	$d_{3/2}$	$h_{11/2}$	$f_{5/2}$	$p_{3/2}$	$p_{1/2}$	$g_{9/2}$
$5/2^-$(g.s.)	1.55	0.13	0.06	0.17	0.09	4.59	1.78	0.32	0.31
$3/2^-_1$	1.59	0.09	0.07	0.14	0.10	4.82	1.60	0.25	0.32
$7/2^-_1$	1.45	0.27	0.04	0.17	0.06	4.63	1.77	0.34	0.26
$9/2^-_1$	1.65	0.14	0.03	0.14	0.04	4.61	1.80	0.31	0.28
$9/2^+_1$	1.52	0.14	0.07	0.18	0.09	4.00	1.51	0.27	1.21
^{89}Br									
	Neutrons					Protons			
State	$d_{5/2}$	$s_{1/2}$	$g_{7/2}$	$d_{3/2}$	$h_{11/2}$	$f_{5/2}$	$p_{3/2}$	$p_{1/2}$	$g_{9/2}$
$5/2^-$(g.s.)	3.18	0.22	0.12	0.33	0.15	4.53	1.77	0.39	0.31
$3/2^-_1$	3.08	0.32	0.12	0.33	0.15	3.85	2.43	0.37	0.35
$7/2^-_1$	3.12	0.32	0.10	0.34	0.12	4.51	1.79	0.39	0.30
$9/2^-_1$	3.07	0.33	0.11	0.37	0.11	4.32	1.94	0.41	0.34
$9/2^+_1$	3.00	0.30	0.13	0.43	0.14	3.68	1.75	0.36	1.21

Table 5.5: Occupation of proton and neutron orbitals for selected states in ^{85,87,89}Br isotopes determined using Large Scale Shell Model calculations.

Conclusion

High lying transitions were added to the ^{87}Br nucleus, extending the known level scheme up to $\sim$ 5 MeV. Excited states were observed for the first time in ^{89,91,93}Br. In the case of the ^{89}Br nucleus, 14 new excited states were identified, establishing the level scheme up to 4 MeV of excitation energy. 11 γ-ray transitions were assigned to ^{91}Br, out of which 7 could be placed in the level scheme. The similarity in structure of excited states in ^{87,89,91}Br was exploited, along with systematics of neighbouring nuclei, to perform tentative spin assignments. The ground state and a series of excited states in these isotopes were attributed to proton configurations involving the $\pi p_{3/2}$, $\pi f_{5/2}$, $\pi p_{1/2}$ and $\pi g_{9/2}$ orbitals. The bands of excited states built on top of single particle excitations were interpreted as originating from the coupling of the single particle to collective excitations of the core. A relatively constant energy of $\sim$ 1.5 MeV for the 9/2+ state, associated to a single particle excitation to the $\pi g_{9/2}$, was observed in the odd-mass Br isotopes with $N > 50$. An upper limit to the lifetime of this state could be set at 5 ns, contrary to the lifetime of 20 ns in the 9/2+ state in ^{87}Br suggested in [79]. The structure built on top of the ^{87}Br and ^{89}Br indicate a smooth increase of collectivity with increasing neutron number. The analysis of ^{93}Br was challenging due to limited statistics, nevertheless one transition could be tentatively assigned to this nucleus. These findings constitute a good first step in the understanding of nuclear structure of odd-mass Br isotopes situated above $N = 50$. Future work is necessary on angular correlation measurements which can conclusively establish the spin values of the observed excited states. A comparison of the experimental results with preliminary Large Scale Shell Model calculations was used to test a new nucleon-nucleon interaction outside of the ^{78}Ni core. These investigations will be further developed in a future publication [181].

Conclusions and future perspectives

In this thesis work, new nuclear structure information for neutron rich Kr and Br isotopes produced in fission reactions was presented. The evolution of deformation in the Kr chain, located in a region of the nuclear chart known for a rapid onset of collectivity, was examined based on the obtained spectroscopic results. In addition, newly observed excited states in neutron rich Br isotopes were compared to predictions from Large Scale Shell Model calculations in order to benchmark the nucleon-nucleon interaction outside of the ^{78}Ni core.

For the first time in these isotopic chains, a systematic study was carried out combining data collected at two state-of-the-art facilities: the AGATA-VAMOS++ setup at GANIL and the FIPPS instrument at the ILL. Excited states in neutron rich Kr and Br isotopes were populated using two different fission reactions: neutron induced fission of ^{235}U and fission of a ^{238}U beam on a Be target. A complete description and characterisation of the first fission campaign that took place at FIPPS, employing an active fission target, was provided in this thesis work. The improved performance with respect to the EXILL campaign, in terms of energy resolution and selectivity provided by the active fission target, was demonstrated. In addition, the techniques employed for the γ-ray spectroscopy analysis and construction of level schemes of both the FIPPS and AGATA-VAMOS++ data-sets were presented. The complementarity of both setups gave access to prompt γ-ray emission of very neutron rich nuclei as well as transitions following isomeric decay in the tens of ns range.

New γ-ray transitions were identified and added to the known level schemes of $^{90-95}$Kr. The level scheme of ^{94}Kr was significantly extended with the observation of 14 new γ-ray transitions and 10 new excited states. The precise time information provided by the active fission target was exploited to carry out investigations across isomeric states, using prompt-delayed coincidences in the FIPPS data-set. In ^{94}Kr a 38(6) ns isomeric state at 3445 keV excitation energy was observed (recently assigned spin-parity of (9-) in [154]). The isomeric nature of the 354 keV (7/2+) state in ^{93}Kr was also confirmed.

New high excitation energy states were added to the known level scheme of ^{87}Br. Excited states in ^{89,91,93}Br were observed for the first time. From the AGATA-VAMOS++ data an upper limit of a 5 ns lifetime to all of the measured excited states could be established. This upper limit is of particular interest for the 9/2+ states, suggested to have isomeric nature in previous publications [79, 81]. An

analysis of the systematics of excited states across the Br chain and neighbouring nuclei allowed spin assignments and an interpretation of the newly observed levels. The obtained results provide further evidence of proton excited states corresponding to configurations involving the $\pi p_{3/2}$, $\pi f_{5/2}$, $\pi p_{1/2}$ and $\pi g_{9/2}$ orbitals, as well as single particle states coupled to collective excitations of the corresponding Se cores. A relatively constant energy of $\sim 1.5\,\text{MeV}$ for the 9/2+ state was observed in the odd-mass Br isotopes with $N > 50$, analogous to the behaviour in the Rb chain. The measured spectroscopic information was compared to preliminary results from Large Scale Shell Model calculations performed with the ANTOINE code [16]. A general good agreement between the calculations and experimental results was observed. The 9/2+ state was confirmed to arise from a single proton in the $\pi g_{9/2}$ orbital.

In order to achieve a complete description of the observed excited states, the excitation energy needs to be complemented with measured spin and parity values as well as lifetimes. The basis of the γ-ray angular correlation technique, used to extract spin values, was described. The analysis of angular correlation measurements in the fission experiment performed using the composite FIPPS+IFIN-HH array was discussed. Additional work is required to apply this technique to obtain spin values of the newly observed excited states in the Kr and Br isotopes. In terms of lifetimes, fast-timing measurements of the lifetime of the 9/2+ state in neutron rich Br isotopes will be of particular interest.

As for future developments of the FIPPS instrument, the HPGe array will be coupled to a large acceptance recoil spectrometer formed by a Gas Filled Magnet (GFM) [182, 183], which will be used in fission experiments to identify the fission fragments. The GFM will increase the selectivity and sensitivity of the instrument for structure studies of fission fragments, in addition to providing essential measurements for fission studies. This new facility will open the possibility for investigations of excited states at the neutron rich border of the Kr and Br isotopes studied in this work. Such are the cases of ^{93}Br, were a single tentative assignment was performed, and ^{96}Kr, where only two transitions are known [52].

Further insight into the nuclear structure along the Kr and Br isotopic chains will be gained through the comparison with theoretical models. Monte Carlo Shell Model calculations, which have been performed for the neighbouring Zr chain [24], are promising and could potentially provide a microscopic description of the evolution of collectivity and the nature of the isomeric states in the neutron rich Kr isotopes. For the case of the neutron rich Br isotopes, the preliminary results from Large Scale Shell Model calculations presented in this work are currently being extended towards more neutron rich nuclei. The comparison between the experimental results obtained in this thesis and the new Shell Model calculations presented will be used to test a new nucleon-nucleon interaction above the ^{78}Ni core.

Bibliography

[1] R. F. Casten. *Nuclear Structure from a Simple Perspective*. Oxford University Press, 1990.

[2] E. Rutherford. "The Scattering of α and β Particles by Matter and the Structure of the Atom". *Philosophical Magazine* Series 6, vol. 21 (1911).

[3] M. G. Mayer. "On Closed Shells in Nuclei. II". *Phys. Rev.* 75, 1969 (1949). DOI: 10.1103/PhysRev.75.1969.

[4] O. Haxel *et al.* "On the Magic Numbers in Nuclear Structure". *Phys. Rev.* 75, 1766 (1949). DOI: 10.1103/PhysRev.75.1766.2.

[5] A. Bohr. K. Dan. Vidensk. Selsk. *Mat. Fys.* 26, 14 (1952).

[6] M. Mumpower *et al.* "The impact of individual nuclear properties on r-process nucleosynthesis". *Prog. Part. Nucl. Phys.* 86, 86 (2016). DOI: 10.1016/j.ppnp.2015.09.001.

[7] Brookhaven National Laboratory NNDC. *https://www.nndc.bnl.gov/nudat2*.

[8] I. Ahmad and W.R. Phillips. "Gamma rays from fission fragments". *Rep. Prog. Phys.* 58, 1415 (1995). DOI: 10.1088/0034-4885/58/11/002.

[9] I. Y. Lee. "Physics with GAMMASPHERE and beyond". *Prog. Part. Nucl. Phys.* 38, 65 (1997). DOI: 10.1016/S0146-6410(97)00009-4.

[10] M. Rejmund. "Performance of the improved larger acceptance spectrometer: VAMOS++". *NIM A* 646, 184 (2011). DOI: 10.1016/j.nima.2011.05.007.

[11] S. Akkoyun *et al.* "AGATA—Advanced GAmma Tracking Array". *NIM A* 668, 26 (2012). DOI: 10.1016/j.nima.2011.11.081.

[12] C. Michelagnoli *et al.* "FIPPS (FIssion Product Prompt γ-ray Spectrometer) and its first experimental campaign". *EPJ Web Conf.* 193, 04009 (2018). DOI: 10.1051/epjconf/201819304009.

[13] H. Hergert. "A Guided Tour of ab initio Nuclear Many-Body Theory". *Front. Phys.* 8 (2020). DOI: 10.3389/fphy.2020.00379.

[14] E. Gapon and D. Iwanenko. "Zur Bestimmung der Isotopenzahl". *Naturwissenschaften* 20, 792 (1932). DOI: 10.1007/BF01494007.

[15] R. D. Woods and D. S. Saxon. "Diffuse Surface Optical Model for Nucleon-Nuclei Scattering". *Phys. Rev.* 95, 577 (1954). DOI: 10.1103/PhysRev.95.577.

[16] E. Caurier *et al.* "The shell model as a unified view of nuclear structure". *Rev. Mod. Phys.* 77, 427 (2005). DOI: 10.1103/RevModPhys.77.427.

[17] L. Coraggio *et al.* "Shell-model calculations and realistic effective interactions". *Prog. Part. Nucl. Phys.* 62, 135 (2009). DOI: 10.1016/j.ppnp.2008.06.001.

[18] B. A. Brown et al. *OXBASH code, MSU-NSCL report number 1289.*

[19] T. Mizukai. *RIKEN Acc. Progr. Report 33, 14 (2000).*

[20] M. Honma *et al.* "Diagonalization of Hamiltonians for Many-Body Systems by Auxiliary Field Quantum Monte Carlo Technique". *Phys. Rev. Lett.* 75, 1284 (1995). DOI: 10.1103/PhysRevLett.75.1284.

[21] T. Otsuka *et al.* "Monte Carlo shell model for atomic nuclei". *Prog. Part. Nucl. Phys.* 47, 319 (2001). DOI: 10.1016/S0146-6410(01)00157-0.

[22] N. Shimizu *et al.* "New-generation Monte Carlo shell model for the K computer era". *Prog. Theor. Exp. Phys.* 01A205 (2012). DOI: 10.1093/ptep/pts012.

[23] T. Mizusaki *et al.* "Quantum Monte Carlo diagonalization with angular momentum projection". *Phys. Rev. C* 53, 2786 (1996). DOI: 10.1103/PhysRevC.53.2786.

[24] T. Togashi *et al.* "Quantum Phase Transition in the Shape of Zr isotopes". *Phys. Rev. Lett.* 117, 172502 (2016). DOI: 10.1103/PhysRevLett.117.172502.

[25] R. Lucas. "Nuclear shapes". *Europhysics News* 32 (2001). DOI: 10.1051/epn:2001101.

[26] A. Bohr and B. R. Mottleson. *Nuclear Structure, Vol II.* World Scientific, 1975.

[27] K. Heyde and J. L. Wood. "Nuclear shapes: from earliest ideas to multiple shape coexisting structures". *Phys. Scr.* 91, 083008 (2016). DOI: 10.1088/0031-8949/91/8/083008.

[28] K. Heyde and J. L. Wood. "Shape coexistence in atomic nuclei". *Rev. Mod. Phys.* 83, 1467 (2011). DOI: 10.1103/RevModPhys.83.1467.

[29] L. P. Gaffney *et al.* "Studies of pear-shaped nuclei using accelerated radioactive beams". *Nature* 497, 199 (2013). DOI: 10.1038/nature12073.

[30] D. L. Hill and J. A. Wheeler. "Nuclear Constitution and the Interpretation of Fission Phenomena". *Phys. Rev.* 89, 1102 (1953). DOI: 10.1103/PhysRev.89.1102.

[31] M. Vetter K.E.G. Löbner and V. Honig. "Nuclear intrinsic quadrupole moment and deformation parameters". *Nucl. Data Tab.* 7, 495 (1970).

[32] C. F. v. Weizsäcker. "Zur Theorie der Kernmassen". *Z. Physik* 96, 431 (1935). DOI: 10.1007/BF01337700.

[33] J. Rainwater. "Nuclear Energy Level Argument for a Spheroidal Nuclear Model". *Phys. Rev.* 79, 432 (1950). DOI: 10.1103/PhysRev.79.432.

[34] J. A. Wheeler. "Molecular Viewpoints in Nuclear Structure". *Phys. Rev.* 52, 1083 (1937). DOI: 10.1103/PhysRev.52.1083.

[35] K. S. Krane. *Introductory Nuclear Physics*. John Wiley & Sons, 1988.

[36] S. G. Nilsson. "Binding states of individual nucleons in strongly deformed nuclei". *Kong. Dan. Vid. Sel. Mat. Fys. Med.* 29N16, 1 (1955).

[37] P. Ring and P. Schuck. *The nuclear many body problem*. Spinger, 1980.

[38] L. N. Cooper J. Bardeen and J. R. Schrieffer. "Microscopic Theory of Superconductivity". *Phys. Rev.* 106, 162 (1957). DOI: 10.1103/PhysRev.106.162.

[39] J. Dechargé and D. Gogny. "Hartree-Fock-Bogolyubov calculations with the $D1$ effective interaction on spherical nuclei". *Phys. Rev. C* 21, 1568 (1980). DOI: 10.1103/PhysRevC.21.1568.

[40] D. Vautherin and D. M. Brink. "Hartree-Fock Calculations with Skyrme's Interaction. I. Spherical Nuclei". *Phys. Rev. C* 5, 626 (1972). DOI: 10.1103/PhysRevC.5.626.

[41] D. Vautherin. "Hartree-Fock Calculations with Skyrme's Interaction. II. Axially Deformed Nuclei". *Phys. Rev. C* 7, 296 (1973). DOI: 10.1103/PhysRevC.7.296.

[42] M. Bender *et al.* "Self-consistent mean-field models for nuclear structure". *Rev. Mod. Phys.* 75, 121 (2003). DOI: 10.1103/RevModPhys.75.121.

[43] S. Hilaire and M. Girod. "Large-scale mean-field calculations from proton to neutron drip lines using the D1S Gogny force". *Eur. Phys. J. A* 33, 237 (2007). DOI: 10.1140/epja/i2007-10450-2.

[44] J. Delaroche *et al.* "Structure of even-even nuclei using a mapped collective Hamiltonian and the D1S Gogny interaction". *Phys. Rev. C* 81, 014303 (2010). DOI: 10.1103/PhysRevC.81.014303.

[45] A. Sobiczewski D. A. Arseniev and V. G. Soloviev. "Equilibrium deformations of neutron-rich nuclei in the A $\sim$ 100 region". *Nucl. Phys. A* 139, 269 (1969). DOI: 10.1016/0375-9474(69)91109-9.

[46] E. Cheifetz *et al.* "Experimental information concerning deformation of neutron rich nuclei in the A$\sim$100 Region". *Phys. Rev. Lett.* 25, 38 (1970). DOI: 10.1103/PhysRevLett.25.38.

[47] J. H. Hamilton *et al.* "New insights from studies of spontaneous fission with large detector arrays". *Prog. Part. Nucl. Phys.* 35, 635 (1995). DOI: 10.1016/0146-6410(95)00048-N.

[48] C. Sotty *et al.* "$^{97}_{37}Rb_{60}$: The Cornerstone of the Region of Deformation around A $\sim$ 100". *Phys. Rev. Lett.* 115, 172501 (2015). DOI: 10.1103/PhysRevLett.115.172501.

[49] G. S. Simpson *et al.* "Near-yrast, medium-spin, excited states of 91Rb, 93Rb, and 95Rb". *Phys. Rev. C* 82, 024302 (2010). DOI: 10.1103/PhysRevC.82.024302.

[50] J. A. Pinston *et al.* "Shape coexistence in the very neutron-rich odd-odd Rb 96". *Phys. Rev. C* 71, 037304 (2005). DOI: 10.1103/PhysRevC.71.064327.

[51] M. Birch B. Pritychenko and B.Singh. "Revisiting Grodzins systematics of B(E2) values". *Nucl. Phys. A* 962, 73 (2017). DOI: 10.1016/j.nuclphysa.2017.03.011.

[52] J. Dudouet *et al.* "$^{96}_{36}Kr_{60}$-Low-Z Boundary of the Island of Deformation at N=60 ". *Phys. Rev. Lett.* 118, 162501 (2017). DOI: 10.1103/PhysRevLett.118.162501.

[53] F. Flavingy *et al.* "Shape Evolution in Neutron-rich Krypton Isotopes beyond N=60: First spectroscopy of ^{98,100}Kr". *Phys. Rev. Lett.* 118, 242501 (2017). DOI: 10.1103/PhysRevLett.118.242501.

[54] S. Michiaki and A. Akito. "Shape transition of nuclei with mass around A = 100". *Nucl. Phys. A* 515, 77 (1990). DOI: 10.1016/0375-9474(90)90323-E.

[55] M. Böyükata *et al.* "Description of nuclei in the $A \approx 100$ mass region with the interacting boson model". *J. Phys. G: Nucl. Part. Phys.* 37, 105102 (2010). DOI: 10.1088/0954-3899/37/10/105102.

[56] R. Rodríguez-Guzmán *et al.* "Charge radii and structural evolution in Sr, Zr, and Mo isotopes". *Phys. Lett B* 691, 202 (2010). DOI: 10.1016/j.physletb.2010.06.035.

[57] P. Moller *et al.* "Nuclear Ground-State Masses and Deformations". *At. Data Nucl. Data Tables* 59, 185 (1995). DOI: 10.1006/adnd.1995.1002.

[58] N. Shimizu *et al.* "Variational procedure for nuclear shell-model calculations and energy-variance extrapolation". *Phys. Rev. C* 85, 054301 (2012). DOI: 10.1103/PhysRevC.85.054301.

[59] C. M. Jensen *et al.* "Gamma rays from thermal neutron capture in ^{86}Kr". *Phys. Rev. C* 15, 1972 (1977). DOI: 10.1103/PhysRevC.15.1972.

[60] K. Haravu *et al.* "^{86}Kr$(d,p)^{87}$Kr Reaction". *Phys. Rev. C* 1, 938 (1970). DOI: 10.1103/PhysRevC.1.938.

[61] E. R. Flynn *et al.* "^{84}Kr$(t,p)^{86}$Kr and ^{86}Kr$(t,p)^{88}$Kr reactions". *Phys. Rev. C* 13, 568 (1976). DOI: 10.1103/PhysRevC.13.568.

[62] T. Rzaca-Urban *et al.* "Shapes of the neutron-rich $^{88-94}$Kr nuclei". *Eur. Phys. J. A* 9, 165 (2000). DOI: 10.1007/s100500070033.

[63] J. K. Hwang *et al.* "Identification of levels in ^{159}Sm and high spin states in ^{89,91}Kr". 78, 017303 (2008). DOI: 10.1103/PhysRevC.78.017303.

[64] J. K. Hwang *et al.* "High spin states in ^{151,153}Pr, ^{157}Sm, and ^{93}Kr". *Phys. Rev. C* 82, 034308 (2010). DOI: 10.1103/PhysRevC.82.034308.

[65] K. Li *et al.* "Identification of high spin states in neutron rich ^{88,90,92} Kr and ^{86} Se". *Int. J. Mod. Phys. E* 20, 1825 (2011). DOI: 10.1142/S0218301311019635.

[66] T. Rzaca-Urban *et al.* "Structure of ^{90,91}Kr nuclei: Solving the puzzle of their population in fission". *Phys. Rev. C* 95, 064302 (2017). DOI: 10.1103/PhysRevC.95.064302.

[67] J. M. Régis *et al.* "B (E2; $2_1^+ \rightarrow 0_1^+$) value in ^{90}Kr". *Phys. Rev. C* 90, 067301 (2014). DOI: 10.1103/PhysRevC.90.067301.

[68] P. Delahaye *et al.* "High-accuracy mass measurements of neutron-rich Kr isotopes". *Phys. Rev. C* 74, 034331 (2006). DOI: 10.1103/PhysRevC.74.034331.

[69] S. Naimi *et al.* "Critical-Point Boundary for the Nuclear Quantum Phase Transition Near $A = 100$ from Mass Measurements of ^{96,97}Kr". *Phys. Rev. Lett.* 105, 032502 (2010). DOI: 10.1103/PhysRevLett.105.032502.

[70] M. Albers *et al.* "Evidence for a Smooth Onset of Deformation in the Neutron-Rich Kr Isotopes". *Phys. Rev. Lett.* 108, 062701 (2012). DOI: 10.1103/PhysRevLett.108.062701.

[71] M. Albers *et al.* "Shape dynamics in neutron-rich Kr isotopes: Coulomb excitation of ^{92}Kr, ^{94}Kr and ^{96}Kr". *Nucl. Phys. A* 899, 1 (2013). DOI: 10.1016/j.nuclphysa.2013.01.013.

[72] J. Genevey *et al.* "First observation of low-lying excited states in the very neutron-rich ^{95}Kr". *Phys. Rev. C* 73, 037308 (2006). DOI: 10.1103/PhysRevC.73.037308.

[73] N. Marginean *et al.* "Evolution of deformation in the neutron-rich krypton isotopes: ^{96}Kr". *Phys. Rev. C* 80, 021301 (2009). DOI: 10.1103/PhysRevC.80.021301.

[74] P. Hosmer *et al.* "Half-lives and branchings for beta-delayed neutron emission for neutron-rich Co–Cu isotopes in the r-process". *Phys. Rev. C* 82,025806 (2010). DOI: 10.1103/PhysRevC.82.025806.

[75] A. Prévost *et al.* "Medium-spin excitations of the neutron-rich ^{84}Se isotope: Possible decrease in energy of the N = 50 neutron-core excitation". *Eur. Phys. J. A* 22, 391 (2004). DOI: 10.1140/epja/i2004-10063-3.

[76] L. Olivier *et al.* "Persistence of the $Z = 28$ Shell Gap Around ^{78}Ni: First Spectroscopy of ^{79}Cu". *Phys. Rev. Lett.* 119, 192501 (2017). DOI: 10.1103/PhysRevLett.119.192501.

[77] F. Nowacki *et al.* "Shape Coexistence in ^{78}Ni as the Portal to the Fifth Island of Inversion". *Phys. Rev. Lett.* 117, 272501 (2016). DOI: 10.1103/PhysRevLett.117.272501.

[78] R. Taniuchi *et al.* "^{78}Ni revealed as a doubly magic stronghold against nuclear deformation". *Nature* 569, 53 (2019). DOI: 10.1038/s41586-019-1155-x.

[79] J. Wiśniewski *et al.* "Excited states in ^{87}Br populated in β decay of ^{87}Se". *Phys. Rev. C* 100, 054331 (2019). DOI: 10.1103/PhysRevC.100.054331.

[80] A. Astier *et al.* "High-spin excitations of $^{84}_{35}\mathrm{Br}_{49}$ and $^{85}_{35}\mathrm{Br}_{50}$: Mapping the proton sub-shells towards ^{78}Ni". *Eur. Phys. J. A* 30, 541 (2006). DOI: 10.1140/epja/i2006-10151-4.

[81] N. Fotiades *et al.* "High-spin states in N = 50 ^{85}Br and ^{87}Rb nuclei". *Phys. Rev. C* 71, 064312 (2005). DOI: 10.1103/PhysRevC.71.064312.

[82] B. M. Nyakó *et al.* "Medium-spin states of the neutron-rich nucleus ^{87}Br". *Phys. Rev. C* 103, 034304 (2021). DOI: 10.1103/PhysRevC.103.034304.

[83] M. Czerwiński *et al.* "Neutron-proton multiplets in the nucleus Br 88". *Phys. Rev. C* 92, 014328 (2015). DOI: 10.1103/PhysRevC.92.014328.

[84] W. Urban *et al.* "Low-spin structure of $^{86}_{35}\mathrm{Br}_{51}$ and $^{86}_{36}\mathrm{Kr}_{50}$ nuclei: The role of the g 7 / 2 neutron orbital". *Phys. Rev. C* 94, 044328 (2016). DOI: 10.1103/PhysRevC.94.044328.

[85] B. M. Nyakó *et al.* "Medium-spin states of the neutron-rich ^{87,89} Br isotopes: configurations and shapes". *J. Phys.: Conf. Ser.* 724, 012051 (2016). DOI: 10.1088/1742-6596/724/1/012051.

[86] O. Hahn and F. Strassmann. "Über den Nachweis und das Verhalten der bei der Bestrahlung des Urans mittels Neutronen entstehenden Erdalkalimetalle". *Naturwissenschaften* 27, 11 (1939). DOI: 10.1007/BF01488241.

[87] L. Meitner and O. R. Frisch. "Products of the Fission of the Uranium Nucleus". *Nature* 143, 471 (1939). DOI: 10.1038/143471a0.

[88] C. Wagemans. *The nuclear fission process*. CRC press, 1991.

[89] A. N. Andreyev *et al.* "Nuclear fission: a review of experimental advances and phenomenology". *Rep. Prog. Phys.* 81, 016301 (2018). DOI: 10.1088/1361-6633/aa82eb.

[90] M. Jentschel *et al.* "EXILL- a high-efficiency, high-resolution setup for γ-spectroscopy at an intense cold neutron beam facility. " *JINST* 12, P11003 (2017). DOI: 10.1088/1748-0221/12/11/P11003.

[91] K.-H. Schmidt and B. Jurado. *General model description of fission observables. Rapport technique, CENBG, CNRS/IN2P3 (2010).*

[92] V. M. Strutinsky. "Shell effects in nuclear masses and deformation energies". *Nucl. Phys. A* 95, 420 (1967). DOI: 10.1016/0375-9474(67)90510-6.

[93] M. Lebois *et al.* "Development of a kinematically focused neutron source with the p(^{7}Li,n)^{7}Be inverse reaction". *NIM A* 735, 145 (2014). DOI: 10.1016/j.nima.2013.07.061.

[94] M. Lebois *et al.* "The ν-ball Campaign at ALTO". *Acta Phys. Pol. B* 50, 425 (2019). DOI: 10.5506/APhysPolB.50.425.

[95] M. Lebois *et al.* "The ν-ball γ-spectrometer". *NIM A* 960, 163580 (2020). DOI: 10.1016/j.nima.2020.163580.

[96] P. A. Söderström *et al.* "Installation and commissioning of EURICA – Euroball-RIKEN Cluster Array". *NIM B* 317, 649 (2013). DOI: 10.1016/j.nimb.2013.03.018.

[97] P. H. Regan *et al.* "Precision Lifetime Measurements Using LaBr3 Detectors With Stable and Radioactive Beams". *EPJ Web of Conferences* 63, 01008 (2013). DOI: 10.1051/epjconf/20136301008.

[98] B. Bucher *et al.* "Direct Evidence of Octupole Deformation in Neutron-Rich ^{144}Ba". *Phys. Rev. Lett.* 116, 112503 (2016). DOI: 10.1103/PhysRevLett.116.112503.

[99] G. Savard *et al.* "Radioactive beams from gas catchers: The CARIBU facility". *NIM B* 266, 4086 (2008). Proceedings of the XVth International Conference on Electromagnetic Isotope Separators and Techniques Related to their Applications. DOI: https://doi.org/10.1016/j.nimb.2008.05.091.

[100] J. Eberth and J. Simpson. "From Ge(Li) detectors to gamma-ray tracking arrays–50 years of gamma spectroscopy with germanium detectors". *Prog. Part. Nucl. Phys* 60, 283 (2008). DOI: 10.1016/j.ppnp.2007.09.001.

[101] C. Michelagnoli. "The lifetime of the 6.79 MeV state in ^{15}O as a challenge for nuclear astrophysics and γ-ray spectroscopy: a new DSAM measurement with the AGATA Demonstrator array". PhD thesis. Università degli Studi di Padova, 2013.

[102] G. Maquart. "Transition de forme à haut spin dans le noyau octupolaire de thorium 223 et autres aspects méthodologiques de la spectroscopie gamma moderne". PhD thesis. Université de Lyon, 2017.

[103] Website of the Institute Laue-Langevin: *https://www.ill.eu/*.

[104] E. G. Kessler *et al.* "The GAMS4 flat crystal facility". *NIM A* 457, 187 (2001). DOI: 10.1016/S0168-9002(00)00753-1.

[105] M. Jentschel. "The GRID Technique: Current Status and New Trends". *J. Res. Natl. Inst. Stand. Technol.* 105, 25 (2000). DOI: 10.6028/jres.105.004.

[106] P. Armbruster *et al.* "The recoil separator Lohengrin: Performance and special features for experiments". *NIM* 139, 213 (1976). DOI: 10.1016/0029-554X(76)90677-7.

[107] F. Azaiez. "EXOGAM: a γ-ray spectrometer for radioactive beams". *Nucl. Phys. A* 654 (1999). DOI: https://doi.org/10.1016/S0375-9474(00)88588-7.

[108] J. M. Régis *et al.* "Germanium-gated $\gamma - \gamma$ fast timing of excited states in fission fragments using the EXILL&FATIMA spectrometer". *NIMA* 763, 210 (2014). DOI: 10.1016/j.nima.2014.06.004.

[109] R. Alvarez. "The GASP array". *Nucl. Phys. News* 3, 10 (1993).

[110] G. Bocchi *et al.* "The mutable nature of particle-core excitations with spin in the one-valence-proton nucleus 133 Sb". *Phys. Lett. B* 760, 273 (2016). DOI: 10.1016/j.physletb.2016.06.065.

[111] L. W. Iskra *et al.* "Medium and high spin structure in the ^{94} Y isotope produced in fission induced by cold neutrons". *Phys. Scr.* 92, 104001 (2017). DOI: 10.1088/1402-4896/aa842a.

[112] S. Ansari *et al.* "Experimental study of the lifetime and phase transition in neutron-rich ^{98,100,102}Zr". *Phys. Rev. C* 96, 054323 (2017). DOI: 10.1103/PhysRevC.96.054323.

[113] M. Barani. "Study of the performance of the upgraded FIPPS HPGe array: Compton background suppression and fission tagging". MA thesis. Universita di Milano, 2019.

[114] F. Kandzia *et al.* "Development of a liquid scintillator based active fission target for FIPPS". *Eur. Phys. J. A* 56, 207 (2020). DOI: 10.1140/epja/s10050-020-00201-0.

[115] G. Bocchi. "Interplay between single-particle and core excitations: gamma-ray spectroscopy of low-lying states in ^{41,49}Ca and ^{133}Sb nuclei". PhD thesis. Universita di Milano, 2016.

[116] G. Belier *et al.* "Characterization and development of an active scintillating target for nuclear reaction studies on actinides". *NIM A* 664, 341 (2012). DOI: 10.1016/j.nima.2011.09.065.

[117] CAEN. *User Manual UM5960, CoMPASS.*

[118] V.T. Jordanov and G.F. Knoll. "Digital synthesis of pulse shapes in real time for high resolution radiation spectroscopy". *NIM A* 345, 337 (1994). DOI: https://doi.org/10.1016/0168-9002(94)91011-1.

[119] J. Dudouet *et al. FIPPS analysis code.*

[120] G. Colombi. "High-resolution gamma-ray spectroscopy of fission fragments: improvement of the performance of the FIPPS instrument at ILL." MA thesis. Universita di Milano, 2020.

[121] G. Duchêne *et al.* "The Clover: a new generation of composite Ge detectors". *NIM A* 432, 90 (1999). DOI: 10.1016/S0168-9002(99)00277-6.

[122] B. Bruyneel *et al.* "Crosstalk properties of 36-fold segmented symmetric hexagonal HPGe detectors". *NIM A* 599, 196 (2009). DOI: 10.1016/j.nima.2008.11.011.

[123] BNM-LNHB/CEA. *Table de radionucleides*.

[124] NNDC data base for thermal neutron capture. *https://www.nndc.bnl.gov/capgam/*.

[125] *Private communication U. Köster*.

[126] D. Radford. *https://radware.phy.ornl.gov/main.html*.

[127] B. Bruyneel *et al.* "Pulse shape analysis and position determination in segmented HPGe detectors: The AGATA detector library". *Eur. Phys. J. A* 52, 70 (2016). DOI: 10.1140/epja/i2016-16070-9.

[128] A. Lopez-Martens *et al.* "γ-ray tracking algorithms: a comparison". *NIM A* 533, 454 (2004). DOI: 10.1016/j.nima.2004.06.154.

[129] E. Clement *et al.* "Conceptual design of the AGATA 1π array at GANIL". *NIM A* 855 (2017). DOI: 10.1016/j.nima.2017.02.063.

[130] J. Ljungvall *et al.* "Performance of the Advanced GAmma Tracking Array at GANIL". *NIM A* 955, 163297 (2020). DOI: 10.1016/j.nima.2019.163297.

[131] J. Allison *et. al.* "Recent developments in Geant4". *NIM A* 835, 186 (2016). DOI: 10.1016/j.nima.2016.06.125.

[132] *Private communication J. Dudouet*.

[133] G. Gilmore and M. Hemingway. *Practical gamma-ray spectroscopy*. John Wiley & Sons, 1995.

[134] I. Y. Lee *et al.* "Developments in large gamma-ray detector arrays". *Rep. Prog. Phys.* 66, 1095 (2003). DOI: 10.1088/0034-4885/66/7/201.

[135] C. A. Ur D. Bazzaco and N. Marginean. *GASP Data Analysis Program Package, GASPware*.

[136] K. H. Schmidt *et al.* "General Description of Fission Observables: GEF Model Code". *Nuclear Data Sheets* 131, 107 (2016). DOI: 10.1016/j.nds.2015.12.009.

[137] L. W. Iskra *et al.* "γ spectroscopy of the ^{96}Y isotope: Searching for the onset of shape coexistence before $N = 60$". *Phys. Rev. C* 102, 054324 (2020). DOI: 10.1103/PhysRevC.102.054324.

[138] S. Devons and L. J. B. Goldfarb. "Angular Correlations". *Kernreaktionen III / Nuclear Reactions III*. Vol. 8 / 42. Springer, 1957. DOI: 10.1007/978-3-642-45878-1_5.

[139] A. J. Ferguson. *Angular correlation methods in gamma-ray spectroscopy*. North-Holland Pub. Co., Wiley, 1965.

[140] K. S. Krane *et al.* "Directional correlations of gamma radiations emitted from nuclear states oriented by nuclear reactions or cryogenic methods". *At. Data Nucl. Data Tables* 11, 351 (1973). DOI: 10.1016/S0092-640X(73)80016-6.

[141] GRIFFIN Collaboration. *Angular correlation calculator*. 2015. DOI: 10.5281/zendodo.45587.

[142] N. Cieplicka-Oryńczak *et al.* "Contrasting properties of particle-particle and hole-hole excitations in ^{206}Tl and ^{210}Bi nuclei". *Phys. Lett. B* 802, 135222 (2020). DOI: 10.1016/j.physletb.2020.135222.

[143] N. Mărginean *et al.* "Shape Coexistence at Zero Spin in ^{64}Ni Driven by the Monopole Tensor Interaction". *Phys. Rev. Lett.* 125, 102502.10 (2020). DOI: 10.1103/PhysRevLett.125.102502.

[144] W. Urban *et al.* "New instrumentation for precise (n,γ) measurements at ILL Grenoble". *JINST* 8, P03014 (2013). DOI: 10.1088/1748-0221/8/03/P03014.

[145] G. Colombi *et al. "Gamma-Gamma angular correlations in a composite array of HPGe clover detectors", In prepration.*

[146] J.K. Smith *et al.* "Gamma–gamma angular correlation analysis techniques with the GRIFFIN spectrometer". *NIM A* 922, 47 (2019). DOI: 10.1016/j.nima.2018.10.097.

[147] The JEFF-3.1 Nuclear Data Library. *JEFF Report 21, OECD/NEA Data Bank (2006).*

[148] Nuball campaign. *Experimentally obtained fast neutron fission yields.*

[149] A.J.M. Plompen *et al.* "The joint evaluated fission and fusion nuclear data library, JEFF-3.3". *Eur. Phys. J. A* 56, 181 (2020).

[150] S. Mukhopadhyay. "Prompt γ spectroscopic studies of fragment nuclei in thermal neutron induced fission of ^{235}U". *Phys. Rev. C* 85, 064321 (2012). DOI: 10.1103/PhysRevC.85.064321.

[151] G. Lhersonneau *et al.* "First decay study of the very neutron-rich isotope ^{93}Br". *Phys. Rev. C* 63, 034316 (2001). DOI: 10.1103/PhysRevC.63.034316.

[152] D. Wilsem. "Nuclear structure studies with neutron-induced reactions : fission fragments in the N=50-60 region, a fission tagger for FIPPS, and production of the isomer Pt-195m". PhD thesis. Université de Caen Normandie, 2018.

[153] D. Reygadas *et al. Bormio Conference February 2020: "Neutron rich Kr isotopes studied at FIPPS".*

[154] R. B. Gerst *et al.* "Prompt and delayed gamma spectroscopy of neutron-rich ^{94}Kr and observation of a new isomer". *Phys. Rev. C* 102, 064323 (2020). DOI: 10.1103/PhysRevC.102.064323.

[155] T. R. Rodríguez. "Structure of krypton isotopes calculated with symmetry-conserving configuration-mixing methods". *Phys. Rev. C* 90, 034306 (2014). DOI: 10.1103/PhysRevC.90.034306.

[156] K. Nomura *et al.* "Structure of krypton isotopes within the interacting boson model derived from the Gogny energy density functional". *Phys. Rev. C* 96, 034310 (2017). DOI: 10.1103/PhysRevC.96.034310.

[157] K. Nomura, R. Rodríguez-Guzmán, and L. M. Robledo. "Description of neutron-rich odd-mass krypton isotopes within the interacting boson-fermion model based on the Gogny energy density functional". *Phys. Rev. C* 97, 064313 (2018). DOI: 10.1103/PhysRevC.97.064313.

[158] M. Keim *et al.* "Laser-spectroscopy measurements of $^{72-96}$Kr spins, moments and charge radii". *Nucl. Phys. A* 586, 219 (1995). DOI: 10.1016/0375-9474(94)00786-M.

[159] J. Skalski *et al.* "Equilibrium shapes and high-spin properties of the neutron-rich A $\sim$ 100 nuclei". *Nucl. Phys. A* 617, 282 (1997). DOI: https://doi.org/10.1016/S0375-9474(97)00125-5.

[160] C. Lizarazo et al. "Metastable States of ^{92,94}Se: Identification of an Oblate K Isomer of ^{94}Se and the Ground-State Shape Transition between N=58 and 60". *Phys. Rev. Lett.* 124, 222501 (2020). DOI: 10.1103/PhysRevLett.124.222501.

[161] T. Rzaca-Urban *et al.* "$\nu(g_{7/2}h_{11/2})_{9-}$ neutron excitation in ^{92,94,96}Sr". *Phys. Rev. C* 79, 024319 (2009). DOI: 10.1103/PhysRevC.79.024319.

[162] V. F. Weisskopf. "Radiative Transition Probabilities in Nuclei". *Phys. Rev.* 83, 1073 (1951). DOI: 10.1103/PhysRev.83.1073.

[163] P. Baczyk *et al.* "Near-yrast excitations in nucleus ^{83}As: Tracing the $\pi g_{9/2}$ orbital in the ^{78}Ni region". *Phys. Rev. C* 91, 047302 (2015). DOI: 10.1103/PhysRevC.91.047302.

[164] Y. X. Luo *et al.* "New level schemes and octupole correlations of light neutron-rich lanthanum isotopes ^{143,144}*La*". *Nucl. Phys. A* 818, 121 (2009). DOI: 10.1016/j.nuclphysa.2008.12.004.

[165] W. Urban *et al.* "Octupole correlations in neutron rich, odd-A lanthanum nuclei". *Phys. Rev. C* 54, 945 (1996). DOI: 10.1103/PhysRevC.54.945.

[166] J. K. Hwang *et al.* "Rotational bands in $^{101-103}$Nb and ^{98,100}Y nuclei and identification of yrast bands in ^{146}La and ^{149}Pr". *Phys. Rev. C* 58, 3252 (1998). DOI: 10.1103/PhysRevC.58.3252.

[167] Y. X. Luo *et al.* "The first observation of a deformed Kπ=1+ ground-state band in ^{100}Nb and the high-spin level scheme of its 4n fission partner ^{148}La". *Nucl. Phys. A* 825 (2009). DOI: https://doi.org/10.1016/j.nuclphysa.2009.04.006.

[168] H. Sievers. *Nucl. Data Sheets* 62, 271 (1991).

[169] E. C. May and S. A. Lewis. "Reaction 86Kr(d,3He)85Br". *Phys. Rev. C* 5 (1972). DOI: 10.1103/PhysRevC.5.117.

[170] K. Sieja and F. Nowacki. "Shell quenching in ^{78}Ni: A hint from the structure of neutron-rich copper isotopes". *Phys. Rev. C* 81, 061303 (2010). DOI: 10.1103/PhysRevC.81.061303.

[171] M.-G. Porquet and O. Sorlin. "Evolution of the N=50 gap from Z=30 to Z= 8 and extrapolation toward ^{78}Ni". *Phys. Rev. C* 85, 014307 (2012). DOI: 10.1103/PhysRevC.85.014307.

[172] T. Materna *et al.* "Low spin structure of ^{86}Se: Confirmation of γ collectivity at N=52". *Phys. Rev. C* 92, 034305 (2015). DOI: 10.1103/PhysRevC.92.034305.

[173] I. Gratchev *et al.* "Identification of excited states and collectivity in ^{88}Se". *Phys. Rev. C* 95, 051302 (2017). DOI: 10.1103/PhysRevC.95.051302.

[174] V. Paar. "Coupling of a three-particle (hole) valence-shell cluster to quadrupole vibrations (Alaga model): The Z = 50 region: odd Ag and I isotopes; and the Z = 28 region: odd Mn and Ga isotopes". *Nucl. Phys. A.* 211, 29 (1973). DOI: 10.1016/0375-9474(73)90763-X.

[175] K. Sieja et al. "Shell model description of zirconium isotopes". *Phys. Rev. C* 79, 064310 (2009). DOI: 10.1103/PhysRevC.79.064310.

[176] K. Sieja et al. "Laboratory versus intrinsic description of nonaxial nuclei above doubly magic ^{78}Ni". *Phys. Rev. C* 88, 034327 (2013). DOI: 10.1103/PhysRevC.88.034327.

[177] M. Honma *et al.* "New effective interaction for f_5pg_9-shell nuclei". *Phys. Rev. C* 80, 064323 (2009). DOI: 10.1103/PhysRevC.80.064323.

[178] E. Caurier et al. "Influence of Pairing on the Nuclear Matrix Elements of the Neutrinoless beta-beta Decays". *Phys. Rev. Lett.* 100 (2008). DOI: 10.1103/PhysRevLett.100.052503.

[179] S. Kahana, H. C. Lee, and C. K. Scott. "Effect of Woods-Saxon Wave Functions on the Calculation of $A = 18, 206, 210$ Spectra with a Realistic Interaction". *Phys. Rev.* 180, 956 (1969). DOI: 10.1103/PhysRev.180.956.

[180] K. Sieja and F. Nowacki. "Core polarization effects in effective Hamiltonians far from stability". *Nucl. Phys. A* 857, 9 (2011). DOI: https://doi.org/10.1016/j.nuclphysa.2011.03.006.

[181] D. Reygadas *et al. In prepration.*

[182] A. Chebboubi *et al.* ""Development of a Gas Filled Magnet spectrometer within the FIPPS project"". *NIM B* 376, 120 (2016). DOI: 10.1016/j.nimb.2016.02.008.

[183] Y. H. Kim *et al.* "Development of a gas filled magnet for FIPPS phase II". *NIM B* 463, 269 (2020). DOI: 10.1016/j.nimb.2019.05.022.